Title
Electron Microscopy and Analytical X-ray Characterization of Compositional and Nanoscale Structural Changes in Fossil Bone

Author
Boatman, Elizabeth

Publication Date
2012

Peer reviewed|Thesis/dissertation

Electron Microscopy and Analytical X-ray Characterization of Compositional and Nanoscale Structural Changes in Fossil Bone

By

Elizabeth Marie Boatman

A dissertation submitted in partial satisfaction of the

requirements for the degree of

Doctor of Philosophy

in

Engineering - Materials Science and Engineering

in the

Graduate Division

of the

University of California, Berkeley

Committee in charge:

Professor Ronald Gronsky, Chair
Professor Robert Ritchie
Professor Angelica Stacy

Fall 2012

Abstract

Electron Microscopy and Analytical X-ray Characterization
of Compositional and Nanoscale Structural Changes in Fossil Bone

By
Elizabeth Marie Boatman

Doctor of Philosophy in Engineering - Materials Science and Engineering
University of California, Berkeley

Professor Ronald Gronsky, Chair

The nanoscale structure of compact bone contains several features that are direct indicators of bulk tissue mechanical properties. Fossil bone tissues represent unique opportunities to understand the compact bone structure/property relationships from a deep time perspective, offering a possible array of new insights into bone diseases, biomimicry of composite materials, and basic knowledge of bioapatite composition and nanoscale bone structure. To date, most work with fossil bone has employed microscale techniques and has counter-indicated the survival of bioapatite and other nanoscale structural features. The obvious disconnect between the use of microscale techniques and the discernment of nanoscale structure has prompted this work.

The goal of this study was to characterize the nanoscale constituents of fossil compact bone by applying a suite of diffraction, microscopy, and spectrometry techniques, representing the highest levels of spatial and energy resolution available today, and capable of complementary structural and compositional characterization from the micro- to the nanoscale. Fossil dinosaur and crocodile long bone specimens, as well as modern ratite and crocodile femurs, were acquired from the UC Museum of Paleontology.

Preserved physiological features of significance were documented with scanning electron microscopy back-scattered imaging. Electron microprobe wavelength-dispersive X-ray spectroscopy (WDS) revealed fossil bone compositions enriched in fluorine with a complementary loss of oxygen. X-ray diffraction analyses demonstrated that all specimens were composed of apatite. Transmission electron microscopy (TEM) imaging revealed preserved nanocrystallinity in the fossil bones and electron diffraction studies further identified these nanocrystallites as apatite. Tomographic analyses of nanoscale elements imaged by TEM and small angle X-ray scattering were performed, with the results of each analysis further indicating that nanoscale structure is highly conserved in these four fossil specimens.

Finally, the results of this study indicate that bioapatite can be preserved in even the most ancient vertebrate specimens, further supporting the idea that fossilization is a preservational process. This work also underlines the importance of using appropriately selected characterization and analytical techniques for the study of fossil bone, especially from the perspective of spatial resolution and the scale of the bone structural features in question.

Acknowledgments

There are several individuals and organizations whom I wish to thank for their pivotal roles in the success of my graduate research. Foremost, I thank Dr. Mark Goodwin of the UC Museum of Paleontology for his constant support of not only my research but my development as a student and young professional scientist. Over the course of a four-year mentorship, Dr. Goodwin played a critical role in my overall success as a student at UC Berkeley; he directed me to courses, collaborators, journal articles, additional financial support, laboratory resources, and much more. Without his support, I would not be who or where I am today, and I look forward to continued work with Dr. Goodwin in the future.

Within my home department, Materials Science and Engineering, I extend tremendous thanks to my research advisers, Professors Ronald Gronsky and Robert Ritchie, for their unending support, both professional and academically. During my time under their mentorship, I was able to present my dissertation work at four professional conferences. Additionally, at two of these conferences, my work was the recipient of student prizes. Without the financial resources and professional support provided by these individuals, my work likely would not have received such esteemed recognition.

I thank the many other individuals and research groups who contributed to the success of my doctoral research. In the department of Chemical Engineering and Materials Science at the UC Davis Professor Nigel Browning and his research group provided me with additional intellectual resources and support, while Fred Hayes and Andrew Thron dedicated many hours to my success in the International Center for Electron Microscopy (ICEM). In the department of Geology at the UC Davis, Sarah Roeske and Nick Botto provided tremendous support for all electron microprobe and wavelength-dispersive X-ray spectroscopy results presented in this work. In the department of Chemistry at the UC Berkeley, Jessica Smith in the research group of Professor Paul Alivisatos dedicated a significant amount of time to overseeing the collection of small-angle X-ray scattering data for this work. Finally, I thank the research groups of Dr. Tony Tomsia (at the Lawrence Berkeley National Laboratory) and Professor Peidong Yang for access to scanning electron microscope resources.

Again within my home department, I thank Riley Reese, who participated in a variety of supporting capacities with respect to my doctoral research while he was an undergraduate. I thank Dr. Chris Kumai for his support with respect to my transmission electron microscopy and X-ray diffraction experiments.

Lastly, I thank the following funding sources for funding not only my graduate academic education but also my research. In total, I received five years of support from the National Defense Science and Engineering Fellowship (3 years) and the UC Berkeley Chancellor's Fellowship (2 years). I received a graduate dissertation fellowship from the Phi Beta Kappa Association of Northern California, providing critical support for the final stages of my work in 2012. I also received a Jurassic Foundation research grant, which provided key funding for specimen preparation resources.

Foreword

Bone is a material of interest to scientists in disciplines spanning academia, from archeology to evolutionary biology to materials engineering, and beyond. Historically, these disciplines have studied bone in near isolation, despite the fact that their pursuits have a striking degree of overlap. From the structural and biological perspectives alone, for example, disparate academic history has led to the use of multiple terms for describing the same features or tissues. In a sense, this disconnected academic history has perpetuated the modern intellectual disconnect between the different disciplines. Only in recent years has an increasing number of bone structure and biological scientific pursuits been put forth by unique, interdisciplinary teams of scientists, engineers, and medical professionals. Long overdue, these interdisciplinary endeavors have catalyzed an entirely new depth of scientific inquiry into bone composition, structure, mechanical properties, and biology.

To date, the materials scientist's interest in bone has established strong relationships with mechanical engineering, bioengineering, and the larger medical community. Meanwhile, paleontology persists as a relatively unexploited potential interdisciplinary relationship. In recent years, only a handful of such relationships have been developed, all of which have been forged at other institutions despite the fact that UC Berkeley not only maintains one of the finest paleontological collections in the country but also has one of the strongest materials science research programs. While engineers have been largely reticent to embrace fossilized tissues, paleontologists have pushed ahead with tremendous amounts of cutting edge inquiry.

Modern paleontological investigations have, on their own, penetrated to the heart of the mechanical engineering and materials science disciplines. Bone morphology is no longer simply used to establish evolutionary relationships but to develop complex, testable hypotheses about the evolution of flight, the jaw mechanics of extinct species, the head-butting and battling behaviors of dinosaurs, and the accessible quadrupedal gaits of gigantic vertebrates whose bones bore exceptional loads in stationary positions alone. There was a point in time where the paleontologist's most advanced characterization tool was an optical microscope. Today, paleontologists are masters of tomography, finite element modeling, X-ray fluorescence, electron microscopy, X-ray scattering and diffraction, *etc*. Paleontologists, in their studies of fossilized tissues, are employing the tools and techniques of modern mechanical engineers and materials scientists and *still* these interdisciplinary relationships have scarcely been forged. Why?

Engineers, while fascinated with the possibility of conducting collaborative research with paleontologists, have a skeptical predisposition toward fossilized tissues, and rightly so. Fossilized bone has undoubtedly been changed from its original composition and form in a cumulative process called diagenetic alteration, which includes any chemical, biological, and physical changes that have occurred to a bone since death of the tissue. Within paleontology, many of these diagenetic processes have only been recently understood in any significant way. In some cases, the precise underlying mechanism for the process is still under exploration. This means that an entire suite of questions surrounding the diagenesis and fossilization of bone still exists in paleontological studies. It is understandable that scientists from the engineering disciplines find this lack of answers disconcerting.

Yet, the picture is not so bleak.

No scientific investigation is ever perfect, and advanced inquiries of fossil bone tissues are indeed accessible and practical as long as they are conducted within well-defined constraints. This is precisely where the mechanical engineers and materials scientists, despite their skepticism and reticence, actually have a set of very useful skills and tremendously important knowledge to impart to paleontological inquiries. Further, this interdisciplinary relationship has the potential to be much more than one-sided.

Many modern mechanical and materials engineering inquiries are transfixed with the biomimicry approach. That is, the solutions to many complex engineering problems are already being sought in nature. Such problems range from composite design for impact absorption to structural material design for strength applications to surface design for medical implants. Bone, especially, is a material under current, intense scientific scrutiny in the engineering fields, with the potential to provide sophisticated solutions to or substantial insight into a variety of crucial problems, some of which I have just listed, above.

These problems, in particular, provide an opportunity to illustrate why not only bone, but *fossil* bone, may offer a very unique perspective that the modern engineer would do well to engage. For example, deer antler is under investigation for impact absorption applications based on its demonstrated crashworthiness in mechanical testing experiments. The stature and rack size of modern deer, however, pale in comparison to that of the extinct *Megaloceros giganteus*, which stood over two meters tall at the withers and possessed an expansive rack measuring nearly 3 m across and weighing nearly 50 kg. By their sheer size, impact forces felt during male combat would have been tremendous. So why not study the antler racks of *Megaloceros giganteus* instead of deer? Because the antlers of *Megaloceros giganteus* survive only as fossils, and the diagenetic changes in antler fossils prevent any form of meaningful direct mechanical testing.

The study of compact bone as a model composite material for load-bearing structural applications provides us with a second example. Most work to date on compact bone mechanical properties and structure/property relationships has come from the analysis of human and cow femur. Meanwhile, the largest terrestrial vertebrates ever to have existed, such as *Paraceratherium* or the sauropods, among many others, are all extinct. Any bone scaling laws predicted based on the observations of small- to medium-sized vertebrates will not be followed by the gigantic vertebrates; yet, the long bones of gigantic vertebrates undoubtedly bore the greater static and dynamic loads. Again, why is composite fabrication work for structural applications only looking at comparatively small, modern species? Because the gigantic vertebrates are all extinct, and their femur compact bone has undergone complex, unique changes that are only partially understood.

Ultimately, demonstrating that the study of fossil bone tissues may be of tremendous value toward modern engineering problems depends on one thing. While fossil bones have undoubtedly changed since they were living tissues, and these changes may be complex and myriad in their own right, nonetheless the capacity to identify and quantify these changes is of critical importance toward engineering endeavors, not just paleontological. Fossil bones may not be directly testable for their mechanical properties but modern bones are, and if the compositional and structural diagenetic changes can be effectively identified and quantified, then this opens the door to the testing of modern tissues that possess similar structures for the back-inference of fossil bone tissue properties by analogy. From there, the tissue properties can be

extrapolated to the whole bone behavior under dynamic loading conditions. Alternatively, if sophisticated structure/property models can be developed from modern bone tissues, then new bone structures observed in fossil specimens can be dissected and applied to these modern bone-based models for the possibility of extracting new, complex structure/property behaviors. Further, the physiological and evolutionary context, or "deep time," perspective that fossil bones can provide has grand implications for our understanding of damage control mechanisms in modern compact bone, which has further implications for engineered materials that have been tuned to specific mechanisms for strength, fatigue, or impact absorption applications. And, finally, this brings us to the motivation for my study.

This dissertation work was developed to address the problem outlined above: whether the diagenetic changes that fossil compact bone tissues have suffered throughout millions of years of burial in sedimentary environments can actually be identified and quantified with modern characterization and analytical techniques. More specifically, this study focuses on the nanoscale constituents of bone (in terms of structure and composition), under the assumption that the preservation of nanoscale constituents has substantial and direct implications for the higher structural orders of bone tissue. Hence, the successful identification and analysis of bioapatite and other nanoscale structural features of interest in the fossil bone specimens selected for analysis is the primary focus of this work.

Table of contents

1. Introduction

This work is at the forefront of interdisciplinary inquiries into the structure/property relationships of bone, tying together the disciplines of materials science and engineering with paleontology. As such, this investigation necessitates a thorough treatment of the relevant background, from the composition and structure of bone, to the mechanical behavior of bone, to the manner in which these characters change as a result of fossilization or in the context of extinct species, such as the dinosaurs. The questions at the heart of this work revolve around the identity of fossil bone from the chemical and structural perspective, particularly with respect to the manner in which chemical and other diagenetic changes have affected the structure of dinosaur bones over the course of millions of years of environmental exposure. Further, in light of the recent push in paleontology to redefine fossilization as a preservational process, this work investigates the chemical and structural changes that occur in fossil bones with respect to modern bone standards. While much of this work incorporates analytical techniques, ultimately this investigation is of a qualitative nature (although based on quantitative approaches), in which comparisons of fossil bone specimens to modern bone specimens are routinely drawn.

To honor the questions at the heart of this work, which address the chemical and other diagenetic changes and their implications for the structural features of interest in fossil bones, the pertinent experimental techniques used must necessarily span from electron microscopy (atomic-scale resolution) to X-ray spectroscopic methods (microscale resolution). As later explored in greater depth, to support the direct relevance of this work to other current investigations of modern bone within the engineering disciplines, the techniques used here have been carried out with every attempt to engage the materials scientist's perspective. Ideally, the end product of this investigation will, therefore, not simply identify and perhaps even quantify the relationships of chemical and diagenetic changes to that of structure (with further implications for properties) but will also shed new light on the appropriate analysis techniques for studying fossil bones at the nano- and microscales.

As indicated above, the remainder of this chapter serves to flush out the necessary background information from both the materials science and paleontology perspectives. First, the engineer's interest in bone is explored in depth, with sub-sections that cover, in order, the bioapatite mineral, the collagen protein, the nanoscale structure of bone, the higher order structures, and our current understanding of structure/property relationships in bone. Second, each of these topics is revisited from the paleontological perspective, with the addition of relevant background information from the paleontological literatures; for example, these sections detail what is known about the consequences of diagenesis for that particular feature (*e.g.*, bioapatite or collagen, *etc.*) in bone. Third, this chapter concludes with a description of the problem statement and a synopsis of the scope of this work.

1.1. Bone as a material of interest

In recent decades, materials scientists and engineers have developed a keen interest in bone. Bone possesses an incredibly unique and intriguing set of mechanical properties; these properties (*e.g.*, a combination of high strength and high toughness) are the direct result of the composite nature and complex hierarchical design of bone tissue. Much recent work has focused

on the structure/property relationships possessed by unique bone tissues (Launey *et al.*, 2010; De Santis *et al.*, 2007). These relationships are inherently complex, with each scale of the hierarchy exhibiting distinct structural features with very particular abilities to bear load or accommodate impact energies (Nyman *et al.*, 2005). Hence, gaining a complete picture of the structure/ property relationships of bone is a vastly complex task (Fratzl, 2007).

Nonetheless, disciplines from across the modern research campus have demonstrated their interest in bone. These interests span from medical applications to engineered materials to basic anthropological, paleontological, and biological questions of weighty intrigue. Many researchers talk of pursuing interdisciplinary lines of inquiry and, indeed, much funding is awarded today based on interdisciplinary endeavors. However, there is, perhaps, no single more interdisciplinary line of inquiry than that of research on or relating to bone.

Bone pathologies have inspired a vast array of investigations, and I begin this discussion with an overview of therapeutic endeavors. In instances of substantial bone lesions, which may be the result of either trauma or the removal of diseased tissue, surgeons have for some time sought replacement materials of sufficient mechanical integrity and biocompatibility. In the past and even today, irradiated cadaveric bone grafts (allografts) have been used for such purposes. Cadaveric bone grafts are gamma-irradiated to prevent host immune responses, which can result in local inflammation *in vivo* as well as tissue rejection. However, the irradiation of bone to kill the native cells (or bacteria, prions, viruses, *etc.*) within the bone tissue is a contentious process, favoring biocompatibility over mechanical integrity (Barth *et al.*, 2011; Nguyen *et al.*, 2007). Recent investigations have demonstrated that the irradiation of cadaveric bone tissue reduces the mechanical integrity of the material, which partially undermines the intent to utilize this tissue for grafting applications.

To combat such dilemmas, other researchers have pursued alternative, biocompatible engineered materials, such as surface-engineered implants or scaffolds of various structures and compositions. In the earliest instances, stainless steels were used, followed by cobalt-chromium alloys (superior resistance to corrosion), then surface-modified titanium (favorable low-weight and mechanical performance as well as high corrosion resistance) (Van Noort, 1987). Other investigations pursued the effects of surface topography (*e.g.*, grooving, sand-blasting, acid etching, *etc.*) and surface TiO_2 thickness, for titanium implants in particular. More recently, porous tantalum (*i.e.*, tantalum trabecular metal or TTM; Balla *et al.*, 2010) and biodegradable magnesium alloys (Witte *et al.*, 2005) have also been investigated for use as bone implants. Today, metal is sometimes foamed to increased the osseointegration volume. Beyond traditional metal, metal alloy, and biodegradable metal implants, there are many other materials implanted in bone today; I will not discuss these further here, as the literature is vast. Instead, now I turn our focus to the engineering of calcium phosphate coatings for implanted bone devices.

Beyond surface topography engineering and metal foaming, hydroxyapatite coatings have also been investigated for reductions in bone ingrowth times. Most metals are bio-inactive, which has prompted further investigations of bio-active ceramic coatings. Specifically, hydroxyapatite is of interest because the ceramic coating provides the precise atomic species needed to form new bone mineral. Studies of hydroxyapatite coatings, in particular, have found reduced ingrowth times due to the presence of the osteophilic hydroxyapatite layer (Thomas *et al.*, 1987). Throughout recent decades, many investigations have pursued the synthetic

fabrication of a variety of calcium phosphates, including hydroxyapatite, the parent structure of bone mineral (Osborn & Newesely, 1980). In the past, hydroxyapatite has proven difficult to grow with sufficient crystallinity, in a nanocrystalline size, or without eliciting an inflammatory response upon implantation. Some recent lines of inquiry have sourced the precursor material from cadaver bone or fossil bone beds (Pesenti *et al*., 2010); in these instances, the bioapatite/ hydroxyapatite undergoes extensive purification processing before the final, fabricated material results. In short, there is a tremendous amount of current work underway with respect to the materials, surface engineering, *etc.*, of bone implanted devices for load-bearing purposes.

The fields interested in these therapeutic applications span from the medical and clinical to the bioengineering to the mechanical or materials engineering disciplines. Clearly, from the perspective of the bionic implant alone, bone is a material of tremendous interdisciplinary interest. However, in addition to medical applications, bone tissue is of interest to engineers for a variety of other applications. These applications seek to harness the unique structure/property relationships of bone (or other natural structural composites) for impact absorption, high strength and high toughness, and other fatigue resistant, load bearing applications.

The natural composite materials of interest to materials engineers include seashell nacre, bone, and antler, among others. A variety of works have explored the hierarchical structures of these materials, with respect to mechanical behavior, and today, many investigators are attempting to fabricate complex ceramic composites based on the identified structure/property relationships in these materials. Again, this is a vast field of scientific inquiry, and I will not explore it in depth. However, I refer the reader to several recent works on the subject (Kulin *et al.*, 2010; Launey *et al.*, 2009; Fratzl, 2007). Engineers' interest in bone begins to overlap with that of the social science and biological science disciplines somewhere between the realm of medical knowledge (*i.e.*, bone pathologies) and engineered materials. In particular, the areas of overlap include the techniques of analysis, the aspects of interest (*e.g.*, growth, pathologies), and questions regarding structure/property relationships, among others.

Anthropological interests in bone have traditionally spanned questions pertaining to prehistoric societies and civilizations. Some scientists have pursued means of identifying different types of animal bone or of discerning animal bone from human bone (Martiniaková *et al.*, 2006). The anthropological and biological disciplines also overlap with each other in the field of osteohistology. Within this field, osteohistological forensics work has become increasingly important, both in the pre-historic and modern time frames. Modern forensic osteohistology explores questions pertaining to the significant trauma incurred by individuals, whether living or dead. In many instances, these skilled scientists search for answers in criminal cases. For example, chronic child abuse can be detected from radiographs. In their pursuit of answers to questions surrounding age, sex, location of origin, occupation, and health, all of which can be used to identify a person or a cause of death, forensic osteohistologists utilize a vast array of incredibly detailed knowledge of human bone growth. In many instances, for both anthropologists and forensic osteohistologists, the bones of an individual may be the sole surviving tissue of a deceased individual; therefore, bone is a crucially important material of interest in these fields.

Many modern paleontologists, geologists, and biologists study bone in a manner similar to that of anthropologists and forensic osteohistologists. Paleontology and geology have tended

to focus on the morphological characters of bone and how the bone has changed as a result of fossilization; while biologists have tended to delve more into the structure and the mechanisms of growth, both normal and pathological. In all of these disciplines, excluding engineering, the genetic and phylogenetic relationships of vertebrates and individuals are crucially important; that is, the "deep time" perspective is a central component. While engineers have not typically been interested in or particularly concerned with the phylogenetic and evolutionary aspects of bone, nonetheless paleontologists have pushed to forge unique relationships with engineers, by asking questions about the performance of extinct vertebrate bones under dynamic loading conditions, *etc*.; simply by exploring modern paleontological literature, which is inexplicably dependent upon bone for its scientific robustness, we have now come full circle back to engineering and the engineer's interest in bone material.

In short, somewhere in the realm of diverse vertebrate lifeforms, and within the context of evolutionary adaptation and origin, we find ourselves in a field of science brimming with unique and intriguing bone structures and tissues. From the engineering and medical perspective, we have developed extensive insight into the structure/property relationships of bone, bone pathologies, and the engineering of biomaterials for implanted devices as well as the engineering of biomimicked materials for other engineering applications. Additionally, from the biological perspective, we realize that no bone structure or tissue (or growth pattern or pathology) exists in isolation; that is, phylogenetic relationships are critical not only for the pursuits of many evolutionary biologists and paleontologists but also for the pursuits of engineers, who are so interested in developing biomimicked materials based on this impressive high-strength, high-toughness material. This is precisely where my work comes in.

1.1.1. Bioapatite

Apatite is a class of brittle ceramic materials, many of which are geologically occurring and some of which are biologically occurring. Today, many apatites are also manufactured by synthetic processes. Hydroxyapatite ($Ca_{10}(PO_4)_6(OH)_2$) is a specific type of apatite and serves as the base structure for bone mineral. Bone mineral was first identified as a crystalline calcium phosphate in 1926; X-ray diffraction analyses were used to determine that the structure of the bone crystal was similar to that of geological apatite. Because of the historical ties between the identity of bone mineral and the already identified geological apatite minerals, the history of bone mineral investigation has included the interest of researchers from across the disciplines, including geologists and chemists. However, it was learned very early that the biological hydroxyapatite was distinctly different from the common geological forms. Such differences include the characteristic composition of the impure hydroxyapatite, the morphology of the crystallites, and the sizes of the crystallites. The remainder of this section will focus on the following: the crystallography of hydroxyapatite, the relationship of hydroxyapatite to the other apatites and calcium phosphates, and the distinct identity of bioapatite and its origin. The mechanical performance aspects of bioapatite will be discussed later, in section 1.1.5, and the consequences of fossilization for bioapatite will be considered in section 1.2.

Hydroxyapatite has hexagonal symmetry (space group $P6_3/m$) with lattice parameters of $a = b = 9.432$ Å and $c = 6.881$ Å, yielding a c/a axis ratio of 0.730 and exhibiting six-fold symmetry about the c-axis (Kay *et al.*, 1964). Hydroxyapatite is inherently brittle, as many

complex ceramics are. The favored slip system of fluorapatite is {001}<100>, which resides within the basal plane (Saka *et al.*, 2008), although nanoindentation data of hydroxyapatite single crystals indicates a lower yield strength in the (100) direction, implying that perhaps bioapatite favorably slips in the direction of bone loading (Zamiri & De, 2011). Geologically derived apatite crystals tend to be hexagonal prisms, as a result of the internal crystallography of the material. The hexagonal hydroxyapatite unit cell structure is essentially defined around the positions of hydroxide ions (OH^-); along the *c*-axis, the lattice points reside within a channel-like column of OH^-. Although the simplest description of hydroxyapatite simplifies to half the stoichiometric equation given above (visualized as an equilateral triangle within the basal plane), the structure is most often depicted as a diamond with twice the reduced stoichiometric equation, because this reflects the symmetry of the structure. A visual depiction of the lattice, as first defined by Kay *et al.* (1964) in *Nature*, is given in Figure 1.1. As can be seen in the figure, the OH^- positions that define the lattice are coordinated by one set of Ca^{2+} (there are six in total). These Ca^{2+} ions are then coordinated by the phosphate (PO_4^{3-}) groups, and beyond, the adjacent sets of PO_4^{3-} groups coordinate the second type of Ca^{2+} position. The second set of Ca^{2+} resides in six-fold symmetry and further defines key points of the hexagonal lattice: these ions sit in the basal (001) and intermediate (002) planes, in columns located at the centers of the equilateral triangles. Both the OH^- and Ca^{2+} stacks form channels that can promote more rapid diffusion and exchange of these species versus the PO_4^{3-} groups or that of the first Ca^{2+} location. This is particularly true for the hydroxide groups. As an ionic crystal, hydroxyapatite must maintain local internal charge balance. These charge balances affect both the diffusion properties of the hydroxyapatite as well as the formation properties, and the consequences are further discussed within the following section and then later in section 1.2, when exploring the consequences of fossilization on the bioapatite structure.

The other apatites can be classified either as end-member (stoichiometric) apatites or substituted apatites; however, they are all structurally and chemically related with their distinctions depending solely on the identities of the cation or the anion, which resides on the lattice points. For example, in fluorapatite ($Ca_{10}(PO_4)_6F_2$), fluoride ions (F^-) substitute for the OH^- positions, resulting in an *a*-axis contraction to 9.398 Å while the *c*-axis parameter remains virtually unchanged (Hughes *et al.*, 1989). Similarly, when chloride ions (Cl^-) substitute for the OH^- position to form chlorapatite ($Ca_{10}(PO_4)_6(OH)_2$), the *a*-axis parameter is extended to 9.598 Å, while the *c*-axis parameter contracts to 6.776 Å. The ionic radii of the anions increases from smallest to greatest in the order of F^-, OH^-, Cl^-; it is the increasing ionic radius of the anion that expands the apatite structure. Other apatite species include various substitutions of the Ca^{2+} positions by divalent cations (Sr^{2+} or Mg^{2+}). Additionally, carbonated (CO_3^{2-}) apatites include at least fractional substitution of the PO_4^{3-} group. Further, a variety of cation impurities are commonly associated with the apatite structure, resulting from either natural occurrences or biological occurrences and substituting for the Ca^{2+} position in a charge-compensating manner (*i.e.*, if Na^+ substitutes for the Ca^{2+} position, then a neighboring OH^- group must be lost to maintain internal local charge balance). In geological literatures, impure calcium apatites (particularly those with partial substitution of CO_3^{2-} for the PO_4^{3-} groups) are often called francolite.

There are other classes of calcium phosphate minerals, some geologically occurring in relatively high purity and others synthetically derived. In many instances, these phases have been identified or investigated for their possible role in bone precipitation/chemistry or for biomedical applications. Further, the poorly crystalline and highly substituted nature of bone mineral has prompted many investigations of the similar, highly pure synthetic calcium phosphate minerals. There are several varieties of tricalcium phosphates (TCP), and β-TCP in particular is perhaps the best researched, in large part because of its potential use as a precursor for the preparation of apatite or in biomedical applications. The crystal structure of β-TCP has been identified as rhombohedral (*R*3*c*) with a = 10.439 Å and c = 37.375 Å (Yashima *et al.*, 2003). Amorphous calcium phosphate (ACP, $Ca_9(PO_4)_6$) and octacalcium phosphate (OCP, $Ca_8H_2(PO_4)_6{\cdot}5H_2O$) have both been proposed as precursors to the hydroxyapatite bone mineral structure (Posner & Betts, 1975; Brown *et al.*, 1987); today, evidence for this remains unsubstantiated overall, yet these phases have remained of interest for other biomedical applications (Rey *et al.*, 2009). While ACP has been reported to be amorphous based on X-ray diffraction studies, other studies of OCP have identified the structure as similar to that of hydroxyapatite. In particular, OCP is defined as belonging to the $P\underline{1}$ space group with an a-axis of 19.692, b-axis of 9.523, c-axis of 6.835, α angle of 90.15°, β angle of 92.54°, and γ angle of 108.65° (Brown, 1962). Despite their apparent compositional and structural similarities to bone mineral, the calcium phosphate minerals are all distinct compounds, and today, it is generally believed that the formation of bone mineral *in vivo* commences with the precipitation of impure, poorly crystalline hydroxyapatite nuclei.

Bone mineral is a specific variant of hydroxyapatite. It is not only uniquely identified by its composition but also by its morphology and size. While there has been much historical controversy over the identity of the bone mineral precursor phase (*i.e.*, which calcium phosphate phase nucleates first), today it is largely accepted that bone mineral nucleates and crystallizes in the hydroxyapatite parent structure (Bonar *et al.*, 1983). Bone mineral precipitates from the interstitial fluid of vertebrates. The interstitial fluid is closely related to the plasma, hence the ionic composition of the interstitial fluid closely resembles that of blood (a high ionic content). In turn, this affects the composition of the precipitating bone mineral, as well as any subsequent ion exchange. Ions such as K^+, Na^+, Ca^{2+}, and Mg^{2+} all play critical roles in the generation of potentials across cellular membranes. These ions are key components of blood, and as such, these ions are also commonly found as impurities in the bone mineral hydroxyapatite structure. Other common impurity ions include F^-, CO_3^{2-}, Sr^{2+}, and Ba^{2+} (Boivin, 2007). Because the composition of vertebrate blood varies relatively little across species, the composition of bone mineral also tends to be highly similar across species. For this reason, the composition of bone mineral can actually be defined as its own class of apatite (although not a stoichiometric member). Throughout the rest of the manuscript, I refer to bone mineral as *bioapatite*; in other works, bone mineral has often been referred to as *carbonated hydroxyapatite* or *impure hydroxyapatite* or simply *hydroxyapatite*/*hydroxylapatite*.

Bioapatite crystals are distinct versus other apatites in large part due to their composition alone (*i.e.*, impure hydroxyapatite of characteristic impurity species). However, bioapatite is also distinct versus other similarly-composed geologically occurring hydroxyapatites by the size and morphology of the mineral crystallites. The minimum energy surfaces of the hydroxyapatite

crystal structure are the basal and prismatic planes, which is why geological hydroxyapatite tends to grow in a hexagonal prism form. In bone, however, the bioapatite precipitates on a rather compact, highly aligned type I collagen fiber network; in healthy bone tissue, the bioapatite crystallites are therefore nanocrystalline (Boskey, 2003). The precise precipitation locations are controlled by various charged groups on the collagen-associated proteins, while the form of the collagen fibers (*i.e.*, many parallel, tightly bundled molecules) forces the growing bioapatite crystallites into a space-confined conformation. The crystallites grow with their *c*-axes parallel to the length of the collagen fibers; in long bones, the majority of bioapatite crystallites are therefore aligned with the length of the bone shaft (high texture). The space-confinement forces the bioapatite into a thin, plate-shaped morphology. The facets of the nanoplate (also referred to as *platelet* in the literature elsewhere, although this terminology is avoided here because it is confusing and ill-suited for biological works) are the {100} prismatic planes and the (001) basal planes, with the {100} surfaces predominating (the large faces of the plate). Additionally, the nanoplates possess pyramidal truncations of the {112} variety. Together, these facets are why the nanoplates are often described as truncated hexagons in cross-section (the transverse plan to the length of the *c*-axis).

Historically, there has been much debate over the morphology of bone and enamel bioapatite crystals. All early works on bone and enamel mineral crystals were carried out on the early generation transmission electron microscopes, which at that time operated solely with film exposures. When plate-like crystals are viewed edge on in the TEM, they scatter electrons more strongly than crystals viewed against their plate-faces. Because the edge-on crystallites generated stronger contrast, the mineral crystals of bone and enamel were often mistaken as needle-like in morphology. Hence, many early works on bone explicitly documented that the crystallites were needle-like in morphology (Currey, 1969; Fernández-Morán & Engström, 1956). Today, it is explicitly known that bone bioapatite exists in a nanoplate morphology (Traub, 1989), yet depictions of bone crystallites are often still misrepresented as hexagonal rods, an oversight that likely remains from the early, highly-contradictory works. Similarly, the crystallites of tooth enamel have universally been determined to be large, rod-like hexagonal prisms (Nylen *et al.*, 1963). In both instances, however, whether in nanoplate or nanorod form, the bioapatite possesses the distinctly biological character of being nano-size. Currently accepted values for bioapatite nanoplate dimensional ranges are on the order of 2-7 nm in thickness, 10-80 nm in width, and 50-200 nm in length, with deviations from those approximate values in accordance with tissue age, particularly for young tissues (Fratzl *et al.*, 2004). Bone nanoplates measuring in excess of 100 nm in length are scarcely seen and considered detrimental for the health of bone tissue, from a mechanical performance perspective.

This section introduced bioapatite, in crystallography, composition, morphology, and size. Additionally, the nucleation and growth parameters of bioapatite nanoplates were introduced, and the significant control that the collagen framework wields in this process was alluded to. The following section will now explore the collagen framework in more depth, in particular, because this framework is the complementary nanoscale structural building block of bone tissue.

1.1.2. Collagen

There are a variety of collagen proteins in the vertebrate body (28 total types known, designated as types I - XXIII in correspondence with genes COL1 - COL28); bone collagen is specifically known as type I collagen (COL1). This is the same type of collagen that forms the elastic structure of the skin, the ocular lens, muscle tissue, tendon, scar tissue, artery walls, fibrocartilage, heart valves, etc. In total, type I collagen is the most abundant protein in the vertebrate body, by weight; this latter fact is, in part, why the genetic diseases associated with type I collagen can be so devastating and often cause extensive deformity of a variety of tissues, including the skeletal structure and connective tissues.

Type I collagen is a triple-strand protein consisting of multiple structural regions; it is distinctly identified by the triple-helix that constitutes the majority of its length. All collagen molecules are triple-stranded; in some, the strands are identical, in others two are of one kind and the third of another, and still in others all three strands may be distinct. In type I collagen, two of the strands are identical and known as the alpha 1 chains; the gene that codes for the type I alpha 1 amino acid chain is called COL1A1. The third strand is distinct but of similar length; this amino acid chain is known as alpha 2, and similarly, the gene that codes for type I alpha 2 is called COL1A2. Once excreted from the cell, the three amino acid chains are bound to each other solely by means of dipole bonding. Together, the three amino acid chains are known as the tropocollagen molecule (*i.e.*, the type I collagen molecule). The sequence of type I collagen is approximately one-third glycine residues, one-third proline or hydroxyproline residues, and the final one-third is a mixture of larger amino acids with various side groups. In particular, the residues are bundled in repeat groups, with the most common groups identified as Gly-X-Y (where X is often proline and Y is often hydroxyproline, in respective units). For this reason, a substantial portion of the molecule is distinguished by a glycine residue in every third position; in fact, this pattern is one factor that makes type I collagen distinct. From a structural perspective, this triple repeat unit forces the molecule into its helical configuration (Boot-Handford & Tuckwell, 2003). The repeat pattern of residues is critical for maintaining the helical nature of the molecule. Finally, each tropocollagen molecule is approximately 300 nm in length and 1.5 nm in width. From a broader perspective, the different types of collagen are classified by all of the parameters described above: length, structural domains, and composition (Cheah, 1985).

In bone, type I collagen is deposited by osteoblast cells into a network of fibrous, rope-like bundles. The osteoblasts wind the collagen molecules into rope-like bundles called microfibrils (hundreds of nm in width). The microfibrils, in turn, are wound into macrofibrils (microns in width). The macrofibrils are the structural unit that osteoblast cells use to craft bone architectures and tissues. As this network is built up into a three-dimensional architecture, generally by the subsequent deposition of layers of bundled collagen (macrofibrils), the morphology of the bone or of the internal structural unit takes hold. That is, the porous cavities within bone (*i.e.*, osteons and the cancellous architecture) are the result of carefully crafted cellular activity. In fact, the depositional patterns of collagen bundles in the construction of bone are incredibly distinct by species; the long bone tissue of rodents (woven) is entirely dissimilar to that of medium-size mammals (lamellar), which is entirely dissimilar to that of large mammals (fibrolamellar; Currey, 2002). Beyond the mammals, the compact bone of reptiles and birds is

also entirely distinct, and each is dissimilar to mammalian bone in its own right. One could go on by adding first the cellular bone of fish, then the acellular bone of fish (Cohen *et al.*, 2012), then the dinosaurs, *etc.* The point here is that neither the micron-size osteoblasts nor the nano-size collagen molecule are to be underestimated; these small cells are masters of craft at fabricating incredibly precise and requisite bone tissue types *at the macro-scale*. These cells work in concert to construct archways, planar surfaces, and struts; they deposit subsequent layers of macrofibrils in a plethora of plies (or simply woven), depending on the necessary mechanical behavior of the resulting tissue. To support this point by analogy, the construction of bone tissues by osteoblast cells is on the order of the complexity of the construction of skyscrapers by humans, except that the scale ratio of bone shaft (1 m) to cell (30×10^{-6} m) versus skyscraper (300 m) to man (2 m) is over 33,000 versus 150, respectively. Truly, osteoblasts and the collagen architecture that they produce are remarkable engineering feats of nature.

With respect to bone, collagen can have a marked impact on the mechanical performance of bone tissues. Several bone diseases, like osteogenesis imperfecta (OI or brittle bone disease), are the result of abnormalities in the type I collagen sequences (Marini *et al.*, 2007; Chavassieux *et al.*, 2007). In incidences of OI, mutations in the DNA cause disruptions in the Gly-X-Y repeat sequence of the collagen amino acid strands. When the small glycine residues are substituted for by bulkier amino acid groups, the structural character or bonding behavior of the resulting collagen molecule can be highly altered. Distortions in structure then lead to further issues, such as the poor infiltration of bioapatite or reduced mechanical integrity of the proteins themselves, which are usually highly elastic and compliant. With respect to poor penetration of the collagen fibrils by bioapatite, the loss of internal stiffening is critical for the mechanical performance of bone. Without infiltration, the bone tissue becomes exceptionally brittle; in some instances, infants born with brittle bone disease can receive multiple bone fractures during birth. In other instances, individuals with osteogenesis imperfecta also suffer a variety of other developmental abnormalities, which tend to be the result of extensively imperfect collagen, affecting the suite of tissues formed of type I collagen. Many instances of OI are lethal prenatal.

The collagen molecules are inter-linked to each other by covalent cross-links. The identities and concentration of these cross-links is a subject of much current scrutiny. Some have proposed that bone in the elderly is embrittled, in part, due to an increased concentration in the collagen cross-links, which reduces the compliance of the collagen fibers (Launey *et al.*, 2010; Paschalis *et al.*, 1998). Other protein molecules interpenetrate the collagen fiber network and are critical for the formation of bone; however, they are not further considered here.

For now, I return this discussion of the structure and composition of type I collagen to the polypeptide sequences. As the primary, critical structural protein in the vertebrate body, one might hypothesize a relatively high degree of sequence and length conservation of type I collagen, particularly in light of the extensive mechanical demands placed on tissues bearing a high content of type I collagen (*e.g.*, bone, skin, tendon, *etc.*). In fact, this is precisely my hypothesis: I now present sufficient background information on the inter-specific similarities of the type I collagen molecule, with particular focus on implications for the identity of dinosaur type I collagen and collagen as a structural protein.

The notion that the collagen proteins have been highly conserved throughout evolution is not new. In fact, it has been the subject of intense investigation for over half a century, even

today. While many papers have been published on the relationships of the various collagen molecules both to each other and among species, I have focused this background only on type I collagen, as most pertinent to this work. Type I collagen is not only found in the vertebrates but also in the invertebrates; further, there is much genetic similarity among the genes that code for these respective type I collagen molecules (Exposito *et al.*, 1992). In fact, it is now believed that the triple helix collagen proteins all share common ancestry, predating the origin of the vertebrates (Aouacheria *et al.*, 2004). Other works have demonstrated strong evolutionary pressure to maintain the Gly-X-Y repeat sequence of the helical domain of type I collagen. For example, the Gly-X-Y repeats and the intron-exon structure of chicken type I collagen are highly similar to that of human type I collagen, even though these phylogenetic groups are separated by hundreds of millions of years of evolution (Chu *et al.*, 1984). In particular, this pressure manifests as the preservation of a glycine residue in every third position in the helical domain, in addition to the conservation of the distribution of charged amino acid groups (Bernard *et al.*, 1983). Referring to the discussion above, in some instances of OI, it is the substitution of glycine that makes the mutation lethal. Varying degrees of similarity or change can be found in the other structural domains of type I collagen. In fact, it has been previously proposed that the compositional and structural identity of type I collagen may hold tremendous clues to vertebrate evolution (Boot-Handford & Tuckwell, 2003). Therefore, it is expected not only that dinosaur (or other extinct vertebrate) type I collagen is coded for by a homologous (same function) gene but also that the genetic sequence and the protein sequence of dinosaur type I collagen should be highly similar to that of its extant relatives. That is, the same evolutionary selective pressures that have maintained the structure and function of type I collagen from the invertebrates to the vertebrates, and then among the birds and the mammals, also would have operated in dinosaurs; the dinosaurs are within the evolutionary link between the chicken and human.

Further, much of the foundational work on the composition of collagen sequences was carried out decades ago (total % quantities only), yet today full sequences of collagen peptides have been documented and are publicly available online. For my own investigation, I consulted the National Center for Biotechnology Information (NCBI). In particular, NCBI has an online database of peptide (and other) sequences, called GenBank® (www.ncbi.nlm.nih.gov/genbank). As of 2011, GenBank contains over 135 million unique sequences. The NCBI website also offers sequence alignment tools, which can be used to determine % similarity of sequences and to generate multiple sequence similarity trees and alignments. The total effort has also recently launched a new tool, called HomoloGene, which is constructed specifically to automatically identify and analyze homologous (a common gene among different organisms) sequences among a particular subset of organisms (21 in total, not all containing complete sequences).

To date, HomoloGene has identified homologs of the COL1A1 gene (the type I collagen alpha 1 chain gene; known as HomoloGene project 73874) for *Homo sapiens* (human), *Canis lupus familiaris* (common dog), *Bos taurus* (cow), *Mus musculus* (house mouse), *Rattus norvegicus* (rat), and *Danio rerio* (zebrafish). The automatically generated HomoloGene 73874 also includes *Pan troglodytes* (chimpanzee) and *Macaca mulatta* (macaque); however, it is worth noting that these sequences are included as *predicted* only. All identified homologs are mammalian, except for the *Danio rerio*. For reference, the full FASTA sequences used in this investigation are given in Appendix A (A.1).

However, the identified homology of the COL1A1 protein sequence from an array of mammals to a species of fish, which are separated by hundreds of millions of years of evolution, perhaps suggests something fundamentally important with respect to the composition of type I collagen. More careful analysis of the homologs, by alignment, indicates the following: the % identity (pairwise alignment scores) of the mammals to *Danio rerio* (fish) ranges between 73.8 - 76.0 for DNA and between 76.5 - 77.9 for protein sequences. Among the mammals, the ranges are all above 80, with the closest similarities observed between the two rodents (*Mus musculus* and *Rattus norvegicus*) and between the remaining group (*Homo sapiens*, *Macaca mulatta*, *Canis lupus*, and *Bos taurus*). The full set of pairwise alignment scores can be found in Appendix A (A. 2).

These pairwise alignments present several preliminary results. One, there is a high degree of conservation of COL1A1 among different species. Two, there is even higher conservation of COL1A1 within a closely related phylogenetic group. And three, the conservation of amino acid group is higher than the conservation of DNA. These results have serious implications. For example, if the mechanical performance of structural collagen is of the utmost important, we might expect a very high degree of conservation with respect to structural character (higher conservation of amino acid sequence than nucleotide sequence). Further, these results suggest that the study of modern type I collagen sequences (COL1A1 and COL1A2) can be used to inform the hypothetical understanding of the collagen of dinosaurs or other extinct species, which has substantial implications for our ability to interpret preserved bone structures for significance with respect to mechanical performance or species relatedness, among others. I use this combination of preliminary results and conclusions to develop my own selection of COL1A1 protein sequences for further investigation of these ideas.

In particular, I used the protein basic local alignment search tool (pBLAST) for my analyses (available at blast.ncbi.nlm.nih.gov), searching the entire protein database for every complete copy of COL1A1 from as many distinct species as possible. There are surprisingly few COL1A1 sequences available today, despite the wealth of interest in collagen proteins; this is an unfortunate constraint on my analysis and also suggests an intriguing area for further study in the future. Nonetheless, based on my selection criteria, I identified the following species for analysis: the eight listed above and *Equus asinus* (donkey), *Xenopus laevis* (African clawed frog), *Oreochromis niloticus* (Nile tilapia), and *Oncorhyncus mykiss* (rainbow trout), *Carassius auratus* (goldfish). Additionally, I located a COL1A1 precursor sequence for *Gallus gallus* (red junglefowl, the chicken). It is worth noting that several of the sequences identified by HomoloGene, above, are also precursors; there are several distinctions between precursor COL1A1 proteins and COL1A1 proteins, such as the use of hydroxyproline instead of proline. Overall, the distinctions are minimal, thus it is sufficient to proceed with an alignment analysis despite the variation in the sample set.

The alignment results ranged from % identity values of approximately 80 (bony fish) to 90 (*Canis lupus familiaris* and *Macaca mulatta*), for a specific comparison against *Gallus gallus*. The red junglefowl was selected for rooting comparison specifically because of the evolutionary association (origin) of modern birds to dinosaurs. Similarly, in accordance with the Extant Phylogenetic Bracketing (EPB) technique first proposed by Witmer (1995), the ideal phylogenetic groupings for such a “soft tissue analysis” include members of the modern reptiles

(crocodiles) and the modern birds (ratites, such as *Struthio* or *Rhea*). My analysis, however, included other phylogenetic groups, such as a variety of fish and mammals. From an evolutionary perspective (include an image of evolutionary phylogenetic tree), fish evolved first; the ray-finned fish existed before the lungfish. Following the lungfish, tetrapods ventured onto land. Amphibians evolved next, followed by an extreme radiation of mammals, dinosaurs, and other reptiles like crocodiles. Finally, birds evolved from dinosaurs. In this manner, one might predict the COL1A1 sequence of dinosaurs to lie somewhere between the sequences of modern crocodiles and birds (such as the chicken). Unfortunately, to date, no member of the crocodile group has been sequenced for COL1A1, and there exist a similarly poor number of bird or ratite sequences (one chicken sequence). Based on the sequences analyzed, however, and in light of our general knowledge of the phylogenetic tree of the origin of vertebrates, one might predict the following relative relationships among the COL1A1 protein sequences:

1. The groups of mammals (sub-sets of primates and rodents) and the bony fish will have the highest internal pairwise alignment scores (or the closest clustering on the multiple sequence tree).
2. The general phylogenetic tree should be reproduced by the COL1A1 sequences of the selected species.
3. Every COL1A1 analyzed will be a homolog.
4. Assuming random changes to DNA, if structural conservation is the most important aspect of type I collagen, then compositional variations will favor the X or Y positions of the Gly-X-Y repeat sequences in the helical structure coding region.
5. If all of the above is true, then a predicted dinosaur COL1A1 protein sequence is possible, and further, based on the EPB technique, high conservation of type I collagen in dinosaurs can be inferred, with direct implications for dinosaur bone structure.

Several variations of the multi-sequence phylogenetic trees are shown in Appendix A (A. 3), including two rooted rectangular trees and two rooted slanted trees. Among each pair, one root was selected based on the pBLAST initial analysis (the root node is determined by the longest pairwise distance) and the other I forced to root at the bony fish - red junglefowl node, which is more consistent with our evolutionary understanding of the phylogenies. Based on these trees and the multi-sequence alignment (Appendix A.4), the following useful conclusions can be drawn, in parallel construct to the five points given above:

1. The expected phylogenetic groups and sub-groups are all readily identifiable.
2. The overall clustering patterns and the relative distance relationships in the experimental multi-sequence trees basically reproduce the phylogenetic tree.
3. The COL1A1 sequences are all homologs, based on the universally high degree of pairwise alignments.
4. By inspecting the multi-sequence alignments, it is clear that substitutions (particularly within the helical structure coding region) favor the X and Y positions over the Gly position in the Gly-X-Y repeat sequence.

5. The dinosaur type I collagen structure is expected to be highly similar to that of the modern collagen sequences, particularly in structural conformation (protein sequence, conservation of Gly-X-Y).

Based on the discussion of the results of other on topics of collagen structure conservation as well as the results of the above comparison, not only might it be possible to predict the collagen type I sequences of dinosaur (and other extinct species), but further work on nanoscale bone structure, which is highly dependent on the type I collagen composition and structure, is a realistic possibility, from this perspective. That is, by invoking the EPB, and interpreting the results in light of the principles of the EPB, it is reasonable to assume that the similar high conservation of COL1A1 (and of type I collagen in general) within dinosaur indicates that a similar nanoscale (and higher orders of D-spacing, microfibril, and macrofibril) can be found.

In short, both this section and the preceding have defined the nanoscale building blocks of bone. We have seen that the bioapatite composition and nanomorphology are highly consistent throughout the vertebrates; we have also seen that the collagen composition and structures are highly conserved. One might presume, therefore, that the nanoscale structure of bone, which is entirely based upon these individual building blocks, is also highly conserved throughout the vertebrates. This is considered in more depth in the following section.

1.1.3. Nanoscale structure of bone

The nanoscale structure of bone is determined almost exclusively by the collagen framework. In particular, it is the architecture of the microfibril that guides where and how densely the bioapatite nanoplates precipitate. Because the maturation process is constituted by infiltration and cladding of the microfibril (stiffening), in a certain respect, the microfibril can be regarded as the nanoscale structural unit of bone (it is the first truly composite feature in the structural hierarchy). The helicity of the collagen molecule is transferred to the microfibril. Although often represented in a very orthogonal motif (originating in the seminal work of Landis *et al.*, 1993), the microfibril is indeed a wound, rope-like structure (Bozec *et al.*, 2007). Microfibrils measure on the order of 100 nm in width (Hassenkam *et al.*, 2004). Given a collagen molecule measuring 1.5 nm in width, the microfibrillar unit can be assumed to possess an internal architecture of at least hundreds of collagen molecules. The structure of the collagen molecule contains several distinct regions; the structure and composition (functional groups of the amino acids) control how adjacent collagen molecules associate with each other.

Typical literature schematics of nanoscale collagen provide the clearest picture for understanding the nanoscale architecture, despite their three-dimensional structural inaccuracy. Collagen molecules stack head-to-toe in long chains; adjacent chains associate with each other in accordance with a characteristic offset. This offset causes several features to appear: one, an approximately 40 nm end gap between the head-to-toe stacked collagen molecules, and two, an overlap region of adjacent head and toe regions on the order of 27 nm (see Figure 1.2). When an extensive array of this stacking pattern is bundled into the rope-like structure, it yields a characteristic banding pattern that is quite distinctive in TEM or AFM investigations. In a TEM micrograph of decalcified collagen, the microfibril exhibits alternating dark and light regions: the

dark regions correspond to the overlap (27 nm), while the light regions correspond to the gap (40 nm) (Nyman *et al.*, 2005). Together, the sum of sequential dark and light bands measures to approximately 67 nm, and this value is known as the D-spacing of collagen. This D-spacing is known to diffract X-rays in small-angle X-ray scattering (SAXS) experiments (Deymier-Black *et al.*, 2012), and such measurements are statistically superior to that of visual inspections of TEM micrographs. Interestingly, across species, the D-spacing is always measured to 67 nm, almost exactly. Having already considered the high conservation of type I collagen across species separated by hundreds of millions of years of evolution, perhaps it is no surprise that even the microfibrillar structure is also conserved. In other words, the entire nanoscale structure of bone is common among vertebrates, a fact that has been little stressed in the literature.

Shortly after the osteoblasts extrude the collagen fibrils, the network, which is bathed in interstitial fluid containing a high content of ions, is subject to precipitation events. The nucleation of bioapatite is currently believed to commence at key locations, likely dictated by specific amino acid functional groups (Cui *et al.*, 2007). The type I collagen network plays cohost to bioapatite, along with other organic molecules such as proteoglycans. The process of bioapatite nucleation and growth within the collagen microfibril is known as biomineralization. The relative openness of the end gap regions between the head-to-toe stacked collagen molecules allows for rapid nucleation and growth of bioapatite. As biomineralization continues, however, the nanoplates also grow in the confined spaces between adjacent collagen molecules. In the gap regions, the bioapatite tends to grow in stacked, parallel plates (Burger *et al.*, 2008). In this way, the D-spacing pattern becomes highly reinforced by the presence of mineral with a high electron density (strong scattering of X-rays). The microfibril is intermittently reinforced by bands of high mineral concentration, with a reduced degree of stiffening in the tightly bundled overlap regions. The nanocrystals grow to lengths of tens or even a hundred nm, with their *c*-axis parallel to the length of the collagen molecules. In the final phases of biomineralization, the microfibrils are clad with bioapatite crystallites, and this infiltrates the spaces between adjacent microfibrils in the macrofibril.

1.1.4. Higher order structures of bone

Many microfibrils are wound to form the macrofibril, and the macrofibril is what is commonly referred to as the bone fibril. This is the fiber laid down by osteoblasts in the construction of bone tissue. Macrofibrils tend to be on the order of several microns in width, a value that is based on measurements from bone tissues in a variety of species. The cortices of the long bones of vertebrates are formed by a variety of depositional mechanisms, which represent relatively high-level ordering. In small rodents, the femur shaft is composed of woven bone, which is relatively porous and has poor mechanical properties; woven bone also tends to mineralize quite heavily. In medium-size mammals, the fetal bone also begins as a woven architecture (Su *et al.*, 2003); however, by the time the offspring is born, remodeling has already commenced, replacing the less organized bone with lamellar bone. The lamellar bone is composed of closely-packed fibrils, which are highly aligned with the shaft length of the long bone; this creates the strong texture for which long bone is known. The layers of lamellar bone (the lamellae or bone lamina) are deposited in sheets with characteristic cross-hatching or radial orientation of the fibers (the rotational pitch between adjacent layers of ply); the specific internal

orientation of each sheet designates the specific type of ply (Weiner *et al.*, 1999). In larger mammals, such as cow and horse, the long bones must grow at very high rates to match the rapidly increasing body mass of the animal. For this reason, the cortical bone tissue must grow in a hybrid form, part-way between the rapidly deposited woven bone tissue and the slowly deposited laminar bone tissue (Mori *et al.*, 2003). The cortical bone tissue of these large mammals is, therefore, called fibrolamellar bone. It is quite evidently deposited in a lamellar fashion, but it contains a great deal of woven bone within its architecture. This tissue is of insufficient mechanical quality, however, and is quickly replaced by secondary osteons of higher mechanical integrity.

Other species exhibit cortical bone tissues of similar or intermediate type. For example, the cortical bone of bird long bones is highly lamellar, but between the lamellae exist substantial cavity spaces (described as longitudinal, circular, radial, or oblique in shape); these cavernous layers are slowly filled in by bone lamina over time to create the osteon structures (De Margerie *et al.*, 2005). The tissue type is often somewhere between reticular and laminar. In some instances, the long bones of birds are described as fibrolamellar; hence, even within birds the cortical bone tissue varies. Remodeling, however, does not occur in young birds, as it does in mammals; in fact, many wing bones in birds (which bear the highest loads of the bird skeleton) exhibit no remodeling tendency whatsoever, even in species as large as the albatross (Simons & O'Connor, 2012). In reptiles, the compact bone tissue of the long bones grows extremely slowly in the fibrolamellar pattern (Tumarkin-Deratzkian, 2007), further following periods of more rapid growth, which are believed to correspond with the cycling of seasons. The bone tissue of reptile long bones also tends to be less vascular, with fewer osteons or later occurrences of secondary osteons (Scheyer, 2009). In these cases, the osteons are clearly seen to be deposited in very thick lamina, sometimes measuring over a hundred microns in width. The compact bone tissue of dinosaurs falls somewhere in between that of the reptiles and the mammals: while the tissue is more vascular (like that of the mammals) and may even remodel at a similar rate, it tends to exhibit similar annual growth cycles (called lines of arrested growth, or LAGs; Horner *et al.*, 2000).

The bone fibrils are most easily identified in two manners: one, by investigating the internal architecture of the osteon or other crafted surface, and two, by fracturing fresh bone, which tends to tear out individual macrofibrils. Other images of embedded (either undecalcified or decalcified) thin-sections are often depicted in the literature, although TEM micrographs of this type of specimen are generally only sufficient for imaging the microfibril (Cui *et al.*, 2007; Suvorova *et al.*, 2007). That is, the preparation process must necessarily thin through the macrofibrillar structure (microns in width) to achieve electron transparency (300 nm in thickness or less). Finally, atomic force microscopy (AFM) investigations occasionally have presented detailed images of the macrofibrillar structure (Bozec *et al.*, 2007; Hassenkam *et al.*, 2004).

Beyond the macrofibril and the tissue ply/lamellar structure, higher order structural features of bone include the osteonal network (density, cross-sectional circularity), the osteocyte lacunae (density, circularity), the cortical thickness, the medullary cavity, and ultimately the bone morphology. Several of these features are also explored in this work, as part of the attempt to justify the presence of preserved bone structural hierarchy in fossil bone. Additionally, these

features are of interest from a physiological perspective, and many investigations of dinosaur physiology have tended to rely on some of these characters.

1.1.5. Structure/property relationships of bone

Each level of the bone structural hierarchy contributes to the structure/property relationships of bone. The nanoscale components and the nanoscale structure are crucial factors toward determining bone quality and performance (Weiner & Wagner, 1998). Recent small-angle X-ray scattering (SAXS) work has indicated that the bioapatite nanoplates internalize strain under load at a ratio of 2:15 that of the bulk bone (Gupta *et al.*, 2006). Similar studies using synchrotron X-rays sources have also explored the mechanical properties of nanocrystalline bioapatite in dentin (Deymier-Black *et al.*, 2009). From a bone mechanics perspective, the size restriction of brittle bioapatite crystals to the nanoscale length is of critical importance for maintaining bone strength: the nanosized crystals approach an ideal mechanical behavior, which rapidly drives up the stress necessary to promote crack formation and propagation (Gao *et al.*, 2002). Recent advances in TEM instrumentation now allow for nanoindentation (nanoscale mechanical property investigations), which has been used to glean property information from individual bioapatite crystallites. Such studies have identified hardness values on the order of 6-7 GPa and elastic moduli up to 150 GPa (Saber-Samandari & Gross, 2009), which are exceptional compared to that of bulk hydroxyapatite. Further analyses of relative strength have indicated that the preferred slip direction in bioapatite may be within the <100> (Zamiri & De, 2011). As the primary load-bearing phase, the bioapatite mineral has distinctly different properties than that of the collagen network, which exhibits a complex polymer-like behavior.

Type I collagen molecules are helical in nature. Internally, their three chains are attracted to one another by hydrogen bonding (dipoles). When collagen is under load, the helical section of the molecule uncoils has the hydrogen bonds are broken; this process is called molecular uncoiling and is one of the intrinsic toughening mechanisms of bone. Hydrogen bonds are intermediately strong (between van der Waals bonds and ionic or covalent bonds), and more critically, they are restorable. The incredibly high surface area of the long chains of collagen increases the total interfacial strength within the collagen microfibril. Further, adjacent collagen molecules bond to each other by covalent cross-links. As microfibrils are placed under load, a combination of internal stretching of molecules with the breakage of both weak (restorable) and strong (unrestorable, covalent) bonds leads to strength. Collagen can exhibit a 50% strain when in tension, bearing loads between 10 and 20 GPa before breaking (Launey *et al.*, 2010). The elastic modulus of collagen is approximately 1-2 GPa (Gupta *et al.*, 2006). Increased concentrations of cross-links reduce the intermolecular sliding; cross-links generally tend to increase the strength of the collagen matrix by restricting the sliding behavior (Uzel & Buehler, 2011). When the cross-link concentration becomes too high, the collagen network is embrittled; this is believed to be a contributing factor to brittle bone in the elderly (Launey *et al*., 2010). Collagen is also a strain-rate sensitive material (viscoelastic), as many polymers are.

The mechanical properties of the bioapatite and collagen combine in the creation of the microfibril: the microfibril can bear load because it is stiffened by bioapatite, and the microfibril exhibits increased toughness because of the presence of collagen of a moderate degree of cross-linkage. Recent measurements place the stiffness of the microfibril in its longitudinal direction to

be approximately 23 GPa and 16.5 GPa in transverse orientation (Fratzl *et al.*, 2004). Highly mineralized bone is stiffer but breaks at lower strains, while less mineralized bone has reduced stiffness but sustains higher strain. It has further been shown that the fibril bears load at one-third that of the bone tissue and over twice that of the bioapatite phase (Gupta *et al.*, 2006). Additionally, the transfer of load within the microfibril, from the collagen network to the individual nanoplates, occurs by a shear mechanism.

Beyond the level of the fibril, the situation becomes more complex: macrofibrils are uniquely used to fabricate different types of cortical bone, which also varies from the macrofibril architecture of the osteon structure. There have been investigations of individual osteons, machined from bulk bone specimens (Ascenzi *et al.*, 1994). These studies have identified a range of mechanical behavior, associated with variations in the organization of the fibrils within the concentric lamellar structure of the osteons. Complementary work has demonstrated the hydraulic strengthening contribution of blood flow within the osteonal structure (Liebschner & Keller, 2005). Osteons are on the order of tens to hundreds of microns in cross-sectional diameter, and the individual bone lamellae of the osteons are 3-7 μm in thickness (Launey *et al.*, 2010). Osteons also impart extrinsic strengthening mechanisms to bone: their discrete edges (longitudinally oriented cement lines) tend to divert propagating cracks, which can mitigate the effect of damage and increases bone toughness. This phenomenon is called crack deflection.

Other regions of structural discontinuity can serve as stress concentrators or crack initiation sites. For example, the initiation of microcracking phenomena around osteocyte lacunae has been observed in tensile specimens (Qiu *et al.*, 2005; Reilly, 2000). Finally, at the tissue level, a variety of mechanical properties have been measured for the compact bone of different species. As a viscoelastic material, the material properties of bone vary based on the experimental strain rate. Bone also fairs differently in compression, tension, bending, and torsion tests. The literature on this subject is vast; I give only a cursory examination of these properties here, largely based on work by J. D. Currey (1999), who is an impressively published author on bone from across the species. Several generalizations can be made, however:

1. The strength of compact femur bone is higher in compression than in tension.
2. The strength of compact femur bone is higher for larger mammals.
3. Primary lamellar bone has superior mechanical properties to secondary osteonal bone, and both are superior to woven bone.
4. Younger bone tissue is both stronger and tougher than older bone tissue, a fact that is dependent on remodeling, cross-linking, and resorption.

These generalizations were extracted from the dataset contained in Appendix B (Table B.1).

1.2. Fossil bone as a material of interest

This introduction to section 1.2 provides not only my motivation (no doubt, there are many) for studying fossil bone from the engineering perspective but also a cursory introduction to the concepts of diagenetic alteration and fossilization. In the following sub-sections, I explore the specific aspects of how diagenetic alteration affects the critical features of interest, in parallel structure to section 1.1. From my perspective, one cannot pursue the engineering of biomimicked

materials based on the structure/property relationships of bone without paying explicit attention to the phylogeny and physiology of the organism in question. Yet, to date, little systematic work has explored the implications of phylogeny and physiology on the structure/property relationships in bone tissue. When seeking to join the various phylogenies of interest to engineers, however, the problem becomes immediately apparent: the bones of modern animals (selected from distinct phylogenies) cannot be truly understood without considering the bones of extinct ancestors. We cannot carry out modern materials engineering work on bone without understanding bone from the deep time perspective.

The seminal work in the area of bone growth was carried out on the mineralizing leg tendons of domestic poultry (chicken, turkey). Other phylogenetic groups of interest have included a variety of fish, rodents and small mammals (mouse, rat, rabbit), various livestock mammals (sheep, cow, pig, horse), flight-capable birds (duck, albatross, *etc.*), and monkeys and apes (human, macaque, chimpanzee). In reality, however, these animals represent distantly related phylogenetic groups; further, there is no simple direct comparison for their physiological and mechanical differences. In short, without incorporating the bones of intermediate species--and the fossil record--any related engineering work is inherently myopic. To truly engineer high-toughness, high-strength materials based on our understanding of the structure/property relationships in modern bone, we must incorporate the study of fossil specimens (the deep time perspective).

My personal interest in this area not only stems from the notion given just above but also from the following. Instead of using the current structure/property knowledge of human and cow bone to conceive of a novel biomimicked material for high-strength, high-toughness applications, why not look to the bones of gigantic terrestrial megafauna? Beyond cows, which are technically classified as terrestrial megafauna (*i.e.*, they are vertebrates weighing over 400 lbs and living on land), elephants are the largest terrestrial megafauna alive today (approximately 7,000 kg, at the largest). Of course, there are a variety of reasons why an engineering dissertation based on the study of elephant femur is an impractical endeavor. Yet, from a purely philosophical perspective, the elephant femur is insufficient because it, too, is simply not the ideal candidate for this particular question. In fact, the mammoth would be much better suited; mammoths easily grew to twice the size (13,000 kg or more) of the largest modern elephant.

At this point, we must consider two things. One, the scaling laws that large terrestrial vertebrates follow in terms of the growth of compact long bone (*e.g.*, the cross-sectional area of the long bones versus the weight of the animal, the length-to-width aspect ratio of the long bones, *etc.*) quickly break down when we move beyond the cow. This is why I have termed the violators of our laws the *gigantic megafauna*, because they are truly in a vertebrate size/ratio class of their own. It is precisely the violation of these laws that excites my interest in their long bone tissues.

My second point, however, really underscores the paleontological context of this dissertation work. That is, the mammoths were not the only gigantic megafauna to walk on land. There was a time, tens of thousands of years before today and even millions of years before that, when multi-ton terrestrial vertebrates roamed the world. *Megatherium*, the ancestor of the modern sloth, was a behemoth by any standards, and possessed skeletal features highly reminiscent of those in the mammoth (long bone aspect ratios, enhanced cortical thickness versus

medullary cavity, *etc.*). Several modern investigators have explored deer antler for crashworthiness investigations; however, the modern deer is dwarfed by its now-extinct ancestor, *Megaloceros giganteus*. *Megaloceros giganteus*, which ranged throughout Ireland, had an antler rack that spanned nearly 3.6 meters across and weighed upwards of 40 kg. The male combatting behaviors of this species would have produced far superior impact loads than that of the modern deer. The largest mammal that ever lived was *Paraceratherium*, which was larger even than the *Tyrannosaurus*. But why stop there? In a manner of only a few million years, the sauropods evolved from bipedal, cow-sized animals into 100-ton, obligate quadrupeds. What is more, their bones remodel at fascinatingly low rates versus the bones of modern mammals.

Now, we truly motivated the underpinnings of my dissertation. As a materials engineer, it is my hypothesis that the long bones of the gigantic megafauna, which are all extinct save for the elephant, are unequivocally the best structure/property analogues for investigations wishing to develop high-strength, high-toughness materials based on bone. And here, from the perspective of bone as a material of interest, we have once more come full circle back to the engineering disciplines. Inarguably, spanning the engineering and paleontological disciplines, my dissertation work underscores why bone is the most interdisciplinary material, or perhaps even *topic*, that has ever been studied in science. However, before I further explore the consequences of diagenetic alteration in depth, I first provide background information on the concept of bone diagenesis and how it relates to fossilization and fossils.

The posthumous processes that a bone encounters are known as *diagenesis*. Frequently, the changes associated with a fossil bone are referred to as diagenetic alteration. Diagenesis is described in terms of the sum of all chemical, physical, and biological alterations that occur to a bone following the death of an animal. The majority of deceased animals experience scavenging, bacterial degradation, and other destructive forces: their skeletal remains suffer a cumulative diagenetic process that ultimately degrades the bones entirely. Fossil bones, however, have suffered a distinctly different set of diagenetic alterations, and one might say, less destructive. This is an important distinction to make, particularly in light of the recent push by many paleontologists to investigate fossilization as a *preservational* process, not destructive. This change in perspective is more significant than terminology alone: by investigating fossilization as a means of preservation, entirely new questions and perspectives are developed, which likely never would have been brought to light otherwise.

The process of fossilization varies between specimens and even within a single specimen or bone. On a grand scale, fossil bones tend to be preserved under a few distinct sets of conditions. For example, acid bogs, tar pits, ice, sand, and sedimentary environments can all preserve tissue remains for long periods of time, and in many of these instances, soft tissues can be recovered in addition to the mineral-based bone tissues. In some cases, such as the encapsulation of leaves or fish within shale, the decayed specimen may remain solely as a carbon imprint. However, the majority of ancient fossil specimens (such as dinosaur) only survive as skeletal or trace remains (trackways, coprolites, skin impressions, *etc.*), with the soft tissue elements (skin, hair, scales, fur, organs, *etc.*) having been largely or entirely degraded.

Most ancient fossil bones are recovered from sedimentary or other earthen-tomb environments. In some cases, these animals were enveloped by mud flows or ash clouds; in others, the specimens were deposited on the bottoms of lakes or other aquatic systems, either by

being washed from the land or because the animal died within the aquatic environment. In both cases, a similar process of relatively rapid burial and encapsulation beneath earthen layers is a common aspect.

The phrasing *relatively rapid* is not meant to imply an actual length of time, but rather, a relative length of time. That is, fossil bones are recovered exhibiting any degree of posthumous alteration, having occurred after death but before burial (or even during). When dead animals are scavenged, their skeletal remains may become disarticulated, and their bones may even exhibit scavenging marks. In other instances, buried skeletal elements can suffer further biological alteration, such as invasion and degradation by fungus or bacteria. In either case, for the bone to survive in some capacity for hundreds of millions of years, its original encapsulation must have occurred within a sufficiently brief amount of time that the local environmental and biological factors were unable to fully degrade it. Therefore, the encapsulation must occur before the bone degrades, and hence, rapid may mean instantaneous, or it may mean within days. The best preserved specimens suffered apparent instantaneous encapsulation. The majority of deceased animals, however, do not become fossil bones: instead, their bones rot and degrade until they are no longer in existence. This is one reason that the fossil record is considered to be imperfect. It is a representation of amazing events that combined in fortuitous circumstances to preserve a specimen (or a collection of specimens, such as a herd).

Dinosaur skeletons are frequently recovered from sandstone and mudstone sedimentary layers. These bones may exhibit any degree of the above-mentioned alterations. However, following subsequent exposure beneath the ground for millions of years, their bones are also subject to an array of other geological (chemical, physical) impositions. Common examples include permineralization and enrichment in iron or other radioactive elements, which leech into the bone over time from the surrounding earthen tomb. This process is aided by aqueous actions, where the bones are intermittently bathed by ion-laden water over the course of millions of years. Additionally, burial beneath tons of layers of sedimentary rock, particularly during periodic aqueous events, slowly distorts bones over time. Many recovered skulls have orbitals that appear to have been crushed, and recovered long bones often appear to have warped shafts. Similarly, bones buried in mudstone are subject to repeated shrinkage and swelling events as the mudstone dehydrates then rehydrates; this action effectively explodes the bones, while maintaining the relative locations of the exploded fragments. The recovery of such specimens can be highly time consuming. The effects of pressure and alternating swelling/shrinkage events are readily evidenced by the appearance of cracks within the bones. These cracks, in turn, provide extra entry routes for the introduction of foreign species.

Indeed, many changes have occurred to most fossil bones posthumously. However, these changes are largely rather well understood, at least from the perspective of identification, if not mechanistic. That said, two points remain to be made in this introduction to fossil bone. One, I wish to reiterate the fact that fossilization is now perceived to be a preservational process, not destructive. Further, it is my hope that this work will continue to contribute to our understanding of fossilization as a preservational process. Two, fossil bones are of interest not only because they shed light on the morphology of extinct species but also because their bones contain extensive information that can better inform our understanding of evolution, as well as our quest

to develop biomimetic materials for high-strength, high-toughness applications in light of the ever-crucial deep time perspective.

The following sections have been written in parallel construction to the sub-sections of section 1.1. In turn, each addresses the concepts laid out in section 1.1 from the perspective of how work with fossils has informed our understanding of the changes that fossilization induces in bone. Additionally, these sections provide an overview of current topics of consideration in the paleontological sciences, many of which have striking overlap with current engineering efforts focused on modern bone. Following section 1.2, the problem statement is addressed, as well as the scope of this work.

1.2.1. Fossil bioapatite

The accurate and precise determination of bone mineral composition is key for verifying the possible presence of preserved bioapatite in fossil bones. In this work, fossil bioapatite is termed *minimally altered* in instances when the composition of fossil bone mineral cannot be statistically distinguished from that of modern bone. The common techniques used to gather data on bone crystal structure and composition include electron microprobe, electron diffraction, synchrotron X-ray fluorescence (synchrotron XRF), energy-dispersive X-ray spectroscopy (EDS), X-ray diffraction (XRD), and Fourier-transform infrared spectroscopy (FTIR). Some of these approaches are also used to produce spatial maps of composition, sensitive to the ppm level. In part, such highly sensitive techniques have been applied to fossil bone for possible determinations of past environments, diets, physiology, *etc.*, which can be recorded in bone mineral as both compositional and isotopic signatures. This section reviews the relevant paleontological literature, with respect to bioapatite mineral and the related diagenetic changes (biological, chemical, physical) that have been commonly documented.

As described in section 1.1.1, the apatite mineral structure is relatively open and highly susceptible to chemical exchange. Additionally, geological apatite is readily distinguished from biological apatite by composition, morphology, and crystallite size. All of these factors are critical for an informed understanding of the following background. Much work from the paleontology literature has documented fossil bone as enriched in various elements, some of which are common, *in vivo* substitutions in the bioapatite structure (*e.g.*, F, Na, Cl, K, Mn, Fe, Sr, Pb) and others of which are not (*e.g.*, Ti, Cr, Ni, Zn, Y, Ce, Nd, U, *etc.*; Goodwin *et al.*, 2007; Elorza *et al.*, 1999). The latter group of elements is largely characteristic of diagenetically altered bone and can even be diagnostic of the particular geological strata from which the bone was recovered. It is also worth noting that the majority of the elements listed above, particularly the less common metal substitutions, were detected by synchrotron methods, which have a ppm threshold for sensitivity.

In some instances, fossil bioapatite has been recorded with approximately 50% conversion to fluorapatite ($Ca_{10}(PO_4)_6F_2$). Elorza *et al*. (1999) identified fluorine contents of 3.36, 3.31, and 3.37 at.% in three different fossil specimens. Hubert *et al.* (1996) documented fluorine contents between 1.50 and 2.37 at.% in 6 different fossil dinosaur bone specimens. Additionally, fluorine substitutes conservatively at the hydroxide position. Because the hydroxide ion only determines approximately 4.8 at. % of the apatite structure (exclusive of hydrogen), a 50% conversion to fluorapatite only implies an enrichment in fluorine of

approximately 2.4 at.%. This degree of chemical substitution is minimal and has nearly no effect on the chemical structure (the lattice parameters of hydroxyapatite and fluorapatite are nearly identical). Further, fluorine readily substitutes due to the relatively open nature of the apatite structure; this is also the reason that such a large number of other ions tend to be absorbed into the apatite structure, particularly metal cations. In short, common chemical changes have been documented in fossil bioapatite. These chemical changes are readily diagnosed with a variety of techniques, and changes to the chemical composition of fossil bioapatite do not necessarily imply changes in the mineral structure (either from the perspective of the motif or the dimensions of the structure).

Small amounts of cation substitution cause little alteration in the bioapatite mineral. The stoichiometric hydroxyapatite structure contains 10 calcium positions for every 42 atoms. Therefore, a compositional change of a few % represents only a fractional change, and such a structure would simply be a chemically polluted form of hydroxyapatite, which bioapatite already is. Both small changes in cation content (as substitutions at the calcium positions) and small changes in anion content (as substitutions at the hydroxide positions) have the same net effect on the structure: that is, these substitutions induce small lattice distortions (strain). Although lattice distortions can be analytically measured by precision spectrometry or diffraction techniques, the expected degree of lattice strain is on the order of several % (hydroxyapatite and fluorapatite are very similar in size). This value, in actual units of distance, equates to fractions of a nm. Various paleontological reports have identified small amounts of strain within the fossil bioapatite lattice (Lonardelli *et al.*, 2005; Elorza *et al.*, 1999). However, there are reasons why these determinations may actually be skewed and not necessarily representative. For example, peak deconvolution is still a challenging endeavor with respect to certain datasets (high degree of overlapping peaks of various heights). In short, despite the general conclusions presented in the literature, background information actually suggests that fossil bioapatite possesses both a readily diagnosable (quantifiable and distinct) chemical signature and a conserved apatite structure. That is, fossil bioapatite is compositionally distinct from modern bioapatite but only to a small degree.

This is not to suggest that fossilization never induces substantial compositional or phase changes in bioapatite. Other diagenetic changes can induce phase changes in fossil bone mineral. For example, bioapatite (and the entire class of apatite minerals) is susceptible to dissolution at low pH or in non-saturated aqueous environments, with respect to the main ions in the mineral structure (Turner-Walker, 2008). This is a point of concern, of course, because the internal environment of most decaying organisms tends to acidify. Further, acidic ground environments can dissolve other local minerals; this is believed to be one reason that fossil bones are often brown in color, enriched by oxidized iron and manganese from the environment (Elorza *et al.*, 1999). Additionally, certain types of biological alteration, called bioerosion, include local dissolution of bioapatite as the invading bacterium or fungus moves through the dead bone tissue (Jans, 2008; Jans *et al.*, 2004). In both of these cases, following dissolution, the mineral can recrystallize. During recrystallization, whether apatite, another calcium phosphate mineral, or some other will form is entirely dependent upon the present, and highly particular, state of the local system. Similarly, as increasing numbers of pressure-induced cracks invade the fossil bone tissue, these cracks provide new pathways directly into the bulk bone tissue. These pathways

provide enhanced access for ion laden water to penetrate into the bulk bone, as well as for possible low pH water, which can further accelerate internal dissolution. That said, based on my background work and what I have read by others, these events are likely minimal in the bulk bone regions. This is probably even more true for thicker, denser bones.

Of course, there are other diagnostic factors that still must be considered, such as crystallite morphology and size. Apatite crystals of geological origin are more likely to grow as hexagonal prisms to larger sizes (micron or more). Bioapatite crystallites, however, grow in a plate-like fashion, extended along the *c*-axis. Bioapatite nanoplates tend to grow to maximum values of 2-7 nm in thickness, 10-80 nm in width, and 50-200 nm in length (Fratzl *et al.*, 2004). Hubert *et al.* (1996) documented the presence of nanocracks in petrographically thinned TEM specimens, with larger, hexagonal crystallites located in proximity of the nanocracks. It is difficult to say, however, whether or not some of this alteration was induced by the specimen preparation method. Many other crystalline forms have been either directly or indirectly identified in fossil bones, ranging from various calcium phosphate phases to other mineral forms, such as iron oxide-based structures. However, it is important to note that these phases are rarely found in increased concentrations in the bulk bone tissue. Instead, they tend to be deposited/ grown in porous regions, such as osteons, the medullary cavity, osteocyte lacunae, *etc.*

Additionally, current paleontology and archaeology literature indicates the common occurrence of a phenomenon known as *coarsening* in diagenetically altered bones (Turner-Walker, 2008; Trueman *et al.*, 2004). The fossilization process begins with the burial of an animal or bone beneath a layer of sediment, encapsulating the carcass or bone in a relatively protected, anoxic environment. Heat and aqueous exposure can drive the diffusion of ions in bone tissue (as in other crystalline forms), resulting in the possible coarsening of bioapatite nanoplates. The phenomenon of coarsening has been identified by two means: one, the increases in crystallinity, indirectly observed by XRD, and two, the direct observations of increased crystallite size based on measurements from TEM images. The description of increased crystallinity as coarsening should be made, instead of increased crystallinity as a measurement of the crystalline fraction to the organic fraction. In the former, crystallinity increases as a result of increased crystallite dimensions, which provide enhanced opportunities for constructive reinforcement in diffraction; in the latter, as organic content is lost over the course of time, which invariably occurs in any diagenetically altered bone specimen, the relative mineral fraction increases. With respect to my work, I take for granted that much of the organic content of the fossil bone specimens has been lost. In particular, I am more interested in the question of coarsening, and whether the fossil bioapatite nanoplates have increased in size or not.

The coarsening phenomenon has also been observed in materials science studies on bioapatite derived from bovine cortical bone, where exposure of ground bone to highly elevated temperatures (>700^{o}C) induced dramatic crystal growth, to length dimensions in excess of 200 nm (Danilchenko *et al.*, 2002). While these conditions are extremely relative to what fossil bones experience in the natural environment, they do demonstrate a relevant, key feature of bone coarsening: when coarsening occurs, it does so in a structurally conservative fashion. That is, the growth of nanoplates occurs preferentially along their *c*-axes, maintaining the original crystallographic orientation of the mineral phase within the overall bone tissue. Thus, even for fossil bones that may exhibit minor coarsening, which may or may not be detectable, the

orientation of the nanoplates is nonetheless expected to be reflective of the original tissue and nanoscale structure.

One final point remains to be made with respect to the three main classes of diagenetic alteration, and their respective effects on nanoscale bone features, such as the bioapatite and the microfibril, during fossilization. Cracking phenomena and morphological distortion are the result of physical changes induced in the bone. While cracking phenomena are defined by the irreversible cleavage of atomic bonds, such behavior is not likely to occur in individual nanoplates, for example. It is possible, however, that cracking may be transferred to the microfibrillar structure or even among the individual nanoplates. Despite the nanoscale cracks identified by Hubert *et al.* (1996), there has been no concrete demonstration of actual nanoscale cracking phenomena in fossil bones as a consequence of diagenetic alteration.

In summary, based on previous work by others in addition to my own, I have drawn several significant conclusions with respect to the biological, chemical, and physical changes that occur in bone as it fossilizes, and these conclusions are what I have used to inform my study and to help shape my assumptions and hypotheses. First, biological alteration (bioerosion) can induce local dissolution and precipitation, which can introduce mineral phase changes and increased local mineral density. However, these changes are readily identified by tracks and pathways, and such areas should always be avoided for analyses seeking to identify minimally altered bioapatite in fossil bone. Second, chemical changes undoubtedly occur, but these changes are either minimal (ppm level) or readily diagnosable (such as fluorine substitution for hydroxide groups); in both cases, actual phases changes have not been identified (the phases are still apatite), except in highly exposed regions. Third, the consequences of physical changes for fossil bioapatite are expected to be minimal or non-existent, because nanoscale crystallites near ideal crystalline strength, and other phases are more likely to be altered by physical changes before bioapatite. Overall, based on background work, I expect to find readily diagnosable, minimally altered bioapatite in the fossil bone specimens.

1.2.2. Fossil collagen

The pursuit of preserved biomolecules in ancient specimens has gained increasing interest in recent years. It has long been known that soft tissues can be preserved for thousands of years under certain circumstances (*e.g.*, ice, desiccation in sand, acid bogs). However, the possible preservation of biomolecules in specimens dating well into millions of years of age seemed doubtful, for various reasons. Then, in 2005, M. H. Schweitzer from North Carolina State University published two articles claiming the exceptional preservation of soft tissues in dinosaur embryos and *Tyrannosaur* (Schweitzer *et al.*, 2005a; Schweitzer *et al.*, 2005b). Other reports, also by Schweitzer's research group and collaborators, were quick to follow: in 2007, a second paper in *Science* on *Tyrannosaurus rex* claimed to have identified preserved protein (Schweitzer *et al.*, 2007a) while two other papers that year were published on protein sequences in mastodon (Asara *et al.*, 2007) and on various preserved skeletal elements (Schweitzer *et al.*, 2007b). Then in 2009, the group published another paper, this time on protein sequences in hadrosaur (Schweitzer *et al.*, 2009). Meanwhile, in the background, another research group challenged their work in both a rebuttal letter to *Science* and a publication in PLoS one (Kaye *et al.*, 2008).

In total, the various publications and efforts use a variety of spectroscopic and microscopic techniques to either justify or refute claims of preserved protein and tissues. Early investigations relied largely on morphological and observational assessments (optical microscopy and scanning electron microscopy). Later observations grew more technical, invoking atomic force microscopy (AFM), immunochemistry fluorescent staining techniques, ion mass spectrometry, energy-dispersive X-ray spectrometry in SEM, and Fourier-transform infrared spectroscopy. Still, no consensus was reached, with the opposing research groups vehemently denying the validity of each others' work.

Although the survival of protein molecules through millions to hundreds of millions of years of environmental exposure seems remote, I have tended to favor an alternative perspective. The rebuttal arguments claimed that the structural features observed by Schweitzer's group were simply bacterial biofilms that had invaded the bones shortly after death and established endocasts of the vascular features and osteocyte lacunae. That is, even these hypothetical biofilms would be millions to hundreds of millions of years old. Hence, from my perspective, the answer to the question is exciting no matter what the outcome.

As part of Schweitzer's collaboration, however, my work on the soft tissue elements has approached the question from the perspective that these are preserved dinosaurian tissues (vessels). Hence, the techniques that I have applied toward this project have been focused on several aspects of blood vessel or bone collagen network composition and structure:

1. X-ray absorption near-edge spectroscopy (XANES), micro-X-ray fluorescence (μXRF), and micro-X-ray diffraction (μXRD) were used to investigate the composition of the samples at the ppm level.
2. Small-angle X-ray scattering (SAXS) was used to probe for the 67 nm D-spacing characteristic diffraction peak of collagen.
3. Optical, scanning electron, and transmission electron microscopies for visualization, as well as energy-dispersive X-ray spectroscopy (EDS) for qualitative compositional analysis.
4. Fourier-transform infrared spectroscopy (FTIR) for the chemical composition of the organic components (complementary to the techniques listed point 1, above).

Toward this end, I also have carefully selected my sampling locations, focusing my attention on an inner compact bone sample for the femur diaphysis of *Tyrannosaurus rex* (MOR 555). It is my belief, based on my work with the bone mineral, that highly encapsulated regions, such as the mid-shaft of a thick cortical bone specimen, are least likely to have suffered extreme alteration.

In these pursuits, I have been interested in the structure and composition of blood vessel and bone collagen network. I have already discussed the type I collagen in detail; however, more consideration of the blood vessel tissue is required here. Blood vessels are multi-walled tissues, composed of fibrous, pliable proteins and cells. These proteins can include type I collagen and elastin, both of which are fibrous, measuring microns in width. Both protein types also tend to be very stretchy. As proteins, the key compositional features (with respect to FTIR analysis) are the amine functional groups. The contrasting hypothesis, however, that these tissues are nothing more than bacterial biofilm, would be better defined by starch-based functional groups.

Therefore, the techniques selected above should be sufficient for distinguishing these tissues (vessels/collagen network versus bacterial biofilm) based on composition and structure.

With respect to the specimen work presented in this manuscript, however, I restrict my overall focus to the set defined specifically for this study (as given in section 2.1 and Table 2.1). In the discussion, although I refer back to the work by M H. Schweitzer and others, as well as some of my own, I do not elaborate on the blood vessel work further. Instead, I present alternative, compelling evidence for the preservation of collagen architecture in bone, as a result of the preservation of the inverse template. That is, I discuss the preservation in light of the fossil bone mineral and how analyses of bone mineral can be used to inform investigations of ancient collagen structure.

1.2.3. Nanoscale structure of fossil bone

Pressure-induced cracking, bioerosion, loss of collagen scaffold, bioapatite chemical changes, and nanocrystallite coarsening all have the potential to alter the nanoscale structural motif of bone during diagenesis. Generally, however, I expect the consequences of these phenomena to be minimal, even in combination. Many of these phenomena are also readily identifiable and can be avoided during spatially resolved analyses with imaging components. Further, as this study will elucidate, even in the presence of some of these diagenetic changes, original structure can still be inferred. This section will further clarify the identities of each of the phenomena recognized as potential contributors to nanoscale structural changes.

As discussed above, in section 1.2.2, chemical substitutions in bioapatite, which is already a relatively impure mineral, tend to occur in a structurally conservative fashion with respect to the lattice. Several at.% of chemical substitutions have been shown to frequently occur in diagenetically altered bone mineral. This degree of chemical change, however, only strains the lattice by a small fraction, with the ultimate consequence that the lattice parameters of diagenetically altered bioapatite are often changed by fractions of nm. Ultimately, therefore, when this degree of strain is propagated throughout an entire crystallite, the crystallite itself exhibits scarcely detectable changes in dimensions. This same logic can be extended further, to the level of the collagen microfibril, and beyond. There are, of course, other phenomena of interest with respect to nanoscale structural features.

Surface and internal cracks in fossil bones are almost ubiquitous phenomena, stemming from the exposure of fossil bones to extreme pressures and intermittent aqueous events over long periods of time. At higher length scales, in particular, cracks are often very apparent and can be readily distinguished as diagenetic artifacts. Although few authors have previously described the presence of nanoscale cracks in fossil bone specimens (Hubert *et al.*, 1996), I have no doubt that they do occur. At this length scale, however, the definition of a crack ultimately becomes somewhat arbitrary. For the purposes of this exploration a nanoscale crack is recognized as any noticeable cleavage in the natural order of the microfibrillar structure, especially one which introduces new chemical or structural phases, particularly in the form of readily identifiable precipitates or extreme coarsening. The concept of a nanoscale crack was formed following the analysis by Hubert *et al.* (1996). However, cracking phenomena can only be reliably distinguished in pristine specimens; any mechanically altered specimen (*i.e.*, a crushed specimen, a mechanically thinned and polished specimen) may have induced artifacts of processing, and

these artifacts are absolutely likely to present as crack-like features. This is especially true for processed sections of bone. In crushed specimens for transmission electron microscope (TEM) imaging analysis, however, the cracks are the boundaries of the discrete particles. Regardless, both direct imaging and indirect spectroscopic methods can be used to probe nanoscale structural features within bone, with each sampling approach possessing its own limitations.

Bioerosion results from the reworking of bone structure by various biological entities, such as bacteria or fungi (Jans, 2008; Jans *et al.*, 2004). In this case, such lifeforms are introduced into the cortex of the bone via open channels such as the osteonal network. Then, as the biological forms continue to infiltrate the bone tissue, they do so by locally dissolving the bioapatite mineral to expose the collagen beneath for metabolic processing. Bioerosion tends to leave visually characteristic patterns, such as long, meandering trails measuring several microns in width (see Figure 1.3). Further, because the organisms begin reworking the bone by locally dissolving the bioapatite, they tend to create ionically saturated local environments. It then follows that calcium phosphate mineral redeposits along the erosion channel, readily evidenced as brighter channel boundaries in back-scattered electron imaging (higher mineral density of reworked calcium phosphate). This latter fact is unsurprising, as bone is, inherently, a semi-porous structure, down to the nanoscale. Regardless, it stands that bioerosion is readily detected by various visual signatures, and such areas exhibiting extensive bioerosion can be excluded from many analyses by simple visual inspection; similarly, if such areas are chosen for analysis, the presence of bioerosion must be indicated in any resulting report.

The loss of the collagen scaffold over time is also a ubiquitous phenomenon in fossil bones (partially responsibility for embrittlement). Organic molecules are inherently much more sensitive to environmental disruptions than the inorganic bioapatite phase. Various contributors to collagen loss include changes in local pH, photooxidation via ultraviolet exposure, biological erosion, and other possible factors. The loss of collagen increases the net porosity of bone, especially at the nanoscale, with the ultimate effect of increasing the potential for diagenetic changes of the bioapatite phase. The loss of collagen in fossil bone generally scales with the fossil age but is also dependent upon other fossilization conditions. Collagen, when explored with electron microscopy, is also substantially susceptible to ionizing beam damage (Hong *et al.*, 2009). Hence, while much relevant work has claimed the extensive coarsening of bone samples *in situ*, as evidenced by the spottiness of diffraction ring patterns in the TEM images (Figure 1.4), I believe that spottiness is more likely an indicator of the relative amount of collagen loss in the region analyzed than an indicator of beam damage. For example, Figure 1.5 shows an electron diffraction pattern obtained from a region of fossil bone, in which the smooth rings are of particular interest.

Combining the collagen with the bioapatite, we develop the microfibrillar structure, which has been discussed in detail in section 1.1.3, above. The microfibrillar structure can be observed by both indirect means (*e.g.*, SAXS) and direct means (*e.g.*, electron microscope imaging). In the literature, there exist many reports of preserved microfibrillar structure in fossil bone (Elorza *et al.*, 1998). However, many of these reports also suggest that the mineral crystallites forming the structure are not original bioapatite but instead are highly altered apatite (such as francolite) or other mineral forms (such as iron oxide-based structures). Additionally, the issue is compounded by issues of nomenclature: the word *fibril* is inconsistently used

throughout the paleontological literatures (and engineering), particularly with respect to decade. Further, the direct observation studies have largely depended on two approaches, both carried out in SEM: one, the imaging of microfibrils within osteons, and two, the imaging of texture on freshly cleaved surfaces. While these approaches in SEM may be sufficient for gathering information such as microfibril width and bone tissue ply organization, they are absolutely insufficient for identifying the internal architecture of the microfibril, which is of paramount interest. For the reasons stated above, I propose to apply additional methods of analysis, such as SAXS and TEM imaging.

The net effect of diagenetic alteration on the microfibrillar structure in fossil bone has substantial implications for the higher orders of bone structure. To summarize the discussion above, biological alteration indeed damages the local nanoscale structure, but it is also readily discernible with visual approaches, and identified regions should not be investigated further (unless of particular interest). Chemical alteration occurs in a conservative fashion; additionally, there are a variety of techniques (WDS, EDS) for chemical analysis that can be carried out in concert with spatially resolved, visual approaches to eliminate more altered regions from analysis. Finally, physical changes, such as distortion or cracking, are more difficult to directly detect with electron microscopic imaging approaches, because the sample preparation processes may impart physical damage. However, combinations of electron microscopic imaging techniques (including dark-field) and indirect sampling by SAXS can be used to more fully understand the microfibrillar structure of fossil bone tissue. The literature descriptions of microfibrillar structure often indicate that the bioapatite has been replaced in a manner that conserves the original texture of the bone; however, it is my belief that the microfibril is more highly conserved within bulk regions of bone. This fact might prove exceptionally true if the identification of collagen within bone holds against further analyses (see section 1.2.2 above).

1.2.4. Higher order structures of fossil bone

The data supporting the preservation of higher orders of structure in fossil bone are heavily weighted toward features that are visible with light microscopy techniques. This is due to several factors. One, in paleontology, it is still common to describe bone tissue by a comparative analysis of its transmitted light micrographs against the associated polarized light micrographs (*e.g.*, Hübner, 2012; Scheyer & Desojo, 2011), which are produced by passing light through a thinned section of bone, mounted onto a glass plate by epoxy. Typically, these specimens have also been embedded with resin for support during the wafering process. While these descriptions undoubtedly provide insight into the relative degree of internal orientation of the interfering structures (*i.e.*, the fibrillar structures) based on the birefringence patterns produced, this is a relatively indirect means of sampling the tissue (*e.g.*, strong birefringence implies “high internal orientation” of the fibrillar structure and *vice versa*). Nonetheless, it does demonstrate the presence of preserved structural order. Two, many features of significance from the physiological perspective have tended to steer the methods utilized for analysis. For example, bone lamellae are deposited in layers ranging up to hundreds of microns in thickness, and osteocyte lacunae are approximately 50 micron in the longest direction. Therefore, it is simply unnecessary to pursue more costly analyses, such as electron microscopy, for investigations focused on these structural features, which are easily accessed with light microscopy alone.

Work in this area has produced a plethora of thin section analyses of fossil bones from a variety of species. Some investigations have included numerical datasets, where values of interest, such as the number of lines of arrested growth (LAGs), have been calculated from the light micrographs (Klein & Sander, 2008; Horner *et al.*, 2000). In some cases, the average morphology of the osteocyte lacunae has been used to develop arguments surrounding the identification of new bone tissue types (Horner & Goodwin, 2009). At even higher orders, other studies have investigated the lamellar/trabecular features of embryonic long bone (Horner *et al.*, 2001); clearly, these are features readily accessible by light microscopy approaches. However, where this type of approach falls short is the direct visualization of the actual fibrillar structure, particularly the upper levels of its hierarchy, which I have defined as the *higher orders*. Additionally, many of these approaches yield qualitative data, whereas techniques such as SAXS can produce immediately manipulatable datasets revealing numerical values.

Few studies have pursued electron microscopy or SAXS studies of fossil bone with respect to the fibrillar structure of bone tissue. In part, owing to the history of technological innovation in the field of electron microscopy and atomic force microscopy (AFM), paleontological work on the structural hierarchy of the fibrillar structure tends to jump from polarized light microscopy directly to TEM thin section analysis. In fact, this is commonly seen in investigations of modern bone, as well, so perhaps it is no surprise that we find the same fact reflected in the paleontological literature. Regardless, there simply are no published studies on the systematic measurements of microfibrillar and macrofibrillar features in fossil specimens.

In instances when SAXS has been applied, the technique has largely been used to glean crystallographic information and generalized texture data from the fossil thin sections (Lonardelli *et al.*, 2005). While this data is inarguably useful, largely because it can supply averaged values for microscale tissue regions, the general field still lacks further insight into the fibrillar structure based on SAXS experiments. Further, in the past, some instances of synchrotron diffraction investigations have actually counterindicated the survival of bone mineral in fossil specimens (Lonardelli *et al.*, 2005). Hence, it is not surprising that these techniques have not been embraced within the paleontological community. This is, of course, where a portion of my research results ideally will shed light on the vast information that this approach can supply.

In short, although this section may seem underdeveloped, that is precisely my point: this is an area that has been highly underexplored. The possibility of investigations in this area, particularly those of a comparative nature wishing to systematically measure feature sizes and architectures, is endless. Further, any work done at this level of the structural hierarchy, when combined with the lower order features and compositional data, will invariably inform future work on the structure/property relationships of fossil bone, which are the subject of the next section.

1.2.5. Structure/property relationships of fossil bone

As diagenetically altered bone tissues, the notion that structure/property relationships can be extracted from fossil bones seems far-fetched, indeed. In some respects, it most certainly is. However, in recent years, a growing body of work has surfaced, focused on inferring the structure/property relationships of fossil bone tissues based on analogy. These studies also have

pursued mechanical analysis investigations of whole bone specimens, such as bite force in skulls, based on a combination of computed tomography (CT) and finite element analysis (FEA) approaches. While the results are far from complete and currently suffer from a lack of robust mechanical property data, the studies are certainly intriguing in their own right. Further, these studies are a marked improvement on the earlier generations of similar studies, which relied solely on features such as bite patterns in prey bones to back-infer, for example, the bite force and pattern of the *Tyrannosaur* jaw.

Unlike modern bone specimens, fossil bones cannot be directly tested for their mechanical properties. That said, there is still controversy in the literature over the appropriate testing protocol for modern bone specimens, and as indicated above, recent results have shown that some testing protocols are, in effect, fossilizing the modern bone specimens of interest (Barth *et al.*, 2011). Fossil bones, however, have suffered an entirely different, and significantly more extensive, degree of diagenetic alteration than recent cadaver bone. These changes include chemical, physical, and biological changes. Chemical alteration disrupts the native bonding within bone tissue. Physical alteration, such as cracking, embrittles the bone specimen; other examples, such as mineral infilling, can reinforce the specimen from within and permeate natural cavity spaces. Biological alteration can leave extensive perforation within fossil bone tissue, intermittently combined with regions of high mineral density. All of these changes counterindicate the possibility of directly extracting meaningful mechanical properties from fossil bone specimens.

Instead, researchers have had to pursue indirect means of investigating the structure/ property relationships in fossil bone specimens. In 2001, Rayfield *et al.* first published on the use of CT and FEA to investigate the bite force in a theropod dinosaur cranium. Through the mid-2000s, Rayfield was particularly prolific in applying the FEA approach to the analysis of cranial sutures and bite forces (Rayfield, 2005a; Rayfield, 2005b; Rayfield 2004). In 2007, Rayfield published a complete overview on the application of FEA to the biomechanics of fossil specimens. Similarly, Sutton (2008) published a review on the application of tomographic techniques to fossil specimens. Later, Snively and Cox (2008) used FEA to investigate the mechanics of head-butting behaviors in pachycephalosaurs, producing results that have been hotly contested by others based on a demonstrated lack of histological evidence to support the claims (Goodwin & Horner, 2004). I mention this as a cautionary tale: the use of computer-based techniques to infer bone mechanics in ancient fossil specimens should always be coupled with direct histological and otherwise analyses.

Above, I suggested that the current level of work carried out with CT and FEA techniques is lacking. Indeed, there are a variety of issues associated with these studies, and the research groups pursuing CT and FEA investigations are currently working to alleviate them. For example, the CT data provide two useful components of the model, the morphology of the bone and the relative local density. The structure (*e.g.*, the cranium) is then meshed based on the output morphology; there are, however, limitations to both the meshing robustness and the assumptions that the CT data are fully representative of the structure. Generally, these issues are taken to be minor. In contrast, the local relative density has substantial implications for the mechanical properties assigned to each mesh unit, and clearly, the density values can be readily altered during diagenesis. Compounding this, in the past, the bone mechanical property data

available for applying to the mesh were based on *Struthio* femur tissue. For a variety of reasons, this might not be the ideal bone tissue to use, for example, in the mechanical analysis of a large theropod skull.

I point out some of these issues for several reasons. One, it is always important to recognize the limitations of using modeling work to back-infer the mechanical properties of fossil bone tissues, bones, and skeletons. Two, the results of my doctoral work support continued work in this area: the demonstration of preserved bone structural hierarchy in fossil bone tissue absolutely justifies the pursuit of structure/property relationships in diagenetically altered specimens. Further, I believe that, with the use of appropriate modern structural analogues, it might be possible to identify best-fit bone tissues for future FEA studies. That is, by comparing the structural hierarchies of fossil specimens to carefully selected modern specimens, it might be possible to select ideal tissue analogues, and then these modern tissues can be directly tested for their structure/property relationship. The results of these investigations can then be used to better inform FEA studies, which in turn, will be able to provide substantially more robust modeling results. Beyond bite force analyses, this approach could allow the biomechanics community to carefully trace the evolution of flight bone microstructure, gigantism, or bone diseases, among others. Clearly, this is an area worth pursuing, and it is my sincere hope that my doctoral work supports the continued success of this field.

1.3. Formulation of the problem

Compact bone tissues are of interest to a variety of disciplines, from engineering to the biological and medical sciences. In particular, most studies of compact bone investigate long bone tissue, such as the tissue in the cortex of the femur diaphysis. For comparison purposes across the fields, studies of femur cortical bone, therefore, are the most readily comparable and often of the highest merit. Investigations of modern cortical bone have successfully explored the hierarchical structure of bone tissue, from the lowest levels (*i.e.*, nanoplates and collagen) to the highest levels (*i.e.*, tissue mechanical property analysis and FEA modeling approaches). However, only recently have studies pursued the nanoscale structural properties of bone tissue in depth. Even today, these studies remain highly incomplete.

In contrast, the fossilized bones of extinct species, which have undergone diagenetic alteration, offer tremendous new insight into structure/property relationships from a deep time perspective, including enhanced understanding of bone diseases, biomimicry of composite materials, and other basic knowledge of bioapatite composition and nanoscale bone structure. Yet, to date, most work on fossil bone has employed microscale techniques, and many of these investigations have counter-indicated the survival of bioapatite and other nanoscale structural features. Further, while similar techniques have been applied across modern and fossil specimens, there remains a substantial disconnect in terms of the species investigated and the data generated.

To begin the complex process of stitching together the work performed in the engineering and biological and medical sciences, the techniques utilized, the species studied, and the evolutionary relationships among those species, I have developed the following doctoral study.

One, ideally, to relate work with fossil bone to work on modern bone, particularly that carried out in the engineering disciplines, it is of the utmost importance that the techniques

applied to modern specimens be vetted for application to fossil bone tissues, as well. Toward this end, I have carefully selected a subset of modern characterization instrumentation commonly utilized in the engineering disciplines. These techniques offer the highest spatial and energy resolution available today and include SEM with EDS, electron microprobe with WDS, SAXS, bulk and powder XRD, and TEM with diffraction, dark-field, and tomography.

Two, to support the emphasis on the importance of understanding bone from the deep time perspective in addition to recognizing the inherent significance of phylogenetic relationships and evolution, I have selected a specimen set of closely related organisms, spanning from pre-history to modern times. This specimen set includes dinosaurs, crocodilians, and ratites; four of the bones are fossil, and three are modern. Additionally, all specimens are long bones; six are femora, and one is a radius. All bone tissue samples were removed from the long bone diaphyses in the cortices. These species were selected based on the Extant Phylogenetic Bracketing technique, such that in ideal conditions the modern specimens offer the best-fit controls for interpreting diagenetic alteration in the fossil specimens.

Three, most centrally, to support the notions that our understanding of the nanoscale structure of bone is currently ubiquitously underdeveloped, that the survival of nanoscale structural features and bioapatite has been counter-indicated in paleontological disciplines, and that the full hierarchical structure of bone tissue is ultimately of interest for interspecific comparative investigations or materials biomimicry, among others, this study investigates the full structural hierarchy of each compact bone specimen. Particular emphasis is placed on the nanoscale structural features and the composition and morphology of the bioapatite. Additionally, this study is focused on the fossil bone specimens, and the supporting phylogenetic bracket has been constructed specifically to support these species, which include several dinosaurs. Further, the selected techniques also have been identified to support these goals; as such, they are weighted toward high-spatial-resolution approaches. This study also will cover higher order structural features not as commonly of interest in the engineering disciplines, including the bone tissue, osteons, and osteocyte lacunae.

In summary, the results of this study are intended to demonstrate (1) the applicability of modern characterization instrumentation to fossil bone specimens, (2) the importance of studying bone from the deep time perspective and the significance of fossil specimens in all microstructural work related to bone, and (3) an enhanced understanding of the nanoscale structure of bone in addition to demonstrating the preservation of the complete hierarchical bone tissue structure in fossil specimens aged over 50 million years in light of the chemical and structural changes that have occurred.

1.4. Scope of work

The scope of this work is defined in light of the overall problem statement given above. In demonstrating the applicability of modern characterization techniques to fossil bone specimens, I will use standard materials science specimen preparation techniques and characterization protocols to prepare and investigate the fossil bone specimens. In materials science, modern bone specimens are prepared by diamond saw sectioning and metallographic polishing. In some cases (*e.g.*, SAXS), the specimens also must be thinned to microscale thickness. In this work, these same preparation procedures will be applied to the fossil

specimens, in as many instances as possible. Further, identical characterization protocols will be used, such as accelerating voltages, scan rates, *etc.*

To support the importance of studying bone from the deep time perspective and the significance of fossil specimens in bone microstructural work, this manuscript presents an in-depth literature review, which not only presents the related works but also explores their significance and presents their strong interrelationships. Further, the results of the characterization component of this study will be interpreted in support of this interdisciplinary goal.

To develop an enhanced understanding of the nanoscale structure of bone and to demonstrate the preservation of bone in excess of tens of millions of years in age, this study will be flushed out with a thorough scientific investigation, spanning a variety of characterization techniques and the entire structural hierarchy. Emphasis will be placed on quantitative analysis.

Ultimately, this work is intended to serve as a foundational piece. While it is expected that some conclusions will be useful toward realigning current perspectives, the majority of this work is intended to support the overall notion that fossil bones contain extensive, highly preserved tissues. Again, the focus here is primarily on nanoscale structure, under the notion that the demonstrated preservation of nanoscale structure supports the idea that higher orders of the structure are preserved, as well. Toward this end, it is the goal of this work to outline a general protocol for locating, identifying, and characterizing minimally altered bone tissue in fossil specimens. In the future, it is my hope that this foundational work will be sufficient to serve as a platform for motivating a variety of other studies, ranging from materials biomimicry and structural analyses of unique bone tissues to comparative structural investigations spanning various phylogenies, from modern to fossil species.

However, it is not the goal of this work to investigate the applicability of every characterization technique demonstrated for use in the analysis of modern bone tissues. The techniques selected are among the most commonly used and are the most straight-forward for supporting the claim that the composition and structure of fossil bone is minimally altered. Similarly, it is not the goal of this work to exhaustively outline all categories of investigations that might wish to incorporate fossil bones. It is not the goal of this work to definitively establish the nanoscale structure of bone but simply to enhance our current understanding, particularly from the perspective of the dinosaurian lineage. It also is not the goal of this work to ubiquitously demonstrate the preservation of minimally altered bone tissue in fossil specimens but rather to demonstrate that extensive, minimally altered bone can be preserved in ancient bone tissues. Finally, although quantitative results will be generated, these results also will be specific to the specimens investigated in this study, and only generalized results will be applicable to other specimens not included here.

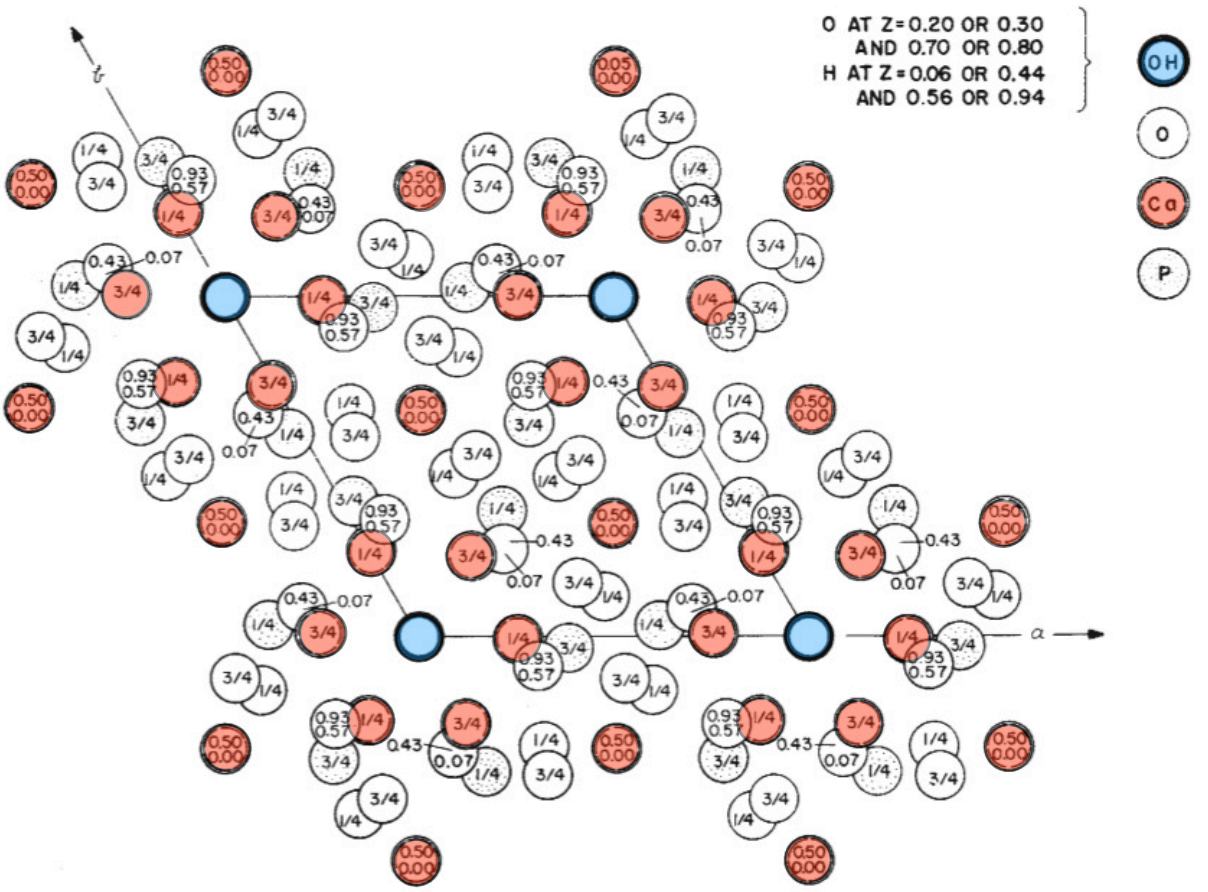

Fig. 1. Hydroxyapatite structure projected on x, y plane

Figure 1.1 The structure of hydroxyapatite, viewed down the *c*-axis. The calcium atoms are highlighted in red, and the hydroxide ions are highlighted in blue, to show symmetry. This figure is reproduced from Kay *et al.* (1964).

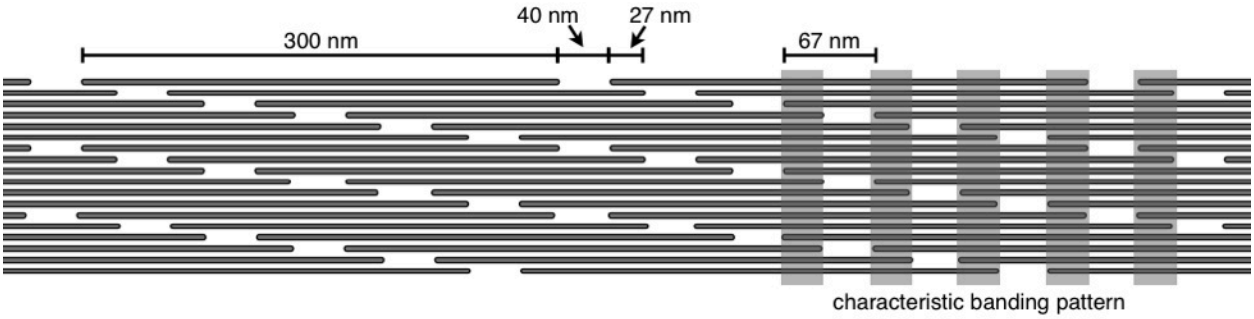

Figure 1.2 The stacking sequence of collagen (300 nm). The molecules stack head-to-toe with a 40-nm gap. Adjacent stacks of molecules are offset by 27 nm. This leads to the 67 nm D-spacing of collagen and the characteristic alternating dark/light banding pattern, which is observable in electron microscopy.

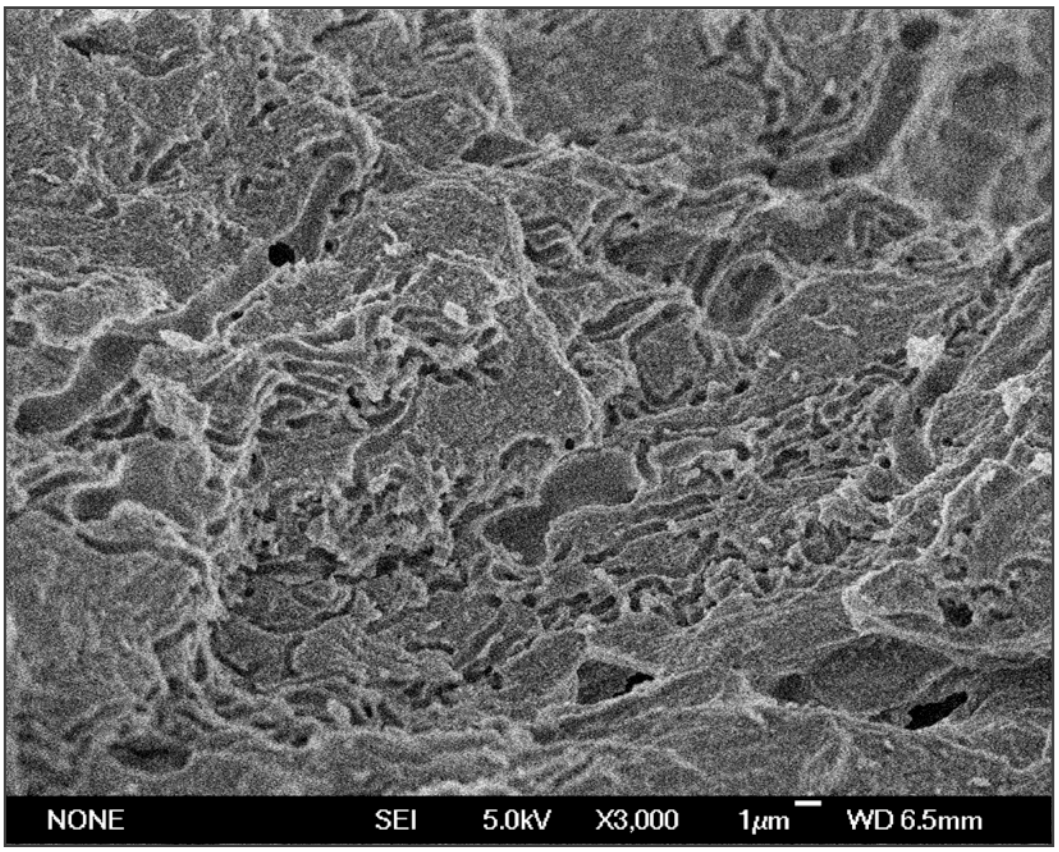

Figure 1.3 An example of bioerosion in *Stegoceras* cranial bone (3k×, secondary electron image). The erosion channels progress throughout the bone in a meandering, worm-like fashion, making them readily identifiable. The edges of the channels tend to appear brighter due to the higher concentration of re-deposited mineral.

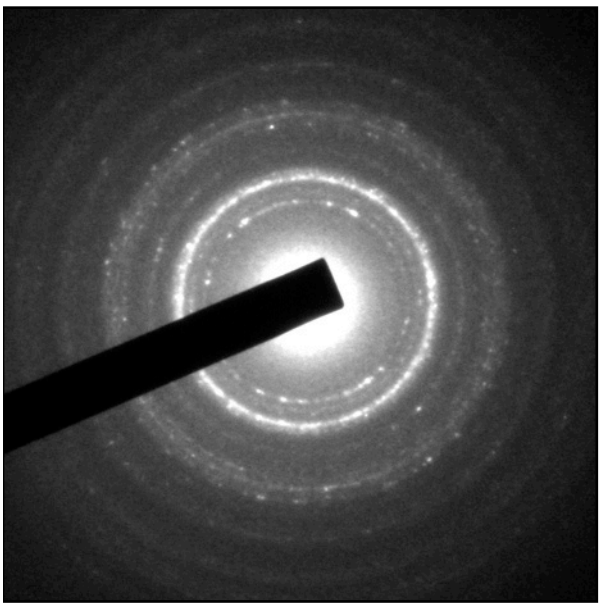

Figure 1.4 Electron diffraction pattern of triceratops bone showing spotty rings.

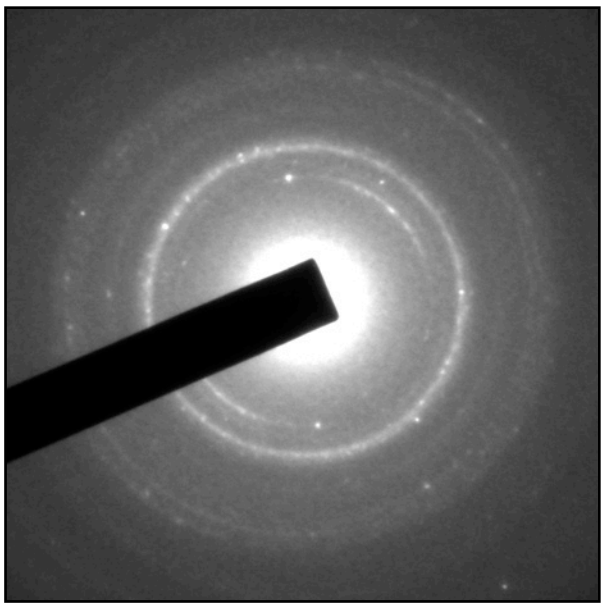

Figure 1.5 Electron diffraction pattern of same triceratops bone, different region.

2. Experimental methods

To explore the degree of chemical and structural change in fossil compact bone, and the interdependency between the two, a suite of characterization techniques was selected. These techniques, together, have the capacity to span from the micro- to the nanoscale structural units, upon which the entire structure of bone is constructed. In particular, the bone mineral composition and nanoscale structure of fossil bones are of critical interest to this study. Because previous paleontological work has focused largely on microscale analyses, which have typically counter-indicated preservation of minimally altered bioapatite and nanoscale structure in fossil bone, this work also aimed to establish the inconsistent nature of applying microscale results to questions of nanoscale composition and structural preservation in fossil compact bone. In particular, the following analyses were defined for this study.

- Scanning electron microscopy back-scattered electron images were recorded over large transverse surface areas of each specimen to demonstrate the possible extraction of useful physiological characters from fossil bone.
- Scanning electron microscopy energy-dispersive X-ray spectroscopy was performed on regions of interest to establish identities of distinct examples of diagenetic alteration as well as on regions that appeared to exhibit striking preservation of the original mineral density variation.
- Electron microprobe wavelength-dispersive X-ray spectroscopy (WDS) was performed on polished bulk sections of each specimen to establish analytical compositional values.
- X-ray diffraction was performed on the same bulk sections to determine the mineral phases present in each specimen. Because partial conversion of impure hydroxyapatite to flourapatite can be very challenging to precisely assess with X-ray diffraction, the diffraction data were combined with the WDS data for final interpretation of the present state of the mineral phase(s).
- Transmission electron microscopy imaging studies were carried out to assess the retention of nanocrystallinity in the fossil specimens. To further verify the identity of the nanocrystallites used for such demonstration, an electron diffraction pattern was recorded at each recorded image location, isolated by an intermediate aperture.
- Transmission electron microscopy dark-field imaging was performed to explore preservation of the nanoscale structural motif of bone (the microfibril). This method was combined with tomography to further demonstrate the possibility of extracting a three-dimensional interpretation of the structural preservation in the fossil bones.
- Small-angle X-ray scattering was carried out on thin sections of each specimen to establish large-scale preservation of the microfibrillar structure.

All of these analyses are further described in detail below. Additionally, it is worth noting both the rationale behind including modern specimens in the overall analysis, as well as the method by which these modern specimens were selected.

Each of the analyses carried out for assessment of the degree of preservation of bioapatite composition and nanoscale structure in the fossil bone specimens is best interpreted in light of standards. While geological or synthetic hydroxyapatite standards provide compositional

calibration, they lack the critical nanoscale structural identity so specific to bone. In other words, to harness the analysis of both composition and structure, the only reasonable standards to use for a study of fossil bone specimens are modern bone specimens. Further, the case is not met simply by employing one modern bone specimen or by selecting modern bone specimens irrelevant of tissue or phylogeny. For this reason, three modern femur bone specimens were selected, from different species. The species of interest were identified to phylogenetically bracket the dinosaur specimens. This is a technique first applied in 1995 by L. M. Witmer for soft tissue analysis studies. While bone mineral is clearly not soft tissue, the nanocrystallite dimensions and nanoscale structure of bone are all explicitly controlled by the original collagen scaffold. For that reason, mindful application of the Extant Phylogenetic Bracketing technique, which is now common practice in the paleontological discipline, was absolutely a key factor in identifying which modern bone specimens were used for this analysis. The standard choices for bracketing the dinosaur clade include crocodiles and ratites, hence the final selection of *Caiman*, *Struthio*, and *Rhea* femur bones.

2.1. Identification of the specimens

The specimen set for this investigation was obtained from the collections of the UC Museum of Paleontology. In total, seven specimens were selected for analysis, including three modern specimens and four fossil specimens. Six of these seven specimens were femurs and the seventh, a radius. The radius belongs to hadrosaur family, which is a genera of large, quadrupedal dinosaurs. Because radii served in a weight-bearing, locomotive capacity in these dinosaurs, the loading conditions are very similar to those of femora, which are the typical long bones used for bone structure/property analyses.

All long bones were sampled at the shaft diaphysis with particular attention given to the compact bone region. In fact, the medullary cavities of both birds and reptiles are often called “hollow,” indicating that they contain no trabecular bone. It is worth noting that, in this specimen set, only the hadrosaur diaphyses contained trabecular bone in the medullary cavity. In both cases, samples of trabecular bone also were recovered, although the remainder of this study focuses specifically on the compact bone. The specimen information is summarized in Table 2.1. Further relevant specimen information is given in Appendix C, including the UC Museum of Paleontology catalogue records.

2.2. Sampling of the whole specimens

Small sections or cores of long bones were removed by various methods. A small cut-off wheel was used to remove half-circumference slices from the *Struthio*, *Rhea*, and *Caiman*. A drill press fitted with a ½” diamond coring bit was used to remove bone cores from the hadrosaur femur and hadrosaur radius diaphyses, sampling both the compact and trabecular bone from periosteum to endosteum. A high-speed rotating table saw was used to remove a section of the *Pristichampsus* femur. Finally, the *Tyrannosaurus* femur selected for analysis was partial and already contained several broken fragments that had been re-attached in place with heat-sensitive epoxy. One of these fragments was removed from the bone by local heating to soften the epoxy until it could be lifted free. These whole bone fragments were all immediately sectioned into two

equal-sized portions. One portion was set aside for bulk specimen polishing, and the other was used for preparation of other samples, as described below.

2.3. Summary of the sampling locations for all analyses

In all instances, the sampling locations of the long bones were carefully selected to be as isolated as possible from free surfaces and likely points of exposure. That is, the periosteum, endosteum, osteons, osteocyte lacunae, and any evident cracks represent very likely places for exposure of bone material to external ion sources, which can alter composition, or to external aqueous environments, whose variable pH can, over time, cause local dissolution and precipitation of new phases. Therefore, to establish the best possible chance for identifying minimally altered bone tissue in the fossil bone specimens, all analyses were carried out at mid-cortex, between osteons, and clear of apparent cracks. This was easier to control for certain specimens and samples than for others.

More specifically, all polished bulk section analyses were readily isolated for bulk regions at mid-cortex. Specimens removed from the larger long bones, such as the *Tyrannosaurus* and the hadrosaurs, were selected precisely at the mid-cortex, while specimens removed from the smaller femora spanned the entire periosteum to endosteum, necessitating further isolation of the region of interest. For electron microprobe analysis, areas analyzed by wavelength-dispersive X-ray spectroscopy were selected mid-way between osteons, representing distances of at least 100 μm from osteon surfaces. Indeed, this distance is an exceptionally long path for diffusion of external ions into the bulk bone; this idea will be explored in more detail later in this study. For scanning electron microscope work, however, any energy-dispersive X-ray spectroscopy compositional work featured compositional variation over distances or diffusion from free surfaces into the bulk bone.

Small-angle X-ray scattering analysis was carried out on thin sections removed from the mid-cortex of each bone. Again, for the smaller femora, this meant isolating the region of interest at the full sample mid-section. Thin sections were mapped by 2-D Nanography for optimal X-ray beam attenuation by 1 mm increments. Several specimens necessitated mapping with higher spatial resolution to more precisely locate appropriate areas for analysis. Because the final beam size was on the order of 0.4 mm, it was not possible to avoid osteons or cracks for this analysis.

Transmission electron microscopy was carried out on two types of samples. All crushed bone samples lost any information regarding location relative to free surfaces such as osteons. Instead, crushed samples could only be isolated from the mid-cortex of the fossil femora. Thin sections were removed in a similar manner described above for the SAXS analysis. Retention of local orientation information allowed for the possibility of isolating mid-cortex regions, as well as regions between osteons, for any diffraction and imaging.

2.4. Preparation of polished bulk sections

A Buehler IsoMet® Low Speed Saw outfitted with a high concentration diamond wafering blade measuring 0.012” in thickness (Allied High Tech Products, Inc.) was used to remove small portions from each of the specimens recovered in section 2.2, above. Bone core samples were sectioned in half, along the length of the cylindrical core. All bulk sections were prepared with full cortical bone intact. Hadrosaur radius and hadrosaur femur were the only bone

specimens that contained trabecular bone in the medullary cavity. The cortical portions of these cores were further prepared, and the trabecular bone was set aside.

Once these smaller portions had been removed, both longitudinal and transverse surfaces of interest were identified for further analysis. These surfaces were then shaped and polished on an XP 8 Grinder/Polisher (Ted Pella, Inc.) using adhesive-backed SiC discs. Polishing was completed in three steps to obtain optically smooth, flat surfaces. Bone sections were first shaped with 600 Grit SiC paper (Allied High Tech Products, Inc.). Shaping involved the removal of sharp, jagged features, the construction of parallel sets of surfaces, and the elimination of large surface aberrations introduced by cutting. Once shaped, the surfaces of interest were further subjected to polishing on 800 Grit SiC paper (Allied High Tech Products, Inc.) until any visible surface roughness had been eliminated. An optical microscope was used to verify the elimination of most micron-sized aberrations. Visually, the specimens exhibited a minimal amount of sheen at this stage. Finally, the surfaces of interest were finely polished with 1200 Grit SiC paper (Allied High Tech Products, Inc.) until highly reflective and exhibiting no surface aberrations when viewed under an optical microscope. (Note: Standard bone surface preparation procedures involve a further step of polishing with a diamond particle suspension. This step was not performed for this analysis, however, because the risk of embedding particulates into the fossil bone features, and therefore introducing artifacts into the study, was considered to be too significant.)

When polishing the surfaces of interest had been carried out to satisfaction, the bulk sections were dried for at least four days in a desiccator, using Drierite anhydrous calcium sulfate as the desiccant (W. A. Hammond Drierite Company, Ltd., Xenia, OH). The desiccation chamber was maintained at normal atmospheric pressure during this time.

Photographs of the polished specimens are included in Figure 2.1.

2.5. Preparation of thin sections for small-angle X-ray scattering

A Buehler IsoMet® Low Speed Saw outfitted with high concentration diamond wafering blade measuring 0.012” in thickness (Allied High Tech Products, Inc.) was used to remove longitudinal thin sections from each cortical bone sample. These sections were hand-thinned against 800 Grit SiC paper (Allied High Tech Products, Inc.) on an XP 8 Grinder/Polisher (Ted Pella, Inc.) until section thicknesses reached 100-200 microns. Each section thickness was measured with a Digimatic Coolant Proof IP 65 Micrometer (Mitutoyo America Corporation). The sections were allowed to fully dry in a desiccator at ambient pressure before being stored in Snap-fit® gelatin capsules Size 00 (Ted Pella, Inc.). Drierite anhydrous calcium sulfate was used as the desiccant (W. A. Hammond Drierite Company, Ltd.). Final specimen thicknesses are recorded in Table 2.2.

2.6. Preparation of disarticulated samples for transmission electron microscopy

Disarticulated samples were prepared by removing small portions of the fossil bones and then grinding those portions with an agate pestle and mortar in 95% ethanol (AlphaTec, Vancouver, WA). Upon sufficient grinding, the solutions were allowed to partially settle, and disposable plastic bulb pipets were used to extract small aliquots of the optically translucent

solution from the top of the mortar well. Individual droplets were transferred to the copper-colored side of ultrathin carbon lacey carbon copper TEM grids (Ted Pella, Inc.). The ultrathin carbon film on these grids had an approximate thickness of 2 nm, which made these grids the ideal choice for nano-particulate dispersed samples intended for EDS analysis. KimTech Science* KimWipes® (Kimberly-Clark Professional) were folded into triangular wicks and used to extract excess solution from the TEM grid surface, followed by an extra droplet addition of the disarticulated suspension in the bulb pipet and then rewicking. This was done three times for each TEM grid to ensure that a sufficient amount of bone material was transferred. To minimize aqueous bioapatite dissolution, 95% ethanol was used as the solvent and exposure was limited to approximately 3 minutes total.

(Note: The modern bone specimens were not analyzed according to this protocol. The modern bones in this specimen set had a very high collagen content and any preparation for disarticulation would have necessitated extra treatment steps to remove the collagen. Such steps would have potentially introduced artifacts into the bioapatite, ultimately violating any attempt to parallel process all bone specimens under identical conditions.)

2.7. Scanning electron microscopy

All scanning electron microscopy work was carried out on a Hitachi S-4300 SE/N environmental scanning electron microscope fitted with a Thermo Electron Corporation energy-dispersive X-ray detector and back-scattered electron (BSE) detector for imaging. All imaging and EDS analyses were performed at 15 kV for the beam accelerating voltage. BSE images were recorded at a chamber pressure of 40 Pa.

The polished bulk specimen transverse faces were investigated with BSE imaging. Surface maps were generated by stitching together multiple, adjacent BSE images recorded at 100×. Features of physiological significance were measured and tabulated. Such features included mean osteon density, mean osteon circularity, mean osteocyte lacunae density, lamellar thickness, and percent bone volume to total volume (BV/TV).

Before the data were tabulated, the images were digitally processed according to the following prescription. The images were first processed to particular thresholds, chosen uniquely for each sample to maximize clarity in the final binary image. That is, some of the specimens exhibited lower contrast between, for example, the bulk bone and the osteocyte lacuna regions. Without special attention to the contrast variation between specimens, and hence individual thresholding, final binary images would in fact be poor representations of the actual specimen. Once the binary image sets were obtained, any obvious crack features still remaining were digitally removed. For all osteon and osteocyte lacunae particle analyses, circularity thresholds were set to the range 0.2 - 1. It should be recognized that this threshold setting excludes some features that might otherwise be counted, such as irregularly shaped osteons; however, establishing such a threshold also holds the analysis to a defendable, objective metric. The features were counted and tabulated over multiple images per specimen. All images used for this analysis were recorded at 100×.

Scanning electron microscopy also was carried out on particular features of interest, such as mineral in-filled osteons, mineral crusts deposited in trabecular regions, or lamellar

depositional growth regions. In these cases, alternative magnification BSE imaging and EDS linescans and spot analyses were performed as needed.

2.8. Electron microprobe and wavelength-dispersive X-ray spectroscopy

Analytical compositional analysis was performed on polished bulk samples with a Cameca SX-100 electron microprobe outfitted with five simultaneously recording wavelength dispersive spectrometers. Using double-sided adhesive copper tape layered on top of double-sided adhesive carbon tape, the polished bone samples were mounted to height-tunable stages with the polished transverse surfaces of interest facing up. The following steps were carried out to enhance the surface conductivity of the bone samples. Each sample was electrically grounded to the metal height-tunable stage with a portion of single-sided adhesive copper tape, pressed onto the edge of the transverse face. All samples were then coated with a 20-nm-thick layer of graphite in a carbon deposition chamber. The thickness of the graphite layer was monitored by assessing the surface color during deposition.

For analytical compositional analysis, the elements of interest were identified as O, F, P, Cl, Ca, Na, Fe, and Mg. Three geological standards were selected for spectrometer calibration. The majority of the elements of interest (O, F, P, Cl, Ca, Na) were calibrated against Wilberforce apatite fluorapatite, which contains 3.7 wt.% F, 0.05 wt.% Cl, 0.39 wt.% Sr, 0.26 wt.% Ce, 0.15 wt.% Nd, and several other rare earth elements each under 0.05 wt.%. This apatite standard had a total O content of 37.84 wt.%, a total cation content of 58.42 wt.%, and a balanced F+Cl content of 3.75 wt.%. The other elements of interest (Fe, Mg) were calibrated against a hematite standard and a calcium magnesium silicate standard, respectively.

Calibration for carbon was not performed, and carbon was not of primary interest in this study. Carbon can have two major sources in bone, including a majority content in organic components and a minority content in apatite carbonates (CO_3^{2-}). Mass balances of all bone specimens were within tolerable limits around 100 wt.%, indicating that dismissal of C from the analysis was not sufficient for disrupting the analytical nature of the technique. All locations for analysis were hand-selected at mid-way between osteons. Since carbonate content in apatite is highest in the regions bordering osteon surfaces, it was assumed that carbonate substitutions in the analyzed locations was negligible.

Locations for WDS analysis were hand-selected and recorded into the automated analysis system. For each specimen, between 8 and 10 locations were selected in back-scattered electron imaging mode, depending on the availability of acceptable regions between osteons and osteocytes. Dwell time at each location was 150 seconds. The incident electron beam was set at 15 kV accelerating voltage, 15 nA of current, and a spot size of 10 μm.

Specimens were analyzed in two separate runs as necessitated by equipment availability. The first run was conducted on September 2, 2011, and included *Struthio*, *Caiman*, *Pristichampsus*, hadrosaur radius, hadrosaur femur, and *Tyrannosaurus*. The second run was conducted on February 13, 2012, and included *Rhea*, as well as a *Triceratops* frill section.

Data processing steps involved tabulating composition averages and standard deviations. Such tabulations were performed to yield a full set of elemental composition values, per specimen.

2.10. X-ray diffraction

X-ray diffraction (XRD) was carried out on polished bulk specimens to determine the majority crystalline phases present in the bone cortices. The X-ray diffractometer used was a Rigaku 4th generation benchtop MiniFlex™ II operated with a tube voltage of 30 kV and current of 15 mA. In long bones, the bioapatite crystallites grow with their *c*-axis largely parallel with the length of the diaphysis. For this reason, analysis of a longitudinal plane guarantees the highest likelihood of sampling all key unit cell dimensions, the *a*, *b*, and *c* axes. Care was taken in mounting the specimens to insure that the longitudinal direction of the bone samples was oriented in the plane of the detector.

A special holder was fabricated for bone specimen analysis on the Rigaku MiniFlex™ II. This holder consisted of two components, a bulk sample mount with a spring-loaded stage and a plexiglass ring spacer. The bulk sample mount was fabricated to clip over the specimen goniometer such that the spring-loaded stage would hold all bulk samples in the focal plane during analysis by pinning the sample in place at three points, two against the goniometer and one against the front side of the bulk sample mount. The plexiglass ring was fabricated to take the place of a typical bulk sample, acting as a spacer between the spring-loaded stage and the three pinning points. Inside this ring, the bone samples were mounted in dye-free polymer clay with the transverse surfaces of interest leveled to the ring spacer surface, thereby guaranteeing the transverse surface to be in the focal plane of the X-ray beam.

All XRD scans were carried out at a scan rate of 1°/min, detector width of 0.05°, and in the range of 20 - 70° (2θ). The starting scan value, 20°, was selected to discount the low-angle, large amorphous plexiglass peak while still allowing for the observation of the 002 apatite peak, which was of primary interest as this peak was used to assess the *c*-axis dimensional parameter of the apatite structure. Scans were ended at 70° to follow convention previously established by the National Institute of Standards and Technology (SRM 2910); similarly, peak intensities were generally too low at these higher angles to be of significance.

2.11. Small angle X-ray scattering

Small angle X-ray scattering (SAXS) patterns can record information in the range of 1 – 150 nm (scattering angles 0 – 5°). For samples containing characteristic repeat distances, pore sizes, or particle distributions, SAXS can elucidate these distributions from a bulk, thinned sample. Bone contains several features of interest that can be detected with SAXS, including dimensions of the crystallites, dimensions of the collagen stacking overlap and gaps, and microfibril bundle widths, all of which manifest in an integrated SAXS spectrum as small but discernible diffraction peaks.

A Bruker AXS NANOSTAR operating at 40 kV tube voltage and 35 mA beam current was used to record all SAXS patterns. The hand-thinned longitudinal bone sections were mounted on double-sided Scotch® tape (3M). Regions of interest were identified by 2-D Nanography mapping with 1 mm spatial resolution, or better, as demanded. Regions of interest were programmed into a single run for automated analysis. Each sample was exposed for a total of 2 hours to guarantee sufficient intensity of any diffraction peaks of interest for extraction against the scattering background. All thin sections were mounted with their original orientation in the same direction. Full patterns were radially integrated in 30 intervals with the primary

wedge of interest selected as -5 – 25° for all specimens. This interval was selected after careful observation of the full pattern orientation. An additional section of -15 - 15° was analyzed for *Pristichampsus*. A background full pattern was also recorded for the Scotch tape with nothing on it.

Integrated wedges were then replotted and inspected for evidence of key nanoscale structural details. Such details included 27 nm, 40 nm, and 67 nm diffraction peaks, other sets of peaks possibly corresponding with nanocrystallite width and length dimensions, and high-order sets of peaks separated by roughly 150 nm of real distance, resulting from hexagonal close-packing of microfibrillar structures.

2.12. Transmission electron microscopy

Transmission electron microscopy work was performed on a JEOL JEM 2011 operated at 200 kV accelerating voltage, for basic imaging and diffraction capabilities as well as for dark-field imaging.

To assess the preservation of nanocrystallinity in the fossil bone specimens, the imaging methodologies were employed. All bone specimens were imaged at multiple locations at two magnifications, 6k× and 100k×. The former, lower magnification was chosen for surveying the degree of disarticulation of the fossil bone specimens dispersed on the ultrathin carbon holey carbon Cu grids. The latter, higher magnification was chosen for surveying regions of nanocrystallites. Electron diffraction patterns were also recorded from the regions imaged at the higher magnification. For this, a selected area aperture was employed to specifically select the regions around the imaged nanocrystallites. The electron diffraction patterns were calibrated against a polcrystalline Al standard (Ted Pella, Inc.) by the standard camera constant calibration method. All diffraction patterns were recorded at 40 cm. See Appendix I for further information regarding electron diffraction pattern processing.

Axial dark-field imaging analyses of the disarticulated fossil bone specimens were carried out on the JEOL 2011 to assess the preservation of nanoscale structure. This method was established in a multi-step process. First, areas of interest were located based on appearance. Second, a selected area aperture was used to generate diffraction patterns from each area of interest. To continue with the analysis, the diffraction pattern also needed to meet certain standards; specifically, the pattern needed to exhibit a high degree of internal orientation, implying that the internal architecture was more likely to contain minimally altered nanoscale structure. Third, an objective aperture was used to select a specific region of the 002 partial ring, and the entire selected assembly was reoriented onto the optic axis for optimal image collection conditions. Fourth, the dark-field image of the region of interest was recorded. Fifth, a process of tilting about the selected 002 orientation was employed to generate subsequent dark-field images of the structure at discrete rotational orientations. Sixth, the dataset was reconstructed for gleaning internal structural details.

Figure 2.1 Photographs of polished bulk specimen sections, prepared for SEM, electron microprobe, and XRD. (a) *Struthio* (125001), (b) *Rhea* (UCMP 129668), (c) *Caiman* (UCMP 63533), (d) *Pristichampsus* (UCMP 170767), (e) *Tyrannosaurus* (UCMP 136517), (f) hadrosaur radius (UCMP 175247), (g) hadrosaur femur (UCMP 169073).

Table 2.1 Summary of specimen information.

Specimen name	Scientific name	Vertebrate locality	Specimen no.
Struthio	*Struthio camelus*	Recent element	125001
Rhea	*Rhea americana*	Recent element	129668
Caiman	*Caiman*	Recent element	63533
Pristichampsus	*Pristichampsus vorax*	V79006	170767
Hadrosaur radius	*Hadrosauridae**	V85091	175247
Hadrosaur femur	*Hadrosauridae**	V85091	169073
Tyrannosaurus	*Tyrannosaurus rex*	V83075	136517

*Specimens only identified to the genus level.

Table 2.2 Thickness values (µm) of thin sections prepared for SAXS.

Specimen	Section (µm)
Struthio	101
Rhea	168
Caiman	89
Pristichampsus	130
Hadrosaur radius	171
Hadrosaur femur	188
Tyrannosaurus	217

3. Results

3.1. Scanning electron microscopy

Back-scattered electron surface map reconstructions of each specimen are presented in Figure 3.1 (the full-size maps are given in Appendix D). In particular, these images were recorded to use for the extraction of physiological characters of interest (*i.e.*, osteon and osteocyte lacunae data, bone lamellae thickness). The data on physiological characters of interest are discussed in section 3.2. Additionally, the surface maps were generated to give broad perspective on the growth patterns of these cortical tissues and the state of preservation of the fossil specimens. The variation in brightness across each individual tile was an inherent consequence of the system setup and should be disregarded.

In particular, the *Pristichampsus* specimen was found to be heavily in-filled with mineral. Based on the EDS results, the in-filled mineral was determined to be $BaSO_4$. The ubiquitous nature of the $BaSO_4$ in-filling in this specimen can be seen in the 100× image (Figure 3.2). This observation prompted an investigation into whether the in-filled mineral constituents had diffused into the bulk of the bone tissues, which has obvious implications for the ultimate goals of this study. Further, in light of the relevance of SEM techniques to the current paleontological and biological research communities, I believed it important to assess whether standard SEM functions could localize ideally minimally altered bone tissue. Toward this end, I performed an EDS linescan on a region of interest (Figure 3.3 (a)), which was identified based on the pronounced degree of $BaSO_4$ in-filling at this precise transverse transect of the bone. The linescan results are depicted in Figure 3.3 (b).

A similar image of pronounced mineral in-filling is presented for the cancellous bone of the *Tyrannosaurus* specimen. As visible in Figure 3.4, the mineral crust has deposited in the large porous cavities of the bone (trabecular bone). Crystal growth direction is evidenced by the radiating nature of the structure. Multiple growth events can be identified from this images, based on the layered structure of the crust. Energy-dispersive X-ray spectroscopy spot analyses were performed both in the mineral crust and in the adjacent bulk bone tissue to verify whether the elements in the mineral crust had infiltrated the highly exposed bone tissue (trabecular bone struts are often several hundred microns in thickness). It was found that the elements of the mineral crust had not infiltrated the trabecular tissue, above background levels. The supporting EDS data (at.% composition) are given in Appendix E.

Other evidence of diagenetic alteration is present in these specimens, garnered from the 100× BSE images. Sharp, intrusive cracking phenomena are present in all fossil specimens (examples are shown in Figures 3.2 and 3.3 (a)). Cracks also are evident in the BSE images of the modern specimens (*Caiman*, in particular, as can be seen in the BSE map in Appendix D); however, these cracks are the result of strikingly different phenomena. Modern specimens have high water contents, and as these specimens sit in the SEM vacuum environment, the water contents vaporize and the tissue cracks as a result. In the fossils, the cracking is the result of embrittlement, due to a loss of collagen and structural resilience as well as encapsulation beneath tons of sedimentary rock and exposure to repeated hydration/dehydration cycles. Sometimes, the osteocyte lacunae in the fossils have a deformed, blotchy appearance. This is particularly true in the regions of newest growth or highest exposure (see Figure 3.4 of the *Tyrannosaurus* trabecular

bone). Finally, none of the specimens present any evidence of biological alteration. The modern specimens are in a distinctly well-preserved condition: marrow tissue can be observed in the trabecular region of the *Caiman* specimen.

3.2. Physiological characters

Representative BSE image tiles (extracted from the maps) are shown for each specimen in Figure 3.5. These images serve two purposes. One, they illustrate the details of the respective tissues (transverse, 100×) of the specimens. Two, they serve as examples of the starting image tiles that can be used for subsequent image processing. In this work, the image processing was carried out to extract data on parameters of physiological significance. At the magnification used in these images, a variety of features of interest can be identified, including osteocyte lacunae, osteons, bone mineral density variation, and bone lamellae. All images are arranged with the periosteum on the left-hand side, such that the growth front is directed to the left-hand side of the page, which implies that the lamellae run vertically with the length of the page.

These figures clearly demonstrate the variety of compact tissue types present in vertebrate long bones. Even after controlling for phylogenetic relationships, there are a variety of highly distinct features present. For example, the ratite (*Struthio* and *Rhea*) bone has a highly lamellar character, which is the result of extremely rapid growth. In these examples, the osteon sizes of the crocodylians and hadrosaurs are approximately equivalent and frequently irregularly shaped. The osteons of the *Tyrannosaurus* bone are noticeably smaller. Of all tissues, the osteocyte lacunae density is the highest in the ratites, which is similarly unsurprising in light of the identification of rapid growth. Similar observations can be made from Figure 3.6, which is a magnified map of several compiled tiles. The growth lamellae, primary and secondary osteons, and other features are highlighted in this map. I give these observations merely to demonstrate the type of information that can be extracted from these images, following image processing.

A more thorough presentation of the physiological parameters of interest is presented in Appendix F for three fossil specimens. Although the identification of these features is a significant result, the detailed measurements of these features are not the focus of this work. Hence, the significance of the identifications is discussed further in the discussion, while the actual measurements are not.

3.3. Electron microprobe and wavelength-dispersive X-ray spectroscopy

The electron microprobe analysis was carried out on bulk polished sections of all seven long bone specimens. The analyzed surfaces were of the transverse orientation. Back-scattered electron imaging was used to locate bulk bone regions midway between osteons. The mineral in-filling of fossil bone often incorporates distinct mineral species into micron-sized porous regions of the bone, such as pressure-induced cracks, osteocyte lacunae, and osteons. In BSE images, these distinct mineral species are readily identifiable as having different brightness values against the bone mineral, tending toward substantially brighter (see Figure 3.2 of *Pristichampsus* in-filled with $BaSO_4$). This is especially advantageous for trying to isolate bulk bone regions least likely to have experienced compositional reworking. In all instances of selecting locations for analysis in the fossil specimens, any visibly enriched regions were strictly avoided to optimize the potential for locating minimally altered bioapatite. For this reason, the composition data

reported here should be viewed as such--optimized; no doubt other regions of the same fossil bones contain more highly altered and compositionally enriched mineral contents.

The data presented in Appendix G are average values calculated from multiple (5 - 10) spots of analysis. A summarized bar plot of the average values for each specimen is given in Figure 3.7; in this figure, each color band represents a specific ion type (red is cation, blue is anion, and gray is phosphate) given in at.%, weighted to 100%. The composition values are given in atomic percentages for elements O, F, Na, Mg, P, Cl, Ca, and Fe, provided as averages, standard deviations, and total weights relative to 100%. Carbon was explicitly neglected from the analysis because it cannot be distinguished from ionically bound carbonates in bioapatite *versus* covalently bound in proteins and other organic structures. Regardless, carbonates were assumed to be negligible based on analysis at regions far from osteons where carbonate substitutions are significantly less probable. This was further supported by preliminary weighting of the *Struthio* bone composition to 100% with a total discrepancy less than 1%, which is considered sufficiently within tolerance for technique error. The full set of average weight values for all specimens in the set also was within the same range, whereas the maximum tolerated weight percent error for this technique is 5%. Because the elements for analysis were selected based on preliminary assessments, it also is assumed that no major elemental components were overlooked in any of these analyses. Similarly, this idea is supported by the low standard deviations of the weight percents for all of the specimens.

Several significant trends can be observed in the dataset. First, all of the fossil bones exhibit increased fluorine contents *versus* the modern bones. Further, the increased fluorine content was explicitly observed with a correlated loss of oxygen content in the fossil bone specimens. Fluoride (F^-) ions, as well as chloride (Cl^-) ions, readily substitute for hydroxide (OH^-) positions in the apatite lattice. Although minimal, any chlorine content also is assumed to reside in this lattice position. Both Mg and Na contents were lower in the fossil bones than in the modern bone specimens. These ions may substitute at the Ca^{2+} cation position within the apatite lattice and are indeed commonly associated with the bioapatite mineral in modern, healthy bone. Despite such decreases in Mg^{2+} and Na^+ cation contents, all fossil bones exhibit overall higher calcium contents *versus* the modern bone specimens; this is intriguing and will be explored further in the discussion, largely because wild animals are more likely to suffer from calcium deficiencies in their diet.

The fossil bones also all contain higher iron contents than the modern bones; enrichment in iron in fossil bones has been extensively documented within the paleontological literatures, although there is still current debate over whether the origin of the enriched Fe is in the red blood cell hemoglobin or simply from the surrounding earth (Fe is one of the most abundant elements in the earth's crust). Either way, it is presumed that the increased Fe content observed in the fossil bone is actually a combination of absorption into the bioapatite crystallites as well as the presence of a goethite (FeO(OH)) minority phase that has formed in discrete locations. Because these phases are indistinguishable with the methods used here and the Fe is clearly a minority component, any further analysis will not be considered.

In summary, electron microprobe WDS was an incredibly successful technique for the precision determination of bone composition, for both the modern and fossil specimens.

3.3. X-ray diffraction

X-ray diffraction (XRD) scans of the polished bulk specimens were obtained with a Rigaku MiniFlex™ II. The surfaces analyzed were the same transverse orientations already analyzed by electron microprobe WDS, above, except in several instances where the longitudinal surface offered more surface area. The intensity *versus* 2θ scans of all seven specimens are shown in Figure 3.9 along with tabulated hydroxyapatite peaks published by the National Institute of Standards and Technology (SRM 2910).

Several features of these scans should be considered before further interpretation. One, there is a leading (20 - 25°) background signal of rather significant height. This is the tail end of a broad diffraction peak from the plexiglass ring spacer and can be neglected. Two, the diffraction peaks are almost universally broad, shallow, and subject to noise. Three, in some cases, not all apatite peaks are visible. Four, there is some horizontal shifting of key peaks between the individual spectra against the NIST hydroxyapatite standard tabulated data (Figure 3.8).

The latter three features will now be considered in more detail. Broad, shallow, and noisy diffraction peaks can result from many factors. Rough specimen surfaces can lead to peak broadening and increased background due to incoherent X-ray scattering. Poor crystallinity and nanocrystallinity also can both lead to similarly reduced XRD spectral peak quality. Misrepresentative changes in the relative peak height can result from extensive net orientation of the grains within polycrystalline specimens. Horizontal shifts in peaks may indicate strain or impurities in lattices that lead to averaged distortions of the crystal lattice parameters. Alternatively, systematic horizontal shifts without a corresponding loss in spectrum quality can be the result of improper placement of a sample surface with respect to the focal point of the X-ray beam.

Inspection of the XRD spectra, combined with specimen and sample mounting knowledge, provides further insight into the most likely causes of the broad, shallow diffraction peaks with misrepresentative relative heights and horizontal shifting of the 2θ locations. To begin with, natural compact bone contains extensive, variously sized porous regions (tens of microns to hundreds of microns). These variously sized porous regions have the potential to introduce scattering artifacts into XRD scans, reducing the apparent sharpness of the diffraction peaks. Bulk compact bone also has extensive internal texture, due to the high degree of net orientation of the bioapatite nanocrystallites in the compact bone tissue. Immature, newly mineralizing compact bone tissue contains poorly crystalline bioapatite nanoplates. All of the modern specimens and the fossil crocodile were relatively young and still growing. Further, their femora had relatively narrow cortices, such that the resulting XRD spectra are absolutely factoring in this very immature bone in addition to the more mature bone of primary interest. In some instances, however, even the more mature bone tissue is only on the order of 6 - 8 weeks old, which is still relatively young. The bulk bone specimens were mounted in a specimen holder fabricated within the Department of Materials Science and Engineering, followed by leveling to the X-ray beam focal plane by depression into dye-free polymer clay against a plexiglass ring spacer. This is an inherently imprecise process and absolutely has the potential to introduce small errors in alignment relative to the X-ray beam focal plane. These errors have the ultimate ability

to cause systematic shifting in the XRD peaks, to different degrees for each specimen. Based on the sum of this information, it is possible to assess the quality of the XRD spectra presented here.

The resulting bulk specimen XRD spectra are plotted in Figure 3.9. By inspection, the most significant features in the XRD spectra are the broad, shallow nature of the peaks, the misrepresentative peak heights relative to published data on the hydroxyapatite standard, and the systematic peak shift, which is more pronounced in some spectra than others. To explore the specific contribution from surface roughness, an XRD scan of finely powdered *Tyrannosaurus* bone also was run in the MiniFlex™ II diffractometer. *Tyrannosaurus* bone fragments from the mid-cortex were finely ground with a pestle and mortar (approximately 15 minutes of processing) until a smooth, fine texture and single powder color were obtained. The *Tyrannosaurus* bone powder (mounted in a glass powder well) was then scanned by the same parameters as used for analysis of the polished bulk *Tyrannosaurus* specimen. The resulting powder XRD spectrum is plotted in Figure 3.10 along with the bulk bone XRD spectrum. In this case, the bone powder actually possesses a higher net porosity and a reduced overall co-planar diffracting surface, which is counter to the effect observed in the bulk bone specimens. It is therefore concluded that the major contributor to the broad, shallow peaks located at the majority of the mineral reflections is in fact the internal texture of the bone.

The horizontal shifts are clearly systematic and, therefore, not representative of any actual changes in the apatite structure lattice parameters (chemical substitutions). Meanwhile, it is worth noting that the powder XRD spectrum for *Tyrannosaurus* closely resembles the bioapatite XRD spectra published by others, suggesting that some contributions to peak broadening due to nanocrystallinity cannot be ruled out; in light of the plate-like morphology of bioapatite, the effect of nanocrystallinity is expected to be more extreme for certain dimensions (300) than for others (002).

Experimental peak values of interest are summarized in Appendix H Table H.1 for the powdered *Tyrannosaurus* specimen. The key peak values for hydroxyapatite, fluorapatite, and chlorapatite are summarized in Table 3.2, for comparison. Because apatite is a hexagonal structure, the 002, 300, 004, and 600 peaks are especially significant for attempting to extract lattice parameter values from experimental precision XRD scans. In short, the XRD spectra presented for the bulk bone specimens can clearly be established as apatite, with major contributions to spectral quality coming from the high degree of texture and slight improper placement of specimen surfaces relative to the X-ray beam focal point.

3.4. Combined WDS and XRD

Electron microprobe WDS and XRD scans were gathered separately to establish a precise bone mineral phase identity. The apatite group is a class of minerals that can incorporate a great array of elements and polyatomic ions. In fact, only in recent years has clarity been established regarding which apatite variants actually represent distinct compounds from a structural perspective. This is because, in addition to the great variety of species that can be incorporated into the apatite structure, all apatites can effectively form complete solid solutions with all other apatites. The currently accepted apatite variants of relevancy to this study are all calcium phosphate-based, including hydroxyapatite, fluorapatite, chlorapatite, and strontium apatite.

As a given structure becomes more enriched with a particular type of atomic substitutions on the lattice, the local distortions of the lattice lead to an overall, average distortion of the lattice parameters, detectable by XRD. Isotropic strain (ε) in a lattice is given by

$$\varepsilon = \Delta d/d \qquad (1)$$

where d is the interplanar distance. Manipulating Bragg's law

$$\lambda = 2d \cdot \sin\theta\,, \qquad (2)$$

the following relationship is obtained:

$$\Delta\theta = -\varepsilon \cdot \tan\theta\,. \qquad (3)$$

For small θ, $\tan\theta \cong \theta$, so the shift in θ is proportional to the lattice strain. Chemical impurities introduce this type of strain (also called uniform dilation or hydrostatic pressure) when uniformly distributed throughout a lattice. Depending on whether the impurities are larger or smaller than the lattice atoms, or whether they reside on the lattice or in interstitial positions, the strain can either be a contraction or dilation. At high values of θ, the peak shift is more noticeable. When this trend is quite nearly linear, the solid solution is said to obey Vegard's Law. More specifically, it is possible to use precision X-ray diffractometry to estimate the degree of substitution of a given mineral structure by an expected impurity (such as fluorine in hydroxyapatite) based on these concepts, which manifest as measurable shifts in 2θ positions. Unfortunately, for complexly impure apatites, this method cannot be applied in a straightforward manner. Further, the lattice parameters of pure fluorapatite are only slightly distinct from the lattice parameters of bioapatite, which creates barely measurable differences that the XRD methods employed here are not likely able to detect, especially in light of questionable sample positioning.

This is why the XRD spectra were intended for combination with the precise compositional data of the electron microprobe WDS technique. Similarly, WDS compositional values alone are clearly insufficient for declaring the mineral phase within the fossil bones, in the least because calcium and phosphorus can be found in a variety of different structures. Because the fluoride ions only substitute for the hydroxide positions in the apatite lattice, their net at.% can be used to specifically describe the degree of conversion of the fossil bioapatite *versus* the modern bone specimens. Based on the hydroxyapatite stoichiometric formula, the oxygen atoms in the hydroxide groups represent approximately 4.8% of the atomic content (hydrogen is not included in this analysis because it cannot be detected by WDS). Then, for example, a measurement of 2.4 at.% fluorine indicates a 50% conversion of the bioapatite to fluorapatite.

In short, combining XRD with WDS offers a new level of robust analysis of fossil bone mineral that neither technique can provide on its own.

3.5. Small angle X-ray scattering

Small angle X-ray scattering (SAXS) was performed on thin sections of bone mounted on double-sided adhesive tape. The sections had thicknesses of approximately 100-200 μm and varying mineral densities. The set up is inherently a transmission mode, producing whole patterns of scattered X-ray intensity. The full set of SAXS whole patterns is shown in Figure 3.11. These patterns were processed with the Nanostar software. Radial integration was carried out in 30° pie wedges to specifically select for certain crystallite orientations. All bone thin sections were removed parallel with the longitudinal direction of the femur cortex. Extreme care was taken in mounting specimens to guarantee that the longitudinal direction of each section was oriented vertically. Of the whole patterns containing readily visible net orientation, it can be observed that the partial *c*-axis rings are relatively in the same position. This was expected based on how the specimens were mounted and is the premise for the pie wedge analysis.

The same wedge positions were selected for all specimens (-5 - 25°), which is the wedge of particular interest for analyzing the longitudinal direction of the bone based on observations of the locations of the partial *c*-axis rings. This direction should not only contain information on the *c*-axis dimension of the nanoplates, but it also should contain any microfibrillar structural information, such as the collagen D-spacing (67 nm constructed from a 40-nm gap and a 27-nm overlap) or hexagonal close-packed bundling of the microfibrils. The radial integration was plotted as Intensity (total counts) *versus* Q-value ($Å^{-1}$) for all specimens, and two overlay plots ((a) includes the modern specimens and (b) includes the fossils) are shown in Figure 3.12.

There are several features of interest in the overlay SAXS plots, explored as follows. First, several specimen plots exhibit two common diffraction peaks, one at approximately 27 nm and the other at approximately 40 nm. These peaks correspond to actual structures in the collagen microfibril, which arise from the intrinsic collagen stacking overlap and end-gap distances, respectively. While the D-spacing (67 nm) of collagen is usually registered as a single peak at Q-value 0.00938 $Å^{-1}$, it is theoretically conceivable to observe it in this manner instead. The 27 nm peak, in particular, is especially prominent in the modern bone specimens (centered at Q-value 0.027383 $Å^{-1}$) but also is visible in the fossils (Figure 3.13 (b)). The modern specimens were all recovered from immature bone tissue and likely had undergone incomplete mineralization at the time of death. This might account for the higher relative scattering intensity of the 27 nm (overlap) peak in the modern specimens. The 40 nm (gap) peak is significantly less distinct but visible as a small shoulder at Q-value 0.016003 $Å^{-1}$, particularly in the modern specimens (Figure 3.12 (a)).

A second feature of interest can be observed in the *Struthio* (replotted in Figure 3.13 (a)), *Rhea*, *Caiman*, and *Pristichampsus* specimen plots as a distinct oscillatory pattern (higher order peaks) over a substantial length of each curve. This pattern was predicted by Suhonen *et al.* (2005) for close-packed fibrillar structures, where the peak-to-peak distance can be measured and converted to microfibril width. In these data, for example, the peak-to-peak distance in the *Pristichampsus* -15 - 15° plot (Figure 3.13 (c)) measures to a Q-value difference of approximately 0.004267 $Å^{-1}$, which yields the resulting microfibrillar width of 147.3 nm. This measurement also is on the order of the standardly accepted microfibril bundle width. This scale of distance (bundling on the order of hundreds of nm), it is worth noting, encompasses the highest orders of the fibrillar structure.

To summarize, a somewhat unconventional SAXS analysis (pie wedges) was applied to the bone specimen set. This method proved useful in the extraction of collagen D-spacing values and fibrillar structure in both the modern and fossil specimens.

3.6. Transmission electron microscopy

Transmission electron microscopy images were gathered from disarticulated samples. Modern bone specimens were not prepared according to this method because, without substantial chemical exposure to degrade the collagen, they cannot actually be ground and disarticulated. Because of this, I only report TEM data on the fossil specimens. Fossil bone specimens are readily disarticulated by grinding with mortar and pestle, which tends to separate the bone tissue at the micron- and nanoscales. Separation, or fracturing, of the tissue occurs along pathways of least resistance, such as between macrofibrils, microfibrils, or adjacent nanocrystallites. By their very nature, the bioapatite nanoplates approach their ideal strength, which means that the usually brittle ceramic material is actually quite strong at the nanoscale. Example images of the specimens after disarticulation can be seen in Figure 3.14, at 6k×. Despite thorough grinding, the specimens clearly do not fully disarticulate, which prompts interesting questions regarding the internal nature of the fragments that resist fracture. Further, these specimens exhibit consistent diamond-shaped fracture patterns.

The nanocrystalline nature of each fossil specimen can clearly be seen in Figure 3.15, at 1M×. Nanocrystallinity is one of the key structural aspects of the impressive mechanical properties of bone tissue. From a general engineering perspective, there is a lot of current interest in questions about average crystallite dimensions. From a paleontological perspective, previous publications have suggested the extensive nature of crystallite coarsening in fossil bones. The images reported here, which are sufficient for demonstrating nanocrystallinity, are not necessarily sufficient for supporting or refuting claims about crystallite coarsening, which should certainly be investigated further.

Also given in Figure 3.15 are the corresponding regions investigated by SAD (gathered from the same location as the 1M× images). Both an example selected region (upper right-hand) and the resulting diffraction pattern (lower right-hand) are shown. The 002 and 300 partial rings are indexed. The diffraction patterns were collected at a camera length of 40 cm and calibrated against a polycrystalline aluminum diffraction standard (Ted Pella, Inc.). All rings measured to expected positions for hydroxyapatite based on the analysis protocol given in Appendix I.

Dark-field images of the fossil bone specimens also were collected. This approach has the power to provide two types of useful information. First, dark-field techniques can be used in conjunction with high-resolution imaging to obtain directly meaningful lattice fringes (*i.e.*, they can be directly measured from the image following calibration of the scalebar). Such a technique is called high-angle annular dark-field (HAADF). An example high-resolution dark-field image (Figure 3.16) is reported here, collected on a Philips CM 200 operated at 200 kV. This instrument is housed at the National Center for Electron Microscopy at the Lawrence Berkeley National Laboratory.

Second, dark-field techniques can be combined with tomography (tilting operations) to develop 3-D reconstructions of the microfibril. Although this was one of the initial goals of this work, the results here merely present preliminary results, which are sufficient to justify future

work geared toward obtaining a more complete result. This focus is critical toward the ultimate goal of developing a more complete understanding of nanoscale structure in bone. Figure 3.17 (a) presents a tubular structure, protruding from a bone fragment. The protrusion has a high-density core (dark in Figure 3.17 (a)), surrounded by nanocrystallites (Figure 3.17 (b)) based on dark-field inspection. Higher magnification images of this same structure are presented in Figure 3.17 (c) and (d). The objective aperture was used to identify crystallites oriented in the 002 direction by selecting electrons scattering to the 002 arc in the corresponding diffraction pattern (not shown). Based on this technique, in the dark-field images, these crystallites appear predominantly along their lengths (often as lines), which are oriented at a slight angle relative to the length of the tubular structure. This is expected for microfibrillar structures, which are internally helical.

Similar findings are demonstrated in Figures 3.18, 3.19, and 3.20. However, these figures incorporate a higher level of investigation into the structure. In Figure 3.18, the black arrow is placed to denote the line length of the microfibrillar structure. In the diffraction pattern, the black arrow coincidentally falls on one end of the 002 arc; hence, a red arrow is placed on the opposite end of the 002 arc. Then, this arrow is placed in the bright-field image. Without using dark-field, this approach has, theoretically identified the angular off-set of the bioapatite nanoplates relative to the length of the microfibril (also called the pitch), which is expected for a helical/wound structure. The identified angle is indicated in the figure. This process can be developed further by using the objective aperture to explore the 002 ring with the end goal of identifying both the collagen bundles composing the microfibril (their angle establishes the pitch) and the relative orientation of the nanoplates within the collagen bundles. Together, these values can be combined with 3-D dark-field imaging to establish the internal structure of the microfibril. The preliminary steps are identified here.

In Figure 3.19 (*Pristichampsus*), a blue arrow is added to the set. As above, first the black arrow (length of the microfibril is established). Then, the objective aperture is applied to select a particular orientation of the 002 arc (nanocrystallites). The corresponding dark-field image is shown in Figure 3.19 (b). Next, the opposite end of the 002 arc is identified with a red arrow, which also maps to the bright band of nanoplates in the dark-field image. This is the winding pitch of the collagen within the microfibril; placed on the bright-field image, the value is given in the figure. A similar process is carried out for the structure in Figure 3.20 (*Stegoceras* skull).

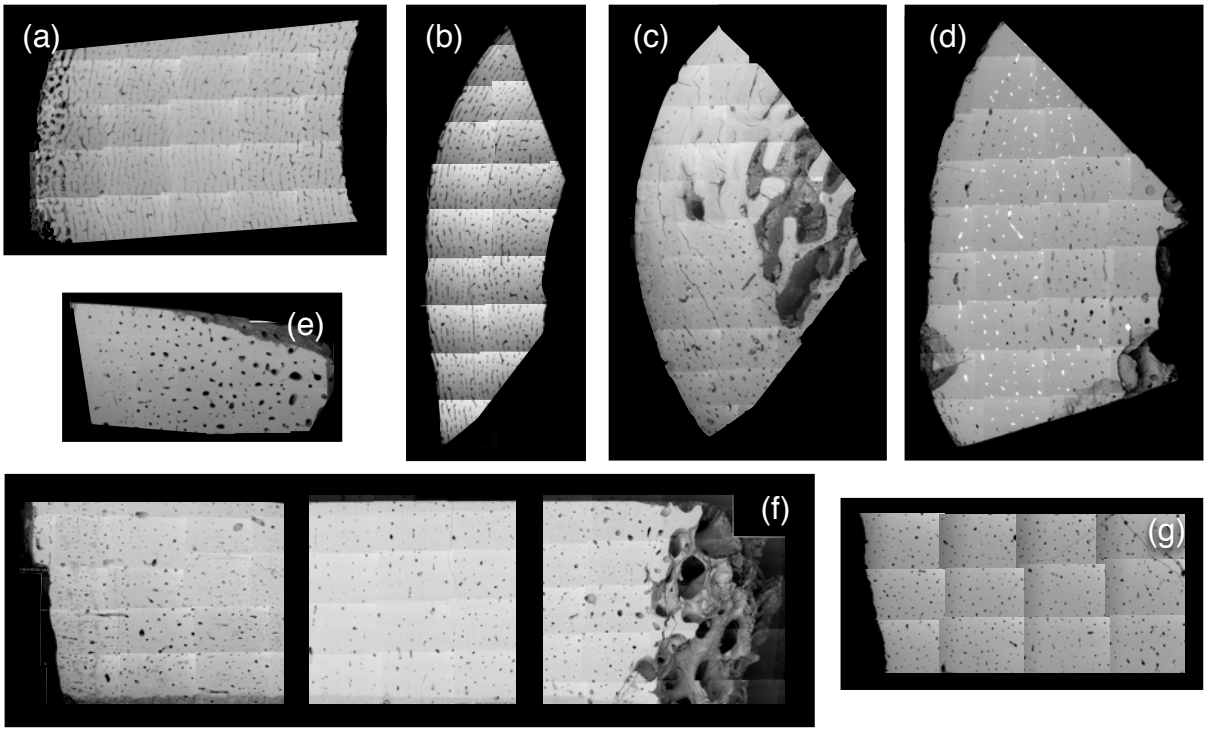

Figure 3.1 Back-scattered electron maps of the modern and fossil specimens. Each tile is a 100× image. All maps are aligned to present the periosteal surface on the left-hand side (endosteal on the right-hand side). The middle section of (f) is the mid-cortex. (a) *Struthio*, (b) *Rhea*, (c) *Caiman*, (d) *Pristichampsus*, (e) hadrosaur femur, (f) hadrosaur radius, and (g) *Tyrannosaurus.*

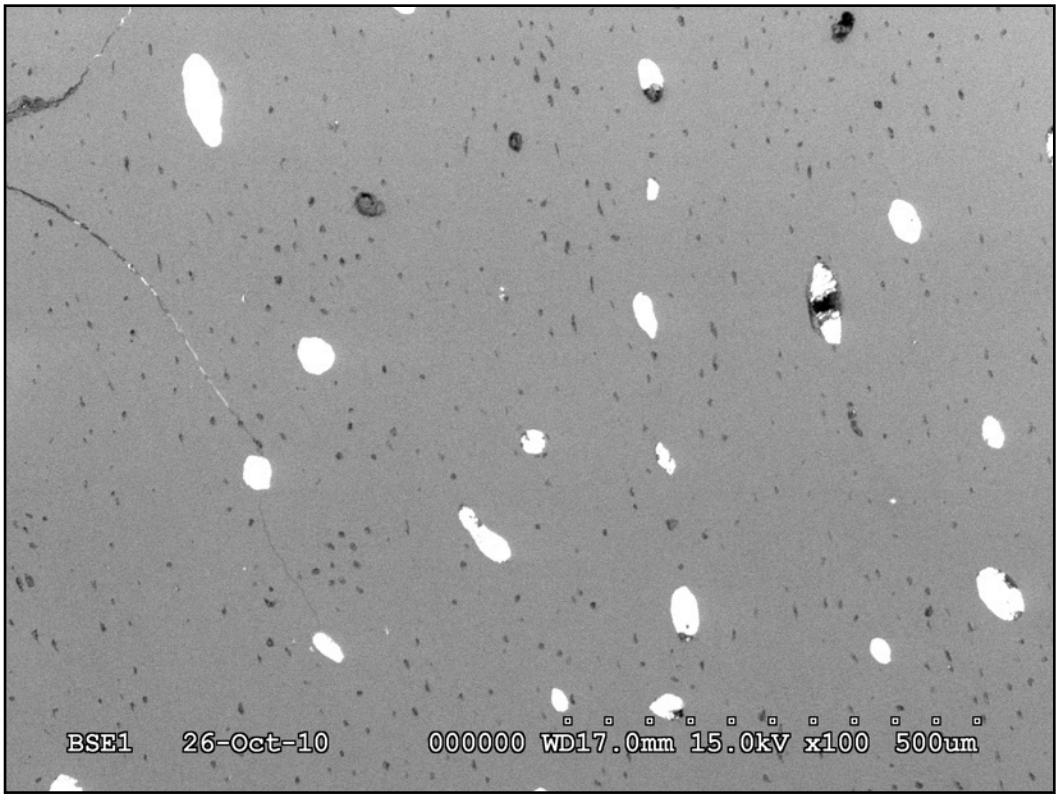

Figure 3.2 Back-scattered electron image of *Pristichampsus* cortical bone (mid-cortex, periosteal surface on the left-hand side). The osteons are almost completely in-filled with $BaSO_4$. The cracks in the upper left-hand corner also have in-filled with mineral. A high concentration of osteocyte lacunae are visible (small black dots). Image magnification is 100×.

Figure 3.3 (a) Back-scattered electron image of the trabecular region in the *Pristichampsus* specimen. The lamellar (layered) deposition of new bone growth is still preserved in this specimen, seen as circular layers inside the marrow channel in the center and along the length of the curved surface on the right-hand side. Cracks also can be seen, as well as osteocyte lacunae. This region was investigated with an EDS linescan (red transect line) to test whether the $BaSO_4$ had diffused into the bulk bone tissue. Trabecular regions have high surface area, which theoretically makes these regions more vulnerable to invasive diffusion over time. Image magnification is 200×. (b) Energy-dispersive X-ray spectroscopy linescan of transect shown in Figure 3.3 (red line), from $BaSO_4$ in-filling into the bulk bone region. The Ca (red) and P (light red) have low concentration in the marrow cavity (hole) and increase sharply at the edge of the feature. The S (blue) and Ba (light blue) behave oppositely, falling off rapidly as the sample progresses into the bulk bone region. Within several microns, both S and Ba are at background levels, which indicates that despite millions of years of exposure, these elements have not significantly diffused into the bulk bone tissue. A closer inspection of a region such as this (lamellar bone deposition) also would highlight variations in bulk bone composition, corresponding to the lamellar deposition of new bone tissue. →

(a)

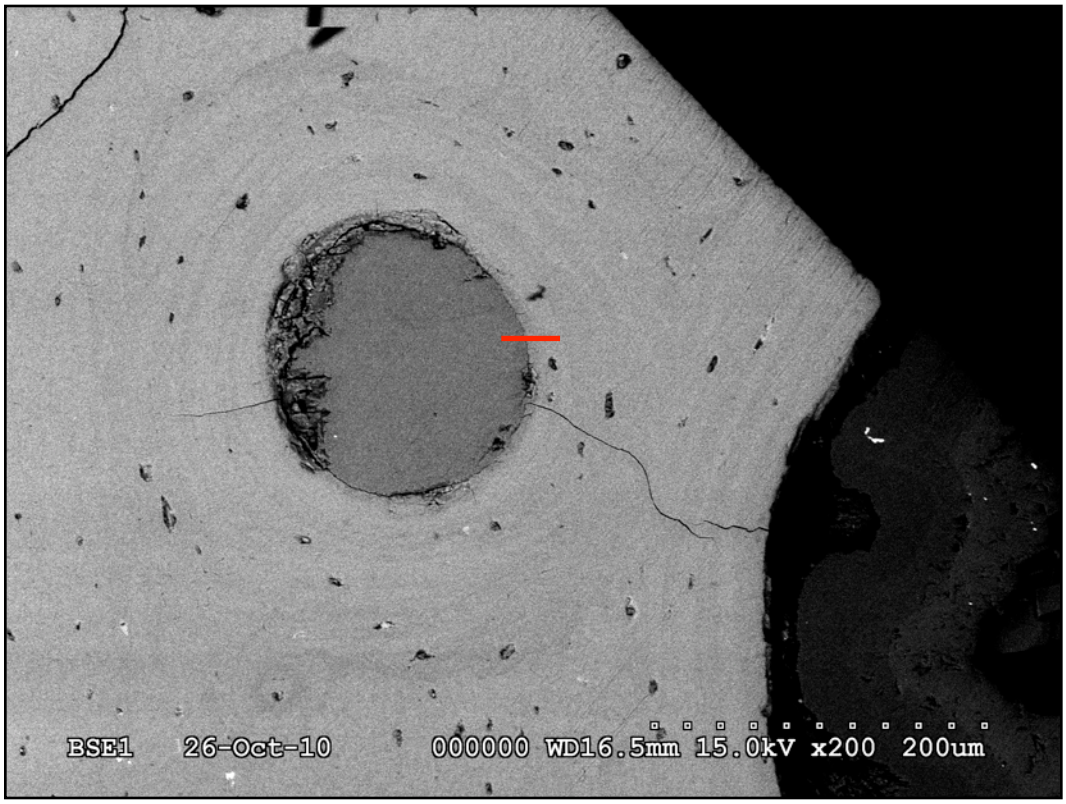
BSE1 26-Oct-10 000000 WD16.5mm 15.0kV x200 200um

(b)

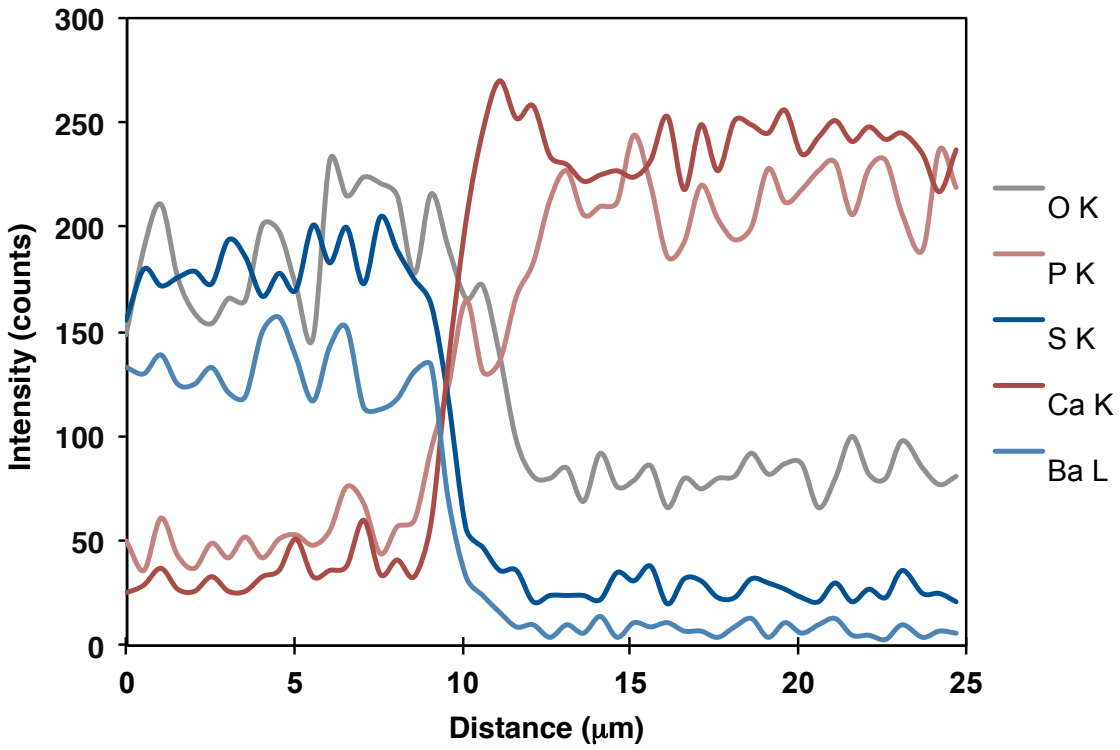
300
250
200
150
100
50
0
Intensity (counts)
0
5
10
15
20
25
Distance (μm)
O K
P K
S K
Ca K
Ba L

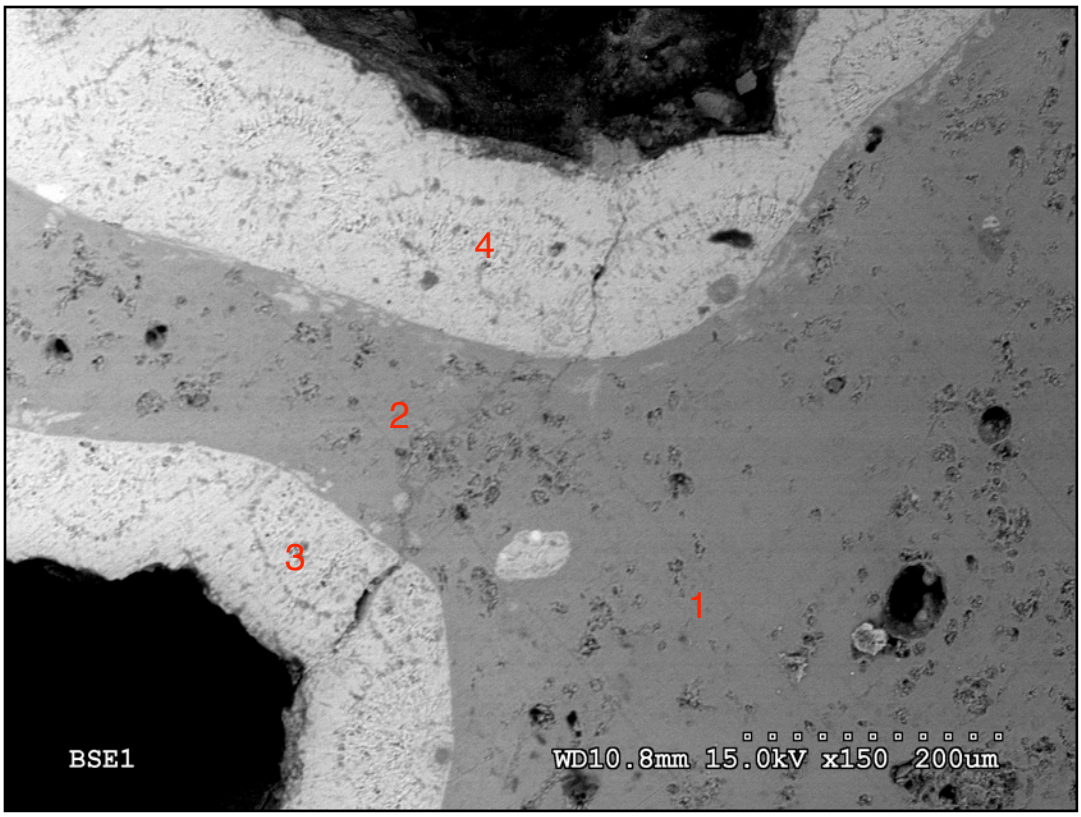

Figure 3.4 Back-scattered electron image of *Tyrannosaurus* trabecular bone. The bone (medium gray) has been covered in a mineral crust (light gray). Highly porous trabecular regions are more susceptible to chemical alteration. Four locations were sampled by EDS spot analysis for chemical composition (1 and 2 in the bone, 3 and 4 in the mineral crust). It was found that the elements composing the mineral crust have not diffused into the bone above background levels (the full data are available in Appendix E). Image magnification is 150×.

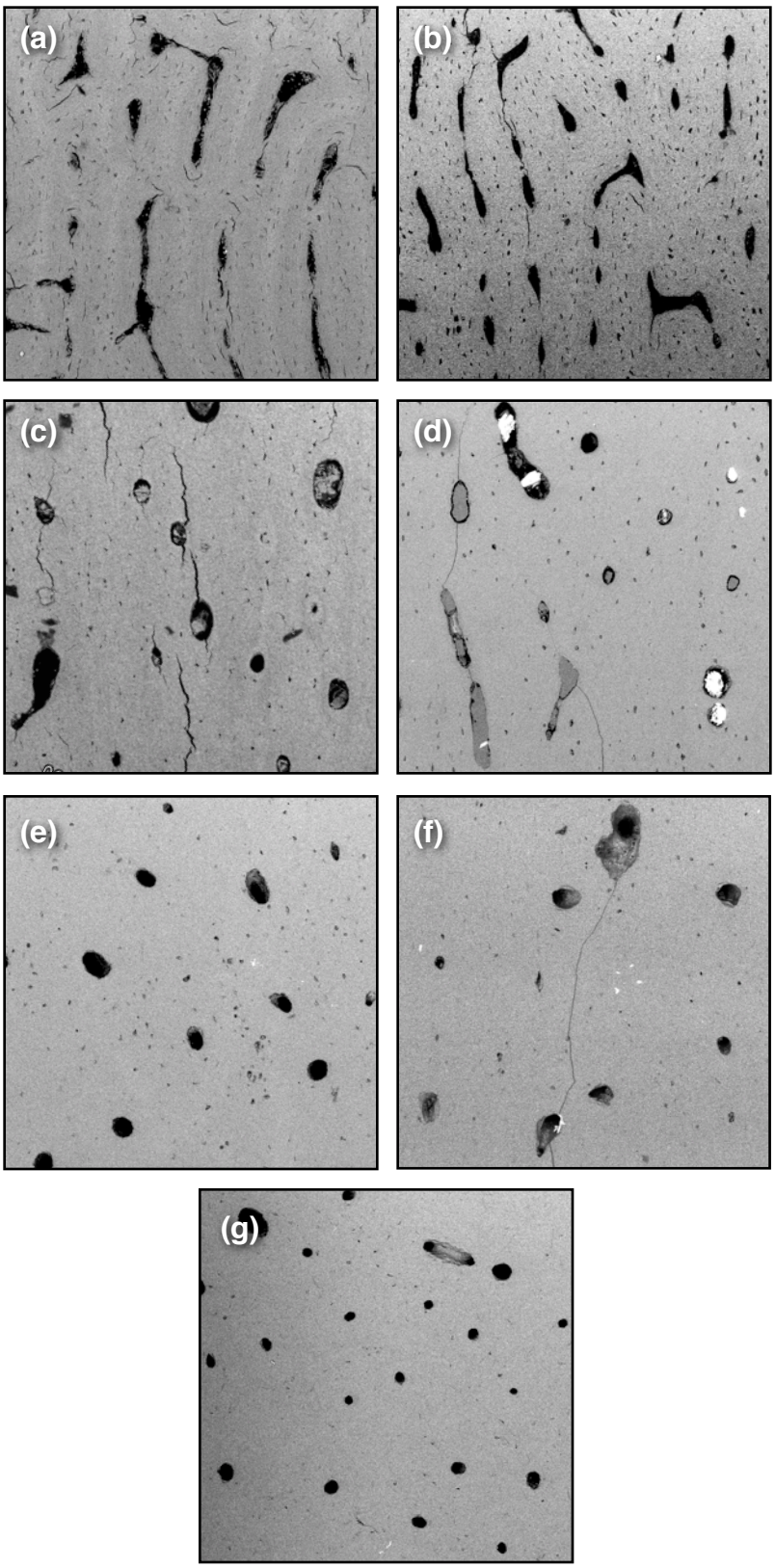

Figure 3.5 Examples of the cortical tissues of each specimen studied in this work. All BSE images were recorded at the same magnification. Features of interest include osteons, osteocyte lacunae, and lamellar growth. Cracks be seen in several specimens; in the modern specimens they are the result of water vapor escaping in the vacuum, whereas in the fossil specimens they are the result of brittle cracking events. (a) *Struthio*, (b) *Rhea*, (c) *Caiman*, (d) *Pristichampsus*, (e) hadrosaur radius, (f) hadrosaur femur, and (g) *Tyrannosaurus.*

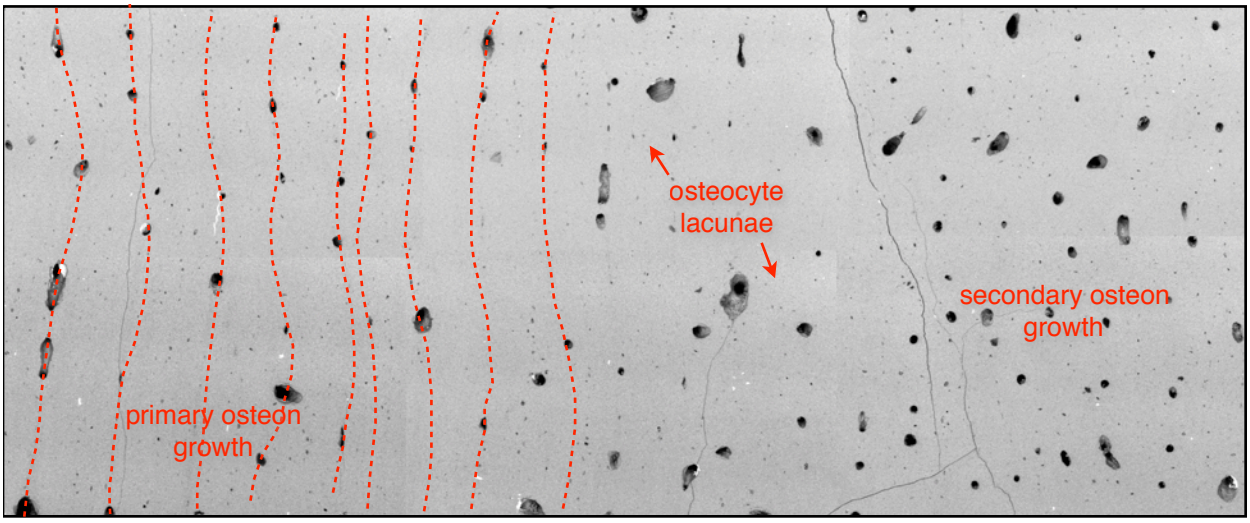

Figure 3.6 A magnified view of the mid-cortex of the compiled hadrosaur radius BSE image tiles. Many of the features of interest are clearly discernible, including fields of primary and secondary osteon growth, the lamellar growth front (traced as dashed lines), and osteocyte lacunae.

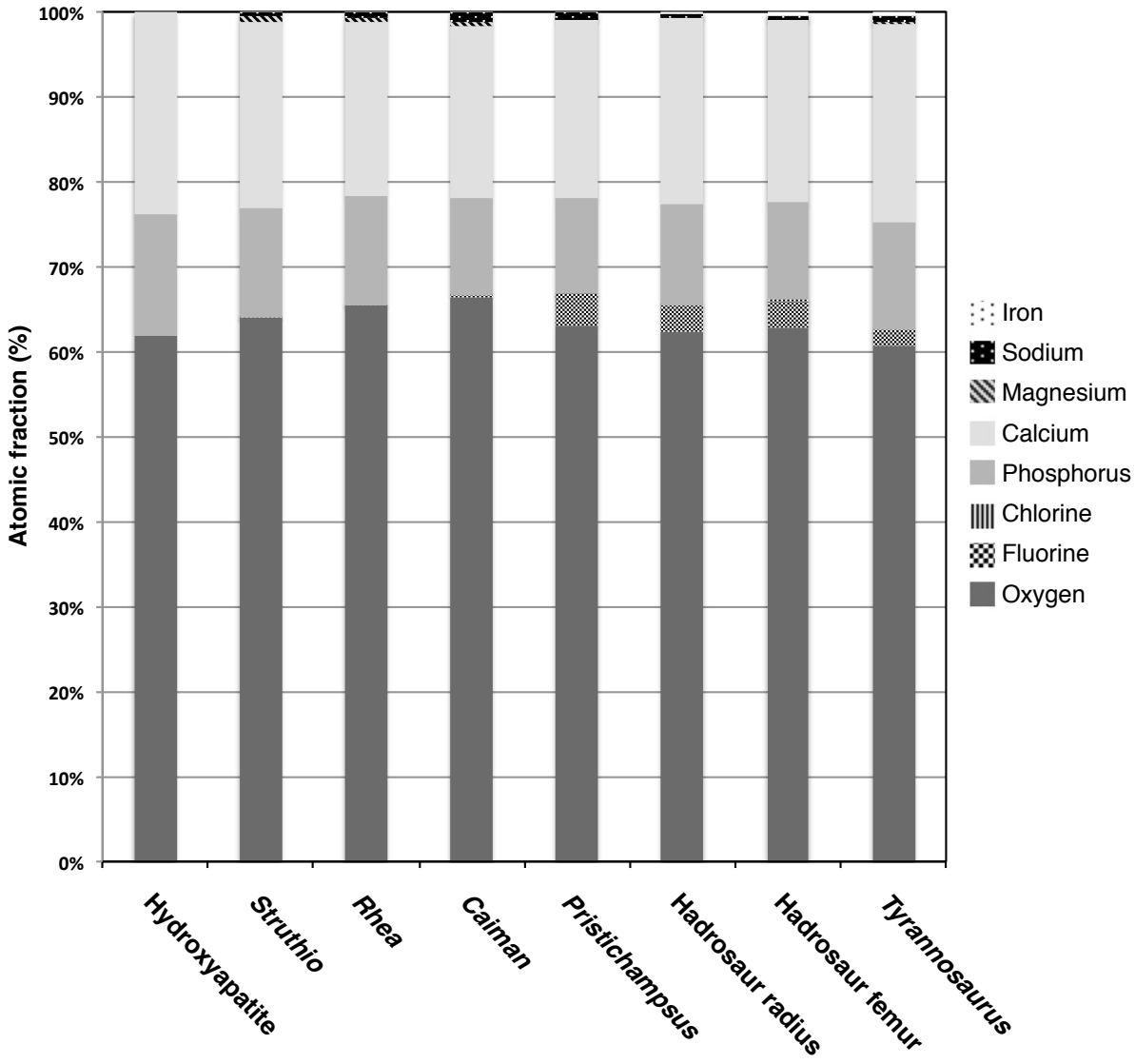

Figure 3.7 A bar plot of the average composition of each specimen. The color bands represent ion classifications, based on the mineral structure of hydroxyapatite. Red are cations, with the predominant type being Ca^{2+}. Gray is phosphorus in the phosphate group. Blue are anions, which in this case includes the oxygen content that would be associated with the phosphate ions. The bar on the left is a representation of stoichiometric hydroxyapatite. Several key points are demonstrated by these data. The red and gray color bands, which are a visual representations of the standard "Ca/P" index ratio have nearly identical range, between modern and fossil. That is, the Ca/P index of the fossil specimens overlaps with that of the modern bones and is indistinguishable in the case of this specimen set. There is universal increase in fluoride content in the fossil specimens, which is widely documented in the paleontological literatures. There are slight losses in the magnesium and sodium contents in the fossil bones and a slight increase in the iron content. However, it is not likely that the iron has substituted into the apatite structure. In summary, electron microprobe with WDS is a highly robust technique for determining the composition of modern and fossil bones. These data not only present the analytical compositions of the fossil bones, but they also suggest that chemical changes in fossil specimens are predictable and readily quantifiable. The full corresponding datasets are given in Appendix G.

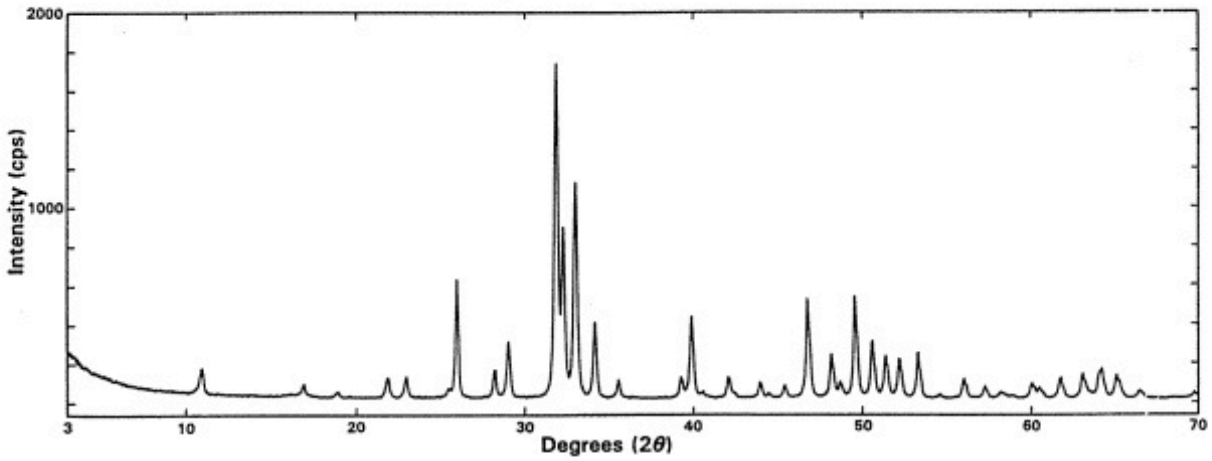

Figure 3.8 The XRD spectrum recorded by NIST for a hydroxyapatite standard (SRM 2910). Both this pattern and the corresponding tabulated data also reported in the NIST publication were used to verify the specimens analyzed in this work.

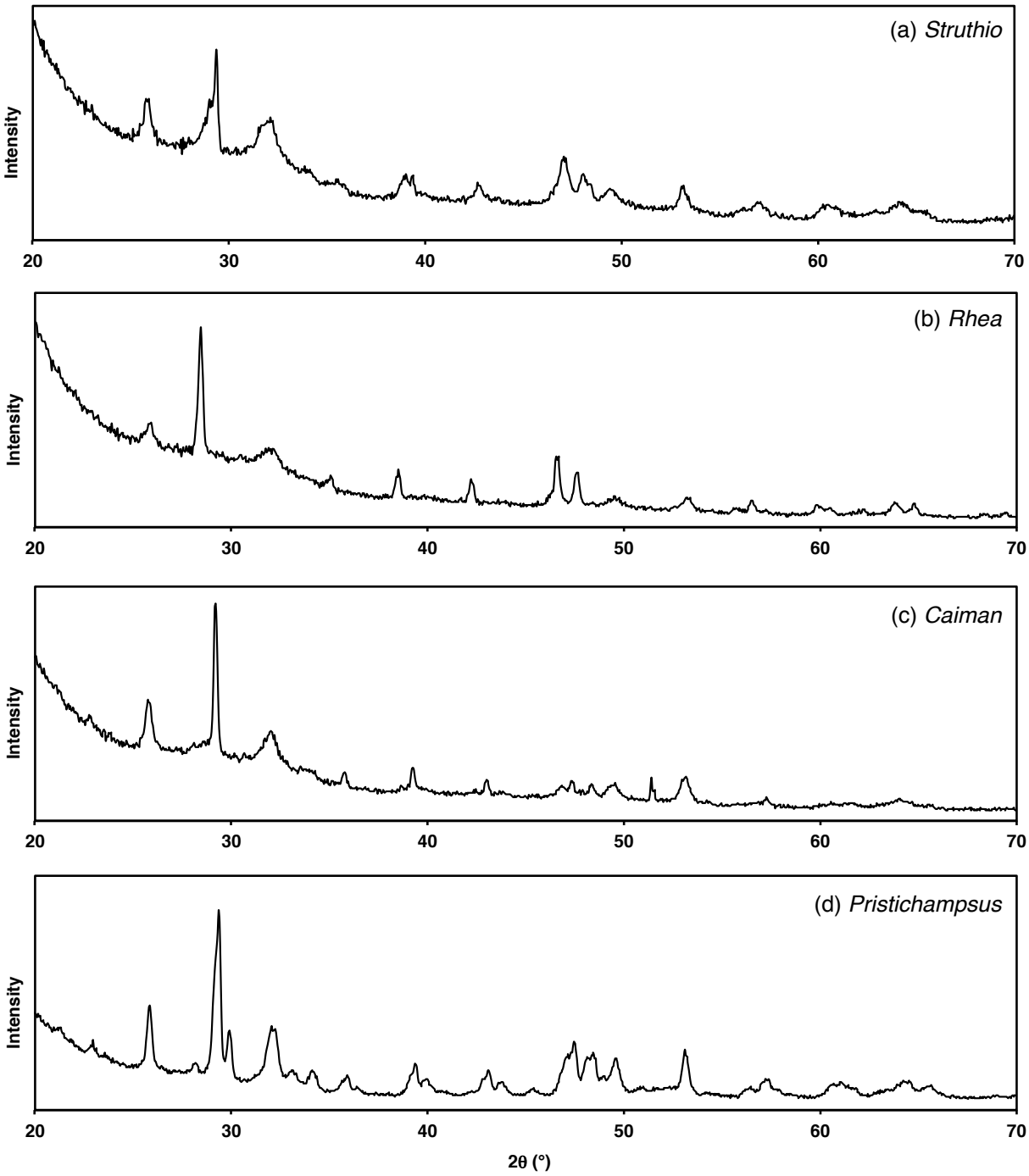

Figure 3.9 The XRD spectra of the bulk bone specimens. The relative peak heights do not match those of the NIST hydroxyapatite standard due to the high degree of internal orientation in the compact bone specimens. This also is the cause of the irregular peak shapes. The leading edge (below 25°) is from the polymer clay in which the specimens were mounted for analysis. (a) *Struthio*, (b) *Rhea*, (c) *Caiman*, (d) *Pristichampsus*, (e) hadrosaur radius, (f) hadrosaur femur. (The *Tyrannosaurus* specimen is shown separately, in Figure 3.10.)

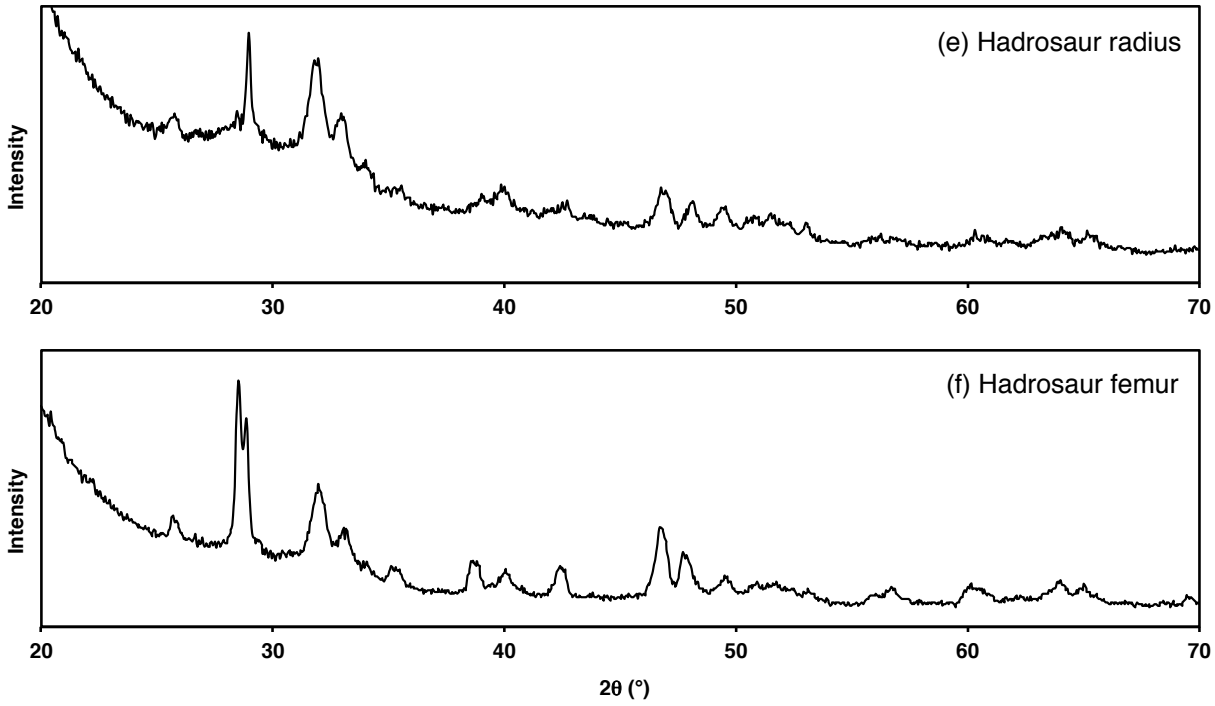

Figure 3.9 (Continued.)

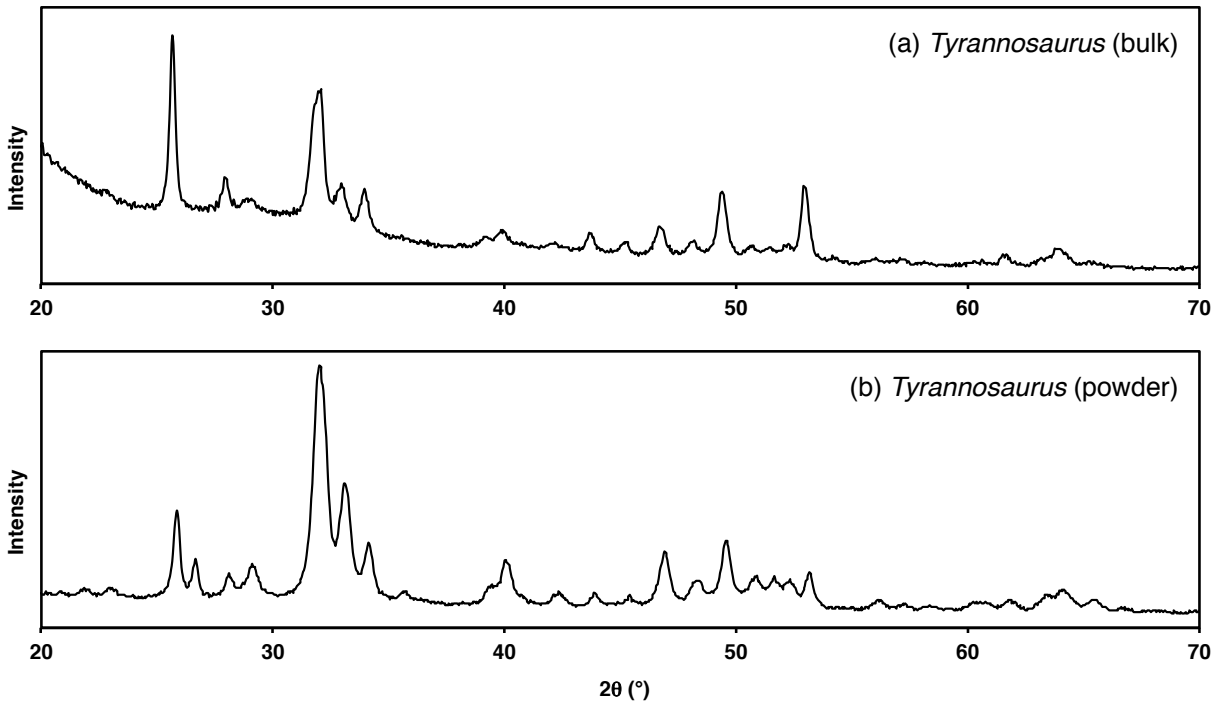

Figure 3.10 The XRD spectrum of the bulk *Tyrannosaurus* specimen suffers similar quality issues as the other bulk bones. However, the powdered bone reproduces the apatite diffraction pattern, which supports the notion that the low spectrum quality is most closely dependent upon the high degree of internal orientation in the bone. Although powdering yields the better spectrum, it is not necessary (and may not be desirable in many instances).

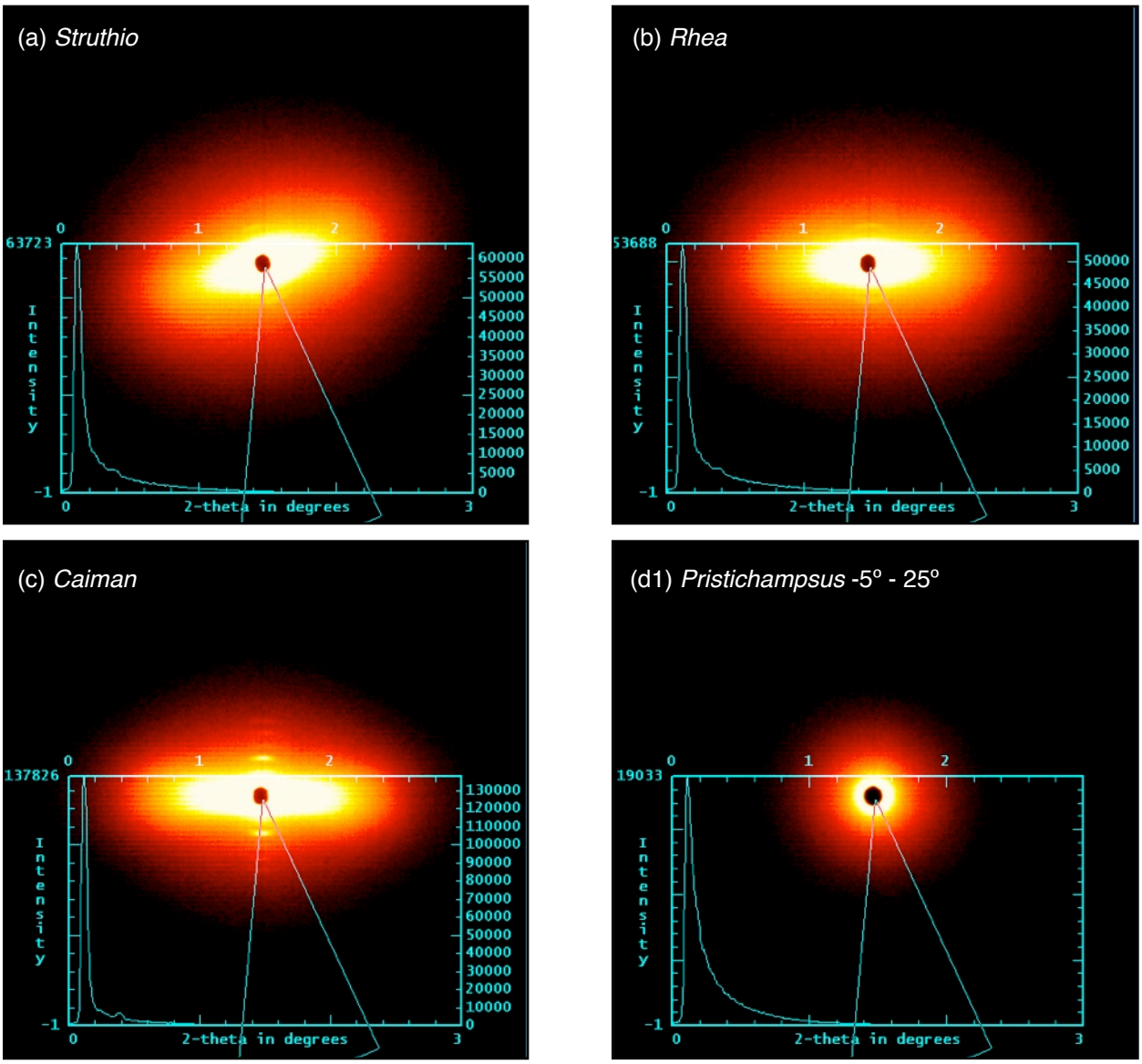

Figure 3.11 SAXS whole patterns recorded for the full specimen set. The inset plots show the radial integration of the corresponding pie wedge denoted in the figure. In all cases except (d2), the pie wedge was integrated from -5 - 25°. The initial sharp rise in the intensity profile is the beam blocker. Oval shapes indicate high net internal orientation. In many cases, the *c*-axis arc pattern also can be seen, including the hadrosaur radius. Specimens are labeled in the individual figures.

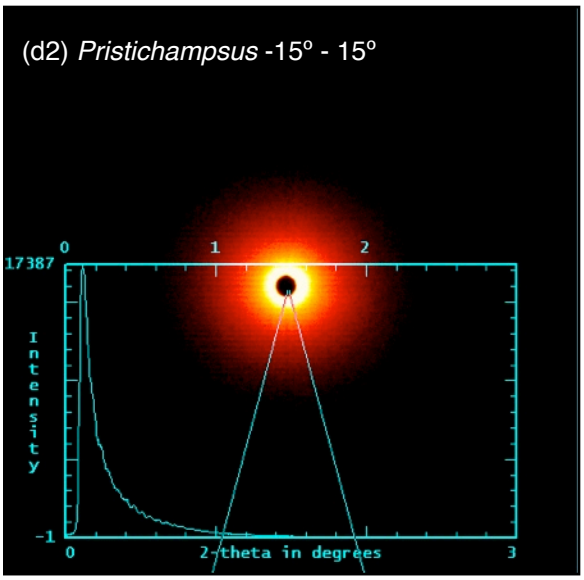

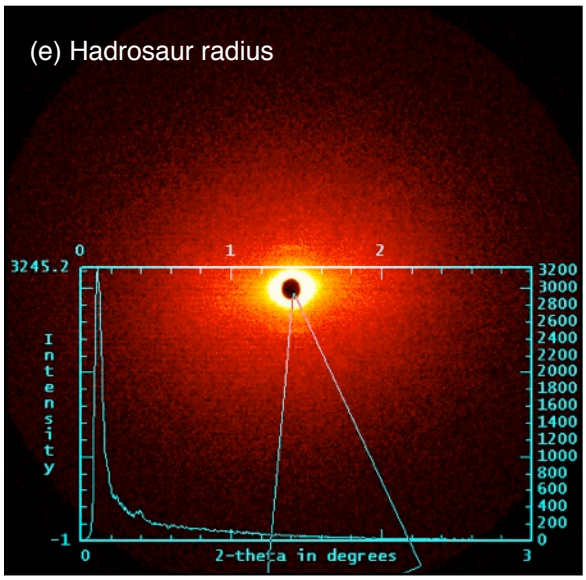

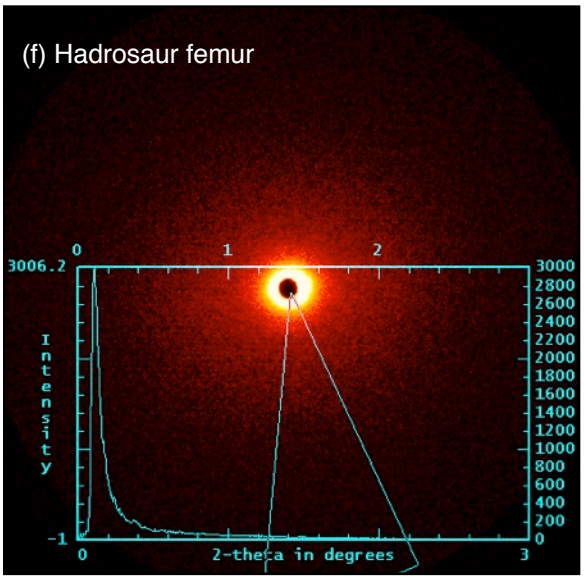

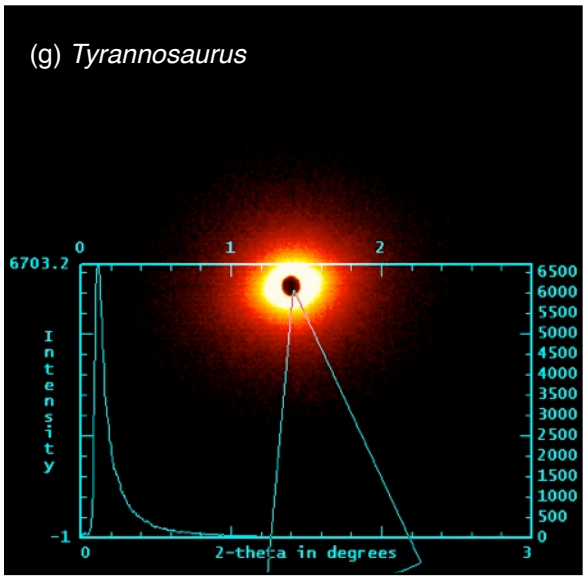

Figure 3.11 (Continued.)

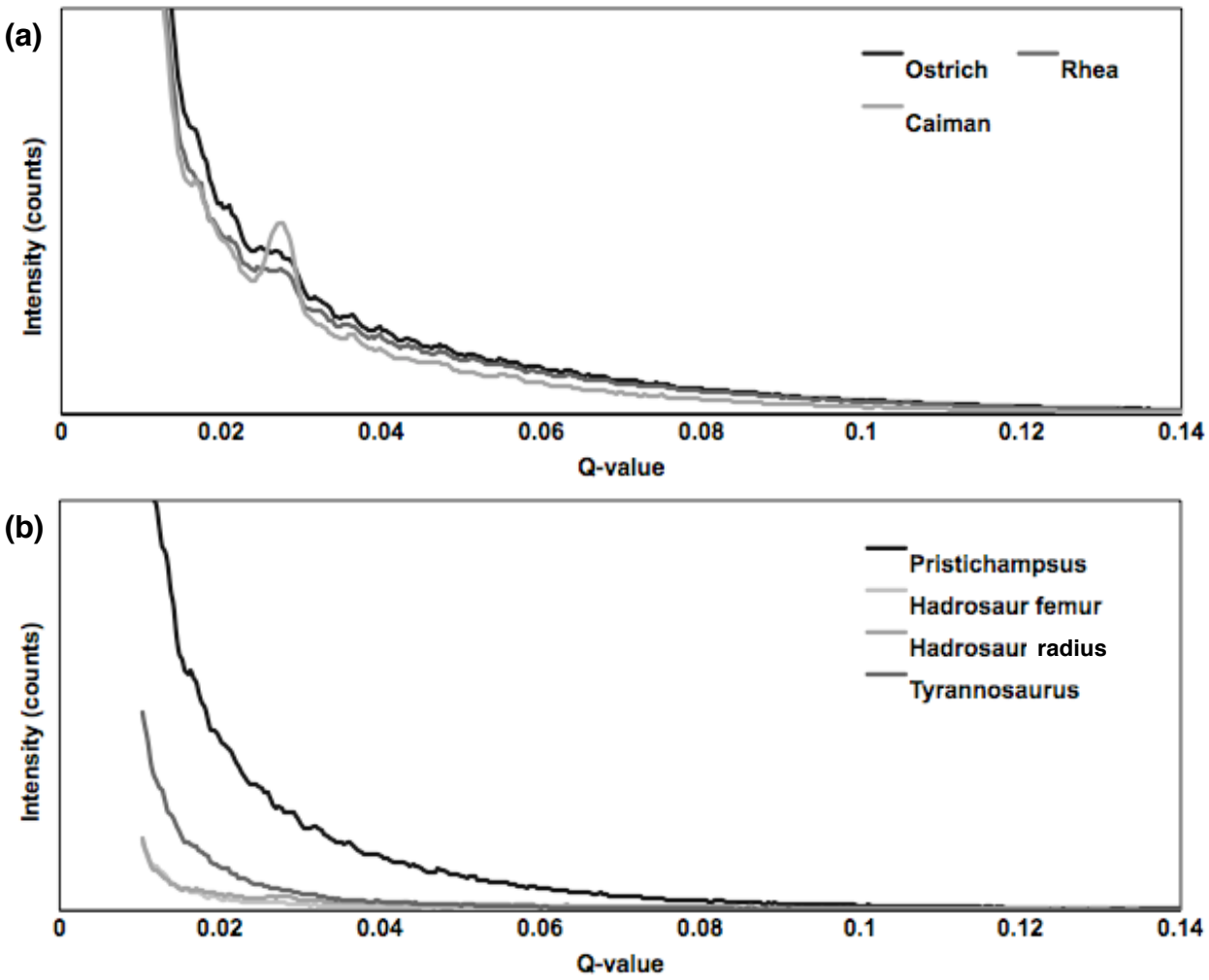

Figure 3.12 Radially integrated plots of the pie wedges indicated in the whole patterns (-5 - 25°). (a) Modern specimens are plotted separately from (b) fossil specimens for clarity because the relative intensities of the spectra were significantly different. Features of interest include small to prominent peaks at Q-values 0.027383 $Å^{-1}$ and 0.016003 $Å^{-1}$. Additionally, a pronounced oscillatory pattern (higher order peaks) can be seen in (a) the modern specimen plots and (b) *Pristichampsus* plot.

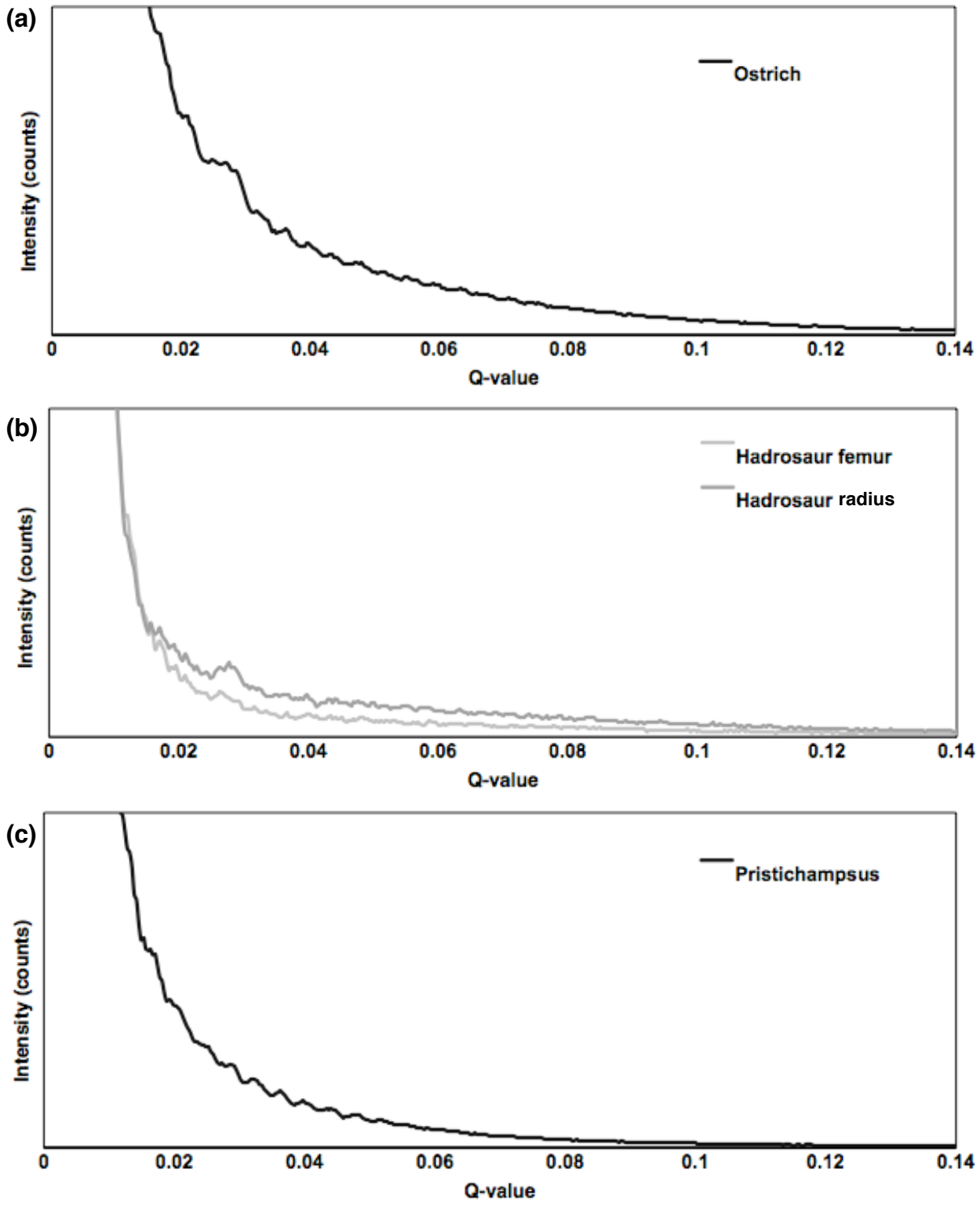

Figure 3.13 SAXS plots of individual specimens demonstrate (a) the prominent oscillatory pattern in modern bone (*Struthio*), (b) the collagen D-spacing 27 nm peak in fossil bone (hadrosaur radius and femur), and (c) the prominent oscillatory pattern also present in the fossil bone (*Pristichampsus*).

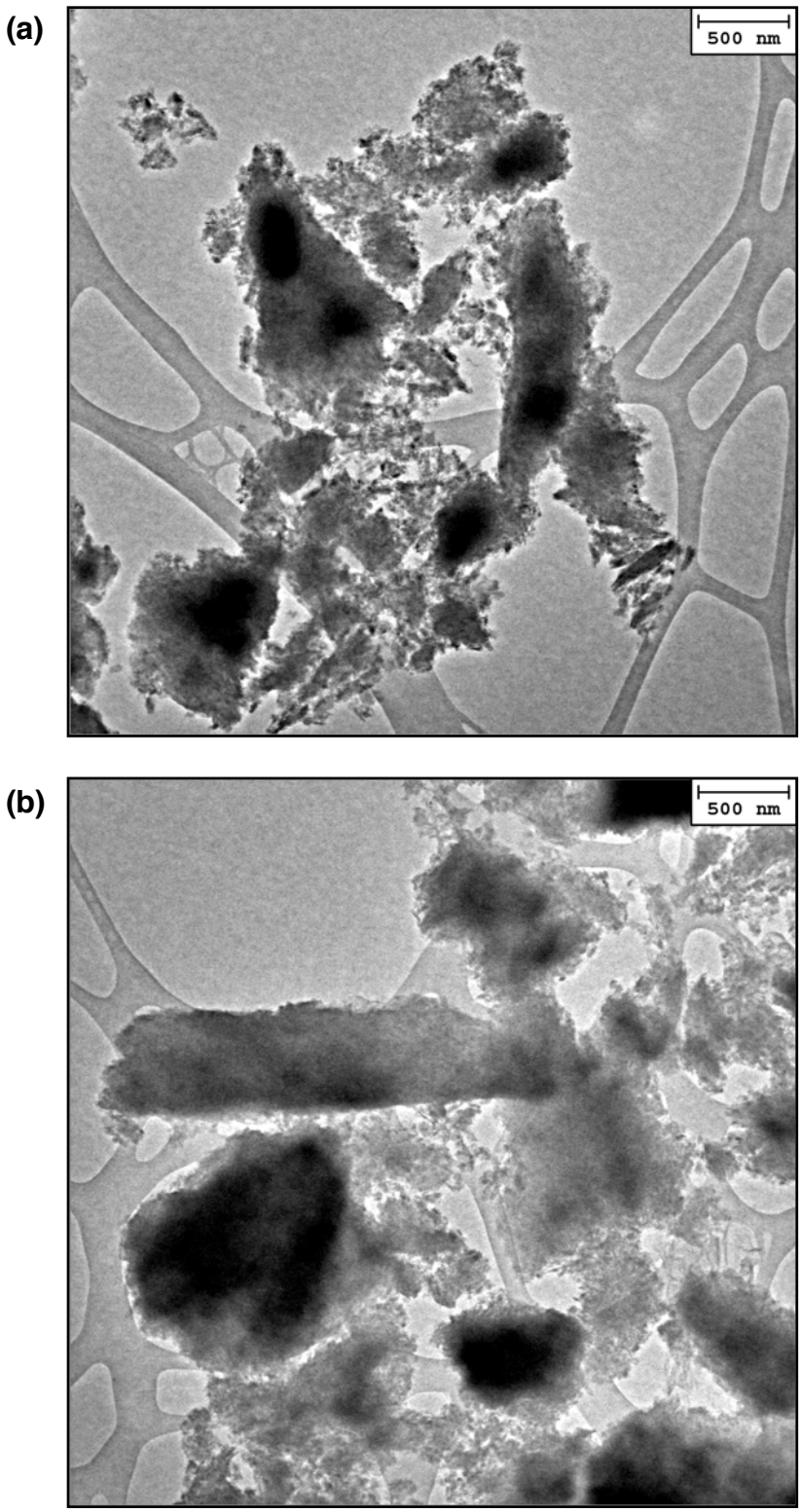

Figure 3.14 (a) and (b) Examples of the level of disarticulation achieved by grinding with pestle and mortar (*Tyrannosaurus* at 6k×). Fossil bone often fractures in diamond shapes or tubular features, which are believed to be representative of the microfibrillar structure (paths of least resistance).

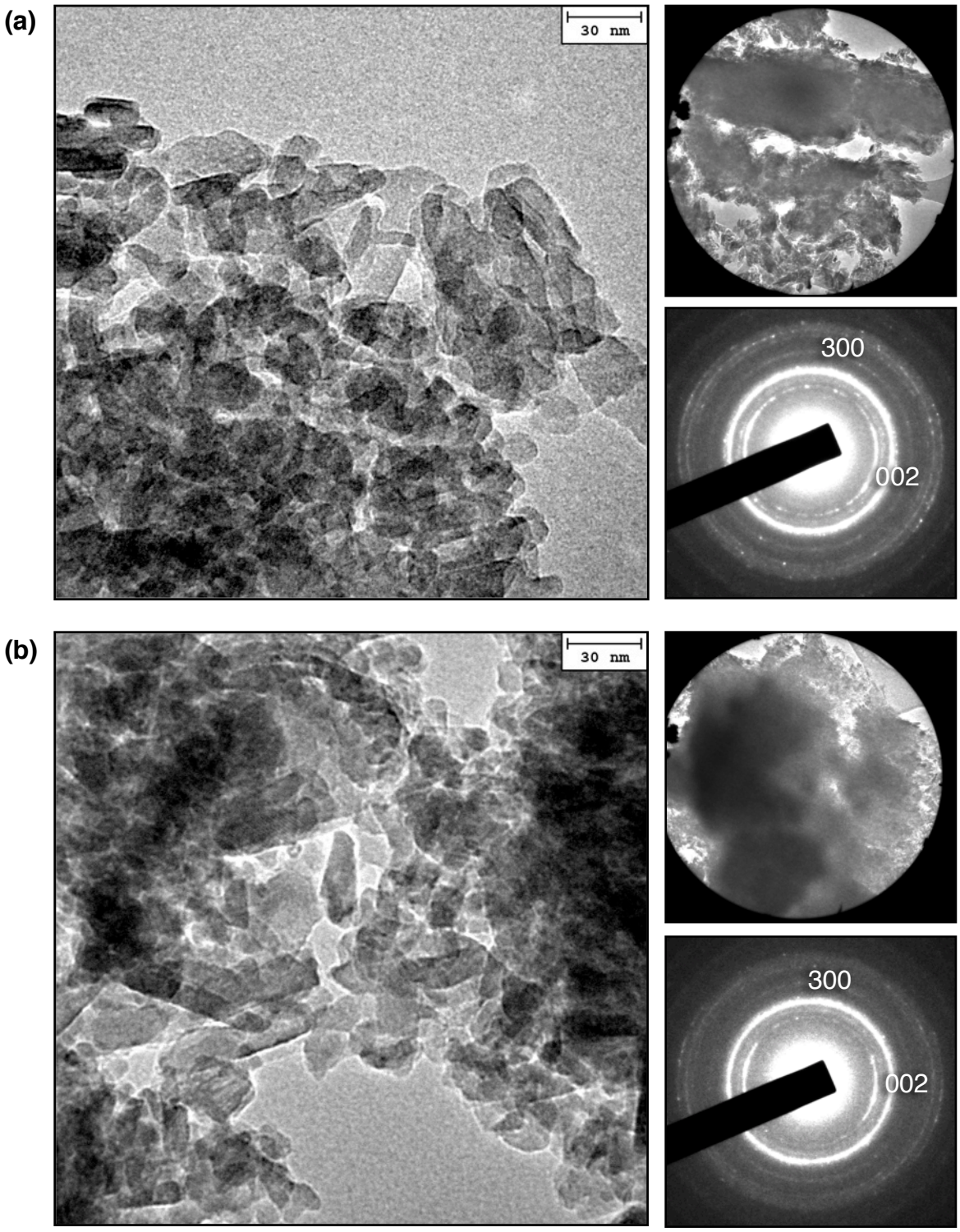

Figure 3.15 The left-hand, bright-field TEM images demonstrate the nanocrystalline nature of the fossil specimens. The small, upper-right hand image is an associated selected region of a large bone fragment within the selected-area aperture. The corresponding SAD pattern is given in the lower-right, with the 002 and 300 partial rings of hydroxyapatite indexed. All investigated fossil specimen fragments exhibited high internal orientation. (a) *Pristichampsus*, (b) hadrosaur radius, (c) hadrosaur femur, (d) *Tyrannosaurus.*

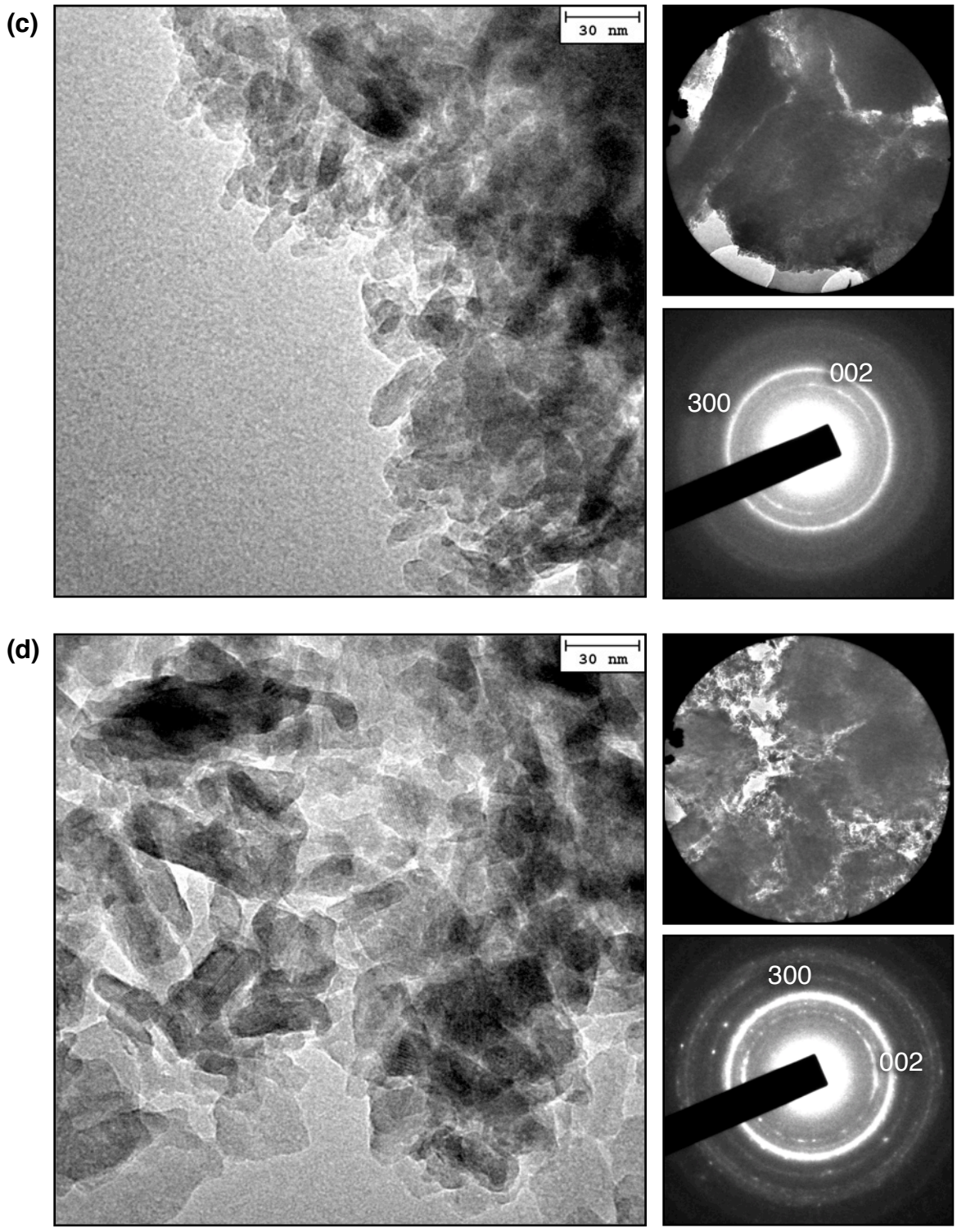

Figure 3.15 (Continued.)

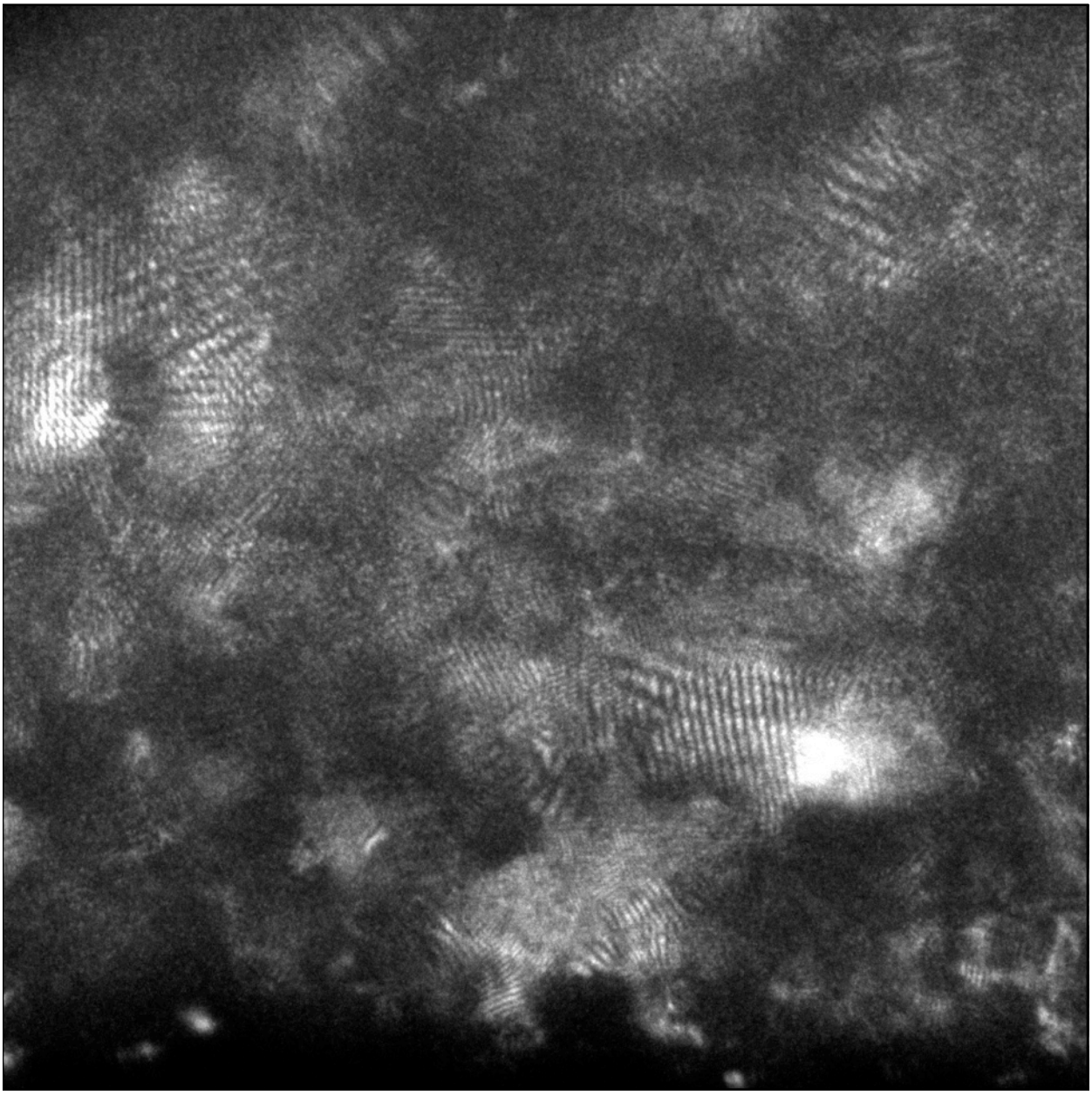

Figure 3.16 A high-angle annular dark-field (HAADF) image of a thin section of *Tyrannosaurus* bone (prepared by ion milling). The TEM used was a Philips CM 200, housed at NCEM (LBNL). The lattice fringes are directly measurable from this type of image. Moire fringes also can be observed, where multiple nanocrystallites overlap. In an ideal situation, this thinned section would be only one or two nanoplates thick at the hole region (bottom of image, black in appearance), allowing for direct measurements to be collected.

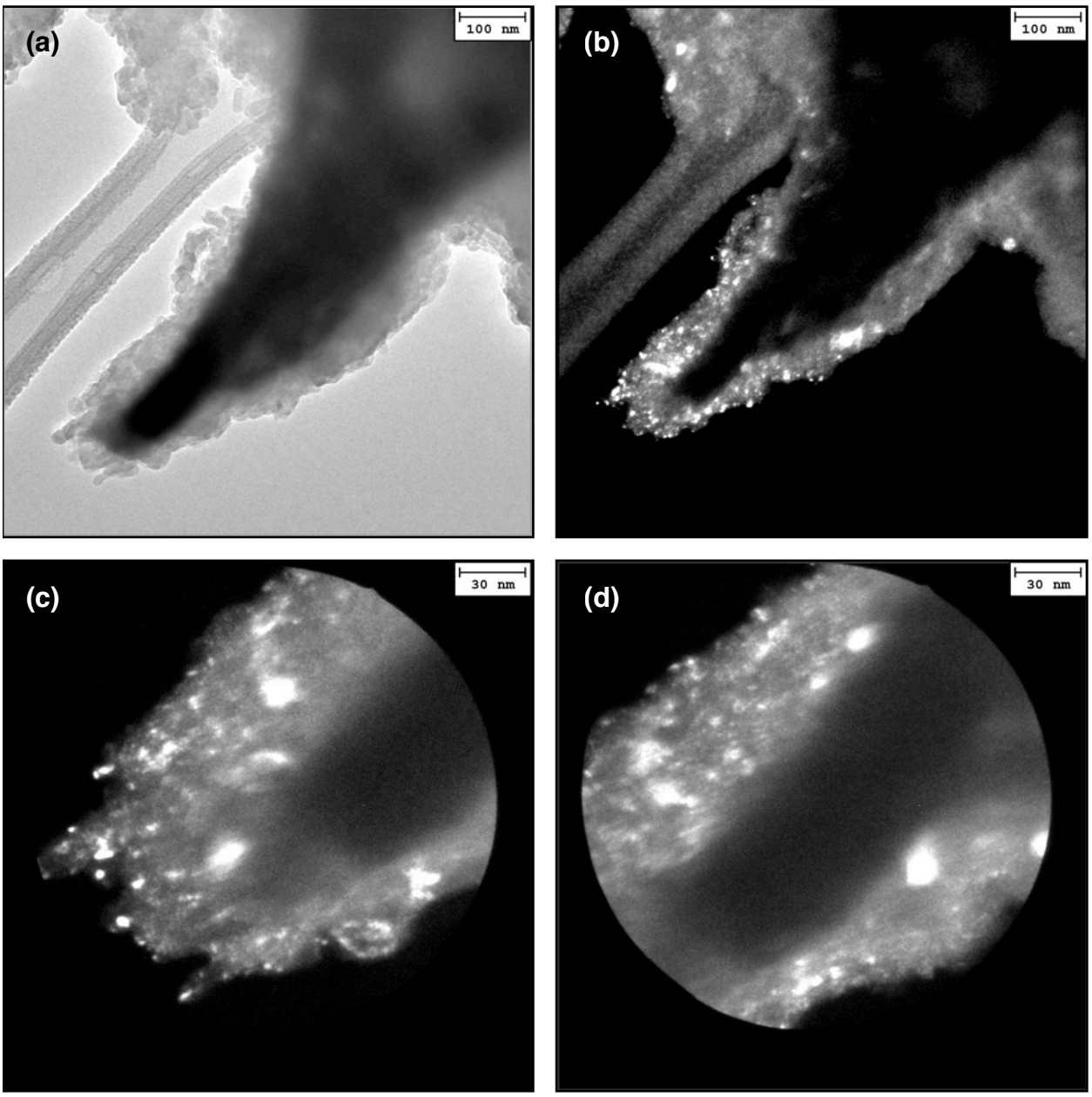

Figure 3.17 (a) A tubular structure protruding from the side of a fossil bone fragment (*Pristichampsus*). The high-density core structure if visible in the upper-left bright-field image and suggests a winding architecture, which is consistent with a microfibril. (b) A corresponding dark-field image. (c) and (d) High magnification dark-field images of the structure demonstrating pervasive nanocrystallinity. These images were generated by selecting a portion of the 002 partial ring in the diffraction pattern. Correspondingly, the stacked linear arrangement of nanoplates is evident within the dark-field images, following the direction of the tubular structure. This, too, is consistent with the expected architecture of a microfibril. Combining this approach with tilting operations has the potential to demonstrate how the crystallites are oriented in 3-D.

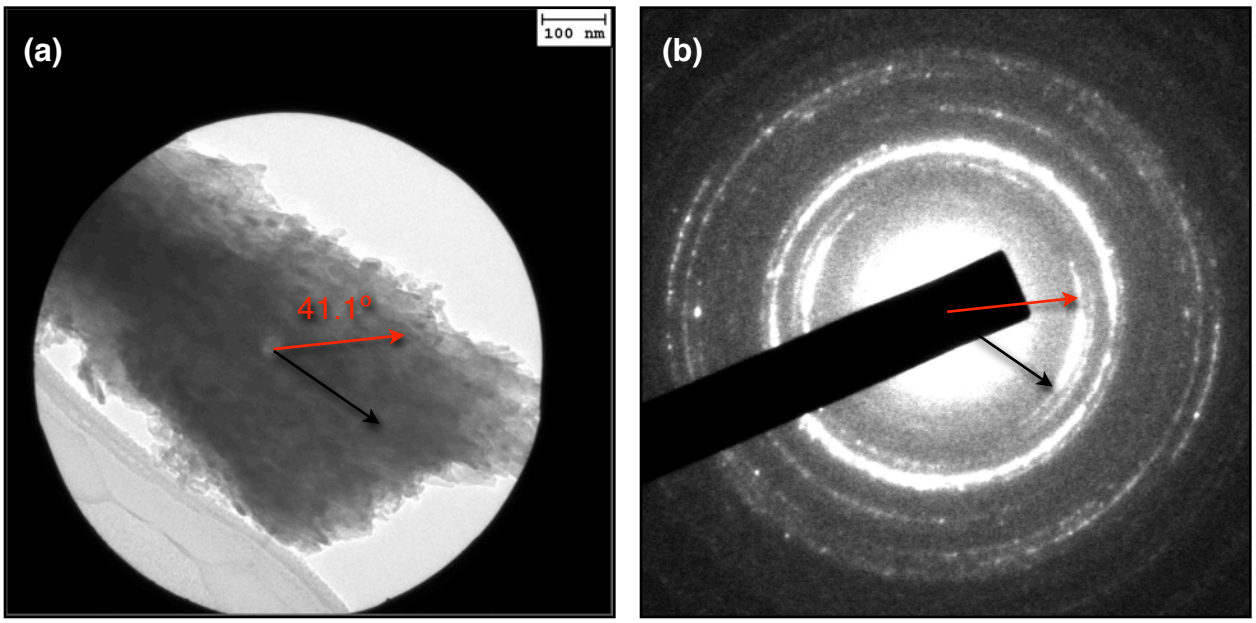

Figure 3.18 (a) A microfibril structure in *Pristichampsus* imaged at 25k×. The dark circle is the objective aperture. (b) The corresponding diffraction pattern. The black line traces the microfibril line, while the red line traces the extreme direction of the 002 arc in the diffraction pattern. The arc implies the microfibril is helical, and using the arc to identify the corresponding direction in the microfibril, the pitch is 41.1°.

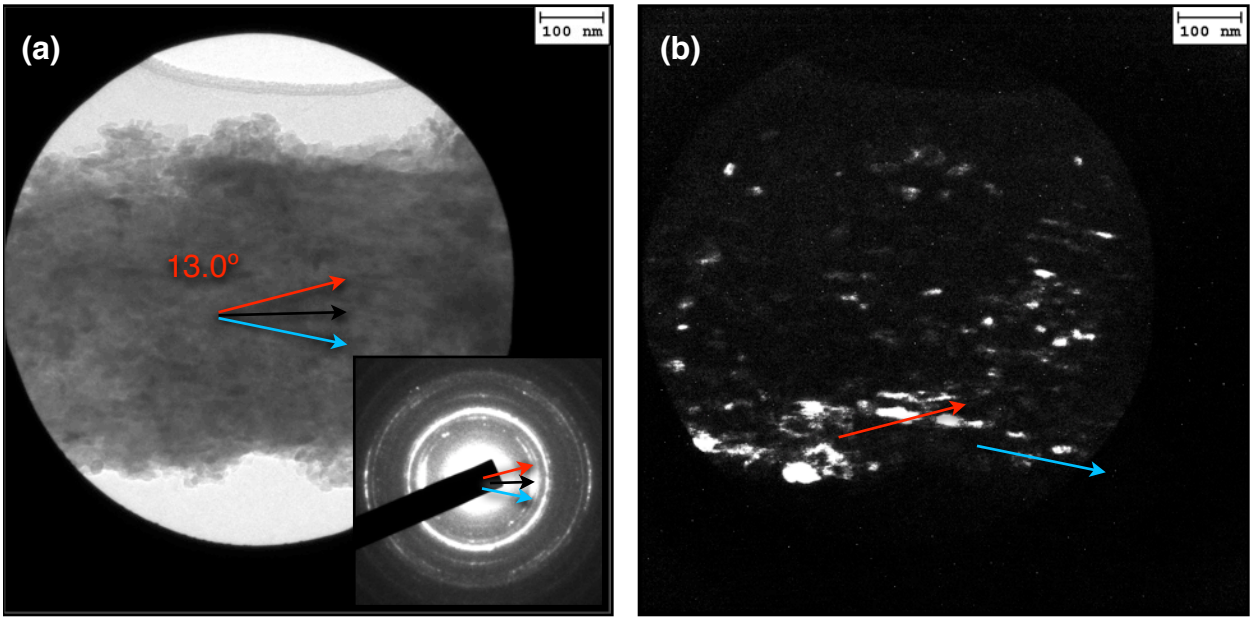

Figure 3.19 (a) A portion of a microfibril in *Pristichampsus* at 25k×. The direction of the microfibril (black arrow) is traced first. (b) The objective aperture was used to select one end of the 002 arc (blue arrow, crystallite lengths in the dark-field image), and the selection highlights a line of increased intensity (red arrow) in the dark-field image. This direction corresponds to the opposite end of the 002 arc. Applying the red arrow to the microfibril line direction (black arrow), the pitch of the structure is 13.0°.

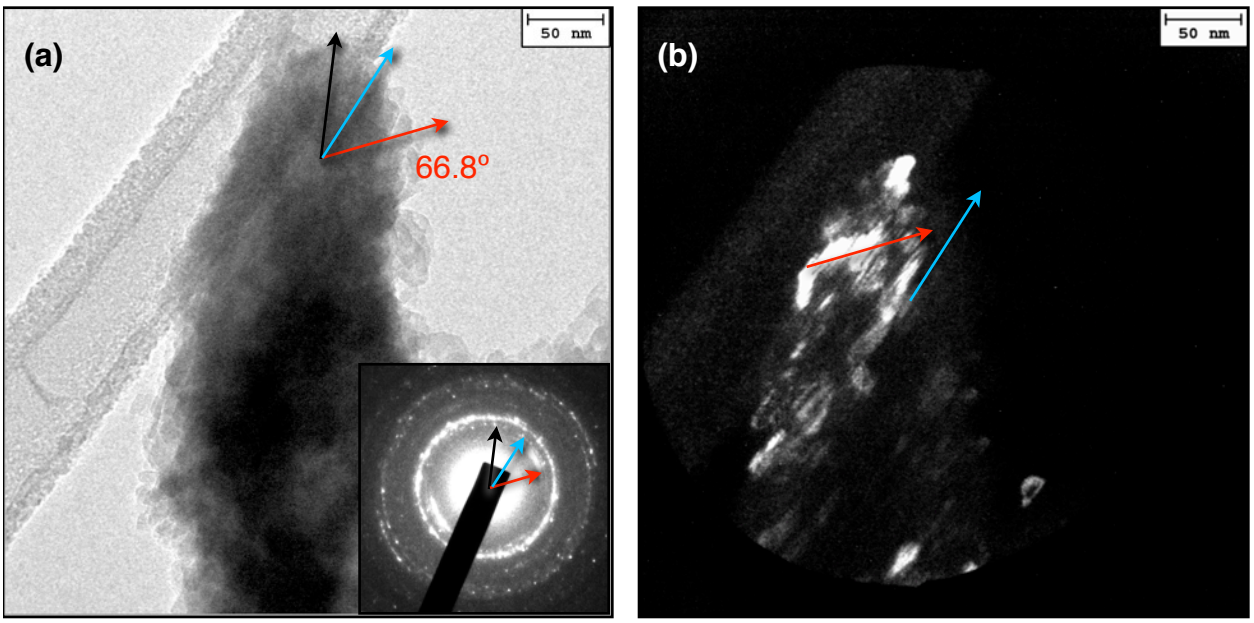

Figure 3.20 The same method as in 3.19 is applied to a dinosaur skull sample (*Stegoceras*). (a) The microfibril structure at 30k× with the length traced (black arrow). The upper end of the 002 arc is selected this time (blue arrow), yielding the crystallite line length. This highlights a band of adjacent crystallites (red arrow), which maps to the opposite end of the 002 arc. The pitch of the structure is 66.8º relative to the length.

4. A case study: *Triceratops* frill

The practical implications of this study include not only the ability to identify and quantify local changes in specific fossil bone tissues but to establish a method for analysis that will allow for the inference of specific tissue mechanical properties and growth mechanisms, while tracing phylogenetic origins. Toward this end, the fossil bone reservoir contains an extensive number of unique, specialized bone tissues and structures, most of which are only understood to the morphological, or possibly histological, levels of the structural hierarchy.

To demonstrate that the characterization method presented in this work is practical and effective toward (1) diagnosing diagenetic changes in a novel fossilized tissue and (2) extracting meaningful interpretations of tissue structure and biological function, an unrelated fossil bone tissue (Museum of the Rockies or MOR specimen 3000) was identified for analysis. The specimen was provided by J. R. Horner. This tissue is a portion of the triceratops cranial frill (Figure 4.1 (a) and (b)). The craniofacial ornamental bone structures of marginocephalian dinosaurs, which include pachycephalosaurs and ceratopsians, are currently under heavy scrutiny in the paleontological community (Goodwin & Horner, 2004; Horner & Goodwin, 2006, Horner & Goodwin, 2008; Horner & Goodwin, 2009; Horner & Lamm, 2011). In particular, these structures exhibit extreme morphological changes, and even directional reorientation, in ontogenetic sequences established from conspecific growth series. There is no known living vertebrate today whose craniofacial ornamentation exhibits similar remodeling patterns, which makes the frill of triceratops a tremendously significant bone tissue.

The early investigations by J. R. Horner and Mark B. Goodwin were based on morphological and histological approaches and were used to preliminarily identify the novel tissue growth patterns and distinguishing parameters of the craniofacial elements of marginocephalia. The preliminary patterns and parameters were documented as, for example, (1) largely acellular, (2) containing extensive Sharpey's fibers, which are commonly associated with fibrous connective insertion points into compact bone, and (3) impressive patterns of reorientation and growth based on levels of periosteal erosion and deposition never previously observed in modern animals, especially within craniofacial elements (Goodwin & Horner, 2004). Based on these distinctive differences, among others, this new bone tissue was termed *metaplastic bone*.

The term metaplastic bone has a very complicated history and is regularly applied to markedly different types of bone tissues, many of which are wholly unrelated from either the perspective of developmental origin or mechanical purpose. The complicated usage of metaplastic bone is the result of a literal translation of its original German form, which has been adopted and re-adopted in similar but disjointed contexts. *Metaplasia* means, simply, to change from one form into another. Tissue metaplasia, therefore, means that one distinct, adult tissue type changes form into another, and this is the loose definition under which J. R. Horner and M. B. Goodwin first adapted the terminology to describe the craniofacial ornamentation of marginocephalia.

Both historically and today, the literature is rife with incidences and descriptions of metaplastic bone. These various descriptions are very important toward developing a complete set of criteria for identifying and diagnosing metaplastic bone tissue in dinosaurian, or otherwise, boney elements, so they will be quickly reviewed here. Osteoderms are, perhaps, the best known

and most extensively documented class of metaplastic bone tissues of non-pathological origin. Osteoderms arise from the dermal tissue and include examples such as the human patella, the armored scutes of ancient and modern crocodylia (Tumarkin-Deratzian, 2007) and amphibia (Witzmann & Soler-Gijón 2010), the plates of stegosaurs (Main *et al*., 2005; Hayashi *et al.*, 2012), and the sub-dermal armor of Xenarthra (Wolf *et al.*, 2012), sauropoda (Cerda & Powell, 2010), and other various archosauria (Scheyer & Desojo, 2011; Cerda & Desojo, 2010). The mineralized tendon is another well-known example of metaplastic bone tissue: early investigations in chickens (Abdalla, 1979) and turkeys (Landis *et al.*, 1993) laid the foundation for our understanding of how bone tissue mineralizes at the nanoscale, while more recent investigations in the paleontological sciences have explored the spinal and leg tendons of dinosauria (Moodie, 1928; Adams & Organ, 2005; Organ & Adams, 2005) *via* histological approaches. Other examples of non-pathological metaplastic bone growth include the cartilaginous growth plates of vertebrate long bones (Haines & Mohuiddin, 1968) and, perhaps, the hyperossification of skeletal elements in amphibia (Clemente-Carvalho, 2009).

Additionally, pathological origins of metaplastic bone have been known for centuries and include neo-ossifications within muscular or dermal tissue as the result of trauma, bone tumors, and *fibrodysplasia ossificans progressiva*, which is a debilitating condition that eventually freezes the sufferer into a bone-locked position. None of the latter pathological metaplastic bone examples have any relevancy to the tissue with which this study is concerned, however, and are merely nominally related, as a result of the historical context of this terminology.

The use of metaplastic bone here will ally with that described by J. R. Horner and M. B. Goodwin and represents the common usage of the term in the paleontological literatures today. Referring back to the set of characters that Drs. Horner and Goodwin initially developed toward the identification and description of metaplastic bone in dinosauria, minor revisions have occurred since the earliest publications on the cranial domes of pachycephalosauria. That is, no longer is metaplastic bone considered to be acellular, and even in instances when it has appeared to be, such as in the cranial dome of pachycephalosauria, either it in fact is not or if it is, such a character is no longer considered atypical or exclusive. The currently accepted group of metaplastic tissues of non-pathological origin that are of interest to paleontologists include craniofacial ornamentation, osteoderms, mineralized tendons, and cartilaginous growth plates. The triceratops frill, therefore, falls within this category, making it of extreme significance not only toward establishing correct ontogenetic sequences but also toward identifying growth characters of this unique type of bone tissue, as relevant toward the correct classification of metaplastic bone tissue within our overall understanding of osteology.

A survey of the literature quickly indicates that all key characters and parameters currently used in paleontological studies are still derived from the morphological and histological levels of specimen analysis. These levels can access only down to the microscale, which represents one of the the highest orders of the bone structural hierarchy. In fact, at this level, these analyses do not even begin the process of accessing and characterizing the hierarchical structure of bone tissue.

Hence, the question quickly arises: do the lower levels of the structural hierarchy support the conclusion that this type of boney tissue is distinct from normal bone tissue? This is where my work steps in as the first application of my suite of analyses for identifying and describing

minimally-altered bone tissue in fossils, with emphasis particularly on the nanoscale level, *i.e.*, the building blocks. Hence, by employing the same techniques already indicated, I have analyzed a section of *Triceratops* frill (MOR 555) across the structural hierarchy. The results, discussion, and conclusions are further presented below.

4.1. Results and discussion of triceratops frill analysis

A back-scattered electron (BSE) image map is presented in Figure 4.1. The bone tissue appears dark gray; all osteons, osteocyte lacunae, and cracks appear black; and regions of $BaSO_4$ in-filling appear white. Osteons and osteocyte lacunae are standard physiological characters of compact bone tissue, and overall, this tissue rather strikingly resembles a combination of compact and transitional compact-spongey bone. A higher magnification BSE image reveals the preservation of mineralized macrofibrils within the osteons (Figure 4.3). The WDS probe was used to generate an elemental map (Figure 4.4) around one $BaSO_4$-infilled osteon to observe whether any of these mineral species have diffused into the bone mineral over millions of years of exposure; the mapped region is indicated in Figure 4.2 as a red rectangle. In WDS, the intensities of the elemental map pixels directly reflect the relative concentrations of atomic species in a specimen. That is, the relative intensities within a given map (a particular element) are a direct measure of the concentration of that element, by location. The bulk bone contains Ca, P, and O, as expected; meanwhile, the mineral in-filling contains Ba, S, and O. The absolute lack of Ba within the bulk bone is especially worth noting. Similarly, the deep blue pixels present in the bulk bone of the S map are on the order of background, and there is no detectable S in the bulk bone. In short, the in-filled mineral ($BaSO_4$) has not diffused into the bone.

The precise chemical composition of the bulk bone tissue of this specimen is reported in Table 4.1. These values are the result of averaging the values obtained from 10 spots, all from random areas mid-way between osteons and not near regions of $BaSO_4$ in-filling. The bold-faced, upper values are the average at.% values, while the normal-faced, lower values are the corresponding standard deviations. The most significant difference between the composition of the frill versus the composition of modern bone is the increased fluorine content, which is regularly observed in fossil bones. The at.% composition of the frill is plotted in a bar graph against the three modern bones from the specimen set analyzed above (*Struthio*, *Rhea*, and *Caiman*) and values for stoichiometric, theoretical hydroxyapatite (Figure 4.5). The most noteworthy feature of this plot is the distinct banding pattern, which represents consistent atomic fractions and proportions of the major bioapatite elements, *i.e.*, Ca, P, and O. This plot also clearly demonstrates the selective substitution of F for the hydroxide position within the bioapatite lattice; that is, the anion band is of similar net size for the frill, which includes a significant fluorine content, as for the modern bones and stoichiometric, theoretical hydroxyapatite.

Of course, as described above, the at.% results from WDS do not take on real significance until paired with XRD. For diffraction analysis, a portion of this specimen was ground with mortar and pestle and then distributed into a powder XRD tray (glass), as shown in Figure 4.6. The surface was smoothed as sufficiently as possible to minimize any introduced aberrations in diffraction peak structure from surface roughness features. The resulting XRD pattern (Figure 4.7), which was recorded at a scan rate of 2°/min and a sampling width of 0.02°,

is highly reminiscent of the powdered *Tyrannosaurus* XRD pattern presented earlier as well as published patterns for modern (nanocrystalline) bone. If aberrant peaks are present, they are minimal and may possibly be identified as goethite or $BaSO_4$. Regardless, this specimen is extensively nanocrystalline apatite with a composition minimally deviated (*i.e.*, fluorine content) from that of modern bioapatite. The powder sample used for XRD analysis was further characterized with EDS to verify its chemical constituents (Figure 4.8) and similar results were obtained as for the WDS analysis. The particular significance of this result for the frill specimen, however, is that it suggests that the nanoscale constituents of the bone may in fact be usable toward further classification and identification of the bone tissue of dinosaur craniofacial ornamentation or metaplastic bone tissue, generally.

Finally, TEM analyses were carried out for inspection of nanocrystalline elements of the bone tissue. Figure 4.9 (a) shows a bright-field TEM image of a frill fragment; small nanocrystals can be seen along the edge of the fragment. The corresponding dark-field image produced by selecting a portion of the electrons in the partial 002 ring in the diffraction pattern (Figure 4.9 (c)) is shown in Figure 4.9 (b). The edges of the dark-field image are particularly bright and highlight the nanocrystallinity of this fragment. The internal region is too thick for careful inspection, causing high inelastic scattering. Figure 4.9 (d) shows a corresponding high-resolution dark-field image from the same fragment, which demonstrates the nano-sized crystalline domains of the fossil bone tissue. The high degree of internal orientation within this individual fragment (partial rings in diffraction pattern) indicates that this is a single portion of the original bone tissue, likely a microfibril fragment, or a portion of a macrofibril bundle. Further, the relative angular offset of the *c*-axis (002 ring) in the diffraction pattern relative to the length of the fragment edges (approximately 30°) further supports the notion that the microfibril is constructed of wound collagen bundles.

4.2. Conclusions and implications for further investigations of marginocephalian craniofacial elements

The main conclusions developed in the discussion section are summarized here. SEM map reconstructions reveal the high porosity of the frill tissue, including the irregularly shaped osteons and the high quantity of osteocyte lacunae. This suggests that the frill tissue was highly vascular, which is a conclusion supported by the previous findings of others who have studied metaplastic bone in marginocephalian dinosaurs. The disorderly array of osteons, however, also suggests that this was not a primary load-bearing structure, which supports the notion that the craniofacial features on marginocephalians were likely used as decorative indicators of sexual maturity. The in-filled mineral is $BaSO_4$, and it has not diffused into the bone tissue in appreciable quantities. The frill mineral is enriched in fluorine, which is an expected finding; however, the bone mineral is still in the hydroxyapatite crystal structure. The fossil bone also contains preserved nanocrystallinity, and microfibrillar structures can be identified.

Not only are these results significant because they represent the highest spatial resolution ever applied to *Triceratops* metaplastic bone tissue but also because the application of my vetted characterization techniques has identified an exceptionally well preserved fossil bone tissue. In this case, the latter finding is highly impressive, due to the highly porous nature of this tissue (Figure 4.1). All data contained within this study support the notion that metaplastic bone is true

bone tissue, in the sense that its hierarchical structure and composition precisely mirror other bone tissues that I have studied. Likely, in time, we will find that the distinction in "metaplastic bone" in dinosauria is given by the erosion and deposition patterns (*i.e.*, these processes are carried out in a unique manner in marginocephalia). In the future, continued investigations such as this will be able to shed new light on the evolutionary origin of metaplastic bone tissue, the growth process and mechanisms of triceratops craniofacial ornamentation, and comparisons between this tissue type and other commonly found bone tissues, such as compact bone. Thin sections analyses (SAXS and TEM) will be useful in more precisely quantifying structural features in the fibrillar hierarchy. Any effort to shed light on the transitional phases in tissue development will prove exceptionally useful toward understanding this tissue.

Figure 4.1 (a) and (b) Photographs of both sides of *Triceratops* frill surface (MOR 3000).

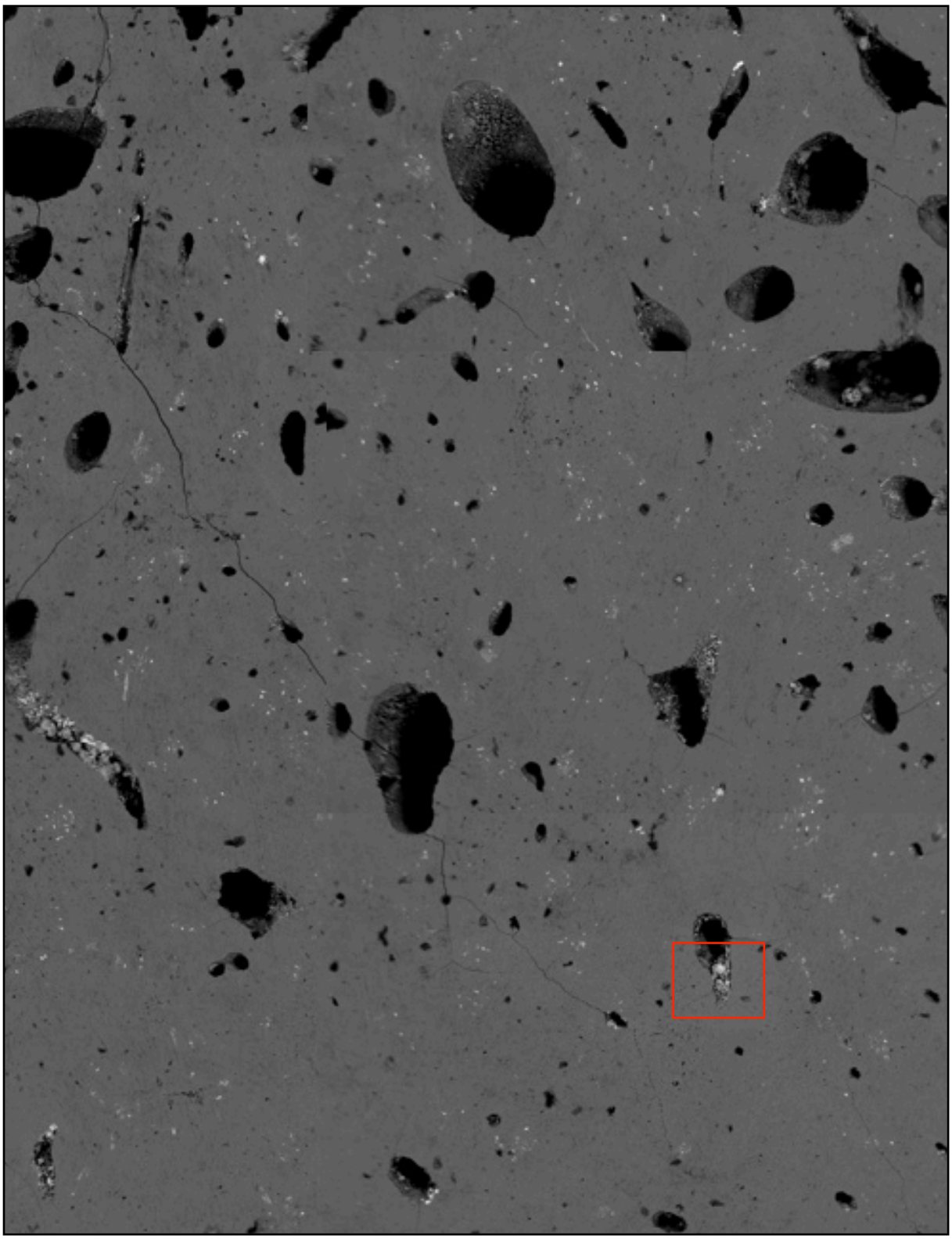

Figure 4.2 BSE image map of the *Triceratops* frill. Gray is bone tissue; white spots are BSO_4; and large black holes are osteons, while small dots are osteocyte lacunae. Some cracks are evident. The red rectangle indicates the region of WDS mapping analysis (see below).

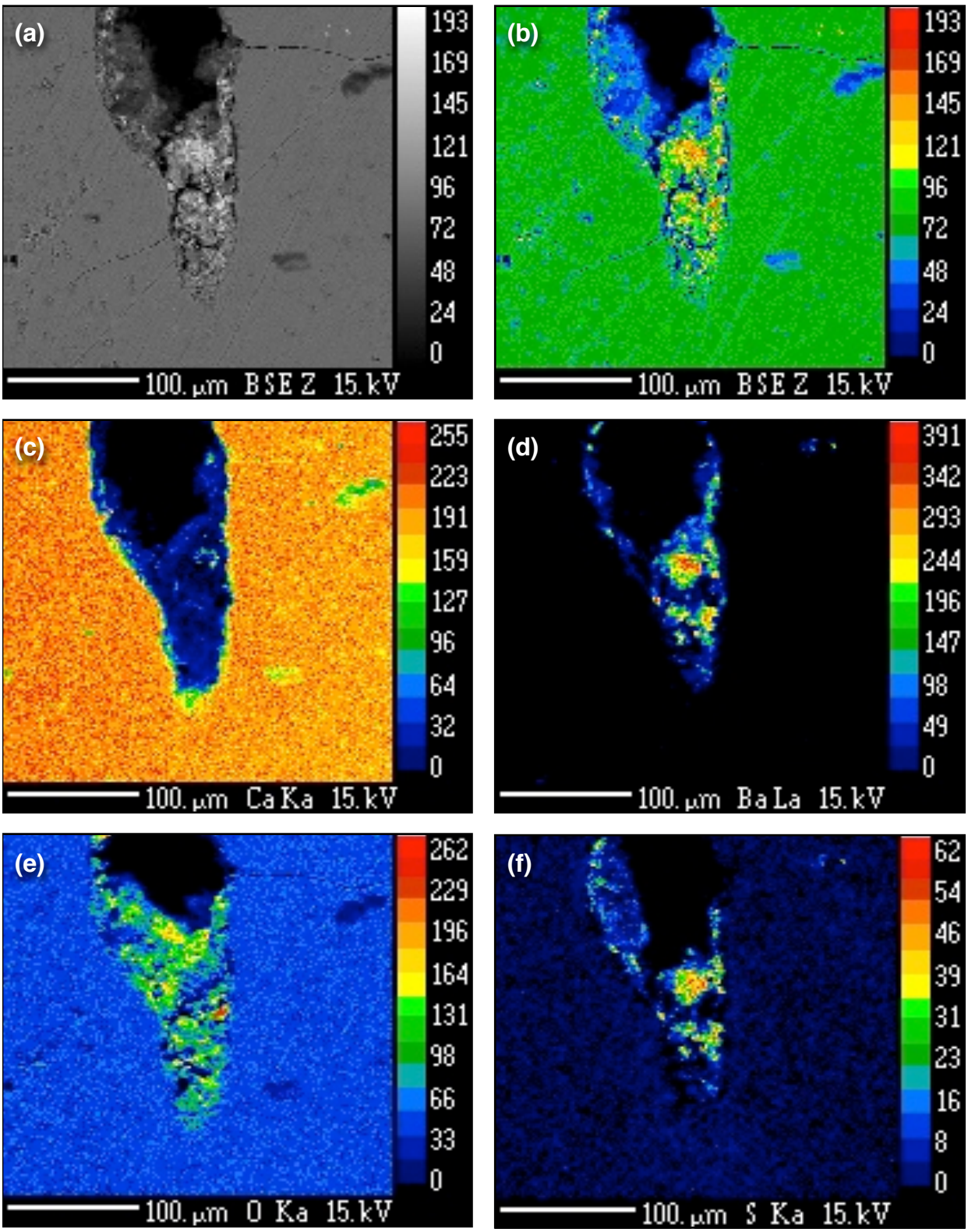

Figure 4.4 Elemental map-based inquiry into whether the in-filling mineral has diffused into the fossil bone tissue. (a), (b) BSE Z images in grayscale and color, respectively. (c) Ca is predominantly located in the bone tissue. (d) Ba, (e) O, and (f) S are all detected in the in-fill, suggesting that its identity is barite ($BaSO_4$). Ba and S are not detected in the bone tissue, implying that diffusion has not occurred.

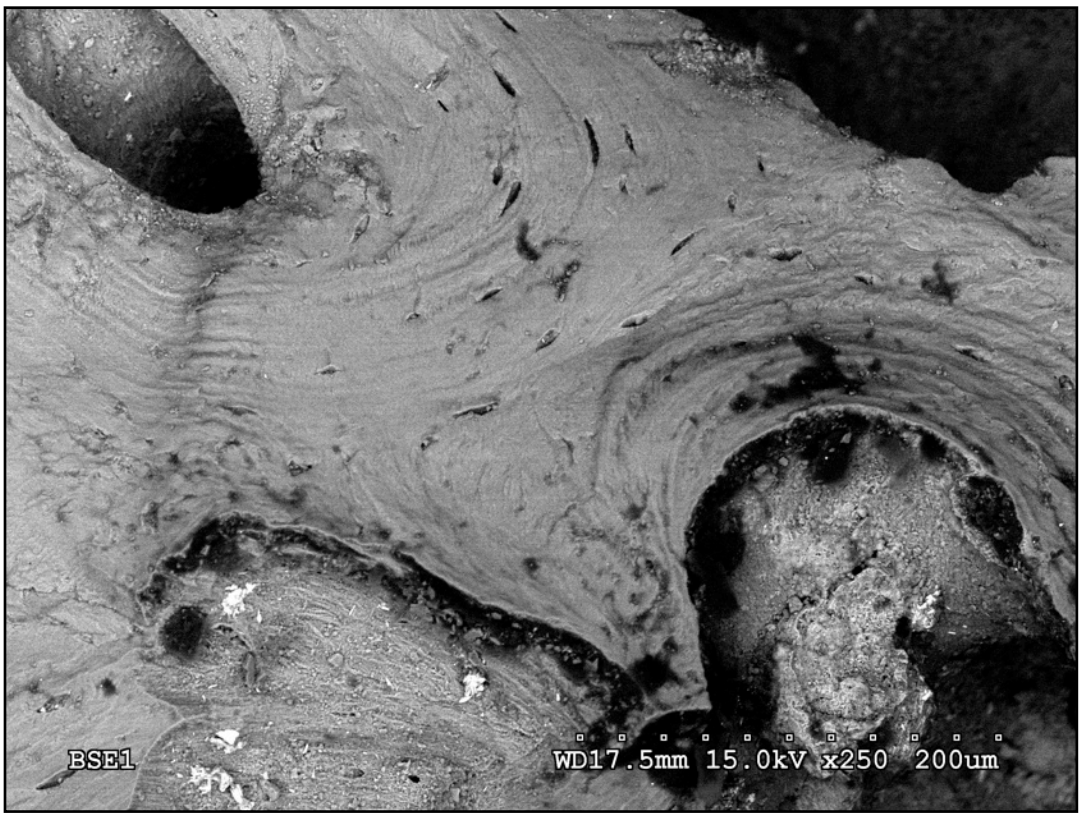

Figure 4.3 BSE image of a fractured region of *Triceratops* frill. Fractured surfaces of fossil bone tend to highlight the original tissue structure, which can be seen as the concentric circles around the osteon features. Oriented within the lamellar deposition are osteocyte lacunae. Extensively preserved mineralized macrofibrils can be observed in the osteon structures. Bright white areas are $BaSO_4$.

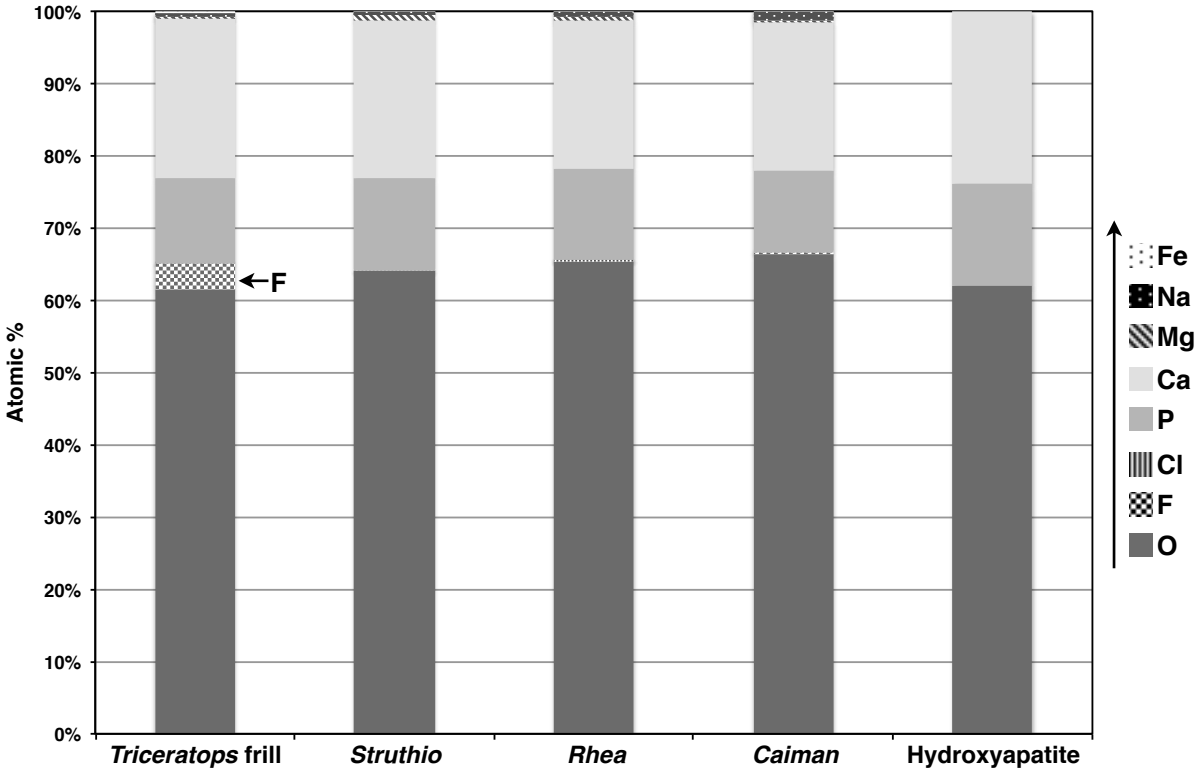

Figure 4.5 Atomic % composition of the *Triceratops* frill versus three modern bones (*Struthio*, *Rhea*, and *Caiman*) and theoretical, stoichiometric hydroxyapatite. Data is from WDS analysis and values are given in Table 4.1. Aside from increased F (3.428 at.%), values are consistent with modern bones.

	Tric. frill	*Struthio*	*Rhea*	*Caiman*	OHAp
Element at.%	**Avg** +/- St Dev	**Avg** +/- St Dev	**Avg** +/- St Dev	**Avg** +/- St Dev	**Avg**
O	**61.6084** +/- 0.3031	**64.0624** +/- 0.6615	**65.4955** +/- 0.5060	**66.4129** +/- 0.4052	**61.9**
F	**3.4277** +/- 0.1468	**0.0291** +/- 0.0392	**0.0045** +/- 0.0142	**0.2410** +/- 0.2594	0
Cl	**0.0079** +/- 0.0069	**0.0545** +/- 0.0169	**0.0481** +/- 0.0079	**0.1078** +/- 0.0147	0
P	**11.8132** +/- 0.1316	**12.8694** +/- 0.2695	**12.7674** +/- 0.2236	**11.2767** +/- 0.1976	**14.29**
Ca	**22.1474** +/- 0.1970	**21.8761** +/- 0.4315	**20.4804** +/- 0.3754	**20.3276** +/- 0.2053	**23.91**
Mg	**0.1490** +/- 0.0222	**0.6340** +/- 0.0329	**0.6045** +/- 0.0333	**0.4538** +/- 0.0217	0
Na	**0.5428** +/- 0.0439	**0.5548** +/- 0.0495	**0.6693** +/- 0.0407	**1.1824** +/- 0.0355	0
Fe	**0.3033** +/- 0.0165	**0.0042** +/- 0.0068	**0.0037** +/- 0.0056	**0.0048** +/- 0.0079	0
Ca/P	**1.875**	**1.701**	**1.604**	**1.803**	**1.67**

Table 4.1 Results of WDS analysis of *Triceratops* frill and three modern bone specimens (*Struthio*, *Rhea*, and *Caiman*). Bold-faced values are averages from 10 spots sampled mid-way between osteons and far from possible mineral in-filling. Normal-faced values are standard deviations. *Triceratops* frill is enriched in F versus the modern bones and has a significantly lower Na content. Values for O, P, Ca, and Ca/P are also reported for stoichiometric, theoretical hydroxyapatite for comparison.

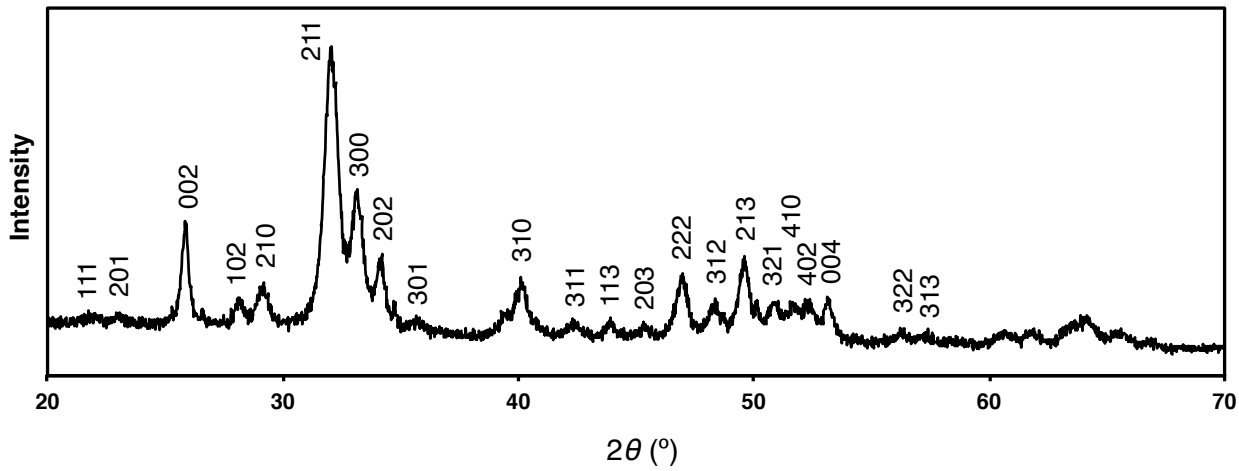

Figure 4.7 Powder XRD pattern of the *Triceratops* frill. Almost all significant hydroxyapatite peaks can be identified. The low peak-to-background ratio is a consequence of nanocrystallinity and is regularly observed in modern bone specimens, as well.

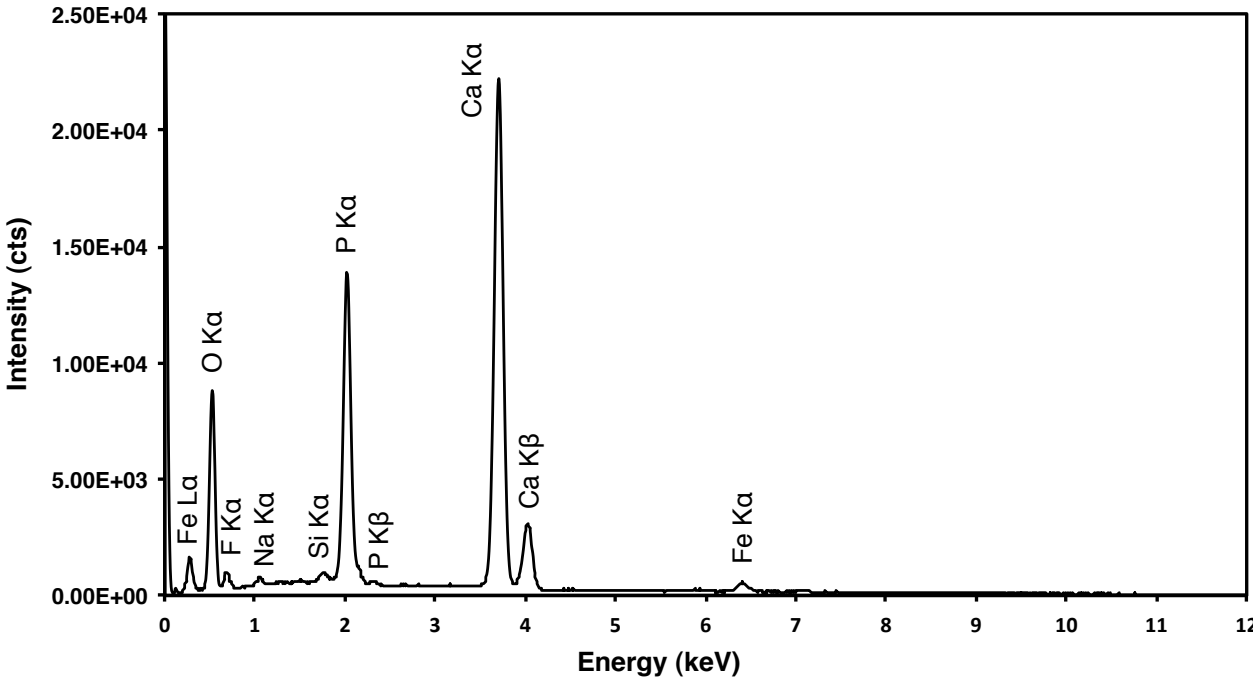

Figure 4.8 EDS spectrum of powdered *Triceratops* frill used for XRD. Constituents match those expected based on WDS analysis and further support the identity of this fossil bone mineral as minimally converted bioapatite (*e.g.*, minor enrichment in fluorine).

5. Discussion

5.1. Fossil bioapatite

Because the apatite family not only contains several closely related end-member species with similar lattice parameters but also can incorporate a variety of metal cation substitutions in solid solution, the characterization of fossil bioapatite is a somewhat difficult task, in the very least from the perspective of nomenclature. Additionally, modern bioapatite is already an impure form of hydroxyapatite. In particular, the substituting chemical species tend to be highly consistent across vertebrate phylogenetic lineages, because the ions are dependent on the composition of interstitial fluid, which is dependent on the composition of vertebrate blood. Even so, the relative amounts of these ions may vary by location in the bone, as the organism's physiology changes during mineralization, and other ionic species can be incorporated in fractions from trace (ppb to ppm) to several at.%. Additionally, there are a variety of other calcium phosphate minerals, which are not apatite forms, and in the past, there has been extensive controversy in the field over the true nature of the bioapatite mineral, particularly in its immature forms.

Hence, depending upon the level of compositional resolution required, not only must a technique be chosen that can sample the mineral crystal structure but also the elemental composition itself, which is not typically a requirement in materials characterization studies. Any other approach simply falls short, particularly with respect to the study of diagenetically altered specimens. In this work, I chose to combine electron microprobe WDS with bulk X-ray diffraction. The electron microprobe is a readily available technique, commonly found in geology departments, and is capable of sampling at the level of thousandths of an at.%. Because of its significantly increased energy resolution, this technique is highly desirable over EDS, which is the elemental analysis technique installed on the typical SEM, and is commonly found in materials science departments. X-ray diffractometers can be found in a variety of departments throughout the typical research university campus, and when using a carefully tuned set up, the typical diffractometer can supply the user with precision diffractometry data. In concert, these two techniques (WDS and XRD) offer the most robust analysis possible under the typical constraints (time, money, access). They are readily available, easily accessible, and data can be obtained within hours. Additionally, one sample set can be prepared for both techniques, assuming the particular equipment constraints are taken into consideration. Therefore it is my recommendation that any future study wishing to investigate the composition of fossil bioapatite should begin with these techniques; they provide average datasets that can be used to infer the status of the specimen on a larger scale.

This specimen set was designed to incorporate modern specimens as controls. Therefore, in as many cases as necessary, the modern specimens were analyzed in precisely the same manner as the fossil specimens. However, before drawing any definitive conclusions regarding the nature of fossil bioapatite, it is important to recall that the bioapatite composition can vary within a single organism, much less between organisms and species. Even today, while a variety of studies have investigated bone mineral composition and crystal structure, there remain disagreements with respect to the true standard composition and the developing crystal structure of the bioapatite nanoplates. In this study, in addition to incorporating my own set of modern

specimens to provide controls during analysis, I also draw on the datasets generated by others, which informed my predictions and analysis approaches. In section 1.1.1, I defined the commonly accepted ionic substitutions in healthy, modern bioapatite, and in section 1.2.1., I described the previously documented changes in fossil bioapatite as a consequence of diagenetic alteration. In particular, however, the data on modern bioapatite (composition, chemical structure, size, morphology) are critical toward the success of this study, because they provide the essential baseline against which the results on fossil bone specimens can be analyzed.

Within the WDS data, there are several features of interest that I discuss here. I have shown a visual representation of the WDS data in Figure 3.7, while the average numerical datasets are given in Appendix G for closer inspection. The most striking feature of the at.% bar plot is the fluoride band, which is significantly larger in the fossil specimens than in the modern specimens. This is unsurprising, in light of the ubiquitous documentation in other studies of increased fluorine content in fossil bones analyzed for composition. However, it is worth noting that the fluorine content of the *Caiman* specimen, which was the only wild modern organism, was 0.2410 $^{+}$/- 0.2594 at.%. Although this value is an order of magnitude less than the values obtained for the fossil specimens and indeed has a very high degree of internal variation (a large standard deviation), it nonetheless demonstrates that the fluorine content of modern bones can vary greatly (*versus* 0.0291 $^{+}$/- 0.0392 at.% in *Struthio* and 0.0045 $^{+}$/- 0.0142 at.% in *Rhea*, which are approximately one and two orders of magnitude less than the *Caiman*, respectively). The UCMP record on the *Caiman* specimen provides insufficient history to say with certainty, but it is possible that this specific organism resided in proximity to saline water sources, which tend to have higher fluoride contents. If so, this could have caused the higher fluorine content of the *Caiman* bone, following the regular uptake of water with a significant fluorine content. In short, future investigations wishing to more carefully develop an understanding of the normal fluoride range of healthy bone tissues should consider both wild and captive specimens, in addition to the water sources (fresh, saline, municipal, *etc.*) of these animals.

Ultimately, however, I present no argument against the notion that the fluoride content of fossil bone is always increased as a result of diagenetic alteration, and the factor of increase is in the range of 10^2 - 10^3. Although fresh water sources are often on the low-end in terms of fluoride concentration (approximately 0.1 ppm *versus* 1.3 ppm in sea water), the fluoride content of earth mineral forms provides a continuous supply of fluoride over time. For example, as the minerals weather, fluoride is continuously reintroduced into the aqueous atmosphere surrounding the submerged fossil specimen. The fluoride ion is quite small (ionic radius = 0.133 nm; for comparison, the ionic radius of chloride is approximately 0.181 nm) and is highly reactive (also called “bone seeking” in the scientific disciplines). Fluoride has a high affinity for the bioapatite structure, hence it substitutes quite readily into the hydroxide position of the lattice, which is located along large, open channels (defining the lattice points, as seen in Figure 1.1). In the example, as the fluoride concentration of the local solution around the fossil specimen decreases due to skeletal uptake, the equilibrium in the aqueous bath changes, and as a consequence, more fluoride dissolves from the surrounding earth. Alternatively, in a percolation environment, the fossil bones are continuously/intermittently bathed with refreshed solutions of fluoride. Eventually, over millions of years of repeated aqueous exposure, the fossil bone becomes enriched in fluoride, in a complete solid solution with the hydroxyapatite (bioapatite).

From a numerical perspective, the stoichiometric hydroxyapatite lattice is approximately 4.8 at.% hydroxide groups (discounting the hydrogens in this calculation assumes only 48 lattice positions in the doubled unit cell, and 2/48 equals approximately 0.048). Therefore, a several at. % substitution of fluoride at the hydroxide positions represents a significant alteration of the mineral structure along the solid solution line from hydroxyapatite to fluorapatite. That said, the respective lattice parameters of these two structures are only minimally different (on the order of thousandths of an Å). Hence, despite the enrichment in fluoride, the substitution itself is insufficient to significantly alter the crystal structure. For this reason, I have termed this a "structurally conservative" substitution. Further, although the pervasive nature of chemical alteration does indeed suggest that these fossil specimens have been highly exposed, which raises skepticism as to whether the bioapatite nanocrystallites and nanoscale structure can be simultaneously retained, I reiterate the fact that the fluoride substitutions occur in large, relatively open channels. Therefore, these substitutions are the easiest to carry out in the hydroxyapatite lattice. For example, in materials science, we would call this a fluoride filter, and there are many examples of mineral systems that act as effective filters without suffering adverse dissolution or morphological alteration. Hence, the presence of fluoride alone is insufficient to suspect pervasive and extensive alteration of fossil bone tissues. In short, based on the WDS data collected here and the findings reported by others, fossil bioapatite possesses increased fluoride content (by several orders of magnitude, representing approximately 50% conversion to fluorapatite), and this change occurs consistently throughout the tissue in a structurally conservative fashion.

Another change of interest is the reduced magnesium content of the fossil specimens in comparison to the modern. Magnesium cation (Mg^{2+}) substitutions occur at the calcium positions, likely along the channels defining the lattice positions, where the calcium ions are adjacent to the hydroxide ions, and not in the positions highly coordinated by phosphate ions. However, it was not the objective of this study to precisely locate these substitutions, so I do not elaborate or speculate further. The magnesium composition data are highly robust in terms of magnesium differences; the fossil specimens are significantly lower in magnesium content (hundredths of an at.% in comparison to 0.4538 $^{+}$/- 0.0217 at.% or greater in the modern specimens). The variation within these datasets also is relatively low. Hence, these data support the notion that the magnesium contents are reduced in the fossil specimens; that is, loss of magnesium cations from bioapatite occurs as a result of diagenetic alteration.

The fossil bones generally exhibit increased calcium contents *versus* the modern bones. It is worth noting, however, that to maintain charge balance within the bioapatite lattice structure, the loss of other cations must be balanced by a corresponding increase in, for example, calcium (Ca^{2+}). Hence, perhaps it is not surprising to find these differences in concert. However, the calcium content of the *Struthio* specimen was higher than the calcium content of the other two modern specimens; most noteworthy is the fact that the calcium contents of the modern specimens overlap with the calcium contents of the fossil specimens. Hence, changes in the calcium fractions alone are insufficient to justify differences between modern and fossil bones.

Generally, the Ca/P index ratio is used to describe bone in terms of crystallinity and composition. The ratio ignores the anion content of bone because the oxygen fraction is contained both within the phosphate ions and the hydroxide groups. Clearly, this index ratio is

insufficient in instances when other metal cations play a significant role in bone composition. However, the situation is further complicated by the fact that metal cations can have various valences (the commonly substituting species are either +1 or +2). Therefore, although I believe a revised index formula is important for fully describing the health or quality of bone (*i.e.*, calcium deficient, poorly crystalline), that ratio also must take into account the valences of the cations, which dictate the compensating charge ratio. Again, the picture is not so simple: new data have indicated that the phosphate ions may sometimes be in the form of hydrogen phosphate (HPO_4^{2-}), which can ideally be identified by FTIR or other means. Similarly, local charge compensation within an ionic crystal structure readily extends to the hydroxide groups, which are discounted in the index ratio; many studies have suggested that the low oxygen contents of modern bone tissues are associated with charge-compensating hydroxide losses. Hence, although I would suggest that the Ca/P index ratio is insufficient for comparing fossil specimens to modern specimens in investigations of the consequences of diagenesis, the development of a new, comparable index ratio is clearly a daunting task. This represents a possible avenue for future studies. For now, in short, both the calcium content and the Ca/P index ratio of modern specimens are values of interest in investigations of bone quality and composition (there are a variety of calcium phosphates, each with their own respective Ca/P ratio, based on stoichiometric compositions). Yet, I would heavily caution against the use of Ca/P ratios for documenting any degree of conversion of the fossil bioapatite from bioapatite to an alternative calcium phosphate structure. Instead, crystallographic studies should be carried out, such as XRD.

Finally, the fossil specimens all contain increased iron contents in comparison to the modern bone specimens. The iron fractions in all modern specimens are 0.0048 +/- 0.0079 at.% (*Caiman*) or less, whereas the iron fractions in all fossil specimens are within the range of 0.0970 +/- 0.0154 at.% to 0.5432 +/- 0.0102 at.%, with values in the other specimens measured at several at.%. Increased iron content in fossil specimens also has been extensively demonstrated in the literature, so this is an expected result. Iron is the fourth most common element in the Earth's crust and is readily incorporated into fossil specimens during diagenesis. This investigation, however, is insufficient to identify the precise chemical form of the iron contents documented here. In other investigations, such as my work with dinosaur soft tissues (not reported here), iron has been extensively found in the FeO(OH) or goethite form. In the literature, most instances concerning the substitution of iron into hydroxyapatite are engineered nanoparticles processed at high temperatures. For this reason, I find it unlikely that these iron fractions are necessarily incorporated into the apatite structure (they are not commonly documented substitutions otherwise). Further, some studies have demonstrated that iron inhibits bioapatite crystal growth; hence, the prevalence of iron in the fossil bones may actually represent a protective means for preserving nanocrystallinity. However, further analysis with techniques of higher energy resolution capability (*i.e.*, EELS or synchrotron X-ray absorption energy-loss spectroscopy (XANES)) is necessary to assess the validity of these claims and conclusively identify the iron chemical form.

At this point, the WDS composition results must be combined with the XRD results to provide useful data regarding the possible conservation of bioapatite in fossil bone tissues. First, however, the XRD results must be reviewed. The use of bulk specimens for XRD analysis is advantageous for several reasons. One, this allows the same surfaces to be investigated as those

studied by WDS, which provides direct correlation between the mineral analyzed; in light of the high degree of internal variation in modern specimens (and similarly predicted in fossil specimens), this is an important issue to consider. Two, fossil specimens are irreplaceable and minimal destruction during analysis allows for their use in subsequent analyses; similarly, other individuals have the opportunity to investigate precisely the same surfaces that I studied in this work because all of my specimens survived analysis and have been returned to the UCMP catalogue. Three, although fossil bone can be readily powdered, modern bone cannot be powdered without aqueous processing (*e.g.*, treatment with dilute sodium hypochlorite) to degrade the collagen, which arguably introduces additional errors into the analysis. Hence, these are several very important reasons to study bulk bone specimens in pursuits intending to document the composition of fossil bones.

That said, the XRD results are distinctly imperfect. As noted in section 1.1.3, compact bone contains a significant degree of internal orientation, which prevents all planes of interest from being properly oriented for Bragg diffraction in the correct proportion. This causes fluctuations in the relative peak heights of different reflections, and the resulting diffraction patterns are reduced in quality, making automated comparisons to hydroxyapatite standards difficult, if not impossible. Further, bone mineral is inherently nanocrystalline; this affects the resulting peak quality by causing peak broadening effects. Nanocrystalline diffraction peaks are not only broad but also relatively low intensity, with their peak heights approaching the background intensity level of the system. Any additional reductions in crystallinity, associated with the impure nature of bioapatite, cause further detriment to the diffraction peaks, and the peaks become susceptible to deviations from ideal shapes. As expected, all of these issues are evident in both the modern and fossil bone XRD spectra, in addition to some horizontal shifting associated with difficulties in locating the specimen surfaces at the precise X-ray beam focal point, which was an unavoidable consequence of the analysis approach used here (home-made specimen mount).

Even so, by careful inspection, it is possible to identify these diffraction patterns as representing the apatite structure. There are no significantly different features present in the fossil bone spectra. To support the claim that these spectra are in fact from apatite minerals, a small portion of the *Tyrannosaurus* bone was powdered. The resulting powder XRD spectrum (Figure 3.10) inarguably reproduces the expected spectrum for an apatite in comparison with the NIST hydroxyapatite standard (Figure 3.8). As can be seen in the tabulated data provided in Appendix H, the peak positions of this powder XRD spectrum clearly match the expected positions for hydroxyapatite. Only several inconsistencies arise, including one unidentifiable peak, and several other peaks that either could not be resolved or were too low in relative intensity to be detected. In the future, to obtain the most meaningful XRD data, fossil specimens should be powdered and analyzed with precision spectrometers or thin sections should be analyzed at synchrotron μ-XRD beamlines. TEM electron diffraction investigations also can be used, depending on the level of spatial resolution desired, but these techniques readily suffer from calibration errors and insufficient camera lengths for precisely defining shifts in ring positions.

Together, the WDS and XRD data offer a powerful, standard technique for the analysis of diagenetic alteration in fossil bone tissues. With respect to my specimen set, the following

conclusions can be drawn. The fossil bone tissues in this specimen set are extensively preserved in the apatite crystal structure with little to no alteration to other calcium phosphate or alternative mineral forms. Further, the composition of this fossil apatite closely resembles that of modern bioapatite, except for several quantifiable and apparently universal changes in composition. Several particular elements (*i.e.*, fluorine, magnesium, and iron) can all be predicted to have changed in specific manners. Even the most significant of these changes (increased fluoride content) occurs in a structurally conservative manner and does not necessarily indicate the alteration of fossil bone tissue to a different mineral form. This analysis provides a basic working definition for "fossil bioapatite," which can be applied and refined in subsequent analyses. That is, fossil bioapatite is approximately 50% converted to fluorapatite, with small increases in magnesium and iron, and such conversion does not necessarily counter-indicate the survival of nanoscale bone tissue.

The fossil bioapatite in this study also was investigated with TEM techniques, including bright-field imaging, electron diffraction, and dark-field. This portion of the study was systematically conducted by dispersing ground portions of fossil bone on ultrathin carbon grids. Isolated regions of bone fragments were identified under the electron beam, and these regions were imaged at high magnification (1M×) followed by the collection of selected-area diffraction (SAD) patterns from associated particle regions (imaged at 6k×). In all instances for each of the investigated fossil specimens, the dispersed fossil bone tissue was nanocrystalline (Figure 3.15). The images presented in this study are representative of a universally observed condition and were not selected to represent idealized conditions. Further, these same nanocrystalline regions (upper right-hand in Figure 3.15 (a) through (d)) all yield SAD patterns (lower right-hand in Figure 3.15 (a) through (d)) with a significant degree of internal orientation, and the rings of all patterns measured to apatite (the measurement protocol is presented in Appendix I). This latter finding is unsurprising, in light of the data presented above regarding the results of the combined WDS and XRD analyses. However, the finding of universally nanocrystalline fossil bioapatite is highly significant and notworthy.

Several other studies have investigated fossil bioapatite, both by preparing disarticulated, dispersed samples and petrographically thinned sections. In all of these studies, the fossil bioapatite was demonstrated to be nanocrystalline. In contrast, many of these studies also documented changes in nanoplate dimensions (called coarsening when dimensions increase, particularly the *c*-axis) and the presence of alternative nanocrystal morphologies (such as hexagonal prisms). As presented in the background information in section 1.2.1, both the size and morphology of biologically occurring hydroxyapatite (bioapatite) are distinct in comparison to that of geologically occurring hydroxyapatite. The structurally confined growth of bioapatite leads to the formation of ultrathin nanoplates elongated in the *c*-axis. They are often called truncated hexagonal plates based on the faceting character that the nanoplates exhibit. Geologically occurring hydroxyapatite, however, tends to grow in hexagonal prisms or rods and achieves micro- to macro-crystalline sizes.

Originally, it was my goal to use SAXS to identify the relative nanocrystallite dimensions within the specimens, particularly in terms of dimensional ranges. The notion here was that the use of pie-wedge processing of orthogonal wedges would be sufficient to extract the *c*-axis dimensions from the basal plane dimensions of the bioapatite. That is, based on the assumption

that all of the bone specimens contained a high degree of internal orientation and assuming careful specimen processing and mounting, it should be possible (even when 002 rings are not distinctly visible in the whole patterns) to integrate orthogonal pie wedges simply by knowing the specimen tissue conditions, and in turn, these pie wedges should represent the orthogonal directions of the lattice structure (*i.e.*, the *a*- and *b*-axes in comparison to the *c*-axis, which are orthogonal). However, in this process, I found a rather unusual result, including not only highly pronounced peaks consistent with the D-spacing values of collagen but also several spectra with strong higher order oscillations. The strong presence of these features prevented me from achieving my initial analysis goal, and instead, I turned my focus on the SAXS data to these features, which were discernible in not only the modern bone specimens but in the fossil bones, as well. Hence, all SAXS findings are discussed in sections 6.2 and 6.3, related to the collagen and nanoscale structure (microfibril) results, respectively. In final consideration here, I wish to acknowledge that the experimental protocol used for this analysis was insufficiently robust for the extraction of the background and/or low-order peaks. That is, based on the particulars of this set-up, the oscillatory patterns dominate the SAXS spectra, preventing further processing for the extraction of crystallite dimensions, as initially intended. For now, I return the discussion to the use of TEM to analyze the nanoplate dimensions.

Despite processing in 95% ethanol, these fossil specimens only exhibit nanoplate morphology, as evident in the TEM bright-field images. Additionally, these nanocrystals are clearly crystalline, as evidenced by the presence of lattice fringes in the defocused images (*e.g.*, Figure 3.16). Dark-field images (Figures 3.17 and 3.18) provide further evidence of the plate widths, which measure to less than 5 nm. This finding is consistent with standardly accepted results; additionally, with further refinement of the dark-field technique, likely the thicknesses of the nanoplates would be reduced (it is artificially increased as a result of the off-axis beam condition utilized to gather this particular dataset). The dark-field images are further discussed in section 6.3. Closer inspection of the high magnification TEM bright-field images reveals that the imaged nanoplates are on the order of 30-80 nm in length and 20-30 nm in width. Again, these sets of dimensions are highly consistent with standardly accepted values in the literature on modern bioapatite. No doubt, more careful inspection is required for the production of statistically robust datasets, particularly with respect to conclusions regarding the proposed coarsening phenomenon. In the past, investigations justifying the occurrence of coarsening have relied on data gleaned from approximately 100 crystallites per specimen, recovered from small regions of surface-weathered modern bones. Based on my observations of the intrinsic ranges present, I believe larger datasets are necessary, and more than one location should be considered without the use of aqueous processing techniques. To date, no such study (*i.e.*, fully relying on fossil specimens) has been conducted.

As presented here, the TEM data not only support the conclusions developed from the WDS and XRD data, but they further demonstrate that the fossil bioapatite has been minimally altered from its original form (based on comparisons to literature). Nanoplate dimensions are of critical interest to studies that may wish to investigate how bone structure has evolved in light of bone diseases or changing stress states. Preliminarily, these data support the notion that future studies wishing to explore nanoscale fossil bone tissue in depth will likely achieve success and should, ideally, incorporate TEM analyses.

Finally, I have several recommendations for future studies in this area, particularly those seeking to develop a more detailed understanding of the nature of fossil bioapatite. In conjunction, these techniques ultimately lack spatial precision. Synchrotron XRD can be used to reduce spatial resolution to fractions of a micron, and TEM techniques can be further used to obtain crystal structure information from very small regions of bone (tens of nm). However, thin sections should be prepared in addition to disarticulated specimen sets. Similarly, TEM EDS with standards can be used to sample very small regions for composition; however, these results are subject to inherent quality issues, because many of the elements of interest suffer from poor X-ray generation efficiency and because bone is relatively porous. In the future, I would suggest the application of electron energy loss spectrometry (EELS) in lieu of EDS. With EELS, it also is possible to sample the chemical environment of the element of interest, which would offer a significantly more detailed perspective of fossil bioapatite composition. These two TEM techniques, electron diffraction and EELS, represent the highest spatial and energy resolution techniques available today, and for the right study, they would certainly be the crucial choice.

5.2. Fossil collagen

Various reports have documented the preservation of collagen through structural and chemical means. For example, AFM has been used to demonstrate preservation of the structural repeat distance in fossil soft tissues, which are composed of collagen in extant organisms. Chemical techniques have included immunohistochemistry (antibody and fluorescent staining with optical microscopy), mass spectrometry for protein sequence rebuilding, and Fourier-transform infrared spectroscopy for identification of functional groups.

Here, because the focus of my investigation is truly on the nanoscale structure of bone, I elected to forego the majority of these techniques and instead to use SAXS alone. In applications to bone or collagen-based soft tissues, SAXS has the ability to identify the preservation of the collagen D-spacing, which is a repeated unit measuring 67 nm throughout the vertebrates. In dehydrated specimens, the protein structure contracts and can yield a D-spacing as small as 64 nm. It is important to understand the principles upon which SAXS works to "detect" the D-spacing. The X-rays scatter from the repeated units; these units can be holes or a material of sufficiently different electron density in comparison to the primary matrix. When the units are repeated with a high degree of order and are almost identical in size, the constructive interference is strong, and sharp diffraction peaks result. When these conditions are imperfectly met (insufficient electron density differences, poor ordering or variability in feature size), the peak quality in the resulting pattern is degraded.

Pure collagen contains high-density overlap regions (approximately 27 nm in length) and gap regions (approximately 40 nm in length). In highly oriented tissues, the experiment must be carried out transverse to the long direction of the fibrils; this yields a highly oriented diffraction pattern (partial rings). In the pattern, the constructive interference (diffraction) originating from the D-spacing of collagen occurs orthogonal to the microfibril length (within the recorded diffraction plane, which is a parallel inverse space projection relative to the sample plane). It should be noted that the Nanostar software automatically rotates the whole patterns by 90º, so that the real-space x-axis of the bone sample is the same orientation as the diffraction space x^*-axis. Hence, in the Nanostar whole patterns, the 002 arcs present approximately along the

vertical axis, even though the specimens were mounted such that the longitudinal direction of the tissue (longitudinal direction of the bone shaft) was vertical. In these patterns, winding of the collagen into fibrillar structures creates the characteristic angular offset of the repeat units, which sweeps what would otherwise be spots into distinct arcs (hence the ellipticality of the whole pattern in the horizontal direction). As the 3-D tissue is built up, subsequent layers of fibrils at various orientations (largely, longitudinally directed in compact bone) further sweep and spread these arcs. Higher order diffraction rings can be detected in specimens of high quality (consistent dimensionality).

In bone, the 40 nm gap distances become heavily filled with bioapatite as the tissue matures (the progression of biomineralization). Due to chemical interactions and spatial confinement, the bioapatite grows with its *c*-axis parallel to the length of the collagen; hence, the crystallites have a tendency to grow in parallel stacks as they fill the gap region. In some cases, the nanoplates infiltrate between the collagen molecules, also parallel to the collagen length. Then, the bioapatite clads the surface, once more parallel to the collagen molecules. Because the gaps are now filled with mineral, SAXS experiments carried out on bone tissue are sensitive to the electron density difference between the bioapatite and the collagen. Visual inspections (TEM and AFM images) carried out by others have documented significantly pronounced banding patterns in bone tissues. In TEM images of demineralized (often called "decalcified") bone, the dark bands (27 nm) correspond to the regions of high electron density, which in this case are the collagen overlap regions. However, the opposite is true in mineralized bone (even immature bone): TEM images of mineralized bone exhibit dark bands (40 nm) where the mineral has deposited in high density in the gap regions. The varying degree of mineralization can lead to incomplete filling of the gap region, which can possibly reduce the constructive reinforcement associated with the 40 nm (gap region) peak; alternatively, the crystallites can protrude into the gaps between adjacent collagen molecules in the overlap region, reducing the measured overlap distance. Typically, SAXS spectra of bone tissue are processed to extract 67 nm peak data (the sum of the gap and overlap regions act as a single diffracting unit). Theoretically, however, individual peaks also can present at 27 and 40 nm.

The SAXS spectra from the modern bone specimens illustrate precisely this fact. The *c*-axis (002) rings are the most prominent features in the whole patterns (Figure 3.11 (a) through (f)), oriented approximately along the perpendicular axis in the patterns. The oval shapes of the patterns also support the notion of a high degree of internal alignment. In Figure 3.12 (a), a prominent peak can be identified in the integrated *Caiman* spectrum, with the peak Q-value 0.027383 $Å^{-1}$ (22.95 nm). Less prominent but certainly present are identical peaks in both the *Struthio* and *Rhea* spectra, plotted in this same figure. In the modern specimens, this peak is a measure of the collagen overlap. The collagen overlap diffraction peak can be explored in more detail by inspecting the full width of the peak, which is arguably somewhat large. On the leading shoulder, the peak rises at the Q-value 0.023115 $Å^{-1}$ (27.18 nm), and on the trailing side, the peak falls off at the Q-value 0.029872 $Å^{-1}$ (21.03 nm). This finding indicates that the crystallites have filled the gap regions (the shoulder increases at 27.18 nm) and have protruded slightly into the overlap region (a reduced dimensional range). A similar argument can be constructed for the data representing the 40 nm gap region. Again, the *Caiman* specimen presents the best spectrum (Figure 3.12 (a)) for analysis. A small peak is visible at the Q-value 0.016003 $Å^{-1}$ (39.26 nm).

This value is precisely that of the gap region measurement standardly recognized for type I collagen.

Further application of curve processing techniques can be used to reveal additional features. The low intensity (poor quality) of the 40 nm gap peak is likely a consequence of the high penetrating beam intensity. Ideally, thicker specimens should be prepared for analysis on this instrument. However, even though my technique differed from the standard approach to SAXS data processing in bone specimens based on the use of a pie wedge integration approach (from -5 - 25º) to process the whole patterns, nonetheless this analysis demonstrates that my technique is capable of yielding modern bone spectra with diffraction peaks sampling both the gap and overlap regions, which together reproduce the D-spacing of collagen in these specimens.

Of course, the picture is not quite so simple in fossil specimens. Undoubtedly, whatever collagen may have been preserved also has been altered (or lost). Based on the notion that these structural features are universal throughout disparately related modern phylogenies and that the protein sequences of COL1A1 are highly conserved, as demonstrated in section 1.1.2 of my introduction, the technique of Extant Phylogenetic Bracketing developed by L. M. Witmer was invoked in this study. Hence, it is fully expected that the gap region in the fossil specimens should be defined by a peak in the range of Q-value 0.023115 to 0.029872 $Å^{-1}$, while the overlap region should be defined by a peak at the approximate Q-value 0.016003 $Å^{-1}$. However, the survival of collagen within bulk fossil bone tissue has not been demonstrated to date. Hence, in this study I must assume that all collagen has been lost; logically, this implies that the overlap regions have become a set of holes. This is counter to the original discussion of SAXS theory in which I described how the gap regions are the holes in a collagen template. However, based on the underlying principles that govern SAXS, all that matters for the production of diffraction peaks is a set of repeated units and a significant electron density difference between the phases. In theory, this is achieved by fossil bone fibrils containing preserved bioapatite in conjunction with a pervasive loss of collagen. Hence, precisely the same diffraction peaks that can be identified in the modern bone specimens also should be identifiable in the fossil bone specimens, even if all collagen has been lost.

This is precisely what I found in my SAXS analysis. After inspecting the whole patterns, several noteworthy features demand attention. Although no discernible arcs or elliptical patterns can be identified in the *Pristichampsus* and hadrosaur femur specimens, the *Tyrannosaurus* specimen demonstrates the elliptic phenomenon, and the hadrosaur radius specimen exhibits inarguable partial diffraction rings. All specimen whole patterns were integrated in the same range, except *Pristichampsus*, which also was integrated in the range of -15 - 15º (Figure 3.11 (d2)), because this pie wedge was found to reveal extensive higher order diffraction events (which will be discussed later in section 6.3). In the radially integrated spectra, a whole spectrum linear intensity plot may be insufficient to highlight all features of interest. However, the twin plots given in Figure 3.12 (a) and (b) demonstrate the consequence of variable specimen density on SAXS data; it was necessary to separate the fossil specimens from the modern specimens into two plots with different *y*-axis values (relative intensities) due to the distinct differences in the scattering contributions from these specimens. In the replotted data in Figure 3.13 (b), the hadrosaur radius has a clearly discernible peak in the range of Q-value 0.024893 to 0.028972 $Å^{-1}$ (25.24 to 21.03 nm), and a slight protruding feature can be identified in the hadrosaur femur

spectrum present in this same plot. The range is somewhat restricted for the hadrosaur radius specimen: the peak rises at Q-value 0.023471 $Å^{-1}$ (26.8 nm) and falls off at Q-value 0.029517 $Å^{-1}$ (21.3 nm). Nonetheless, this feature is consistent with the 27 nm overlap region of type I collagen. Additionally, though subtle, there are slight, protruding shoulders present in both hadrosaur plots (Figure 3.13 (b)) at the approximate Q-value 0.016003 $Å^{-1}$; this feature is consistent with the 40 nm gap region of type I collagen.

Collectively, these fossil bone spectra present evidence that the structural features associated with the original dimensions of the collagen scaffold have been preserved. While this evidence does not directly support the preservation of collagen itself, nonetheless based on the design of this study, these data are sufficient to provide the first ever documentation of the structure of dinosaur collagen, by using the preserved bioapatite as an inverse template (mineral replaced the original gap regions by biomineralization, and the original collagen-filled regions have likely become gaps due to collagen loss). However, the documentation of preserved collagen in other studies, as well as in my work on vessel structures recovered from *Tyrannosaurus* (not shown here), suggests that it is possible for collagen to be preserved in ancient bone tissues; hence, the possible survival of collagen in these tissues should not be discounted and is worth investigating further in the future. There are other highly significant findings evident in these SAXS patterns that will be discussed in section 6.3. For now, the final comments that I provide are given as follows.

The SAXS spectra collected from these bone specimens required two hours of exposure each. The Nanostar system was programmed to collect data over night to accommodate this constraint; the use of an automated stage expedited this process. Even so, the data collected from the fossil bone specimens suffered from underexposure, compounded by structural alteration (loss of collagen), which is the result of varying degrees of diagenetic alteration. In the future, the use of longer exposure times would enhance this type of analysis. Thicker specimen sections also would be desirable in the future, to guarantee sufficient scattering (diffraction peak intensity) against the background. Alternatively, the use of synchrotron SAXS beamlines, which have vastly higher beam intensities, is recommended.

5.3. Nanoscale structure of fossil bone

Insight into the nanoscale structure of fossil bone can be gleaned from multiple sources, including SAXS and TEM dark-field with tomography. AFM is an alternative technique that has been used by others but sometimes provides insufficient spatial resolution. In this work, I used SAXS to gather average structural values from microscale regions of thinned bone sections (actual thicknesses are reported in Table 2.2). This approach also yields data that are correlated to the tissue structure and the bone shaft length. Additionally, I applied TEM dark-field techniques to crushed specimens to demonstrate the feasibility of gleaning enhanced understanding of nanoscale structural information from fossil bone; this type of approach offers the added benefit of visual representations of actual features (instead of indirect sampling methods, like scattering). Combined with tomography (in which the sample is rotated in the beam path), TEM dark-field imaging can be used to extract crucial 3-D structural information of nanoscale bone features. Historically, bone (in fact, mineralizing turkey leg tendon and not true bone) has been prepared into thin sections for tomographic TEM analyses. In the introduction section, I explained why

this approach may not actually be sufficient for gleaning a comprehensive understanding of bone architecture at the nanoscale. Here, I only demonstrate the feasibility of this approach, providing examples of data that can be extracted in addition to recommended specimen conditions. In the future, however, these are studies that I would very much like to pursue on a larger scale with the direct purpose to begin building a deep time understanding of bone growth.

The most unexpected and exciting results of this study, to me, were found in the SAXS spectra. Not only does one fossil specimen exhibit a whole pattern with discernible partial ring features (hadrosaur radius in Figure 3.11 (e)) while other spectra exhibit subtle peaks at expected positions for the 27 and 40 nm characteristic spacings of collagen, but the *Pristichampsus* spectrum (-15 - 15º as shown in Figure 3.11 (d2) and plotted in Figure 3.12 (c)) displays inarguable evidence of highly preserved fibrillar structure. The higher order peaks evident in this pie wedge integration correspond to theoretically predicted features for close-packed bundling in the macrofibrillar structure. The close-packed bundling gives rise to the rounded humps overlain on the spectrum. These features are distinctly different in shape from normal diffraction peaks. Further, their characteristic spacing can be converted into a measurement of the microfibril width in this specimen. Identifying the maximum Q-values of two adjacent peaks as 0.032006 $Å^{-1}$ and 0.036273 $Å^{-1}$, the resulting microfibrillar width is calculated to be 147.3 nm. This is a highly reasonable value for a microfibril width. The pronounced nature of the features within the SAXS spectrum also suggests that the microfibril bundles have a highly uniform width throughout the sampled *Pristichampsus* tissue. A similar calculation can be carried out for the modern specimens; the resulting values give microfibrillar widths of 196.3 nm in *Struthio*, 160.7 nm in *Rhea*, and 220.8 nm in *Caiman*. Two of the three other fossil specimens exhibit evidence of this feature; however, the statistical power of the data are not trusted, and instead it is recommended that future data with increased exposure times and thicker bone sections be used instead.

However, as stated above, SAXS is an inherently indirect sampling method. In complex applications, it can be used to rebuild 3-D structures with the aid of automated stage movements and computer programming. This was not possible with the SAXS equipment utilized in this study (the Nanostar is a standalone benchtop unit). Instead, TEM dark-field imaging also was carried out to glean further insight into the nanoscale structures of these fossil bone tissues. Because it was necessary to process the specimens by grinding/disarticulation techniques, only the fossil specimens were analyzed in this manner. In the future, the modern specimens also should be incorporated by preparing a full set of thin sections to complement any disarticulated analysis. However, this was not the focus here, because thin section analysis is a vetted approach, whereas disarticulated specimen analysis is not.

The example dark-field (HAADF, in particular) image reported in Figure 3.16 was obtained from a thin section of *Tyrannosaurus* imaged on a Philips CM 200. Although this section was ultimately too thick for careful analysis, and the section was highly susceptible to bright-field beam damage, nonetheless it demonstrates the presence of a high quantity of variable nanocrystalline domains. In the future, an idealized version of this technique could readily be used to assess weighted domain orientations. That is, it would be possible to develop a computer program with the ability to quantify each domain orientation as a fraction of the whole image or of larger regions of interest. Such an approach would provide useful information on the degree of local texture (orientation of the bioapatite) and could be used to provide rapid comparative

assessments, for example, on the domain (ply) changes around osteons or in lamellar growth regions. Additionally, this approach could better inform our understanding of the nature of metaplastic bone tissue in marginocephalian craniofacial elements, as discussed in section 4.

However, the currently used techniques for this type of analysis are dependent on the use of polarized optical light, which suffers from inherent limitations in spatial resolution. Of course, I also argued that thin section analyses are insufficient for gleaning a full and accurate understanding of the nanoscale bone tissue structures (microfibrils). While I hold by this assertion, I do believe that thin section analyses can provide additional, powerful information that disarticulation inherently cannot, such as relative orientation with respect to the overall bone tissue and bone itself. In addition to similar SAXS investigations (oriented thin sections), it becomes clear just how invaluable the contributions from investigations of fossil bone thin section texture with preserved orientation integrity potentially could be toward understanding bone tissue from the deep time perspective or in light of specific mechanical constraints imposed on the developing bone tissues (*e.g.*, longitudinal compression in the cortices of the limb bones of terrestrial vertebrates).

Additionally, if collected in specific orientations (such as transverse to the shaft), the possibility of transecting a high quantity of nanocrystallites is increased, allowing rapid quantification of nanoplate thickness in specimens. Similarly, transverse section analysis also should provide the best possible approach for obtaining quantitative data on microfibril widths. Traditionally, investigators have used longitudinal sections for this purpose, presenting their images with the lengths of the microfibrils visible. However, the microfibrils tend to wander into and out of the longitudinal thin section plane; it is impossible to know with certainty whether the widest region of such a transect is in fact the microfibril diameter, which counter-indicates the extraction of long-range structural order. Instead, the use of a transverse section guarantees that transected microfibrils will be obtained, making possible measurement of the width values toward the development of sets of useful data, such as the variation in microfibril width in an individual tissue or among species. In serendipitous instances in which a single microfibril can be traced over long distances in a longitudinal section, it might be possible to detect correlations between nanoplate orientation and the microfibril banding pattern. This type of investigation would certainly be aided by the use of TEM dark-field in which the objective aperture is used to select, for example, portions of the *c*-axis (002) ring/arc. According to this approach, repeat patterns (bands) containing identically oriented nanoplates should be highly visible while the remainder of the structure is invisible.

Finally, the limitations of all of the above are associated with the fact that thin section preparation ultimately thins through the 3-D structure of interest. As reported in the discussion of SAXS spectra processing, the microfibrils in this specimen set were found to be in the range of 147 - 208 nm. These features are on the upper end of the thickness range accessible by TEM analyses, which almost exclusively depend on electron transmission geometries (EDS and secondary electron detectors are exceptions). This is one reason that I pursued fracture specimens in this work. Even though a significant fraction of the bone particles in a fracture specimen (see Figure 3.14) are too large for ideal electron transmission, nonetheless cleavage occurs on pathways of least resistance, and in many cases, this actually defines portions of the fibrillar structure, which is why diamond-shaped and tubular structures are often revealed. Further, many

of these fragments contain small protrusions on their ends, which are frequently electron-transparent portions of microfibrils that have survived partially intact (see Figure 3.17) or are microfibrils themselves. These are the structures of interest in the dark-field analyses presented in my work.

The tubular projection depicted in Figure 3.17 appears to contain a wound core coated with nanocrystallites. The corresponding diffraction pattern (not shown) verified the region to be of apatite character, and the specimen (*Pristichampsus*) was otherwise demonstrated to be preserved bioapatite based on the combined WDS and XRD analyses presented above. Therefore, the nanocrsytallites in this image also are taken to be preserved bioapatite. These dark-field images were generated with TEM using an objective aperture. Images (c) and (d) are magnified views of (b). In the magnified views, not only can semi-discrete nanocrystalline domains be identified (discrete regions of brightness) but an inherently linear texture of brightness can be detected in the region encasing the dense core. These images were generated by selecting a portion of the 002 arc of electrons, which were diffracted by the basal planes in the fossil bioapatite nanoplates. That is, by using basic spatial relationships, it can be determined that the line lengths of the texture are the direction of the nanoplate *c*-axes. This is not unexpected because bioapatite nanoplates have consistently been demonstrated to grow parallel to the length of the microfibril; hence, one expects the lengths of the fossil bioapatite nanoplates to follow the length of the protruding structure in the event that the structure is actually a fractured microfibril.

Further, it is worth noting that the directionality of the linear texture appears as stacks of parallel lines (again, this was specifically selected by the experiment protocol) with a characteristic angular offset relative to the length of the fractured protrusion. This is precisely what one might expect for a wound, rope-like bundle: in a rope, the fibers reside at an angular offset with respect to the rope length, and this angle is called the pitch. This angular offset also has been identified as the pitch in the macrofibril in which the rope fibers are microfibrils. As a hierarchical structure, of course, both the microfbril and the macrofibril may have their own respective pitches, and the fibers in each case are the collagen molecules and the microfibrils, respectively. Unfortunately, this structure could not be investigated with tilting operations at the time due to equipment issues. Since I collected this data, I have further developed the notion that the amorphous region of the diffraction pattern also should be investigated; in many cases, the amorphous halo is quite pronounced, and such an investigation might elucidate, for example, the composition of the dark central shaft in this protrusion (*i.e.*, a dense protein bundle).

The potential for this technique to elucidate the internal structure of fractured microfibrils is further demonstrated in Figure 3.18. Figure 3.18 (a) clearly presents a fractured, tubular structure. This structure is an appropriate width to be a microfibril and is composed of nanocrystallites (as investigated at higher magnification, images not shown here). The black circle in the image is the intermediate aperture, which was used to select a precise segment of the tubular structure to generate the associated selected area diffraction pattern. The pattern (Figure 3.18 (b)) presents partial 002 arcs, as expected for a bone tissue fragment containing a high degree of internal orientation. Based on all diagnostic criteria (including images not shown here), I identified this fiber as a fractured microfibril. Overlaying the line length of the microfibril structure (black arrow) on the diffraction pattern, it is apparent that the long axes of the nanoplates range from approximately parallel to the microfibril structure to an angular offset of

41.1º, which is the pitch of the structure. The opposite end of the 002 arc (41.1º offset, red arrow) denotes the extreme rotation of the nanocrystallites inside the microfibril; this rotation is due to the wound, bundled nature of the microfibril. Further use of the dark-field technique can elucidate the internal architecture of this structure, as demonstrated in the subsequent image sets.

Figure 3.19 takes this analysis to a higher level. After the black and red arrows have been established, a third arrow is applied to trace the orientation of the opposite end of the 002 arc in the SAD pattern. In this case, the range of crystallite orientations in the microfibril is not restricted by the line length of the microfibril. Using an objective aperture to select the crystallites in the red arrow orientation (their line lengths are distinctly visible in Figure 3.19 (b)), a new feature of increased intensity becomes apparent in this image. Shown in the lower center of the dark-field image, a band of increased intensity is traced by this analysis. The line direction of this band matches the orientation of the blue arrow in the diffraction pattern. That is, this analysis reveals the presence of another level of structure within the microfibril, appearing as a sub-fiber. The pitch of this microfibril is calculated to be 13.0º. Carrying out a similar analysis on the structure in Figure 3.20, the pitch of the microfibril is found to be 66.8º.

There are several features of interest worth discussing, in a general sense. In each of these microfibrils, including two from one specimen and a third from another, the structure of each microfibril is found to be unique. In each case, the net relative orientation of the nanoplates is unique, including the angular size of the 002 arc and the fiber pitch. These microfibril structures were all recovered from fossil specimens. Hence, beyond the details of nanoscale structure that can be gleaned from fossil specimens with SAXS, TEM techniques can provide additional information, such as the details of individual microfibril structures. Additionally, the average microfibril width was calculated for the *Pristichampsus* specimen (147.3 nm) earlier in this section. The structures presented in Figures 3.18 and 3.19 are larger, measuring approximately 230 - 250 nm in width. These latter values are still within the overall range observed for the specimens in this study and are not significantly different from other values reported in the literature.

Of course, the goal is to take this analysis even further. Ideally, complete 3-D models of the nanoscale structure of bone can be built based on composite knowledge obtained from SAXS and TEM analyses. The dark-field analysis can be used with tomographic packages to extract complete angular sets of data, which can be processed to rebuild the microfibril structure into an exact 3-D model replica. This information is important to our understanding of the nanoscale structure of bone, which has implications for our understanding of structure/property relationships in bone, including the consequences of changes in nanoscale structure. Additionally, comparative analyses of modern and fossil specimens can provide a deep time perspective of the evolution of bone tissue, including how bone tissues have evolved to accommodate changes in mechanical loading as well as the general nature of bone tissue evolution. From here, the nanoscale bone tissue structure (microfibril) is used to construct the higher orders, including the macrofibril and then the bone tissue lamellae/plies, which are deposited in layered form to construct 3-D tissue morphologies (osteons, trabeculae, *etc.*). Other higher order features of interest include osteocyte lacunae, which are the small holes enclosing osteocytes that become embedded within the bulk bone tissue during formation, and mineral density variation. These features are discussed in the next section. For now, I will close this

section by reinforcing the point that this is preliminary data gathered in an approach never before demonstrated. This is the first time ever that data on nanoscale structure have been presented for fossil bone tissues. In the future, I would like to apply tremendous focus in this area, with the ultimate goal of developing a more accurate 3-D model of the nanoscale structure of bone as well the first demonstration of nanoscale structure in fossil bone specimens.

5.4. Higher orders of fossil bone structure

The higher order features of bone tissue considered in this work include the osteon density and circularity, the osteocyte lacunae density and circularity, the bone volume *versus* total volume (BV/TV), the lamellar thickness, the secondary growth patterns, and the preservation of mineral density variation (a representative of tissue mineral density and as an indicator of secondary osteon growth). For the purposes of this work, these features are not the integral focus. However, survival of these features is predicated based on survival of the lower-level features of the structural hierarchy (the nanoplates, the nanoscale structure, *etc.*). Hence, in this work, the presence of these features was investigated to further support the notion that the nanoscale components of the bone tissue have survived. While the higher order features have been presented in other works (indeed, these are the features of interest in most paleontological studies), the nanoscale structure has not been presented previously. Therefore, the presentation of higher orders of fossil bone structure, while not original or new in itself, is significant in the context of this work, because it provides supporting evidence for the conclusions articulated above. The relevant data are given in Appendix F.

BSE 100× image tiles were collected from each specimen, with particular focus on the mid-cortex region of each bone tissue (transverse orientation). In some instances, the full cortical section was sampled, as reported in the BSE image maps generated (Figure 3.1). However, only select regions were analyzed, in light of the predominant focus of this study on the mid-cortex. Each BSE image was first processed to remove any crack features present. This was a necessary step for BV/TV calculations, although it should be noted that the crack (space) is replaced with "BV", which means that the BV/TV values obtained from specimens initially exhibiting cracks are slightly larger than actual. After the cracks were removed, each image was converted to a black and white binary scale by the thresholding command in ImageJ, which is available for free download from http://rsbweb.nih.gov/ij/. Once binary, it was possible to use other ImageJ processing commands to calculate the particle densities and circularities of interest (osteons, osteocyte lacunae). Thresholds for circularity were established, and structures not meeting these criteria were not included in the analysis. Alternatively, this process can be carried out by hand according to standard materials science techniques for determining particle densities, *etc.* The binary images also were used to generate BV/TV measurements, which assess the ratio of white (bone) to black (porosity) pixels in the image. Finally, lamellar thickness values were measured directly from the BSE tiles. The values are reported in Appendix F.

Again, the significance of this data set resides in the fact that it can be collected and not in the particular values reported here. Generally, these measurements are used for explorations of physiological parameters, such as growth rate. However, I believe that the capacity to collect these measurements, in light of the ultimate goal of this study, represents something even more significant: these features are measurable because they have been preserved in the fossil bone

specimens. Alone, as the highest orders of the bone tissue, their preservation suggests that, perhaps, the lower orders of the bone structural hierarchy also have been preserved. In this study, it was found that all fossil specimens demonstrated extensive nanocrystallinity and a bone mineral composition that was determined to be (minimally) altered in a predictable and identifiable manner. Additionally, TEM images presented ubiquitous nanocrystallinity, and SAXS demonstrated the preservation of collagen D-spacing values, indicating preserved order of the nanocrystallites. Hence, in order of the presentation of data in this study, it is of little surprise that the higher order features are preserved after the extensive preservation of the lower order structures was demonstrated. However, the true potential for this data lies in the reverse: specimens exhibiting extensive preservation of higher order structural features in bone likely also retain (to varying degrees not yet systematically explored) the lower order structural features. This notion also is supported by other SEM results, including the EDS analyses carried out on trabecular features in the highly in-filled *Pristichampsus* and *Tyrannosaurus* specimens.

In short, the preservation of higher order structural features in fossil bone specimens has been extensively demonstrated in the paleontological literatures. In fact, these features are frequently used to develop hypotheses regarding the physiology and phylogenetic relationships of extinct species. The preservation of these features suggests that lower order structural features also may be preserved in fossil specimens; and conversely, the documentation of extensive preservation of the lower order features in fossil bone tissues supports the notion that higher order structural levels are preserved.

However, it should be noted that these generalizations may break down at a certain scale. For example, most fossil bones exhibit some degree of morphological distortion. Even so, investigations carried out at the nano- and microscales have the potential to elucidate the cause of such distortion, because the presence of diagenetic alteration visible at the lower levels may indicate the post-mortem causality of morphological distortion (*versus* pathogenic, having occurred during the organism's lifetime). Hence, there is every reason to carry out hierarchical assessments of fossil tissue quality in any investigation, regardless of the structural level on which the investigation is explicitly focused. These features are key diagnostic criteria and cataloguing their presence and degree has the potential not only to inform individual studies but the larger concept of fossilization within the paleontological community. Additionally, many of these physiological features of interest have significant implications for studies on structure/property relationships in fossil bone, as discussed in the next section.

5.5. Structure/property relationships in fossil bone

While the goal of this study was not to directly assess the structure/property relationships in these fossil bone specimens, the goals do have a clear association with such studies, which are currently being carried out by several research groups across the globe. Further, the results of this study have the potential to better inform studies seeking to explore the structure/property relationships in fossil bone tissues.

Several investigators have used a combination of CT and FEA to explore the behavior of fossil bone tissues under mechanical loading events. Thus far, these analyses have ranged from bite forces to cranial impact loads. Of course, there are a variety of other studies with the potential to shed light on bone from a deep time perspective, such as the evolution of compact

bone tissue in the long bones of sauropods and other extinct species that underwent rapid gigantism events. From a materials engineering perspective, the ability to identify and target the critical structural features in these bone tissues has the potential to significantly inform the modern development of composite materials for similar structural applications.

All of these studies, however, as currently carried out, suffer from several limitations, which must be alleviated at least in part. Earlier, I mentioned some of these limitations, such as the assumption that the density variation observed in CT scans of fossil bone tissues is truly representative of the original bone tissue mineral density. In this case, the results of my work suggest this may be true for the bone mineral but that (1) the corresponding loss of collagen in fossil bone tissues has not been thoroughly explored and (2) fossil tissues are frequently invaded by foreign mineral species. In response to the first concern, a protocol for the (quantitative) identification of collagen in fossil bone tissues must be developed; then, this protocol should be applied to CT analyses of fossil tissues to further inform the final model. In response to the second concern, small samples of the fossil specimen should be removed and polished for electron microprobe WDS analysis. For example, the presence of a mineral such as $BaSO_4$, which has a significantly higher electron density than bioapatite, has the potential to drastically alter the density results of a CT scan, which relies on X-ray wavelengths. This must be accounted for, or at least acknowledged, in the modeling process. To date, it has not been. That said, overall, the results of my work (in combination with the results of other studies) do indicate that a significant fraction of the fossil bone tissue present in specimens of interest is likely to be minimally altered.

However, beyond such a condition, this study also was carried out to demonstrate the successful application of these readily available and comparatively simple forms of analysis for assessing the precise fossil specimen bone tissue quality. Hence, it also is my recommendation that future studies on structure/property relationships should present a hierarchical assessment of fossil tissue quality that attempts to develop an overview of the diagenetic conditions present in the specimen of interest. For example, SEM should be carried out to locate the possible consequences of bioerosion, which also can affect local tissue density values. Currently, this type of data is not reported.

Finally, the notion that nanoscale tissue is preserved in fossil bones is striking for several reasons. To begin with, it suggests that comparative analyses of fossil and best-guess (Extant Phylogenetic Bracketing, *etc.*) extant tissues can be carried out to identify extant tissues for mechanical testing, based on physical similarity; from here, the extant tissue properties can be applied to the fossil tissues. Through back-inference, FEA models can be developed that incorporate more distinctly relevant tissue mechanical properties (*e.g.*, some of the published studies on dinosaur jaw mechanics have been based on *Struthio* femur bone properties, which is arguably insufficient). This process can be carried out at any level of the structural hierarchy that is of particular interest, whether simulated tests of fibrillar performance, osteon performance, or larger-scale tissue sections (even whole bones or entire skeletons).

Hence, most significantly, the results of my study suggest that, because nanoscale bone tissue is extensively preserved in fossil specimens, it should first be characterized, then an extant tissue should be identified based on structural similarity. Once the extant tissue has been analyzed, its mechanical properties should be used to better inform the investigation on the fossil

specimen. The new concept here is the use of nanoscale (and possibly higher) structural similarity to identify analogous tissues, which has not been done to date. Accordingly, the results of my work, which demonstrate the extensive preservation of nanoscale structures as well as preliminary efforts toward developing characterization protocols, also support the notion that this is a conceivable and practical approach for future structure/property investigations of fossil bone tissues.

6. Conclusions and implications for future work

6.1. Conclusions of this study

The focus of this study was on the preservation and description of nanoscale structural (and chemical) changes in fossil bone tissues as a result of diagenesis. A suite of characterization techniques and specimen preparation protocols were invoked to explore the notion that fossil bone contains preserved structural hierarchy, particularly with respect to the fossil bioapatite (composition, morphology, size) and the nanoscale structure of the bone tissue (microfibrillar structure). In part, these features were selected as the study focus under the idea that demonstration of their preservation logically supports the notion that higher levels of the bone structure have been preserved in concert. However, there is significant information lacking in studies on both modern and fossil bone tissues with respect to nanoscale bone structure; hence, this investigation not only serves as the first systematic investigation into preservation of the lowest levels of fossil bone tissue structural hierarchy but also as an effort to re-focus the materials engineering, medical, and related communities on the notion that our concept of the nanoscale structure of bone remains incomplete.

That said, fossil bones represent tremendous potential for understanding bone from the deep time perspective; without the study of fossil bones, we simply can not truly understand why extant bone tissues possess the structure/property relationships that they do. The bones of all modern vertebrates are significantly more than structures and tissues optimized for specific mechanical loading requirements: these tissues are subject to the constraints of a multi-million-year evolutionary lineage. The evolutionary constraints on bone tissue development can not be ignored in the engineer's quest to understand the mechanical performance of bone toward therapeutic implant development or the design and development of materials through the biomimicry of bone, among others. While evolutionary adaptation often depicts structural tissue development as an optimization process, the picture is not so simple. Bone is not simply a structural tissue: bone plays an extensive and critical role in metabolic processes and the preservation of homeostasis. Additionally, bone is a living tissue; the billions of cells contained within an organism's skeleton place extensive metabolic demands on the organism. Hence, bone is not simply mechanically optimized but has evolved under highly specific evolutionary constraints, which range beyond mechanical adaptation to encompass metabolic dependencies and more. To date, this fact has been underappreciated in modern studies of bone tissue aimed at developing structurally optimized biomimicked materials for engineering applications. In short, beyond the concentrated focus of this study, which was simply to systematically explore the preservation of bioapatite and nanoscale features of interest in a set of carefully selected (and phylogenetically related) fossil bone compact tissues, the results discussed above have significantly grander implications.

I reiterate in brevity the major conclusions of this work, as presented in order within the preceding text:

- To fully characterize the mineral of fossil bone tissues, it is necessary to use a combination of a crystallographic scattering technique (XRD, electron diffraction) with an elemental analysis approach (ideally, WDS). Additionally, care should be taken to

analyze the same region of interest for each respective technique, to provide the most robust correlation of data. Further, in the ideal case, chemical techniques sensitive to electronic fine structure should be carried out, such as synchrotron XANES or TEM EELS, opening the possibility for the highest degrees of spatial correlation, spatial resolution, and energy resolution by coupling with μ-XRD and electron diffraction, respectively.

- The universal changes in fossil bone composition, as readily detected by WDS, include increased contents of fluoride (by a factor of 10^2-10^3) and iron as well as decreased magnesium fractions. The fluoride change represents an approximate 50% conversion of the hydroxyapatite parent structure to fluorapatite in a continuous solid solution; because the lattice parameters of these chemical species are nearly identical, however, this is a "structurally conservative" change in composition and does not necessarily distort the structure. These findings further support the results of others. However, this is the first time that additional attempts have been made to interpret these chemical changes in light of structural alteration, resulting in the conclusion that the typical class of chemical substitutions occurring in bioapatite as a result of diagenesis are structurally conservative and do not imply alteration of either the bioapatite nanoplate size/morphology or the nanoscale structure (microfibril) of the tissue.
- Changes in calcium contents alone are insufficient to assess the quality of preservation in fossil bone tissues against modern bone. Similarly, the standard Ca/P index ratio should not be used to classify fossil bone tissues, in part due to changes in other cation species within the fossil bioapatite. These changes are inherently complex, involving ions of several valence states, with alteration on the order of several at.%, which is not an insignificant degree of change.
- XRD investigations of bulk bone tissues may require hand-processing due to the high degree of internal orientation within the specimen tissue. Although powdering improves the XRD pattern quality, modern bones cannot be powdered without possible alteration of the bioapatite constituent. The use of alternative techniques that collect scans from several orientations and then extract peak data following spectral overlap may alleviate these problems in instances where bulk bone samples are preferred.
- The fossil specimens in this work are extensively apatite. Further, their composition s(based on WDS) provide a quantification of the chemical changes that occur as a result of diagenesis. For the first time ever, a focused definition of "fossil bioapatite" has been developed. With continued refinement, this definition can be applied as an approximate base line for investigations wishing to characterize the extent of diagenetic alteration of specific samples against typically altered specimens.
- Extensive nanocrystallinity is contained within fossil bone specimens. This finding, as presented here, marks the first time that the documentation of extensive nanocrystallinity has been unanimously declared, particularly in concert with other chemical indications suggesting minimal alteration.
- SAXS data suggest that the nanocrystalline fossil bioapatite acts as an inverse template for the collagen scaffold, preserving the original scaffold laid by the osteoblasts that

formed the type I collagen network (the osteoid). This is the first time that such data have been reported in ancient fossil bone tissues.

- A combination of TEM and SAXS can be used to both directly and indirectly image, respectively, the microfibrillar structure in fossil bone. Together, these techniques demonstrate the extensive preservation of the nanoscale structure of bone in these fossil specimens, which has significant implications for studies wishing to pursue the study of fossil bone tissue from the deep time perspective. This is the first time that the preservation of nanoscale structures in fossil bone tissue has been demonstrated.
- The preservation of lower orders of bone structure support the preservation of higher orders, and conversely. Features of physiological significance are highly preserved in fossil specimens in concert with the nanoscale constituents/structures of which they are composed. Similarly, standard image processing techniques can be used to extract full sets of data on physiological parameters of interest in fossil bone, not just modern bone.
- The strong preservation of nanoscale structure in fossil bone tissues suggests that it is possible to develop an enhanced protocol for computer-based (FEA) studies on structure/property relationships in fossil bone. These approaches should seek to develop a thorough description of the fossil tissue of interest, then should identify a modern tissue of analogous structure. That modern tissue should be tested for its mechanical properties, and the resulting properties should be back-inferred within the fossil tissue.

In summary, however, the overarching contributions and findings of this study can be given in a single sentence, phrased to support the original focus of my work: when applied in conjunction, incorporating the highest levels of energy and spatial resolution available today, electron microscopic and X-ray spectroscopic techniques can be used to identify explicit chemical changes in fossil bioapatite and to clearly demonstrate the extensive preservation of nanoscale structure in fossil bone tissues.

6.2. Implications for future work

Based on the findings presented above, I have developed a set of suggestions for future work in this area, which I detail below. Additionally, while some of these suggestions are targeted at work currently under pursuit by various researchers, others are examples of work that I would like to pursue as my career progresses beyond graduate school.

- A revised Ca/P index ratio that takes into account other metal cations, particularly those with different valences, should be developed for the continued study of fossil bioapatite. Based on the results of this work, the specific metal cations of interest include sodium and magnesium. Future work elucidating the location of enriched iron may indicate that iron species should be included in this index ratio, as well.
- The possibility that the presence of iron inhibits nanoplate coarsening should be investigated. Additionally, the precise nature of the chemical form of iron in the fossil bones should be identified, based on either TEM EELS or synchrotron XANES.
- Changes in the chemical composition of bioapatite should be further explored with a combination of high-energy-resolution and high-spatial-resolution techniques, which

have not been carried out to date. Ideally, thin sections should be used for these approaches because they offer the potential for spatial correlation with other features of significance (osteons, osteocyte lacunae, medullary canal, *etc*.) and the overall orientation/position of the bulk bone tissue.

- AFM studies should be added to the protocol presented here, to incorporate enhanced study of the macrofibrillar structure. Ideally, AFM studies also should investigate modern specimens for direct comparison and technique vetting, which has not been performed to date.
- Studies focused on the identification of surviving collagen in bulk bone tissue should be carried out. The techniques suggested for these studies include SAXS, FTIR techniques, and Raman spectroscopy. Low-dose TEM imaging also should be performed for direct visual imaging of any reported preserved collagen tissues. Likely, electron imaging studies will require the incorporation of staining protocols to enhance the electronic density of the tissues intended for investigation, for optimal imaging contrast.
- Systematic investigations of fossil and modern bone tissues, as presented in both fractured and thin section specimens, should be carried out with tomography to develop complete 3-D models of the nanoscale structure of bone. By incorporating phylogenetic explorations among related taxa, a more complete picture of bone tissue evolution will be developed, tracing development of the vertebrate skeleton through deep time.
- Dark-field analyses of microfibrillar structures also should explore the amorphous region surrounding the forward scattered beam, particularly with respect to identifying the core composition of some structures identified in TEM images.
- Future studies conducted in the area of structure/property analysis should carry out hierarchical analyses of the current condition of preservation in fossil bone specimens of interest.

It is my personal hope, of course, that not only will some of the resulting publications and presentations based on this work inspire the work of others but also that in the future I will be able to continue many of these investigations myself.

References

Abdalla, O. 1979. “Ossification and mineralization in the tendons of the chicken (*Gallus domesticus)*.” *Journal of Anatomy* **129**(2):351-359

Adams, JS, and CL Organ. 2005. “Histologic determination of ontogenetic patterns and processes in hadrosaurian ossified tendons.” *Journal of Vertebrate Paleontology* **25**(3):614-622

Aouacheria, A, C Cluzel, C Lethias, M Gouy, R Garrone, and J-Y Exposito. 2004. “Invertebrate Data Predict an Early Emergence of Vertebrate Fibrillar Collagen Clades and an Anti-incest Model.” *The Journal of Biological Chemistry* **279**(46):47711-47719

Asara, JM, MH Schweitzer, LM Freimark, M Phillips, and LC Cantley. 2007. “Protein Sequences from Mastodon and *Tyrannosaurus Rex* Revealed by Mass Spectrometry.” *Science* **316**:280-285

Ascenzi, A, P Baschieri, and A Benvenuti. 1994. “Torsional properties of single selected osteons.” *Journal of Biomechanics* **27**(7):875-884

Balla, VK, S Bodhak, S Bose, and A Bandyopadhyay. 2010. “Porous tantalum structures for bone implants: Fabrication, mechanical and in vitro biological properties.” *Acta Biomaterialia* **6**:3349-3359

Barth, HD, EA Zimmermann, E Schaible, SY Tang, T Alliston, and RO Ritchie. 2011. “Characterization of the effects of x-ray irradiation on the hierarchical structure and mechanical properties of human cortical bone.” *Biomaterials* **32**(34):8892-8904

Bernard, MP, JC Myers, M-L Chu, F Ramirez, EF Eikenberry, and DJ Prockop. 1983. “Structure of a cDNA for the Proα2 Chain of Human Type I Procollagen, Comparison with Chicken cDNA for Proα2(I) identifies Structurally Conserved Features of the Protein and the Gene.” *Biochemistry* **22**:1139-1145

Boivin, G. 2007. “The hydroxyapatite crystal: a closer look.” *Medicographia* **29**(2):126-132

Bonar, LC, AH Roufosse, WK Sabine, MC Grynpas, and MJ Glimcher. 1983. “X-ray Diffraction Studies of the Crystallinity of Bone Mineral in Newly Synthesizes and Density Fractionated Bone.” *Calcified Tissue International* **35**:202-209

Boot-Handford, RP, and DS Tuckwell. 2003. “Fibrillar collagen: the key to vertebrate evolution? A tale of molecular incest.” *BioEssays* **25**:142-151

Boskey, A. 2003. “Bone mineral crystal size.” *Osteoporosis International* **14**(Suppl 5):S16-S21

Bozec, L, G vander Heijden, and M Horton. 2007. “Collagen Fibrils: Nanoscale Ropes.” *Biophysical Journal* **92**:70-75

Brown, WE. 1962. “Octacalcium Phosphate and Hydroxyapatite: Crystal Structure of Octacalcium Phosphate.” *Nature* **196**:1048-1050

Brown, WE, N Eidelman, and B Tomazic. 1987. “Octacalcium phosphate as a precursor in biomineral formation.” *Advanced Dental Research* **1**(2):306-313

Burger, C, H-W Zhou, H Wang, I Sics, BJ Hsiao, B Chu, L Graham, and MJ Glimcher. 2008. "Lateral Packing of Mineral Crystals in Bone Collagen Fibrils." *Biophysical Journal* **95**:1985-1992

Cerda, IA, and JB Desojo. 2010. "Dermal armour histology of aetosaurs (Archosauria: Pseudosuchia), from the Upper Triassic of Argentina and Brazil." *Lethaia* **44**:417-428

Cerda, IA, and JE Powell. 2010. "Dermal armor histology of *Saltasaurus loricatus*, an Upper Cretaceous sauropod dinosaur from northwest Argentina." *Acta Palaeontologica Polonica* **55**(3): 389-398

Chavassieux, P, E Seeman, and PD Delmas. 2007. "Insights into Material and Structural Basis of Bone Fragility from Diseases Associated with Fractures: How Determinants of the Biomechanical Properties of Bone are Compromised by Disease." *Endocrine Reviews* **23**(2): 151-164

Cheah, KSE. 1985. "Review article: Collagen genes and inherited connective tissue disease." *Biochemical Journal* **229**:287-303

Chu, M-L, W de Wet, M Bernard, J-F Ding, M Morabito, J Myers, C Williams, and F Ramirez. 1984. "Human proα1(I) collagen gene structure reveals evolutionary conservation of a pattern of introns and exons." *Nature* **310**:337-340

Cohen, L, M Dean, A Shipov, A Atkins, E Monsonego-Ornan, and R Shahar. 2012. "Comparison of structural, architectural and mechanical aspects of cellular and acellular bone in two teleost fish." *The Journal of Experimental Biology* **215**:1983-1993

Clemente-Carvalho, RBG, MM Antoniazzi, C Jared, CFB Haddad, ACR Alves, HS Rocha, GR Pereira, DF Oliveira, RT Lopes, and SF dos Reis. 2009. "Hyperossification in miniaturized toadlets of the genus *Brachysephalus* (Amphibia: Anura: Brachycephalidae): Microscopic structure and macroscopic patterns of variation." *Journal of Morphology* doi: 10.1002/jmor. 10755

Cui, F-Z, Y Li, and J Ge. 2007. "Self-assembly of mineralized collagen composites." *Materials Science and Engineering R* **57**:1-27

Currey, JD. 2002. "Bone: Structure and Mechanics." Princeton University Press.

Currey, JD. 1999. "The design of mineralised hard tissues for their mechanical functions." *The Journal of Experimental Biology* **202**:3285-3294

Currey, JD. 1969. "The relationship between the stiffness and the mineral content of bone." *J. Biomechanics* **2**:477-480

Danilchenko, SN, OG Kukharenko, C Moseke, IY Protsenko, LF Sukhodub, and B Sulkio-Cleff. 2002. "Determination of Bone Mineral Crystallite Size and Lattice Strain from Diffraction Line Broadening." *Crystal Research Technology* **37**(11):1234-1240

De Margerie, E, S Sanchez, J Cubo, and J Castanet. 2005. "Torsional Resistance as a Principal Component of the Structural Design of Long Bones: Comparative Multivariate Evidence in Birds." *The Anatomical Record Part A* **282A**:49-66

De Santis, R, L Ambrosio, F Mollica, P Netti, and L Nicolais. 2007. “Mechanical Properties of Mineralized Connective Tissues.” Modeling of Biological Materials: 211-261

Deymier-Black, AC, F Yuan, A Singhal, JD Almer, LC Brinson, and DC Dunand. 2012. “Evolution of load transfer between hydroxyapatite and collagen during creep deformation of bone.” *Acta Biomaterialia* **8**:253-261

Deymier-Black, AC, JD Almer, SR Stock, DR Haeffner, and DC Dunand. 2009. “Synchrotron X-ray diffraction study of load partitioning during elastic deformation of bovine dentin.” *Acta Biomaterialia* **6**:2172-2180

Elorza, J, H Astibia, X Murelaga, and X Pereda-Suberbiola. 1999. “Francolite as a diagenetic mineral in dinosaur and other Upper Cretaceous reptile bones (Laño, Iberian Peninsula): microstructural, petrological and geochemical features.” *Cretaceous Research* **20**:169-187

Exposito, J-Y, M D’alessio, M Solursh, and F Ramirez. 1992 “Sea Urchin Collagen Evolutionarily Homologous to Vertebrate Pro-α2(I) Collagen.” *The Journal of Biological Chemistry* **267**(22):15559-15562

Fratzl, P. 2007. “Biomimetic materials research: what can we really learn from nature’s structural materials?” *Journal of the Royal Society Interface* **4**:637-642

Fratzl, P, HS Gupta, EP Paschalis, and P Roschger. 2004. “Structure and mechanical quality of the collagen-mineral nano-composite in bone.” *Journal of Materials Chemistry* **14**:2115-2123

Fernández-Morán, H, and A Engström. 1956. “Electron microscopy and X-ray diffraction of bone.” *Biochimica et Biophysica Acta* **23**:260-264

Gao, H, B Ji, IL Jager, E Arzt, and P Fratzl. 2003. “Materials become insensitive to flaws at nanoscale: Lessons from nature.” *PNAS* **100**(10):5597-5600

Goodwin, MB, and JR Horner. 2004. “Cranial histology of pachycephalosaurs (Ornithischia: Marginocephalia) reveals transitory structures inconsistent with head-butting behavior.” *Paleobiology* **30**(2):253-267

Goodwin, MB, PG Grant, G Bench, and PA Holroyd. 2007. “Elemental composition and diagenetic alteration of dinosaur bone: Distinguishing microscale spatial and compositional heterogeneity using PIXE.” *Palaeogeography, Palaeoclimatology, Palaeoecology* **253**:458-476

Haines, R. W. and A. Mohuiddin. 1968. Metaplastic bone. *Journal of Anatomy* **103**(3):527-538

Hassenkam, T, GE Fantner, JA Cutroni, JC Weaver, DE Morse, and PK Hansma. 2004. “High-resolution AFM imaging of intact and fractured trabecular bone.” *Bone* **35**:4-10

Hayashi, S, K Carpenter, M Watabe, and LA McWhinney. 2012. “Ontogenetic histology of *Stegosaurus* plates and spikes.” *Palaeontology* **55**(1):145-161

Horner, JR, A De Ricqlès, and K Padian. 2000. “Long Bone Histology of the Hadrosaurid Dinosaur Maiasaura peeblesorum: Growth Dynamics and Physiology Based on an Ontogenetic Series of Skeletal Elements.” *Journal of Vertebrate Paleontology* **20**(1):115-129

Horner, JR, and E-T Lamm. 2011. "Ontogeny of parietal frill of Triceratops: A preliminary histological analysis." *Comptes Rendus Palevol* **10**:439-452

Horner, JR, K Padian, and A de Ricqlès. 2001. "Comparative osteohistology of some embryonic and perinatal archosaurs: developmental and behavioral implications for dinosaurs." *BioOne* **27**(1):39-58

Horner, JR, and MB Goodwin. 2009. "Extreme cranial ontogeny in the Upper Cretaceous dinosaur *Pachycephalosaurus*." *PLoS One* **4**(10): e7626. doi:10.1371journal.pone.0007626

Horner, JR, and MB Goodwin. 2008. "Ontogeny of cranial epi-ossifications in *Triceratops*." *Journal of Vertebrate Paleontology* **28**(1):134-144

Horner, JR, and MB Goodwin. 2006. "Major cranial changes during *Triceratops* ontogeny." *Proceedings of the Royal Society B* **273**:2757-2761

Hubert, JF, PT Panish, DJ Chure, and KS Prostak. 1996. "Chemistry, microstructure, petrology, and diagenetic model of Jurassic dinosaur bones, Dinosaur National Monument, Utah." *Journal of Sedimentary Research* **66**(3):531-547

Hübner, TR. 2012. "Bone Histology in *Dysalotosaurus lettowvorbecki* (Ornithischia: Iguanodontia) - Variation, Growth, and Implications." *PLoS ONE* **7**(1):e29958

Hughes, JM, M Cameron, and KD Crowley. 1989. "Structural variations in natural F, OH, and Cl apatites." *American Mineralogist* **74**:870-876

Jans, MME. 2008. "Microbial bioerosion of bone - a review." Current Developments in Bioerosion Springer-Verlag Berlin Heidelberg

Jans, MME, CM Nielsen-Marsh, CI Smith, MJ Collins, and H Kars. 2004. "Characterisation of microbial attack on archaeological bone." *Journal of Archaeological Science* **31**:87-95

Kay, MI, RA Young, and AS Posner. 1964. "Crystal structure of hydroxyapatite." *Nature* **204**:1050-1052

Kaye, TG, G Gaugler, and Z Sawlowicz. 2008. "Dinosaurian Soft Tissues Interpreted as Bacterial Biofilm." *PLoS ONE* **3**(7):e2808

Klein, N, and M Sander. 2008. "Ontogenetic stages in the long bone histology of sauropod dinosaurs." *Paleobiology* **34**(2):247-263

Kulin, RM, P-Y Chen, F Jiang, J McKittrick, and KS Vecchio. 2010. "Dynamic fracture resilience of elk antler: Biomimetic inspiration for improved crashworthiness." *JOM* **62**(1):41-46

Landis, WJ, MJ Song, A Leith, L McEwan, and BJ McEwan. 1993. "Mineral and Organic Matrix Interaction in Normally Calcifying Tendon Visualized in Three Dimensions by High-Voltage Electron Microscopic Tomography and Graphic Image Reconstruction." *Journal of Structural Biology* **110**:39-54

Launey, ME, E Munch, DH Alsem, HB Barth, E Saiz, AP Tomsia, and RO Ritchie. 2009. "Designing highly toughened hybrid composites through nature-inspired hierarchical complexity. *Acta Materialia* **57**:2919-2932

Launey, ME, MJ Buehler, and RO Ritchie. 2010. “On the Mechanistic Origins of Toughness in Bone.” *Annual Review of Materials Research* **40**:25-53

Liebschner, MAK, and TS Keller. 2005. “Hydraulic Strengthening Affects the Stiffness and Strength of Cortical Bone.” *Annals of Biomedical Engineering* **33**(1):26-38

Lonardelli, I, H-R Wenk, L Lutterotti, and M Goodwin. 2005. “Texture analysis from synchrotron diffraction images with the Rietveld method: dinosaur tendon and salmon scale.” *Journal of Synchrotron Radiation* **12**:354-360

Main, RP, A de Ricqlès, JR Horner, and K Padian. 2005. “The evolution and function of thyreophoran dinosaur scutes and implications for plate function in stegosaurs.” *Paleobiology* **31**(2):291-314

Marini, JC, A Forlina, WA Cabral, AM Barnes, JD San Antonio, S Milgrom, JC Hyland, J Körkkö, DJ Prockop, A De Paepe, P Coucke, S Symoens, FH Glorieux, PJ Roughley, AM Lund, K Kuurila-Svahn, H Hartikka, DH Cohn, D Krakow, M Mottes, U Schrwarze, D Chen, K Yang, C Kuslich, J Troendle, R Dalgleish, and PH Byers. 2007. “Consortium for Osteogenesis Imperfecta Mutations in the Helical Domain of Type I Collagen: Regions Rich in Lethal Mutations Align With Collagen Binding Sites for Integrins and Proteoglycans.” *Human Mutation* **28**(3):209-221

Martiniaková, M, B Grosskopf, R Omelka, M Vondráková, and M Bauerová. 2006. “Differences Among Species in Compact Bone Tissue Microstructure of Mammalian Skeleton: Use of a Discriminant Function Analysis for Species Identification.” *Journal of Forensic Science* **51**(6): 1235-1239

Moodie, RL. 1928. “The histological nature of ossified tendons found in dinosaurs.” *American Museum Novitates* **311**

Mori, R, T Kodaka, T Sano, N Yamagishi, M Asari, and Y Naito. 2003. “Comparative Histology of the Laminar Bone between Young Calves and Foals.” *Cells Tissues Organs* **175**:43-50

Nguyen, H, DAF Morgan, and MR Forwood. 2007. “Sterilization of allograft bone: effects of gamma irradiation on allograft biology and biomechanics.” *Cell Tissue Banking* **8**:93-105

Nylen, MU, ED Eanes, and K-A Omnell. 1963. “Crystal growth in rat enamel.” *The Journal of Cell Biology* **18**:109-123

Nyman, JS, M Reyes, and X Wang. 2005. “Effect of ultrastructural changes on the toughness of bone.” *Micron* **36**:566-582

Organ, CL, and J Adams. 2005. “The histology of ossified tendon in dinosaurs.” *Journal of Vertebrate Paleontology* **25**(3):602-613

Osborn, JF, and H Newesely. 1980. “The material science of calcium phosphate ceramics.” *Biomaterials* **1**:108-111

Paschalis, EP, A Ilg, K Verdelis, M Yamauchi, R Mendelsohn, and AL Boskey. 1998. "Spectroscopy determination of collagen cross-links at the ultrastructural level and its application to osteoporosis." *Bone* **23**:S342

Pesenti, H, M Leoni, A Motta, and P Scardi. 2010. "Fossils as Candidate Material for Orthopedic Applications." *Journal of Applied Biomaterials (OnlineFirst)* **00**:doi:10.1177/0885328209358630

Posner, AS, and F Betts. 1975. "Synthetic Amorphous Calcium Phosphate and Its Relation to Bone Mineral Structure." *Accounts of Chemical Research* **8**:273-281

Qiu, S, DS Rao, DP Fyhrie, S Palnitkar, and AM Parfitt. 2005. "The morphological association between microcracks and osteocyte lacunae in human cortical bone. *Bone* **37**:10-15

Rayfield, EJ. 2007. "Finite Element Analysis and Understanding the Biomechanics and Evolution of Living and Fossil Organisms." *Annual Review of Earth and Planetary Sciences* **35**:541-576

Rayfield, EJ. 2005a. "Using finite-element analysis to investigate suture morphology: A case study using large carnivorous dinosaurs." *The Anatomical Record* **283A**(2):349-365

Rayfield, EJ. 2005b. "Aspects of comparative cranial mechanics in the theropod dinosaurs *Coelophysis*, *Allosaurus* and *Tyrannosaurus*." *Zoological Journal of the Linnean Society* **144**(3): 309-316

Rayfield, EJ. 2004. Cranial mechanics and feeding in *Tyrannosaurus rex*." *Proceedings of the Royal Society of London B* **271**:1451-1459

Rayfield, EJ, DB Norman, CC Horner, JR Horner, PM Smith, JJ Thomason, and P Upchurch. 2001. "Cranial design and function in a large theropod dinosaur." *Nature* **409**:1033-1037

Reilly, GC. 2000. "Observations of microdamage around osteocyte lacunae in bone." *Journal of Biomechanics* **33**:1131-1134

Rey, C, C Combes, C Drouet, and MJ Glimcher. 2009. "Bone mineral: update on chemical composition and structure." *Osteoporosis International* **20**:1013-1021

Saber-Samandari, S, and KA Gross. 2009. "Micromechanical properties of single crystal hydroxyapatite by nanoindentation." *Acta Biomaterialia* **5**:2206-2212

Saka, H, D Goto, and W-J Moon. 2008. "Dislocations in plastically deformed apatite." *Journal of Materials Science* **43**:3234-3239

Scheyer, TM. 2009. "Conserved bone microstructure in the shells of long-necked and short-necked chelid turtles (Testudinata,Pleurodira)." *Fossil Record* **12**(1):47-57

Scheyer, TM, and JB Desojo. 2011. "Palaeohistology and external microanatomy of Rauisuchian osteoderms (Archosauria: pseudosuchia)." *Palaeontology* **54**(6):1289-1302

Schweitzer, MH, JL Wittmeyer, and JR Horner. 2007b. "Soft tissue and cellular preservation in vertebrate skeletal elements from the Cretaceous to the present." *Proc. R. Soc. B.* **274**:183-197

Schweitzer, MH, JL Wittmeyer, JR Horner, and JK Toporski. 2005a. “Soft-Tissue Vessels and Cellular Preservation in *Tyrannosaurus rex*.” *Science* **307**:1952-1955

Schweitzer, MH, L Chiappe, AC Garrido, JM Lowenstein, and SH Pincus. 2005b. “Molecular preservation in Late Cretaceous sauropod dinosaur eggshells.” *Proceedings of the Royal Society B* **272**:775-784

Schweitzer, MH, W Zheng, CL Organ, R Avci, Z Suo, LM Freimark, VS Lebleu, MB Duncan, MG Vander Heiden, JM Neveu, WS Lame, JS Cottrell, JR Horner, LC Cantley, R Kalluri, and JM Asara. 2009. “Biomolecular Characterization and Protein Sequences of the Campanian Hadrosaur *B. canadensis*.” *Science* **324**:626-631

Schweitzer, MH, Z Suo, R Avci, JM Asara, MA Allen, FT Arce, and JR Horner. 2007a. “Analyses of Soft Tissue from *Tyrannosaurus rex* Suggest the Presence of Protein.” *Science* **316**:277-280

Simons, ELR, and PM O’Connor. 2012. “Bone Laminarity in the Avian Forelimb Skeleton and Its Relationship to Flight Mode: Testing Functional Interpretations.” *The Anatomical Record* **295**:386-396

Snively, E, and A Cox. 2008. “Structural mechanics of *Pachycephalsaur* crania permitted head-butting behavior.” *Palaeontologia Electronica* **11**(1):11.1.3A

Su, X, K Sun, FZ Cui, and WJ Landis. 2003. “Organization of apatite crystals in human woven bone.” *Bone* **32**:150-162

Suhonen, H, M Fernandez, R Serimaa, and P Suortti. 2005. “Simulation of small-angle x-ray scattering from collagen fibrils and comparison with experimental patterns.” *Physics in Medicine and Biology* **50**:5401-16

Sutton, MD. 2008. “Tomographic techniques for the study of exceptionally preserved fossils.” *Proceedings of the Royal Society B* **275**:1587-1593

Suvorova EI, PP Petrenko, and PA Buffat. 2007. “Scanning and Transmission Electron Microscopy for Evaluation of Order/Disorder in Bone Structure.” *Scanning* **29**(4):162-170

Thomas, KA, JF Kay, SD Cook, and M Jarcho. 1987. “The effect of surface macrotexture and hydroxylapatite coating on the mechanical strengths and histologic profiles of titanium implant materials.” *Journal of Biomedical Research* **21**:1395-1414

Traub, W, T Arad, and S Weiner. 1989. “Three-dimensional ordered distribution of crystals in turkey tendon collagen fibers.” *PNAS* **86**:9822-9826

Trueman, CNG, AK Behrensmeyer, N Tuross, and S Weiner. 2004. “Mineralogical and compositional changes in bones exposed in soil surfaces in Amboseli National Park, Kenya: diagenetic mechanisms and the role of sediment pore fluids.” *Journal of Archaeological Science* **31**:721-739

Tumarkin-Deratzian, AR. 2007. “Fibrolamellar Bone in Wild Adult *Alligator Mississippiensis*.” *Journal of Herpetology* **41**(2):341-345

Turner-Walker, G. 2008. “The Chemical and Microbial Degradation of Bones and Teeth.” Advances in Human Palaeopathology Eds. R Pinhasi and S Mays. John Wiley & Sons, Ltd.

Uzel, SGM, and MJ Buehler. 2011. “Molecular structure, mechanical behavior and failure mechanism of the C-terminal cross-link domain in type I collagen.” *Journal of the Mechanical Behavior of Biomedical Materials* **4**:152-161

Van Noort, R. 1987. “Titanium: The implant material of today.” *Journal of Materials Science* **22**:3801-3811

Weiner, S, W Traub, and HD Wagner. 1999. “Lamellar Bone: Structure-Function Relations.” *Journal of Structural Biology* **126**:241-255

Witmer, LM. 1995. “Functional morphology of vertebrate paleontology.” Ed. Jeff Thomason. Cambridge University Press.

Witte, F, V Kaese, H Haferkamp, E Switzer, A Meyer-Lindenberg, CJ Wirth, and H Windhagen. 2005. “In vivo corrosion of four magnesium alloys and the associated bone response.” *Biomaterials* **26**:3357-3563

Witzmann, F, and R Soler-Gijón. 2010. “The bone histology of osteoderms in temnospondyl amphibians and in the chronosuchian *Bystrowiella.*” *Acta Zoologica* **91**:96-114

Wolf, D, DC Kalthoff, and PM Sander. 2012. “Osteoderm histology of the Pampatheriidae (Cingulata, Xenartha, Mammalia): Implications for systematics, osteoderm growth, and biomechanical adaptations.” *Journal of Morphology* **273**:388-404

Yashima, M, A Sakai, T Kamiyama, and A Hoshikawa. 2003. “Crystal structure analysis of *β*-tricalcium phosphate $Ca_3(PO_4)_2$ by neutron powder diffraction.” *Journal of solid State Chemistry* **175**:272-277

Zamiri, A, and S De. 2011. “Mechanical properties of hydroxyapatite single crystals from nanoindentation data.” *Journal of the Biomechanical Behavior of Biomedical Materials* **4**:146-152

Appendix A. Collagen (COL1A1) sequence data and alignments.

This section is laid out in the following order. In section A.1., the FASTA sequences for the investigated species are given. In section A.2., the pairwise alignment % identity scores are given based on the automatically generated HomoloGene results. In section A.3., the full set of multiple sequence trees is provided. In section A.4., several partial sequence alignments are given to illustrate the preservation of the characteristic repeat of the amino acid residues in type I collagen.

A.1. The FASTA sequences

The COL1A1 sequences are given for the species discussed in the text. It should be noted that several sequences are precursor COL1A1 sequences; in such cases, the sequence is further denoted as "*Precursor" for clarity. Similarly, any predicted sequence is denoted "*Predicted." The following format reflects the FASTA format used by NCBI. The sequences are identified by the following format: *Species name* (Common name, GenBank accession number, # of amino acids in sequence).

Homo sapiens (Human, AAH36531.1, 1464 aa)

```
>gi|22328092|gb|AAH36531.1| Collagen, type I, alpha 1 [Homo sapiens]
MFSFVDLRLLLLLAATALLTHGQEEGQVEGQDEDIPPITCVQNGLRYHDRDVWKPEPCRICVCDNGKVLCDDVICDETKNCPGAEVPEGECCPVCPD
GSESPTDQETTGVEGPKGDTGPRGPRGPAGPPGRDGIPGQPGLPGPPGPPGPPGPPGLGGNFAPQLSYGYDEKSTGGISVPGPMGPSGPRGLPGPPG
APGPQGFQGPPGEPGEPGASGPMGPRGPPGPPGKNGDDGEAGKPGRPGERGPPGPQGARGLPGTAGLPGMKGHRGFSGLDGAKGDAGPAGPKGEPGS
PGENGAPGQMGPRGLPGERGRPGAPGPAGARGNDGATGAAGPPGPTGPAGPPGFPGAVGAKGEAGPQGPRGSEGPQGVRGEPGPPGPAGAAGPAGNP
GADGQPGAKGANGAPGIAGAPGFPGARGPSGPQGPGGPPGPKGNSGEPGAPGSKGDTGAKGEPGPVGVQGPPGPAGEEGKRGARGEPGPTGLPGPPG
ERGGPGSRGFPGADGVAGPKGPAGERGSPGPAGPKGSPGEAGRPGEAGLPGAKGLTGSPGSPGPDGKTGPPGPAGQDGRPGPPGPPGARGQAGVMGF
PGPKGAAGEPGKAGERGVPGPPGAVGPAGKDGEAGAQGPPGPAGPAGERGEQGPAGSPGFQGLPGPAGPPGEAGKPGEQGVPGDLGAPGPSGARGER
GFPGERGVQGPPGPAGPRGANGAPGNDGAKGDAGAPGAPGSQGAPGLQGMPGERGAAGLPGPKGDRGDAGPKGADGSPGKDGVRGLTGPIGPPGPAG
APGDKGESGPSGPAGPTGARGAPGDRGEPGPPGPAGFAGPPGADGQPGAKGEPGDAGAKGDAGPPGPAGPAGPPGPIGNVGAPGAKGARGSAGPPGA
TGFPGAAGRVGPPGPSGNAGPPGPPGPAGKEGGKGPRGETGPAGRPGEVGPPGPPGPAGEKGSPGADGPAGAPGTPGPQGIAGQRGVVGLPGQRGER
GFPGLPGPSGEPGKQGPSGASGERGPPGPMGPPGLAGPPGESGREGAPGAEGSPGRDGSPGAKGDRGETGPAGPPGAPGAPGAPGPVGPAGKSGDRG
ETGPAGPAGPVGPVGARGPAGPQGPRGDKGETGEQGDRGIKGHRGFSGLQGPPGPPGSPGEQGPSGASGPAGPRGPPGSAGAPGKDGLNGLPGPIGP
PGPRGRTGDAGPVGPPGPPGPPGPPGPPSAGFDFSFLPQPPQEKAHDGGRYYRADDANVVRDRDLEVDTTLKSLSQQIENIRSPEGSRKNPARTCRD
LKMCHSDWKSGEYWIDPNQGCNLDAIKVFCNMETGETCVYPTQPSVAQKNWYISKNPKDKRHVWFGESMTDGFQFEYGGQGSDPADVAIQLTFLRLM
STEASQNITYHCKNSVAYMDQQTGNLKKALLLQGSNEIEIRAEGNSRFTYSVTVDGCTSHTGAWGKTVIEYKTTKTSRLRIIDVAPLDVGAPDQEFG
FDVGHVCFL
```

*Pan troglodytes** (Chimpanzee, XP_001169409.1, 1464 aa)

*Predicted

```
>gi|114669268|ref|XP_001169409.1| PREDICTED: collagen alpha-1(I) chain isoform 9 [Pan
troglodytes]
MFSFVDLRLLLLLAATALLTHGQEEGQVEGQDEDIPPITCVQNGLRYHDRDVWKPEPCRICVCDNGKVLCDDVICDETKNCPGAEVPEGECCPVCPD
GSESPTDQETTGVEGPKGDTGPRGPRGPAGPPGRDGIPGQPGLPGPPGPPGPPGPPGLGGNFAPQLSYGYDEKSTGGISVPGPMGPSGPRGLPGPPG
APGPQGFQGPPGEPGEPGASGPMGPRGPPGPPGKNGDDGEAGKPGRPGERGPPGPQGARGLPGTAGLPGMKGHRGFSGLDGAKGDAGPAGPKGEPGS
PGENGAPGQMGPRGLPGERGRPGAPGPAGARGNDGATGAAGPPGPTGPAGPPGFPGAVGAKGEAGPQGPRGSEGPQGVRGEPGPPGPAGAAGPAGNP
GADGQPGAKGANGAPGIAGAPGFPGARGPSGPQGPGGPPGPKGNSGEPGAPGSKGDTGAKGEPGPVGVQGPPGPAGEEGKRGARGEPGPTGLPGPPG
ERGGPGSRGFPGADGVAGPKGPAGERGSPGPAGPKGSPGEAGRPGEAGLPGAKGLTGSPGSPGPDGKTGPPGPAGQDGRPGPPGPPGARGQAGVMGF
PGPKGAAGEPGKAGERGVPGPPGAVGPAGKDGEAGAQGPPGPAGPAGERGEQGPAGSPGFQGLPGPAGPPGEAGKPGEQGVPGDLGAPGPSGARGER
GFPGERGVQGPPGPAGPRGANGAPGNDGAKGDAGAPGAPGSQGAPGLQGMPGERGAAGLPGPKGDRGDAGPKGADGSPGKDGVRGLTGPIGPPGPAG
APGDKGESGPSGPAGPTGARGAPGDRGEPGPPGPAGFAGPPGADGQPGAKGEPGDAGAKGDAGPPGPAGPAGPPGPIGNVGAPGAKGARGSAGPPGA
TGFPGAAGRVGPPGPSGNAGPPGPPGPAGKEGGKGPRGETGPAGRPGEVGPPGPPGPAGEKGSPGADGPAGAPGTPGPQGIAGQRGVVGLPGQRGER
GFPGLPGPSGEPGKQGPSGASGERGPPGPMGPPGLAGPPGESGREGAPGAEGSPGRDGSPGAKGDRGETGPAGPPGAPGAPGAPGPVGPAGKSGDRG
ETGPAGPAGPVGPVGARGPAGPQGPRGDKGETGEQGDRGIKGHRGFSGLQGPPGPPGSPGEQGPSGASGPAGPRGPPGSAGAPGKDGLNGLPGPIGP
PGPRGRTGDAGPVGPPGPPGPPGPPSAGFDFSFLPQPPQEKAHDGGRYYRADDANVVRDRDLEVDTTLKSLSQQIENIRSPEGSRKNPARTCRD
LKMCHSDWKSGEYWIDPNQGCNLDAIKVFCNMETGETCVYPTQPSVAQKNWYISKNPKDKRHVWFGESMTDGFQFEYGGQGSDPADVAIQLTFLRLM
STEASQNITYHCKNSVAYMDQQTGNLKKALLLQGSNEIEIRAEGNSRFTYSVTVDGCTSHTGAWGKTVIEYKTTKTSRLPIIDVAPLDVGAPDQEFG
FDVGPVCFL
```

*Macaca mulatta** (Rhesus macaque, AFH31111.1, 1464 aa)

*Predicted, precursor

>gi|383415795|gb|AFH31111.1| collagen alpha-1(I) chain preproprotein [Macaca mulatta]
MFSFVDLRLLLLLAATALLTHGQEEGQVEGQDEDIPPITCVQNGLRYHDRDVWKPEPCRICVCDNGKVLCDDVICDETKNCPGAEVPEGECCPVCPD
GSESPTDQETTGVEGPKGDTGPRGPRGPAGPPGRDGIPGQPGLPGPPGPPGPPGPPGLGGNFAPQLSYGYDEKSTGGISVPGPMGPSGPRGLPGPPG
APGPQGFQGPPGEPGEPGASGPMGPRGPPGPPGKNGDDGEAGKPGRPGERGPPGPQGARGLPGTAGLPGMKGHRGFSGLDGAKGDAGPAGPKGEPGS
PGENGAPGQMGPRGLPGERGRPGAPGPAGARGNDGATGAAGPPGPTGPAGPPGFPGAVGAKGEAGPQGPRGSEGPQGVRGEPGPPGPAGAAGPAGNP
GADGQPGAKGANGAPGIAGAPGFPGARGPSGPQGPGGPPGPKGNSGEPGAPGSKGDTGAKGEPGPVGVQGPPGPAGEEGKRGARGEPGPTGLPGPPG
ERGGPGSRGFPGADGVAGPKGPAGERGSPGPAGPKGSPGEAGRPGEAGLPGAKGLTGSPGSPGPDGKTGPPGPAGQDGRPGPPGPPGARGQAGVMGF
PGPKGAAGEPGKAGERGVPGPPGAVGPAGKDGEAGAQGPPGPAGPAGERGEQGPAGSPGFQGLPGPAGPPGEAGKPGEQGVPGDLGAPGPSGARGER
GFPGERGVQGPPGPAGPRGANGAPGNDGAKGDAGPAGPAGPSGQAGPLQGMPGERGAAGLPGPKGDRGDAGPKGADGSPGKDGVRGLTGPIGPPGPAG
APGDKGETGPSGPAGPTGARGAPGDRGEPGPPGPAGFAGPPGADGQPGAKGEPGDAGAKGDAGPPGPAGPAGPPGPIGNVGAPGPKGARGSAGPPGA
TGFPGAAGRVGPPGPSGNAGPPGPPGPAGKEGGKGPRGETGPAGRPGEVGPPGPPGPAGEKGSPGADGPAGAPGTPGPQGIAGQRGVVGLPGQRGER
GFPGLPGPSGEPGKQGPSGASGERGPPGPMGPPGLAGPPGESGREGAPGAEGSPGRDGSPGPKGDRGETGPAGPPGAPGAPGAPGPVGPAGKSGDRG
ETGPAGPAGPVGPVGARGPAGPQGPRGDKGETGEQGDRGIKGHRGFSGLQGPPGPPGSPGEQGPSGASGPAGPRGPPGSAGTPGKDGLNGLPGPIGP
PGPRGRTGDAGPVGPPGPPGPPGPPGPPSGGFDFSFLPQPPQEKAHDGGRYYRADDANVVRDRDLEVDTTLKSLSQQIENIRSPEGSRKNPARTCRD
LKMCHSDWKSGEYWIDPNQGCNLDAIKVFCNMETGETCVYPTQPSVAQKNWYISKNPKDKRHVWFGESMTDGFQFEYGGEGSDPADVAIQLTFLRLM
STEASQNITYHCKNSVAYMDQQTGNLKKALLLQGSNEIEIRAEGNSRFTYSVTVDGCTSHTGAWGKTVIEYKTTKTSRLPIIDVAPLDVGAPDQEFG
FDVGPVCFL

Bos taurus (Cow, AAI05185.1, 1463 aa)

>gi|75775290|gb|AAI05185.1| Collagen, type I, alpha 1 [Bos taurus]
MFSFVDLRLLLLLAATALLTHGQEEGQEEGQEEDIPPVTCVQNGLRYHDRDVWKPVPCQICVCDNGNVLCDDVICDELKDCPNAKVPTDECCPVCPE
GQESPTDQETTGVEGPKGDTGPRGPRGPAGPPGRDGIPGQPGLPGPPGPPGPPGPPGLGGNFAPQLSYGYDEKSTGISVPGPMGPSGPRGLPGPPGA
PGPQGFQGPPGEPGEPGASGPMGPRGPPGPPGKNGDDGEAGKPGRPGERGPPGPQGARGLPGTAGLPGMKGHRGFSGLDGAKGDAGPAGPKGEPGSP
GENGAPGQMGPRGLPGERGRPGAPGPAGARGNDGATGAAGPPGPTGPAGPPGFPGAVGAKGEGGPQGPRGSEGPQGVRGEPGPPGPAGAAGPAGNPG
ADGQPGAKGANGAPGIAGAPGFPGARGPSGPQGPSGPPGPKGNSGEPGAPGSKGDTGAKGEPGPTGIQGPPGPAGEEGKRGARGEPGPAGLPGPPGE
RGGPGSRGFPGADGVAGPKGPAGERGAPGPAGPKGSPGEAGRPGEAGLPGAKGLTGSPGSPGPDGKTGPPGPAGQDGRPGPPGPPGARGQAGVMGFP
GPKGAAGEPGKAGERGVPGPPGAVGPAGKDGEAGAQGPPGPAGPAGERGEQGPAGSPGFQGLPGPAGPPGEAGKPGEQGVPGDLGAPGPSGARGERG
FPGERGVQGPPGPAGPRGANGAPGNDGAKGDAGPAGPSGQAGPLQGMPGERGAAGLPGPKGDRGDAGPKGADGAPGKDGVRGLTGPIGPPGPAGA
PGDKGEAGPSGPAGPTGARGAPGDRGEPGPPGPAGFAGPPGADGQPGAKGEPGDAGAKGDAGPPGPAGPAGPPGPIGNVGAPGPKGARGSAGPPGAT
GFPGAAGRVGPPGPSGNAGPPGPPGPAGKEGSKGPRGETGPAGRPGEVGPPGPPGPAGEKGAPGADGPAGAPGTPGPQGIAGQRGVVGLPGQRGERG
FPGLPGPSGEPGKQGPSGASGERGPPGPMGPPGLAGPPGESGREGAPGAEGSPGRDGSPGAKGDRGETGPAGPPGAPGAPGAPGPVGPAGKSGDRGE
TGPAGPAGPIGPVGARGPAGPQGPRGDKGETGEQGDRGIKGHRGFSGLQGPPGPPGSPGEQGPSGASGPAGPRGPPGSAGSPGKDGLNGLPGPIGPP
GPRGRTGDAGPAGPPGPPGPPGPPSGGYDLSFLPQPPQEKAHDGGRYYRADDANVVRDRDLEVDTTLKSLSQQIENIRSPEGSRKNPARTCRDL
KMCHSDWKSGEYWIDPNQGCNLDAIKVFCNMETGETCVYPTQPSVAQKNWYISKNPKEKRHVWYGESMTGGFQFEYGGQGSDPADVAIQLTFLRLMS
TEASQNITYHCKNSVAYMDQQTGNLKKALLLQGSNEIEIRAEGNSRFTYSVTYDGCTSHTGAWGKTVIEYKTTKTSRLPIIDVAPLDVGAPDQEFGF
DVGPACFL

Equus asinus (Donkey, ACM24774.1, 1463 aa)

>gi|221665286|gb|ACM24774.1| collagen alpha-1 type I chain [Equus asinus]
MFSFVDLRLLLLLAATALLTHGQEEGQEEGQEEDIPAVTCIQDGLRYHDRAVWKPEPCRVCICDNGNVLCDDVICEDTKNCPGASVPKDECCPVCPE
GQVSPTDDQTTGVEGPKGDTGPRGPRGPAGPPGRDGIPGQPGLPGPPGPPGPPGPPGLGGNFAPQLSYGYDEKSAGISVPGPMGPSGPRGLPGPPGA
PGPQGFQGPPGEPGEPGASGPMGPRGPPGPPGKNGDDGEAGKPGRPGERGPPGPQGARGLPGTAGLPGMKGHRGFSGLDGAKGDAGPAGPKGEPGSP
GENGAPGQMGPRGLPGERGRPGAPGPAGARGNDGATGAAGPPGPTGPAGPPGFPGAVGAKGEAGPQGARGSEGPQGVRGEPGPPGPAGAAGPAGNPG
ADGQPGAKGANGAPGIAGAPGFPGARGPSGPQGPSGPPGPKGNSGEPGAPGNKGDTGAKGEPGPTGIQGPPGPAGEEGKRGARGEPGPTGLPGPPGE
RGGPGARGFPGADGVAGPKGPAGERGAPGPAGPKGSPGEAGRPGEAGLPGAKGLTGSPGSPGPDGKTGPPGPAGQDGRPGPPGPPGARGQAGVMGFP
GPKGAAGEPGKAGERGVPGPPGAVGPAGKDGEAGAQGPPGPAGPAGERGEQGPAGSPGFQGLPGPAGPPGESGKPGEQGVPGDLGAPGPSGARGERG
FPGERGVQGPPGPAGPRGSNGAPGNDGAKGDAGPAGPSGQAGPLQGMPGERGAAGLPGPKGDRGDAGPKGADGSPGKDGVRGLTGPIGPPGPAGA
PGDKGETGPSGPAGPTGARGAPGDRGEPGPPGPAGFAGPPGADGQPGAKGEPGDAGAKGDAGPPGPAGPTGPPGPIGSVGAPGPKGARGSAGPPGAT
GFPGAAGRVGPPGPSGNAGPPGPPGPVGKEGGKGPRGETGPAGRPGEAGPPGPPGPAGEKGSPGADGPAGAPGTPGPQGIAGQRGVVGLPGQRGERG
FPGLPGPSGEPGKQGPSGASGERGPPGPVGPPGLAGPPGESGREGSPGAEGSPGRDGSPGPKGDRGETGPAGPPGAPGAPGAPGPVGPAGKSGDRGE
AGPAGPAGPIGPVGARGPAGPQGPRGDKGETGEQGDRGIKGHRGFSGLQGPPGPPGSPGEQGPSGASGPAGPRGPPGSAGAPGKDGLNGLPGPIGPP
GPRGRTGDAGPVGPPGPPGPPGPPSAGFDFSFLPQPPQEKSHDGGRYYRADDANVVRDRDLEVDTTLKSLSQQIENIRSPEGSRKNPARTCRDL
KMCHSDWKSGEYWIDPNQGCNLDAIKVFCNMETGETCVYPTQPQVAQKNWYISKNPKDKRHVWYGESMTDGFQFEYGGQGSDPADVAIQLTFLRLMS
TEASQNITYHCKNSVAYMDQQTGNLKKALLLQGSNEIEIRAEGNSRFTYSVTYDGCTSHTGAWGKTVIEYKTTKTSRLPIIDVAPLDIGAPDQEFGI
DIGPVCFL

*Canis lupus familiaris** (Common dog, AAD34619.1, 1460 aa)

*Precursor

>gi|4960163|gb|AAD34619.1|AF153062_1 type I collagen pre-pro-alpha1(I) chain [Canis lupus familiaris]
MFSFVDLRLLLLLAATALLTHGQEEGQEEDIPPVTCVQNGLRYYDRDVWKPEACRICVCDNGNVLCDDVICDETKNCPGAQVPPGECCPVCPDGEAS
PTDQETTGVEGPKGDTGPRGPRGPAGPPGRDGIPGQPGLPGPPGPPGPPGPPGLGGNFAPQMSYGYDEKSTGGISVPGPMGPSGPRGLPGPPGAPGP
QGFQGPPGEPGEPGASGPMGPRGPPGPPGKNGDDGEAGKPGRPGERGPPGPQGARGLPGTAGLPGMKGHRGFSGLDGAKGDAGPAGPKGEPGSPGEN
GAPGQMGPRGLPGERGRPGAPGPAGARGNDGATGAAGPPGPTGPAGPPGFPGAVGAKGEAGPQGARGSEGPQGVRGEPGPPGPAGAAGPAGNPGADG
QPGAKGANGAPGIAGAPGFPGARGPSGPQGPSGPPGPKGNSGEPGAPGNKGDTGAKGEPGPTGIQGPPGPAGEEGKRGARGEPGPTGLPGPPGERGG
PGSRGFPGADGVAGPKGPAGERGSPGPAGPKGSPGEAGRPGEAGLPGAKGLTGSPGSPGPDGKTGPPGPAGQDGRPGPPGPPGARGQAGVMGFPGPK
GAAGEPGKAGERGVPGPPGAVGPAGKDGEAGAQGPPGPAGPAGERGEQGPAGSPGFQGLPGPAGPPGEAGKPGEQGVPGDLGAPGPSGARGERGFPG
ERGVQGPPGPAGPRGANGAPGNDGAKGDAGAPGAPGSQGAPGLQGMPGERGAAGLPGPKGDRGDAGPKGADGSPGKDGVRGLTGPIGPPGPAGAPGD
KGEAGPSGPAGPTGARGAPGDRGEPGPPGPAGFAGPPGADGQPGAKGEPGDAGAKGDAGPPGPAGPTGPPGPIGNVGAPGPKGARGSAGPPGATGFP

GAAGRVGPPGPSGNAGPPGPPGPAGKEGGKGARGETGPAGRPGEVGPPGPPGPAGEKGSPGADGPAGAPGTPGPQGIAGQRGVVGLPGQRGERGFPG
LPGPSGEPGKQGPSGTSGERGPPGPMGPPGLAGPPGESGREGSPGAEGSPGRDGSPGPKGDRGETGPAGPPGAPGAPGAPGPVGPAGKNGDRGETGP
AGPAGPIGPVGARGPAGPQGPRGDKGETGEQGDRGIKGHRGFSGLQGPPGPPGSPGEQGPSGASGPAGPRGPPGSAGSPGKDGLNGLPGPIGPPGPR
GRTGDAGPVGPPGPPGPPGPPGPPSGGFDFSFLPQPPQEKAHDGGRYYRADDANVVRDRDLEVDTTLKSLSQQIENIRSPEGSRKNPARTCRDLKMC
HSDWKSGEYWIDPNQGCNLDAIKVFCNMETGETCVYPTQPQVAQKNWYISKNPKEKRHVWYGESMTDGFQFEYGGQGSDPADVAIQLTFLRLMSTEA
SQNITYHCKNSVAYMDQQTGNLKKALLLQGSNEIEIRAEGNSRFTYSVTYDGCTSHTGAWGKTVIEYKTTKTSRLPIIDVAPLDVGAPDQEFGMDIG
PVCFL

Rattus norvegicus (Rat, AAI33729.1, 1453 aa)

>gi|126631239|gb|AAI33729.1| Col1a1 protein [Rattus norvegicus]
MFSFVDLRLLLLLGATALLTHGQEDIPEVSCIHNGLRVPNGETWKPDVCLICICHNGTAVCDGVLCKEDLDCPNPQKREGECCPFCPEEYVSPDAEV
IGVEGPKGDPGPQGPRGPVGPPGQDGIPGQPGLPGPPGPPGPPGPPGLGGNFASQMSYGYDEKSAGVSVPGPMGPSGPRGLPGPPGAPGPQGFQGPP
GEPGEPGASGPMGPRGPPGPPGKNGDDGEAGKPGRPGERGPPGPQGARGLPGTAGLPGMKGHRGFSGLDGAKGDTGPAGPKGEPGSPGENGAPGQMG
PRGLPGERGRPGPPGSAGARGNDGAVGAAGPPGPTGPTGPPGFPGAAGAKGEAGPQGARGSEGPQGVRGEPGPPGPAGAAGPAGNPGADGQPGAKGA
NGAPGIAGAPGFPGARGPSGPQGPSGAPGPKGNSGEPGAPGNKGDTGAKGEPGPAGVQGPPGPAGEEGKRGARGEPGPSGLPGPPGERGGPGSRGFP
GADGVAGPKGPAGERGSPGPAGPKGSPGEAGRPGEAGLPGAKGLTGSPGSPGPDGKTGPPGPAGQDGRPGPAGPPGARGQAGVMGFPGPKGTAGEPG
KAGERGVPGPPGAVGPAGKDGEAGAQGAPGPAGPAGERGEQGPAGSPGFQGLPGPAGPPGEAGKPGEQGVPGDLGAPGPSGARGERGFPGERGVQGP
PGPAGPRGNNGAPGNDGAKGDTGAPGAPGSQGAPGLQGMPGERGAAGLPGPKGDRGDAGPKGADGSPGKDGVRGLTGPIGPPGPAGAPGDKGETGPS
GPAGPTGARGAPGDRGEPGPPGPAGFAGPPGADGQPGAKGEPGDTGVKGDAGPPGPAGPAGPPGPIGNVGAPGPKGSRGAAGPPGATGFPGAAGRVG
PPGPSGNAGPPGPPGPVGKEGGKGPRGETGPAGRPGEVGPPGPPGPAGEKGSPGADGPAGSPGTPGPQGIAGQRGVVGLPGQRGERGFPGLPGPSGE
PGKQGPSGASGERGPPGPMGPPGLAGPPGESGREGSPGAEGSPGRDGAPGAKGDRGETGPAGPPGAPGAPGAPGPVGPAGKNGDRGETGPAGPAGPI
GPAGARGPAGPQGPRGDKGETGEQGDRGIKGHRGFSGLQGPPGSPGSPGEQGPSGASGPAGPRGPPGSAGSPGKDGLNGLPGPIGPPGPRGRTGDSG
PAGPPGPPGPPGPPGPPSGGYDFSFLPQPPQEKSQDGGRYYRADDANVVRDRDLEVDTTLKSLSQQIENIRSPEGSRKNPARTCRDLKMCHSDWKSG
EYWIDPNQGCNLDAIKVYCNMETGQTCVFPTQPSVPQKNWYISPNPKEKKHVWFGESMTDGFQFEYGSEGSDPADVAIQLTFLRLMSTEASQNITYH
CKNSVAYMDQQTGNLKKSLLLQGSNEIELRGEGNSRFTYSTLVDGCTSHTGTWGKTVIEYKTTKTSRLPIIDVAPLDIGAPDQEFGMDIGPACFV

Mus musculus (House mouse, AAH50014.1, 1453 aa)

>gi|29476768|gb|AAH50014.1| Collagen, type I, alpha 1 [Mus musculus]
MFSFVDLRLLLLLGATALLTHGQEDIPEVSCIHNGLRVPNGETWKPEVCLICICHNGTAVCDDVQCNEELDCPNPQRREGECCAFCPEEYVSPNSED
VGVEGPKGDPGPQGPRGPVGPPGRDGIPGQPGLPGPPGPPGPPGPPGLGGNFASQMSYGYDEKSAGVSVPGPMGPSGPRGLPGPPGAPGPQGFQGPP
GEPGEPGGSGPMGPRGPPGPPGKNGDDGEAGKPGRPGERGPPGPQGARGLPGTAGLPGMKGHRGFSGLDGAKGDAGPAGPKGEPGSPGENGAPGQMG
PRGLPGERGRPGPPGTAGARGNDGAVGAAGPPGPTGPTGPPGFPGAVGAKGEAGPQGARGSEGPQGVRGEPGPPGPAGAAGPAGNPGADGQPGAKGA
NGAPGIAGAPGFPGARGPSGPQGPSGPPGPKGNSGEPGAPGNKGDTGAKGEPGATGVQGPPGPAGEEGKRGARGEPGPSGLPGPPGERGGPGSRGFP
GADGVAGPKGPSGERGAPGPAGPKGSPGEAGRPGEAGLPGAKGLTGSPGSPGPDGKTGPPGPAGQDGRPGPAGPPGARGQAGVMGFPGPKGTAGEPG
KAGERGLPGPPGAVGPAGKDGEAGAQGAPGPAGPAGERGEQGPAGSPGFQGLPGPAGPPGEAGKPGEQGVPGDLGAPGPSGARGERGFPGERGVQGP
PGPAGPRGNNGAPGNDGAKGDTGAPGAPGSQGAPGLQGMPGERGAAGLPGPKGDRGDAGPKGADGSPGKDGARGLTGPIGPPGPAGAPGDKGEAGPS
GPPGPTGARGAPGDRGEAGPPGPAGFAGPPGADGQPGAKGEPGDTGVKGDAGPPGPAGPAGPPGPIGNVGAPGPKGPRGAAGPPGATGFPGAAGRVG
PPGPSGNAGPPGPPGPVGKEGGKGPRGETGPAGRPGEVGPPGPPGPAGEKGSPGADGPAGSPGTPGPQGIAGQRGVVGLPGQRGERGFPGLPGPSGE
PGKQGPSGASGERGPPGPMGPPGLAGPPGESGREGSPGAEGSPGRDGAPGAKGDRGETGPAGPPGAPGAPGAPGPVGPAGKNGDRGETGPAGPAGPI
GPAGARGPAGPQGPRGDKGETGEQGDRGIKGHRGFSGLQGPPGSPGSPGEQGPSGASGPAGPRGPPGSAGSPGKDGLNGLPGPIGPPGPRGRTGDSG
PAGPPGPPGPPGPPGPPSGGYDFSFLPQPPQEKSQDGGRYYRADDANVVRDRDLEVDTTLKSLSQQIENIRSPEGSRKNPARTCRDLKMCHSDWKSG
EYWIDPNQGCNLDAIKVYCNMETGQTCVFPTQPSVPQKNWYISPNPKEKKHVWFGESMTDGFPFEYGSEGSDPADVAIQLTFLRLMSTEASQNITYH
CKNSVAYMDQQTGNLKKALLLQGSNEIELRGEGNSRFTYSTLVDGCTSHTGTWGKTVIEYKTTKTSRLPIIDVAPLDIGAPDQEFGLDIGPACFV

*Gallus gallus** (Red fowl, P02457.3, 1453 aa)

*Precursor

>gi|152031574|sp|P02457.3|CO1A1_CHICK RecName: Full=Collagen alpha-1(I) chain; AltName: Full=Alpha-1 type I collagen; Flags: Precursor
MFSFVDSRLLLLIAATVLLTRGEGEEDIQTGSCVQDGLTYNDKDVWKPEPCQICVCDSGNILCDEVICEDTSDCPNAEIPFGECCPICPDVDASPVY
PESAGVEGPKGDTGPRGDRGLPGPPGPRGDGIPGQPGLPGPPGPPGPPGLGGNFAPQMSYGYDEKSAGVAVPGPMGPAGPRGLPGPPGAPGPQGFQGPP
GEPGEPGASGPMGPRGPAGPPGKNGDDGEAGKPGRPGQRGPPGPQGARGLPGTAGLPGMKGHRGFSGLDGAKGQPGPAGPKGEPGSPGENGAPGQMG
PRGLPGERGRPGPSGPAGARGNDGAPGAAGPPGPTGPAGPPGFPGAAGAKGETGPQGARGSEGPQGSRGEPGPPGPAGAAGPAGNPGADGQPGAKGA
TGAPGIAGAPGFPGARGPSGPQGPSGAPGPKGNSGEPGAPGNKGDTGAKGEPGPAGVQGPPGPAGEEGKRGARGEPGPAGLPGPAGERGAPGSRGFP
GADGIAGPKGPPGERGSPGAVGPKGSPGEAGRPGEAGLPGAKGLTGSPGSPGPDGKTGPPGPAGQDGRPGPAGPPGARGQAGVMGFPGPKGAAGEPG
KPGERGAPGPPGAVGAAGKDGEAGAQGPPGPTGPAGERGEQGPAGAPGFQGLPGPAGPPGEAGKPGEQGVPGNAGAPGPAGARGERGFPGERGVQGP
PGPQGPRGANGAPGNDGAKGDAGAPGAPGNEGPPGLEGMPGERGAAGLPGAKGDRGDPGPKGADGAPGKDGLRGLTGPIGPPGPAGAPGDKGEAGPP
GPAGPTGARGAPGDRGEPGPPGPAGFAGPPGADGQPGAKGETGDAGAKGDAGPPGPAGPTGAPGPAGZVGAPGPKGARGSAGPPGATGFPGAAGRVG
PPGPSGNIGLPGPPGPAGKZGSKGPRGETGPAGRPGEPGPAGPPGPPGEKGSPGADGPIGAPGTPGPQGIAGQRGVVGLPGQRGERGFPGLPGPSGE
PGKQGPSGASGERGPPGPMGPPGLAGPPGEAGREGAPGAEGAPGRDGAAGPKGDRGETGPAGPPGAPGAPGAPGPVGPAGKNGDRGETGPAGPAGPP
GPAGARGPAGPQGPRGDKGETGEQGDRGMKGHRGFSGLQGPPGPPGAPGEQGPSGASGPAGPRGPPGSAGAAGKDGLNGLPGPIGPPGPRGRTGEVG
PVGPPGPPGPPGPPGPPSGGFDLSFLPQPPQEKAHDGGRYYRADDANVMRDRDLEVDTTLKSLSQQIENIRSPEGTRKNPARTCRDLKMCHGDWKSG
EYWIDPNQGCNLDAIKVYCNMETGETCVYPTQATIAQKNWYLSKNPKEKKHVWFGETMSDGFQFEYGGEGSNPADVAIQLTFLRLMSTEATQNVTYH
CKNSVAYMDHDTGNLKKALLLQGANEIEIRAEGNSRFTYGVTEDGCTSHTGAWGKTVIEYKTTKTSRLPIIDLAPMDVGAPDQEFGIDIGPVCFL

Xenopus laevis (African clawed frog, AAH49829.1, 1449 aa)

>gi|29436389|gb|AAH49829.1| Col1a1 protein [Xenopus laevis]

MFSFVDTRTLLLIAATILVARCQGEHDVQTSDCVQHGITYSNRDVWKPEDCQICVCDNGNILCDEVMCEDADCPNPVIVPGECCPVCTDNDAQYSEV
TGVEGPKGDVGPKGDKGIAGPPGRDGIPGQPGIPGPPGPPGPPGLGGNFAPQMSYGYDEKSAGISMPGPMGPMGPRGPPGPSGSPGPQGFQGPPGEP
GEPGASGAMGPRGSSGPPGKNGEDGEAGKPGRPGERGPPGPQGARGLPGTAGLPGMKGHRGFNGLDGAKGDSGPAGPKGEPGSPGENGAPGQVGPRG
LSGERGRPGPSGPAGARGNDGAPGAAGPPGSTGPSGPPGFPGGVGPKGDAGPQGSRGSDGPQGGRGEPGAPGQAGAAGPSGNPGSDGQPGAKGATGA
PGIAGAPGFPGARGAPGAQGPGGSPGPKGNNGEPGAQGNKGEAGAKGEPGPAGVQGPPGPSGEEGKRGSRGEPGPAGPPGPAGERGGPGSRGFPGSD
GASGPKGAPGERGPVGPAGPKGSSGESGRPGEPGLPGAKGLTGSPGSPGSDGKTGPAGAPGQDGRAGPPGPPGARGQSGVMGFPGPKGAAGEPGKNG
EKGVAGPPGAVGLPGKDGDAGAQGPPGPAGPAGERGEQGPAGGPGFQGLPGPPGPAGESGKPGEQGVPGDVGPSGPAGARGERGFPGERGAQGPPGP
QGARGSNGAPGNDGAKGEAGAAGAPGGQGPPGLQGMPGERGSSGLPGAKGDRGDQGVKGSDGTPGKDGVRGLTGPIGPPGPGGAPGDKGEAGPAGPA
GPTGARGAPGERGESGPPGPAGFAGPPGADGQPGAKGEQGDSGAKGDAGPPGPAGPTGAPGPAGALGSPGPKGARGAPGPPGATGFPGAAGRLGPPG
PSGNAGPPGPSGPAGKEGAKGPRGETGPAGRSGEPGAAGPPGPPGEKGSPGSDGPAGAPGIPGPQGVAGSRGTVGLPGMRGERGFSGLPGPAGEPGK
QGPSGPSGERGPPGPSGPPGLGGPPGESGREGAPGSEGAPGRDGAVGPKGDRGEGGPAGPPGAPGAPGAPGPVGPAGKSGDRGETGPSGPAGPAGTA
GARGPAGPQGPRGDKGEAGEQGERGMKGHRGFNGPSGPPGPPGSSGEQGPSGASGPAGPRGPPGSSGNPGKDGSNGLPGPIGPPGPRGRTGDVGPAG
PPGPPGPPGPPGQSGGGFDFSFMPQPPQEKSHDGRFYRADDANVMRDRDLEVDSTLKSLSKQIENIRSPEGTRKNPARTCRDLKMCHSDWKSGEYWI
DPNQGCILDAIKVYCNMETGETCIYPTQSSIPQKSWYTSKNLREKKHVWFGEAMSDGFQFEYGSEGSNSADVTIQLTFLRLMATEASQNITYHCKNS
VAYMDQATGNLKKALLLQGSNEIEIRAEGNSRFTYSVVEDGCTQHTGEWGKTVIDYKTTKTSRLPITDVAPMDIGAPDQEFGIDIGPVCFV

Danio rerio (Zebrafish, AAH63249.1, 1447 aa)

>gi|38649122|gb|AAH63249.1| Collagen, type I, alpha 1 [Danio rerio]
MFSFVDIRLALLLSATVLLARGQGEDDRTGGSCTLDGQVYNDRDVWKPEPCQICVCDSGTVMCDEVICEDTSDCPNPVIPHDECCPVCPDDDFQEPS
VEGPRGSPGDKGERGPAGPPGNDGIPGQPGLPGPPGPPGPPGLGGNFSPQMSGGFDEKSSPMAVPGPMGPMGPRGAPGPPGPSGPQGFTGPPGEPGE
AGAPGPMGPRGAAGPPGKNGEDGESGKPGRPGERGPPGPQGARGFPGTPGLPGIKGHRGFSGLDGAKGDAGPAGPKGEPGAPGENGTPGAMGPRGLP
GERGRAGPPGAAGARGNDGAAGAAGPPGPTGPAGPPGFPGGPGSKGEVGPQGSRGAEGPQGARGEAGNPGPAGPAGPAGNNGADGAPGAKGAPGAPG
IAGAPGFPGPRGPPGAAGAAGAPGPKGNTGEAGAPGAKGEAGAKGEAGAQGVQGPPGPPGEEGKRGPRGEPGAGGARGPTGERGAPGARGFPGADGA
AGPRGAPGERGGPGVVGPKGATGEPGRNGEPGMPGSKGMTGSPGSPGPDGKTGLAGAPGQDGRPGPPGPVGARGQPGVMGFPGPKGAAGEAGKPGER
GVMGAIGATGAPGKDGDVGAPGAPGPAGPAGERGEQGAAGPPGFQGLPGPQGATGEPGKSGEQGAPGEAGAPGPSGSRGDRGFPGERGAPGPAGPVG
ARGSPGSAGNDGAKGESGAAGAPGAQGPPGLQGMPGERGAAGLPGLKGDRGDQGAKGADGAAGKDGIRGMTGPIGPPGPAGAPGDKGESGAQGLVGP
TGARGPPGERGETGAPGPAGFAGPPGADGLPGAKGEPGDNGAKGDAGAPGPAGATGAPGPQGPVGATGPKGARGAAGPPGATGFPGAAGRVGPPGPS
GNSGPPGPPGPAGKEGQKGNRGETGPAGRTGEVGAAGPPGAPGEKGNPGAEGATGPAGIPGPQGIGGQRGIVGLPGQRGERGFPGLPGPSGEIGKQG
PSGPSGERGPPGPMGPPGLAGPPGEPGREGTPGNEGSAGRDGAAGPKGDRGETGPSGTPGAPGPPGAAGPIGPAGKTGDRGETGPAGVPGPAGPSGP
RGPSGPAGARGDKGETGEAGERGMKGHRGFTGMPGPPGPPGPSGESGPAGASGPAGPRGPAGSAGSAGKDGMSGLPGPIGPPGPRGRNGEIGPAGPP
GPPGPPGAPGPSGGGFDIGFIAQPQEKAPDPFRHFRADDANVMRDRDLEVDTTLKSLSQQIESIISPDGTKKNPARTCRDLKMCHPDWKSGEYWIDP
DQGCNQDAIKVYCNMETGETCVNPTESAIPKKNWYTSKNIKEKKHVWFGEAMTDGFQFEYGSEGSKPEDVNIQLTFLRLMSTEASQNITYHCKNSIA
YMDQASGNLKKALLLQGSNEIEIRAEGNSRFTYSVTEDGCTSHTGAWGKTVIDYKTTKTSRLPIIDIAPMDVGAPNQEFGIEVGPVCFL

Oreochromis niloticus (Nile tilapia, BAL40987.1, 1447 aa)

>gi|359804080|dbj|BAL40987.1| collagen type I alpha 1 [Oreochromis niloticus]
MFSFVDLRLALLLSAAVLLVRAQGEDDRTGKSCTLDGQVFADRDVWKPEPCQICVCDSGTVMCDEVICEDTTDCPNPIIPHDECCPICPDDGFQEPQ
TEGTVGARGPKGDRGLPGPPGRDGMPGQPGLPGPPGPPGPPGLGGNFSPQMSGGYDEKSPAMPVPGPMGPMGPRGPPGPPGSSGPQGFTGPPGEAGE
PGSPGPMGPRGPAGPPGKNGEDGESGKPGRPGERGPPGPQGARGFPGTPGLPGIKGHRGFSGLDGAKGDTGPAGPKGEAGTPGENGTPGAMGPRGLP
GERGRAGATGAAGARGNDGAAGAAGPPGPTGPAGPPGFPGGPGAKGDAGAQGGRGPEGPAGARGEPGNPGPAGPAGPAGNPGSDGAPGAKGAPGAAG
VAGAPGFPGPRGPSGPQGAAGAPGPKGNTGEAGAPGSKGEAGAKGEAGAPGVQGPPGPPGEEGKRGARGEPGAAGARGGPGERGAPGGRGFPGSDGP
AGPKGATGERGAPGLVGPKGATGEPGRTGEPGLPGAKGMTGSPGNPGPDGKIGPSGAPGQDGRPGPPGPGGARGQPGVMGFPGPKGAAGEAGKPGER
GTMGPTGPAGAPGKDGDVGAQGPPGPAGPAGERGEQGPAGSPGFQGLPGPQGAVGETGKPGEQGVPGEAGAPGPAGARGDRGFPGERGAPGAIGPAG
ARGSPGASGNDGAKGDAGAPGTPGAQGPPGLQGMPGERGAAGLPGLRGNRGDQGPKGADGTPGKDGPRGLTGPIGLPGPAGSPGDKGEPGAQGPVGP
SGARGPPGERGEAGPPGPAGFAGPPGADGQPGAKGEPGDNGAKGDSGPPGPAGPTGAPGPAGPVGNTGPKGARGPAGPPGATGFPGAAGRVGPPGPA
GNAGPPGPPGPAGKEGPKGNRGETGPAGRPGELGAAGPPGPPGEKGSPGADGAPGSAGIPGPQGIAGQRGIVGLPGQRGERGFPGLAGPVGEPGKQG
PSGPSGERGPPGPMGPPGLAGAPGEPGREGTPGNEGAAGRDGAPGPKGDRGESGPAGAPGAPGPPGAPGPVGPAGKTGDRGETGPAGPAGAAGPAGP
RGPAGAPGLRGDKGETGEAGERGMKGHRGFTGMQGPPGPPGTSGESGPAGAAGPAGPRGPSGAAGAPGKDGVSGLPGPTGPPGPRGRSGEMGPAGPP
GPPGPPGAPGAPGGGFDLGFMVQPQEKAPDPFRMYRADDANVLRDRDLEVDSTLKSLSQQIEQIRSPDGTRKNPARTCRDLKMCHPDWKSGEYWIDP
DQGCTQDAIKVYCNMETGETCVSPTQREVAKKNWYISKNIKEKKHVWFGEAMNEGFQFEYGSEGSLPEDVNIQMTFLRLMSTEASQNITYHCKNSVA
YMDAAAGNLKKALLLQGSNEIEIRAEGNSRFTYSVLEDGCTSHTGTWGKTVIDYKTSKTSRLPIIDIAPMDVGAPDQEFGFEVGPVCFL

*Oncorhynchus mykiss** (Rainbow trout, NP_001117649.1, 1449 aa)

*Precursor

>gi|185133699|ref|NP_001117649.1| collagen 1a1 precursor [Oncorhynchus mykiss]
MFSFVDIRLALLLSATVLLARGQGEDDRTAGSCTLDGQFYNDRDVWKPEPCQICVCDSGTVMCDEVICEDTSDCPNPVIPHDECCPICPDDGFQEPK
VEGPQGDRGAKGEPGPAGFPGNDGIPGQPGLPGPPGPPGPPGLGGNFSPQMSGGFDEKSGGGMSMPGPMGPMGPRGPPGPPGSSGPQGFTGPPGEPG
EAGSSGPMGPRGPAGPPGKNGDDGESGKPGRPGERGASGPQGARGFPGTPGLPGIKGHRGFSGLDGAKGESGPAGPKGEGGASGENGAAGAMGPRGL
PGERGRAGPNGAAGARGNDGAAGAAGPPGPTGPAGAPGFPGGPGAKGEVGAQGARGGEGPQGSRGEAGNPGPAGAAGPAGNNGADGNPGTKGAPGSS
GIAGAPGFPGPRGPPGPQGAGGAPGPKGNTGEVGANGAKGEAGAKGESGPAGVQGPAGPAGEEGKRGGRGEPGGAGARGAPGERGAPGSRGFPGSDG
ASGPKGGPGERGGAGVAGAKGNTGEPGRNGEPGMPGSKGMTGSPGSPGPDGKTGPSGAGGQDGRPGPPGPVGARGQPGVMGFPGPKGAAGEGGKPGE
RGVMGPSGAVGAPGKDGDVGAPGAPGVAGPSGERGEQGAGGPPGFQGLSGPQGAIGETGKPGEQGLPGEGGAPGSAGSRGDRGFPGERGAPGPSGPA
GARGSPGSAGNDGGKGEAGAAGAPGGQGPPGLQGMPGERGAGGLPGLKGDRGDQGVKGADGAGGKDGVRGMTGPIGPNGPAGSPGDKGETGAPGAVG
PSGARGAPGERGESGAPGPAGFAGPPGGDGQPGAKGEAGDNGAKGDGGAQGPAGPTGAPGPQGPAGNTGAKGARGAAGPPGATGFPGAAGRFGPPGP
SGNNGPPGTPGPGGKEGQKGNRGETGPAGRPGELGAAGPPGPKGEKGQPGGDGPNGPSGTPGPQGIGGQRGIVGLPGQRGERGFPGLAGQLGEPGKQ
GPGGPFGERGPPGPMGPPGLAGAPGEPGREGTPGNEGSSGRDGAAGPKGERGESGVAGASGAPGPPGAPGAVGPAGKSGDRGESGPAGPAGIAGPAG
PRGPSGPAGARGDKGESGEAGERGMKGHRGFTGMQGPPGPSGQSGESGPAGASGPAGPRGPSGSAGAAGKDGMSGLPGPIGPPGPRGRSGEMGPSGT
PGPPGPPGPPGPPGGGFDMGFIAQPAQEKAPDPFRHFRADDANVMRDRDLEVDTTLKSLSQQIENIRSPEGTKKNPARTCRDLKMCHPDWKSGEYWI

DPDQGCTQDAIKVYCNMETGETCVYPTEADIPKKSWYTSKNIKEKKHVWFGEAMTDGFQFEYGSEGSNAKDVNIQLTFLRLMATEASQNITYHCKNS
IAYMDQQSGNLKKSLLLQGSNEIEIRAEGNSRFTYSVTEDGCTSHTGAWGKTVIDYKTTKTSRLPIIDIAPMDVGAPNQEFGIEVGPVCFL

Carassius auratus (Goldfish, BAG72200.1, 1448 aa)

>gi|208609645|dbj|BAG72200.1| collagen type I alpha 1 [Carassius auratus]
MFSFVDIRLALLLSATVLLARGQGEDDRTGGSCTLDGQVYNDRDVWKPEPCQICVCDSGTVMCDEVICEDTTHCPNPVIPHDECCPVCPDDEFLEPS
VEGPSGPAGEKGDRGPPGPPGNDGIPGQPGLPGPPGPPGPPGLGGNFSPQMSGGYDEKSGGAMAVPGPMGAMGPRGPPGPPGTPGPQGFTGPPGEPG
EAGAPGPMGPRGAAGPPGKNGEDGESGKPGRPGERGPPGAQGARGFPGTPGLPGIKGHRGFSGLDGSKGDTGPAGPKGEPGAAGENGTPGAMGPRGL
PGERGRAGPPGAAGARGNDGAAGAAGPPGPTGPAGPPGFPGGPGAKGEVGAQGARGAEGPQGARGEPGNPGPAGAAGPAGNNGADGAPGLKGAPGAP
GIAGAPGFPGPRGPSGPAGAAGAPGPKGNTGEVGAPGAKGEAGAKGEAGAQGVQGPPGPSGEEGKRGPRGEPGSAGSRGPPGERGAPGARGFPGADG
SAGPKGATGERGGPGIVGPKGATGEPGRNGEPGLPGSKGMTGSPGSPGPDGKTGAPGNPGQDGRPGPPGPVGARGQPGVMGFPGPKGAAGEAGKPGE
RGVMGALGATGAPGKDGDVGAPGAPGPAGPTGERGEQGPAGPPGFQGLTGPQGATGEPGKAGEQGVPGEAGAPGPSGSRGDRGFPGERGAPGPAGPA
GARGSPGSAGNDGAKGDAGAPGAPGAQGPPGLQGMPGERGSAGLPGLKGDRGDQGAKGTDGAPGKDGIRGMTGPIGPPGPAGAPGDKGETGAPGLVG
PNGARGPPGERGETGAPGPAGFAGPPGADGLPGAKGEPGDNGAKGDAGAPGPAGATGAPGPQGPVGSTGPKGARGAAGPPGATGFPGAAGRVGPPGP
AGNAGPAGPSGAPGKEGQKGNRGETGPAGRTGEVGAAGPPGAPGEKGNPGAEGAPGSAGTPGPAGIAGQRGIVGLPGQRGERGFPGLPGQSGEPGKQ
GPSGPSGERGPPGPMGPPGLAGPPGEPGREGTPGNEGSAGRDGAAGPKGDRGETGSAGTPGAPGPPGAPGPIGPAGKTGDRGESGPAGPAGAVGPAG
PRGPAGPAGARGDRGETGEAGERGMKGHRGFTGMQGPPGPPGPSGEPGPAGASGPAGPRGPGGSAGAAGKDGMSGLPGPIGPPGPRGRNGEIGPAGP
PGPPGLPGPPGPSGGGFDIGFIAQPMEKAPDPFRSYRADDANVMRDRDLEVDTTLKSLSQQIESIMSPDGTKKNPARTCRDLKMCHPDWKSGEYWID
PDQGCNQDAIKVYCNMETGETCVYPAESSIPKKNWYTSKNIKEKKHVWFGEAMTDGFQFEYGSEGSKPEDVNIQLTFLRLMSTEASQNITYHCKNSI
AYMDQASGNLKKALLLQGSNEIEIRAEGNSRFTYSVTEDGCTSHTGAWGKTVIDHKTTKTSRLPIIDIAPMDVGAPNQEFGIEVGPVCFL

A.2. Pairwise alignment % identity of HomoloGene candidates

The following pairwise alignment scores were produced by HomoloGene, which automatically identified the COL1A1 homologs for this subset of the genomes in its database (not all genomes are complete). The highest alignment scores can be found for sub-groups of mammals (primates, rodents). The lowest scores are found between the fish (*Danio rerio*) and all other mammals. The protein scores are consistently higher than the DNA scores.

Species	% Identity	
H. SAPIENS	**Protein**	**DNA**
*P. troglodytes**	100.0	99.5
*M. mulatta**	99.0	97.8
C. lupus	97.8	93.3
B. taurus	97.5	93.6
M. musculus	92.4	89.6
R. norvegicus	92.8	90.2
D. rerio	77.7	76.0

Species	% Identity	
P. TROGLODYTES*	**Protein**	**DNA**
H. sapiens	100.0	99.5
*M. mulatta**	99.0	97.7
C. lupus	97.8	93.3
B. taurus	97.5	93.5
M. musculus	92.4	89.6
R. norvegicus	92.8	90.2
D. rerio	77.7	75.9

Species	% Identity	
M. MULATTA*	**Protein**	**DNA**
H. sapiens	99.0	97.8
*P. troglodytes**	99.0	97.7
C. lupus	97.3	92.8
B. taurus	96.9	93.0
M. musculus	88.1	85.9
R. norvegicus	88.2	86.2
D. rerio	74.7	73.8

Species	% Identity	
C. LUPUS	**Protein**	**DNA**
H. sapiens	97.8	93.3
*P. troglodytes**	97.8	93.3
*M. mulatta**	97.3	92.8
B. taurus	97.5	93.1
M. musculus	93.0	88.7
R. norvegicus	93.2	89.2
D. rerio	77.9	74.9

Species	% Identity	
B. taurus	**Protein**	**DNA**
H. sapiens	97.5	93.6
*P. troglodytes**	97.5	93.5
*M. mulatta**	96.9	93.0
C. lupus	97.5	93.1
M. musculus	92.7	88.7
R. norvegicus	92.8	89.1
D. rerio	77.8	75.2

Species	% Identity	
M. musculus	**Protein**	**DNA**
H. sapiens	92.4	89.6
*P. troglodytes**	92.4	89.6
*M. mulatta**	88.1	85.9
C. lupus	93.0	88.7
B. taurus	92.7	88.7
R. norvegicus	97.9	96.0
D. rerio	76.5	74.8

Species	% Identity	
R. norvegicus	**Protein**	**DNA**
H. sapiens	92.8	90.2
*P. troglodytes**	92.8	90.2
*M. mulatta**	88.2	86.2
C. lupus	93.2	89.2
B. taurus	92.8	89.1
M. musculus	97.9	96.0
D. rerio	76.6	75.2

Species	% Identity	
D. rerio	**Protein**	**DNA**
H. sapiens	77.7	76.0
*P. troglodytes**	77.7	75.9
*M. mulatta**	74.7	73.8
C. lupus	77.9	74.9
B. taurus	77.8	96.0
M. musculus	76.5	74.8
R. norvegicus	76.6	75.2

A.3. Multiple sequence trees

Four multiple sequence trees are included. Each tree was generated by pBLAST and includes the entire COL1A1 dataset given in section A.1. Trees 1 and 2 are rooted based on distance alone, while trees 3 and 4 were force-rooted at the bony fish node, to more accurately reflect evolutionary knowledge. The COL1A1 trees reproduce all expected clusters (bony fish, primates, rodents, mammals). The force-rooted trees (3 and 4) also reproduce the evolutionary relationship of the major phylogenetic groups. The fact that the COL1A1 protein trees reproduce the evolutionary phylogenetic tree suggests that differences in COL1A1 are associated with time since major evolutionary branching events occurred.

Further, these results substantiate the hypothesis that modern collagen sequences can be carefully selected to predict the dinosaur collagen sequences (or other extinct species) based on the Extant Phylogenetic Bracketing technique. This is highly significant: the structure of type I collagen informs the growth of bioapatite-impregnated bone tissue. One, the alignment scores associated with these trees (also, distance measurements of branches, by using the scale bars included) demonstrate that dinosaurs likely had COL1A1 sequences of strikingly high similarity to that of modern birds and mammals. To fully investigate such a claim, a more carefully selected sequencing study should be carried out, one that includes crocodiles and other ratites. Two, the nanoscale structure and higher order structural features (microfibril and macrofibril structure) of dinosaur bone tissue were likely highly similar to that of modern birds and mammals. This conclusion, of course, is further supported by many other investigations of bone, although these investigations have tended only to focus on discrete aspects of my overall project (*i.e.*, the bioapatite dimensions, the composition of bioapatite, the osteocyte density, etc.). Regardless, based on previously published findings by other, my preliminary work on bone, and the data presented here, I developed my concept of what I would expect to find in dinosaur bone, which was critical toward constructing a more complete concept of how I would be able to distinguish minimally altered bone from more significantly altered.

Tree 1. Rooted by pairwise alignment distances. (Rectangle)

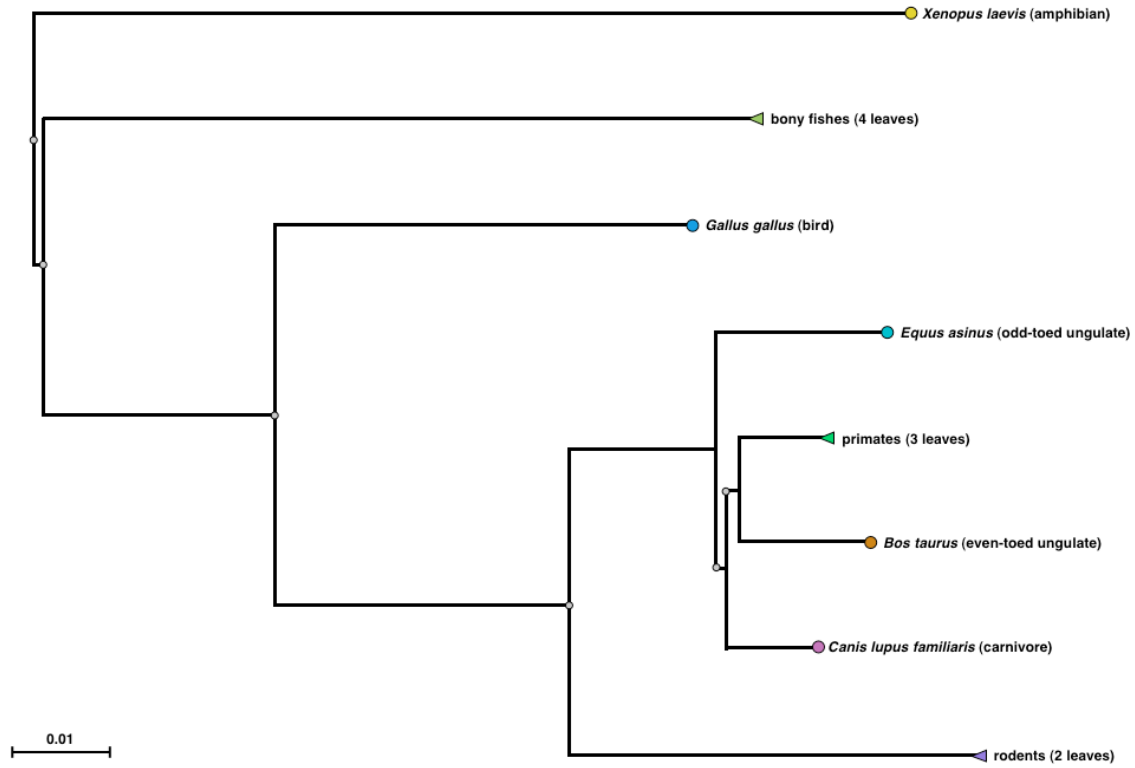

Tree 2. Rooted by pairwise alignment distances. (Slant)

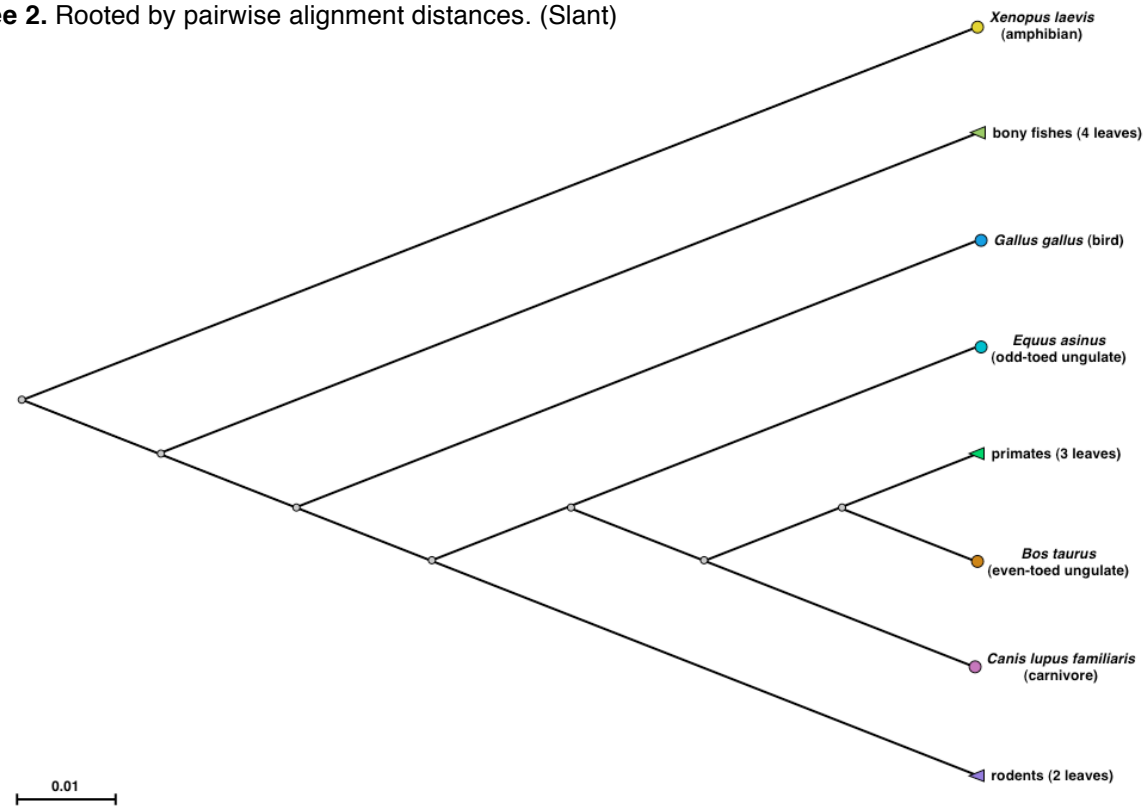

Tree 3. Force-rooted. (Rectangle)

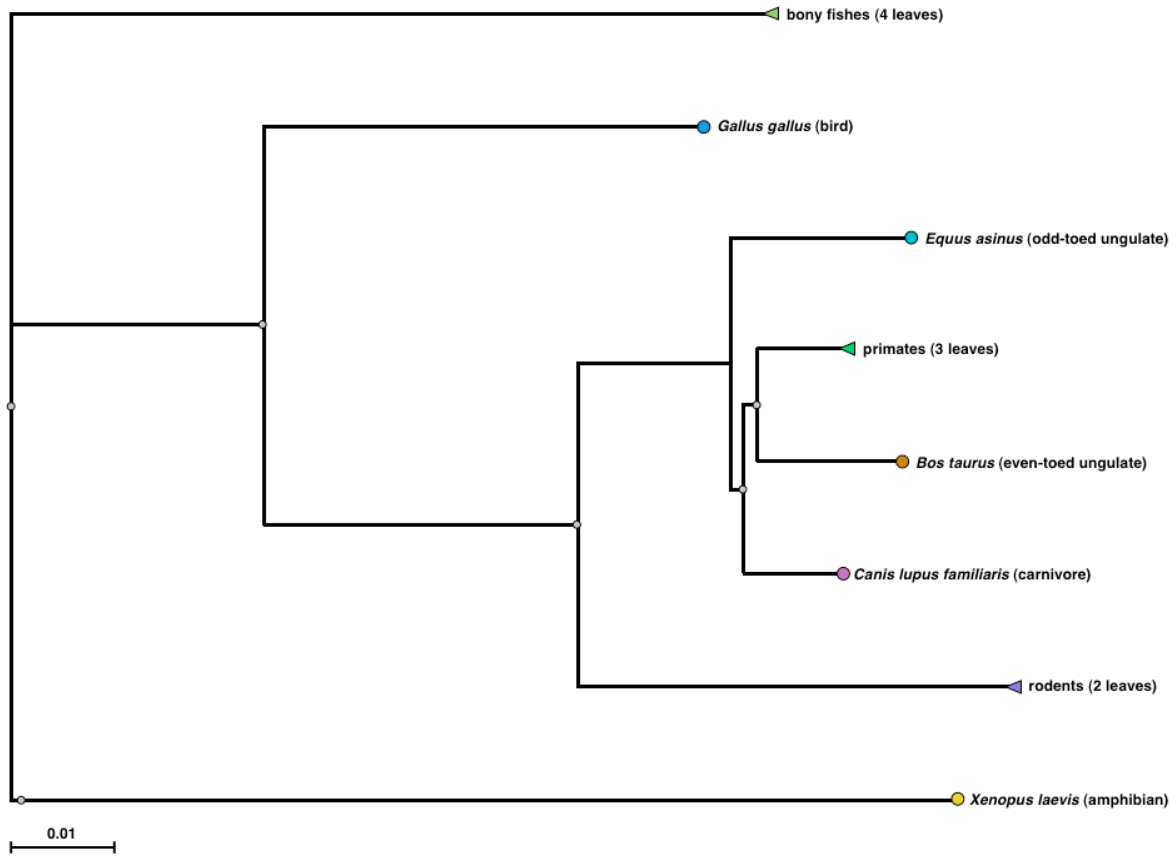

Tree 4. Force-rooted. (Slant)

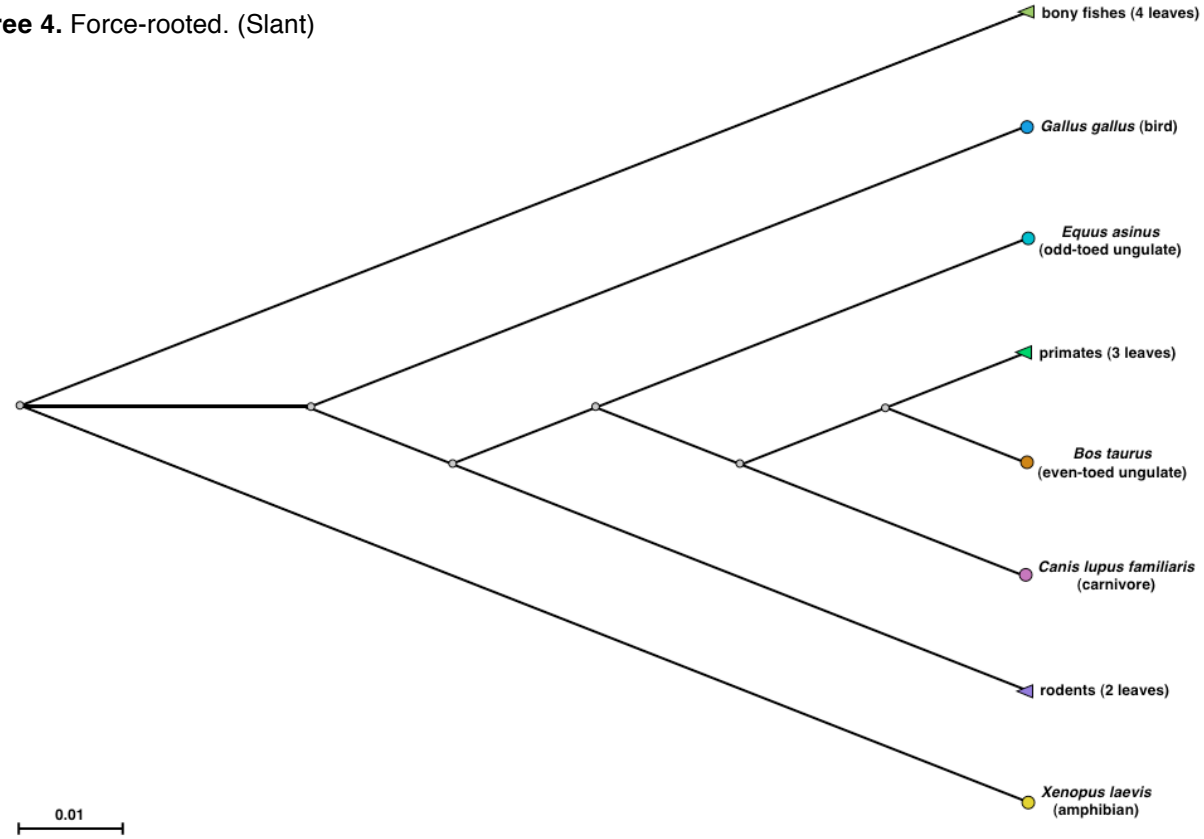

A.4. Sequence alignments for analysis of repeat sections

Multiple sequence alignments (all COL1A1 protein sequences in sample set). The order identity is given to the left. See text for further discussion.

```
G. gallus          1    MFSFVDSRLLLLIAATVLLTRGEGE-------EDIQTGSCVQDGLTYNDKDVWKPEPCQICVCDSGNILCDEVICEDTSD   73
H. sapiens         1    MFSFVDLRLLLLLAATALLTHGQEEGQVEGQDEDIPPITCVQNGLRYHDRDVWKPEPCRICVCDNGKVLCDDVICDETKN   80
P. troglodytes     1    MFSFVDLRLLLLLAATALLTHGQEEGQVEGQDEDIPPITCVQNGLRYHDRDVWKPEPCRICVCDNGKVLCDDVICDETKN   80
M. mulatta         1    MFSFVDLRLLLLLAATALLTHGQEEGQVEGQDEDIPPITCVQNGLRYHDRDVWKPEPCRICVCDNGKVLCDDVICDETKN   80
B. taurus          1    MFSFVDLRLLLLLAATALLTHGQEEGQEEGQEEDIPPVTCVQNGLRYHDRDVWKPVPCQICVCDNGNVLCDDVICDELKD   80
E. asinus          1    MFSFVDLRLLLLLAATALLTHGQEEGQEEGQEEDIPAVTCIQDGLRYHDRAVWKPEPCRVCICDNGNVLCDDVICEDTKN   80
C. lupus fam.      1    MFSFVDLRLLLLLAATALLTHGQEEGQ----EEDIPPVTCVQNGLRYYDRDVWKPEACRICVCDNGNVLCDDVICDETKN   76
R. norvegicus      1    MFSFVDLRLLLLLGATALLTHGQE---------DIPEVSCIHNGLRVPNGETWKPDVCLICICHNGTAVCDGVLCKEDLD   71
M. musculus        1    MFSFVDLRLLLLLGATALLTHGQE---------DIPEVSCIHNGLRVPNGETWKPEVCLICICHNGTAVCDDVQCNEELD   71
X. laevis          1    MFSFVDTRTLLLIAATILVARCQGE-------HDVQTSDCVQHGITYSNRDVWKPEDCQICVCDNGNILCDEVMCED-AD   72
D. rerio           1    MFSFVDIRLALLLSATVLLARGQGE-------DDRTGGSCTLDGQVYNDRDVWKPEPCQICVCDSGTVMCDEVICEDTSD   73
O. niloticus       1    MFSFVDLRLALLLSAAVLLVRAQGE-------DDRTGKSCTLDGQVFADRDVWKPEPCQICVCDSGTVMCDEVICEDTTD   73
O. mykiss          1    MFSFVDIRLALLLSATVLLARGQGE-------DDRTAGSCTLDGQFYNDRDVWKPEPCQICVCDSGTVMCDEVICEDTSD   73
C. auratus         1    MFSFVDIRLALLLSATVLLARGQGE-------DDRTGGSCTLDGQVYNDRDVWKPEPCQICVCDSGTVMCDEVICEDTTH   73

G. gallus         74    CPNAEIPFGECCPICPDVDASPVYPESAGVEGPKGDTGPRGDRGLPGPPGRDGIPGQPGLPGPPGPPGPPG---LGGNFA  150
H. sapiens        81    CPGAEVPEGECCPVCPDGSESPTDQETTGVEGPKGDTGPRGPRGPAGPPGRDGIPGQPGLPGPPGPPGPPGPPGLGGNFA  160
P. troglodytes    81    CPGAEVPEGECCPVCPDGSESPTDQETTGVEGPKGDTGPRGPRGPAGPPGRDGIPGQPGLPGPPGPPGPPGPPGLGGNFA  160
M. mulatta        81    CPGAEVPEGECCPVCPDGSESPTDQETTGVEGPKGDTGPRGPRGPAGPPGRDGIPGQPGLPGPPGPPGPPGPPGLGGNFA  160
B. taurus         81    CPNAKVPTDECCPVCPEGQESPTDQETTGVEGPKGDTGPRGPRGPAGPPGRDGIPGQPGLPGPPGPPGPPGPPGLGGNFA  160
E. asinus         81    CPGASVPKDECCPVCPEGQVSPTDDQTTGVEGPKGDTGPRGPRGPAGPPGRDGIPGQPGLPGPPGPPGPPGPPGLGGNFA  160
C. lupus fam.     77    CPGAQVPPGECCPVCPDGEASPTDQETTGVEGPKGDTGPRGPRGPAGPPGRDGIPGQPGLPGPPGPPGPPGPPGLGGNFA  156
R. norvegicus     72    CPNPQKREGECCPFCPEEYVSP-DAEVIGVEGPKGDPGPQGPRGPVGPPGQDGIPGQPGLPGPPGPPGPPGPPGLGGNFA  150
M. musculus       72    CPNPQRREGECCAFCPEEYVSP-NSEDVGVEGPKGDPGPQGPRGPVGPPGRDGIPGQPGLPGPPGPPGPPGPPGLGGNFA  150
X. laevis         73    CPNPVIVPGECCPVCTDNDAQ--YSEVTGVEGPKGDVGPKGDKGIAGPPGRDGIPGQPGIPGPPGPPGPPG---LGGNFA  147
D. rerio          74    CPNPVIPHDECCPVCPDDDFQE-----PSVEGPRGSPGDKGERGPAGPPGNDGIPGQPGLPGPPGPPGPPG---LGGNFS  145
O. niloticus      74    CPNPIIPHDECCPICPDDGFQE-----PQTEGTVGARGPKGDRGLPGPPGRDGMPGQPGLPGPPGPPGPPG---LGGNFS  145
O. mykiss         74    CPNPVIPHDECCPICPDDGFQE-----PKVEGPQGDRGAKGEPGPAGFPGNDGIPGQPGLPGPPGPPGPPG---LGGNFS  145
C. auratus        74    CPNPVIPHDECCPVCPDDEFLE-----PSVEGPSGPAGEKGDRGPPGPPGNDGIPGQPGLPGPPGPPGPPG---LGGNFS  145

G. gallus        151    PQMSYGYDEKSAG-VAVPGPMGPAGPRGLPGPPGAPGPQGFQGPPGEPGEPGASGPMGPRGPAGPPGKNGDDGEAGKPGR  229
H. sapiens       161    PQLSYGYDEKSTGGISVPGPMGPSGPRGLPGPPGAPGPQGFQGPPGEPGEPGASGPMGPRGPPGPPGKNGDDGEAGKPGR  240
P. troglodytes   161    PQLSYGYDEKSTGGISVPGPMGPSGPRGLPGPPGAPGPQGFQGPPGEPGEPGASGPMGPRGPPGPPGKNGDDGEAGKPGR  240
M. mulatta       161    PQLSYGYDEKSTGGISVPGPMGPSGPRGLPGPPGAPGPQGFQGPPGEPGEPGASGPMGPRGPPGPPGKNGDDGEAGKPGR  240
B. taurus        161    PQLSYGYDEKSTG-ISVPGPMGPSGPRGLPGPPGAPGPQGFQGPPGEPGEPGASGPMGPRGPPGPPGKNGDDGEAGKPGR  239
E. asinus        161    PQLSYGYDEKSAG-ISVPGPMGPSGPRGLPGPPGAPGPQGFQGPPGEPGEPGASGPMGPRGPPGPPGKNGDDGEAGKPGR  239
C. lupus fam.    157    PQMSYGYDEKSTGGISVPGPMGPSGPRGLPGPPGAPGPQGFQGPPGEPGEPGASGPMGPRGPPGPPGKNGDDGEAGKPGR  236
R. norvegicus    151    SQMSYGYDEKSAG-VSVPGPMGPSGPRGLPGPPGAPGPQGFQGPPGEPGEPGASGPMGPRGPPGPPGKNGDDGEAGKPGR  229
M. musculus      151    SQMSYGYDEKSAG-VSVPGPMGPSGPRGLPGPPGAPGPQGFQGPPGEPGEPGGSGPMGPRGPPGPPGKNGDDGEAGKPGR  229
X. laevis        148    PQMSYGYDEKSAG-ISMPGPMGPMGPRGPPGPSGSPGPQGFQGPPGEPGEPGASGAMGPRGSSGPPGKNGEDGEAGKPGR  226
D. rerio         146    PQMSGGFDEKSS-PMAVPGPMGPMGPRGAPGPPGPSGPQGFTGPPGEPGEAGAPGPMGPRGAAGPPGKNGEDGESGKPGR  224
O. niloticus     146    PQMSGGYDEKSP-AMPVPGPMGPMGPRGPPGPPGSSGPQGFTGPPGEAGEPGSPGPMGPRGPAGPPGKNGEDGESGKPGR  224
O. mykiss        146    PQMSGGFDEKSGGGMSMPGPMGPMGPRGPPGPPGSSGPQGFTGPPGEPGEAGSSGPMGPRGPAGPPGKNGDDGESGKPGR  225
C. auratus       146    PQMSGGYDEKSGGAMAVPGPMGAMGPRGPPGPPGTPGPQGFTGPPGEPGEAGAPGPMGPRGAAGPPGKNGEDGESGKPGR  225
```

G. gallus	230	PGQRGPPGPQGARGLPGTAGLPGMKGHRGFSGLDGAKGQPGPAGPKGEPGSPGENGAPGQMGPRGLPGERGRPGPSGPAG	309
H. sapiens	241	PGERGPPGPQGARGLPGTAGLPGMKGHRGFSGLDGAKGDAGPAGPKGEPGSPGENGAPGQMGPRGLPGERGRPGAPGPAG	320
P. troglodytes	241	PGERGPPGPQGARGLPGTAGLPGMKGHRGFSGLDGAKGDAGPAGPKGEPGSPGENGAPGQMGPRGLPGERGRPGAPGPAG	320
M. mulatta	241	PGERGPPGPQGARGLPGTAGLPGMKGHRGFSGLDGAKGDAGPAGPKGEPGSPGENGAPGQMGPRGLPGERGRPGAPGPAG	320
B. taurus	240	PGERGPPGPQGARGLPGTAGLPGMKGHRGFSGLDGAKGDAGPAGPKGEPGSPGENGAPGQMGPRGLPGERGRPGAPGPAG	319
E. asinus	240	PGERGPPGPQGARGLPGTAGLPGMKGHRGFSGLDGAKGDAGPAGPKGEPGSPGENGAPGQMGPRGLPGERGRPGAPGPAG	319
C. lupus fam.	237	PGERGPPGPQGARGLPGTAGLPGMKGHRGFSGLDGAKGDAGPAGPKGEPGSPGENGAPGQMGPRGLPGERGRPGAPGPAG	316
R. norvegicus	230	PGERGPPGPQGARGLPGTAGLPGMKGHRGFSGLDGAKGDTGPAGPKGEPGSPGENGAPGQMGPRGLPGERGRPGPPGSAG	309
M. musculus	230	PGERGPPGPQGARGLPGTAGLPGMKGHRGFSGLDGAKGDAGPAGPKGEPGSPGENGAPGQMGPRGLPGERGRPGPPGTAG	309
X. laevis	227	PGERGPPGPQGARGLPGTAGLPGMKGHRGFNGLDGAKGDSGPAGPKGEPGSPGENGAPGQVGPRGLSGERGRPGPSGPAG	306
D. rerio	225	PGERGPPGPQGARGFPGTPGLPGIKGHRGFSGLDGAKGDAGPAGPKGEPGAPGENGTPGAMGPRGLPGERGRAGPPGAAG	304
O. niloticus	225	PGERGPPGPQGARGFPGTPGLPGIKGHRGFSGLDGAKGDTGPAGPKGEAGTPGENGTPGAMGPRGLPGERGRAGATGAAG	304
O. mykiss	226	PGERGASGPQGARGFPGTPGLPGIKGHRGFSGLDGAKGESGPAGPKGEGGASGENGAAGAMGPRGLPGERGRAGPNGAAG	305
C. auratus	226	PGERGPPGAQGARGFPGTPGLPGIKGHRGFSGLDGSKGDTGPAGPKGEPGAAGENGTPGAMGPRGLPGERGRAGPPGAAG	305

G. gallus	310	ARGNDGAPGAAGPPGPTGPAGPPGFPGAAGAKGETGPQGARGSEGPQGSRGEPGPPGPAGAAGPAGNPGADGQPGAKGAT	389
H. sapiens	321	ARGNDGATGAAGPPGPTGPAGPPGFPGAVGAKGEAGPQGPRGSEGPQGVRGEPGPPGPAGAAGPAGNPGADGQPGAKGAN	400
P. troglodytes	321	ARGNDGATGAAGPPGPTGPAGPPGFPGAVGAKGEAGPQGPRGSEGPQGVRGEPGPPGPAGAAGPAGNPGADGQPGAKGAN	400
M. mulatta	321	ARGNDGATGAAGPPGPTGPAGPPGFPGAVGAKGEAGPQGPRGSEGPQGVRGEPGPPGPAGAAGPAGNPGADGQPGAKGAN	400
B. taurus	320	ARGNDGATGAAGPPGPTGPAGPPGFPGAVGAKGEGGPQGPRGSEGPQGVRGEPGPPGPAGAAGPAGNPGADGQPGAKGAN	399
E. asinus	320	ARGNDGATGAAGPPGPTGPAGPPGFPGAVGAKGEAGPQGARGSEGPQGVRGEPGPPGPAGAAGPAGNPGADGQPGAKGAN	399
C. lupus fam.	317	ARGNDGATGAAGPPGPTGPAGPPGFPGAVGAKGEAGPQGARGSEGPQGVRGEPGPPGPAGAAGPAGNPGADGQPGAKGAN	396
R. norvegicus	310	ARGNDGAVGAAGPPGPTGPTGPPGFPGAAGAKGEAGPQGARGSEGPQGVRGEPGPPGPAGAAGPAGNPGADGQPGAKGAN	389
M. musculus	310	ARGNDGAVGAAGPPGPTGPTGPPGFPGAVGAKGEAGPQGARGSEGPQGVRGEPGPPGPAGAAGPAGNPGADGQPGAKGAN	389
X. laevis	307	ARGNDGAPGAAGPPGSTGPSGPPGFPGGVGPKGDAGPQGSRGSDGPQGGRGEPGAPGQAGAAGPSGNPGSDGQPGAKGAT	386
D. rerio	305	ARGNDGAAGAAGPPGPTGPAGPPGFPGGPGSKGEVGPQGSRGAEGPQGARGEAGNPGPAGPAGPAGNNGADGAPGAKGAP	384
O. niloticus	305	ARGNDGAAGAAGPPGPTGPAGPPGFPGGPGAKGDAGAQGGRGPEGPAGARGEPGNPGPAGPAGPAGNPGSDGAPGAKGAP	384
O. mykiss	306	ARGNDGAAGAAGPPGPTGPAGAPGFPGGPGAKGEVGAQGARGGEGPQGSRGEAGNPGPAGAAGPAGNNGADGNPGTKGAP	385
C. auratus	306	ARGNDGAAGAAGPPGPTGPAGPPGFPGGPGAKGEVGAQGARGAEGPQGARGEPGNPGPAGAAGPAGNNGADGAPGLKGAP	385

G. gallus	390	GAPGIAGAPGFPGARGPSGPQGPSGAPGPKGNSGEPGAPGNKGDTGAKGEPGPAGVQGPPGPAGEEGKRGARGEPGPAGL	469
H. sapiens	401	GAPGIAGAPGFPGARGPSGPQGPGGPPGPKGNSGEPGAPGSKGDTGAKGEPGPVGVQGPPGPAGEEGKRGARGEPGPTGL	480
P. troglodytes	401	GAPGIAGAPGFPGARGPSGPQGPGGPPGPKGNSGEPGAPGSKGDTGAKGEPGPVGVQGPPGPAGEEGKRGARGEPGPTGL	480
M. mulatta	401	GAPGIAGAPGFPGARGPSGPQGPGGPPGPKGNSGEPGAPGSKGDTGAKGEPGPVGVQGPPGPAGEEGKRGARGEPGPTGL	480
B. taurus	400	GAPGIAGAPGFPGARGPSGPQGPSGPPGPKGNSGEPGAPGSKGDTGAKGEPGPTGIQGPPGPAGEEGKRGARGEPGPAGL	479
E. asinus	400	GAPGIAGAPGFPGARGPSGPQGPSGPPGPKGNSGEPGAPGNKGDTGAKGEPGPTGIQGPPGPAGEEGKRGARGEPGPTGL	479
C. lupus fam.	397	GAPGIAGAPGFPGARGPSGPQGPSGPPGPKGNSGEPGAPGNKGDTGAKGEPGPTGIQGPPGPAGEEGKRGARGEPGPTGL	476
R. norvegicus	390	GAPGIAGAPGFPGARGPSGPQGPSGAPGPKGNSGEPGAPGNKGDTGAKGEPGPAGVQGPPGPAGEEGKRGARGEPGPSGL	469
M. musculus	390	GAPGIAGAPGFPGARGPSGPQGPSGPPGPKGNSGEPGAPGNKGDTGAKGEPGATGVQGPPGPAGEEGKRGARGEPGPSGL	469
X. laevis	387	GAPGIAGAPGFPGARGAPGAQGPGGSPGPKGNNGEPGAQGNKGEAGAKGEPGPAGVQGPPGPSGEEGKRGSRGEPGPAGP	466
D. rerio	385	GAPGIAGAPGFPGPRGPPGAAGAAGAPGPKGNTGEAGAPGAKGEAGAKGEAGAQGVQGPPGPPGEEGKRGPRGEPGAGGA	464
O. niloticus	385	GAAGVAGAPGFPGPRGPSGPQGAAGAPGPKGNTGEAGAPGSKGEAGAKGEAGAPGVQGPPGPPGEEGKRGARGEPGAAGA	464
O. mykiss	386	GSSGIAGAPGFPGPRGPPGPQGAGGAPGPKGNTGEVGANGAKGEAGAKGESGPAGVQGPAGPAGEEGKRGGRGEPGGAGA	465
C. auratus	386	GAPGIAGAPGFPGPRGPSGPAGAAGAPGPKGNTGEVGAPGAKGEAGAKGEAGAQGVQGPPGPSGEEGKRGPRGEPGSAGS	465

G. gallus	470	PGPAGERGAPGSRGFPGADGIAGPKGPPGERGSPGAVGPKGSPGEAGRPGEAGLPGAKGLTGSPGSPGPDGKTGPPGPAG	549
H. sapiens	481	PGPPGERGGPGSRGFPGADGVAGPKGPAGERGSPGPAGPKGSPGEAGRPGEAGLPGAKGLTGSPGSPGPDGKTGPPGPAG	560
P. troglodytes	481	PGPPGERGGPGSRGFPGADGVAGPKGPAGERGSPGPAGPKGSPGEAGRPGEAGLPGAKGLTGSPGSPGPDGKTGPPGPAG	560
M. mulatta	481	PGPPGERGGPGSRGFPGADGVAGPKGPAGERGSPGPAGPKGSPGEAGRPGEAGLPGAKGLTGSPGSPGPDGKTGPPGPAG	560
B. taurus	480	PGPPGERGGPGSRGFPGADGVAGPKGPAGERGAPGPAGPKGSPGEAGRPGEAGLPGAKGLTGSPGSPGPDGKTGPPGPAG	559
E. asinus	480	PGPPGERGGPGARGFPGADGVAGPKGPAGERGAPGPAGPKGSPGEAGRPGEAGLPGAKGLTGSPGSPGPDGKTGPPGPAG	559
C. lupus fam.	477	PGPPGERGGPGSRGFPGADGVAGPKGPAGERGSPGPAGPKGSPGEAGRPGEAGLPGAKGLTGSPGSPGPDGKTGPPGPAG	556
R. norvegicus	470	PGPPGERGGPGSRGFPGADGVAGPKGPAGERGSPGPAGPKGSPGEAGRPGEAGLPGAKGLTGSPGSPGPDGKTGPPGPAG	549
M. musculus	470	PGPPGERGGPGSRGFPGADGVAGPKGPSGERGAPGPAGPKGSPGEAGRPGEAGLPGAKGLTGSPGSPGPDGKTGPPGPAG	549
X. laevis	467	PGPAGERGGPGSRGFPGSDGASGPKGAPGERGPVGPAGPKGSSGESGRPGEPGLPGAKGLTGSPGSPGSDGKTGPAGAPG	546
D. rerio	465	RGPTGERGAPGARGFPGADGAAGPRGAPGERGGPGVVGPKGATGEPGRNGEPGMPGSKGMTGSPGSPGPDGKTGLAGAPG	544
O. niloticus	465	RGGPGERGAPGGRGFPGSDGPAGPKGATGERGAPGLVGPKGATGEPGRTGEPGLPGAKGMTGSPGNPGPDGKIGPSGAPG	544
O. mykiss	466	RGAPGERGAPGSRGFPGSDGASGPKGGPGERGGAGVAGAKGNTGEPGRNGEPGMPGSKGMTGSPGSPGPDGKTGPSGAGG	545
C. auratus	466	RGPPGERGAPGARGFPGADGSAGPKGATGERGGPGIVGPKGATGEPGRNGEPGLPGSKGMTGSPGSPGPDGKTGAPGNPG	545

G. gallus	550	QDGRPGPAGPPGARGQAGVMGFPGPKGAAGEPGKPGERGAPGPPGAVGAAGKDGEAGAQGPPGPTGPAGERGEQGPAGAP	629
H. sapiens	561	QDGRPGPPGPPGARGQAGVMGFPGPKGAAGEPGKAGERGVPGPPGAVGPAGKDGEAGAQGPPGPAGPAGERGEQGPAGSP	640
P. troglodytes	561	QDGRPGPPGPPGARGQAGVMGFPGPKGAAGEPGKAGERGVPGPPGAVGPAGKDGEAGAQGPPGPAGPAGERGEQGPAGSP	640
M. mulatta	561	QDGRPGPPGPPGARGQAGVMGFPGPKGAAGEPGKAGERGVPGPPGAVGPAGKDGEAGAQGPPGPAGPAGERGEQGPAGSP	640
B. taurus	560	QDGRPGPPGPPGARGQAGVMGFPGPKGAAGEPGKAGERGVPGPPGAVGPAGKDGEAGAQGPPGPAGPAGERGEQGPAGSP	639
E. asinus	560	QDGRPGPPGPPGARGQAGVMGFPGPKGAAGEPGKAGERGVPGPPGAVGPAGKDGEAGAQGPPGPAGPAGERGEQGPAGSP	639
C. lupus fam.	557	QDGRPGPPGPPGARGQAGVMGFPGPKGAAGEPGKAGERGVPGPPGAVGPAGKDGEAGAQGPPGPAGPAGERGEQGPAGSP	636
R. norvegicus	550	QDGRPGPAGPPGARGQAGVMGFPGPKGTAGEPGKAGERGVPGPPGAVGPAGKDGEAGAQGAPGPAGPAGERGEQGPAGSP	629
M. musculus	550	QDGRPGPAGPPGARGQAGVMGFPGPKGTAGEPGKAGERGLPGPPGAVGPAGKDGEAGAQGAPGPAGPAGERGEQGPAGSP	629
X. laevis	547	QDGRAGPPGPPGARGQSGVMGFPGPKGAAGEPGKNGEKGVAGPPGAVGLPGKDGDAGAQGPPGPAGPAGERGEQGPAGGP	626
D. rerio	545	QDGRPGPPGPVGARGQPGVMGFPGPKGAAGEAGKPGERGVMGAIGATGAPGKDGDVGAPGAPGPAGPAGERGEQGAAGPP	624
O. niloticus	545	QDGRPGPPGPGGARGQPGVMGFPGPKGAAGEAGKPGERGTMGPTGPAGAPGKDGDVGAQGPPGPAGPAGERGEQGPAGSP	624
O. mykiss	546	QDGRPGPPGPVGARGQPGVMGFPGPKGAAGEGGKPGERGVMGPSGAVGAPGKDGDVGAPGAPGVAGPSGERGEQGAGGPP	625
C. auratus	546	QDGRPGPPGPVGARGQPGVMGFPGPKGAAGEAGKPGERGVMGALGATGAPGKDGDVGAPGAPGPAGPTGERGEQGPAGPP	625

G. gallus	630	GFQGLPGPAGPPGEAGKPGEQGVPGNAGAPGPAGARGERGFPGERGVQGPPGPQGPRGANGAPGNDGAKGDAGAPGAPGN	709
H. sapiens	641	GFQGLPGPAGPPGEAGKPGEQGVPGDLGAPGPSGARGERGFPGERGVQGPPGPAGPRGANGAPGNDGAKGDAGAPGAPGS	720
P. troglodytes	641	GFQGLPGPAGPPGEAGKPGEQGVPGDLGAPGPSGARGERGFPGERGVQGPPGPAGPRGANGAPGNDGAKGDAGAPGAPGS	720
M. mulatta	641	GFQGLPGPAGPPGEAGKPGEQGVPGDLGAPGPSGARGERGFPGERGVQGPPGPAGPRGANGAPGNDGAKGDAGAPGAPGS	720
B. taurus	640	GFQGLPGPAGPPGEAGKPGEQGVPGDLGAPGPSGARGERGFPGERGVQGPPGPAGPRGANGAPGNDGAKGDAGAPGAPGS	719
E. asinus	640	GFQGLPGPAGPPGESGKPGEQGVPGDLGAPGPSGARGERGFPGERGVQGPPGPAGPRGSNGAPGNDGAKGDAGAPGAPGS	719
C. lupus fam.	637	GFQGLPGPAGPPGEAGKPGEQGVPGDLGAPGPSGARGERGFPGERGVQGPPGPAGPRGANGAPGNDGAKGDAGAPGAPGS	716
R. norvegicus	630	GFQGLPGPAGPPGEAGKPGEQGVPGDLGAPGPSGARGERGFPGERGVQGPPGPAGPRGNNGAPGNDGAKGDTGAPGAPGS	709
M. musculus	630	GFQGLPGPAGPPGEAGKPGEQGVPGDLGAPGPSGARGERGFPGERGVQGPPGPAGPRGNNGAPGNDGAKGDTGAPGAPGS	709
X. laevis	627	GFQGLPGPPGPAGESGKPGEQGVPGDVGPSGPAGARGERGFPGERGAQGPPGPQGARGSNGAPGNDGAKGEAGAAGAPGG	706
D. rerio	625	GFQGLPGPQGATGEPGKSGEQGAPGEAGAPGPSGSRGDRGFPGERGAPGPAGPVGARGSPGSAGNDGAKGESGAAGAPGA	704
O. niloticus	625	GFQGLPGPQGAVGETGKPGEQGVPGEAGAPGPAGARGDRGFPGERGAPGAIGPAGARGSPGASGNDGAKGDAGAPGTPGA	704
O. mykiss	626	GFQGLSGPQGAIGETGKPGEQGLPGEGGAPGSAGSRGDRGFPGERGAPGPSGPAGARGSPGSAGNDGGKGEAGAAGAPGG	705
C. auratus	626	GFQGLTGPQGATGEPGKAGEQGVPGEAGAPGPSGSRGDRGFPGERGAPGPAGPAGARGSPGSAGNDGAKGDAGAPGAPGA	705

G. gallus	710	EGPPGLEGMPGERGAAGLPGAKGDRGDPGPKGADGAPGKDGLRGLTGPIGPPGPAGAPGDKGEAGPPGPAGPTGARGAPG	789
H. sapiens	721	QGAPGLQGMPGERGAAGLPGPKGDRGDAGPKGADGSPGKDGVRGLTGPIGPPGPAGAPGDKGESGPSGPAGPTGARGAPG	800
P. troglodytes	721	QGAPGLQGMPGERGAAGLPGPKGDRGDAGPKGADGSPGKDGVRGLTGPIGPPGPAGAPGDKGETGPSGPAGPTGARGAPG	800
M. mulatta	721	QGAPGLQGMPGERGAAGLPGPKGDRGDAGPKGADGSPGKDGVRGLTGPIGPPGPAGAPGDKGESGPSGPAGPTGARGAPG	800
B. taurus	720	QGAPGLQGMPGERGAAGLPGPKGDRGDAGPKGADGAPGKDGVRGLTGPIGPPGPAGAPGDKGEAGPSGPAGPTGARGAPG	799
E. asinus	720	QGAPGLQGMPGERGAAGLPGPKGDRGDAGPKGADGSPGKDGVRGLTGPIGPPGPAGAPGDKGETGPSGPAGPTGARGAPG	799
C. lupus fam.	717	QGAPGLQGMPGERGAAGLPGPKGDRGDAGPKGADGSPGKDGVRGLTGPIGPPGPAGAPGDKGEAGPSGPAGPTGARGAPG	796
R. norvegicus	710	QGAPGLQGMPGERGAAGLPGPKGDRGDAGPKGADGSPGKDGVRGLTGPIGPPGPAGAPGDKGETGPSGPAGPTGARGAPG	789
M. musculus	710	QGAPGLQGMPGERGAAGLPGPKGDRGDAGPKGADGSPGKDGARGLTGPIGPPGPAGAPGDKGEAGPSGPPGPTGARGAPG	789
X. laevis	707	QGPPGLQGMPGERGSSGLPGAKGDRGDQGVKGSDGTPGKDGVRGLTGPIGPPGPGGAPGDKGEAGPAGPAGPTGARGAPG	786
D. rerio	705	QGPPGLQGMPGERGAAGLPGLKGDRGDQGAKGADGAAGKDGIRGMTGPIGPPGPAGAPGDKGESGAQGLVGPTGARGPPG	784
O. niloticus	705	QGPPGLQGMPGERGAAGLPGLRGNRGDQGPKGADGTPGKDGPRGLTGPIGLPGPAGSPGDKGEPGAQGPVGPSGARGPPG	784
O. mykiss	706	QGPPGLQGMPGERGAGGLPGLKGDRGDQGVKGADGAGGKDGVRGMTGPIGPNGPAGSPGDKGETGAPGAVGPSGARGAPG	785
C. auratus	706	QGPPGLQGMPGERGSAGLPGLKGDRGDQGAKGTDGAPGKDGIRGMTGPIGPPGPAGAPGDKGETGAPGLVGPNGARGPPG	785

G. gallus	790	DRGEPGPPGPAGFAGPPGADGQPGAKGETGDAGAKGDAGPPGPAGPTGAPGPAGZVGAPGPKGARGSAGPPGATGFPGAA	869
H. sapiens	801	DRGEPGPPGPAGFAGPPGADGQPGAKGEPGDAGAKGDAGPPGPAGPAGPPGPIGNVGAPGAKGARGSAGPPGATGFPGAA	880
P. troglodytes	801	DRGEPGPPGPAGFAGPPGADGQPGAKGEPGDAGAKGDAGPPGPAGPAGPPGPIGNVGAPGPKGARGSAGPPGATGFPGAA	880
M. mulatta	801	DRGEPGPPGPAGFAGPPGADGQPGAKGEPGDAGAKGDAGPPGPAGPAGPPGPIGNVGAPGAKGARGSAGPPGATGFPGAA	880
B. taurus	800	DRGEPGPPGPAGFAGPPGADGQPGAKGEPGDAGAKGDAGPPGPAGPAGPPGPIGNVGAPGPKGARGSAGPPGATGFPGAA	879
E. asinus	800	DRGEPGPPGPAGFAGPPGADGQPGAKGEPGDAGAKGDAGPPGPAGPAGPPGPIGSVGAPGPKGARGSAGPPGATGFPGAA	879
C. lupus fam.	797	DRGEPGPPGPAGFAGPPGADGQPGAKGEPGDAGAKGDAGPPGPAGPTGPPGPIGNVGAPGPKGARGSAGPPGATGFPGAA	876
R. norvegicus	790	DRGEPGPPGPAGFAGPPGADGQPGAKGEPGDTGVKGDAGPPGPAGPAGPPGPIGNVGAPGPKGSRGAAGPPGATGFPGAA	869
M. musculus	790	DRGEAGPPGPAGFAGPPGADGQPGAKGEPGDTGVKGDAGPPGPAGPAGPPGPIGNVGAPGPKGPRGAAGPPGATGFPGAA	869
X. laevis	787	ERGESGPPGPAGFAGPPGADGQPGAKGEQGDSGAKGDAGPPGPAGPTGAPGPAGALGSPGPKGARGAPGPPGATGFPGAA	866
D. rerio	785	ERGETGAPGPAGFAGPPGADGLPGAKGEPGDNGAKGDAGAPGPAGATGAPGPQGPVGATGPKGARGAAGPPGATGFPGAA	864
O. niloticus	785	ERGEAGPPGPAGFAGPPGADGQPGAKGEPGDNGAKGDSGPPGPAGPTGAPGPQGPVGNTGPKGARGPAGPPGATGFPGAA	864
O. mykiss	786	ERGESGAPGPAGFAGPPGGDGQPGAKGEAGDNGAKGDGGAQGPAGPTGAPGPQGPAGNTGAKGARGAAGPPGATGFPGAA	865
C. auratus	786	ERGETGAPGPAGFAGPPGADGLPGAKGEPGDNGAKGDAGAPGPAGATGAPGPQGPVGSTGPKGARGAAGPPGATGFPGAA	865

G. gallus	870	GRVGPPGPSGNIGLPGPPGPAGKZGSKGPRGETGPAGRPGEPGPAGPPGPPGEKGSPGADGPIGAPGTPGPQGIAGQRGV	949
H. sapiens	881	GRVGPPGPSGNAGPPGPPGPAGKEGGKGPRGETGPAGRPGEVGPPGPPGPAGEKGSPGADGPAGAPGTPGPQGIAGQRGV	960
P. troglodytes	881	GRVGPPGPSGNAGPPGPPGPAGKEGGKGPRGETGPAGRPGEVGPPGPPGPAGEKGSPGADGPAGAPGTPGPQGIAGQRGV	960
M. mulatta	881	GRVGPPGPSGNAGPPGPPGPAGKEGGKGPRGETGPAGRPGEVGPPGPPGPAGEKGSPGADGPAGAPGTPGPQGIAGQRGV	960
B. taurus	880	GRVGPPGPSGNAGPPGPPGPAGKEGSKGPRGETGPAGRPGEVGPPGPPGPAGEKGAPGADGPAGAPGTPGPQGIAGQRGV	959
E. asinus	880	GRVGPPGPSGNAGPPGPPGPVGKEGGKGPRGETGPAGRPGEAGPPGPPGPAGEKGSPGADGPAGAPGTPGPQGIAGQRGV	959
C. lupus fam.	877	GRVGPPGPSGNAGPPGPPGPAGKEGGKGARGETGPAGRPGEVGPPGPPGPAGEKGSPGADGPAGAPGTPGPQGIAGQRGV	956
R. norvegicus	870	GRVGPPGPSGNAGPPGPPGPVGKEGGKGPRGETGPAGRPGEVGPPGPPGPAGEKGSPGADGPAGSPGTPGPQGIAGQRGV	949
M. musculus	870	GRVGPPGPSGNAGPPGPPGPVGKEGGKGPRGETGPAGRPGEVGPPGPPGPAGEKGSPGADGPAGSPGTPGPQGIAGQRGV	949
X. laevis	867	GRLGPPGPSGNAGPPGPSGPAGKEGAKGPRGETGPAGRSGEPGAAGPPGPPGEKGSPGSDGPAGAPGIPGPQGVAGSRGT	946
D. rerio	865	GRVGPPGPSGNSGPPGPPGPAGKEGQKGNRGETGPAGRTGEVGAAGPPGAPGEKGNPGAEGATGPAGIPGPQGIGGQRGI	944
O. niloticus	865	GRVGPPGPAGNAGPPGPPGPAGKEGPKGNRGETGPAGRPGELGAAGPPGPPGEKGSPGADGAPGSAGIPGPQGIAGQRGI	944
O. mykiss	866	GRFGPPGPSGNNGPPGTPGPGGKEGQKGNRGETGPAGRPGELGAAGPPGPKGEKGQPGGDGPNGPSGTPGPQGIGGQRGI	945
C. auratus	866	GRVGPPGPAGNAGPAGPSGAPGKEGQKGNRGETGPAGRTGEVGAAGPPGAPGEKGNPGAEGAPGSAGTPGPAGIAGQRGI	945

G. gallus	950	VGLPGQRGERGFPGLPGPSGEPGKQGPSGASGERGPPGPMGPPGLAGPPGEAGREGAPGAEGAPGRDGAAGPKGDRGETG	1029
H. sapiens	961	VGLPGQRGERGFPGLPGPSGEPGKQGPSGASGERGPPGPMGPPGLAGPPGESGREGAPGAEGSPGRDGSPGAKGDRGETG	1040
P. troglodytes	961	VGLPGQRGERGFPGLPGPSGEPGKQGPSGASGERGPPGPMGPPGLAGPPGESGREGAPGAEGSPGRDGSPGPKGDRGETG	1040
M. mulatta	961	VGLPGQRGERGFPGLPGPSGEPGKQGPSGASGERGPPGPMGPPGLAGPPGESGREGAPGAEGSPGRDGSPGAKGDRGETG	1040
B. taurus	960	VGLPGQRGERGFPGLPGPSGEPGKQGPSGASGERGPPGPMGPPGLAGPPGESGREGAPGAEGSPGRDGSPGAKGDRGETG	1039
E. asinus	960	VGLPGQRGERGFPGLPGPSGEPGKQGPSGASGERGPPGPVGPPGLAGPPGESGREGSPGAEGSPGRDGSPGPKGDRGETG	1039
C. lupus fam.	957	VGLPGQRGERGFPGLPGPSGEPGKQGPSGTSGERGPPGPMGPPGLAGPPGESGREGSPGAEGSPGRDGSPGPKGDRGETG	1036
R. norvegicus	950	VGLPGQRGERGFPGLPGPSGEPGKQGPSGASGERGPPGPMGPPGLAGPPGESGREGSPGAEGSPGRDGAPGAKGDRGETG	1029
M. musculus	950	VGLPGQRGERGFPGLPGPSGEPGKQGPSGSSGERGPPGPMGPPGLAGPPGESGREGSPGAEGSPGRDGAPGAKGDRGETG	1029
X. laevis	947	VGLPGMRGERGFSGLPGPAGEPGKQGPSGPSGERGPPGPSGPPGLGGPPGESGREGAPGSEGAPGRDGAVGPKGDRGEGG	1026
D. rerio	945	VGLPGQRGERGFPGLPGPSGEIGKQGPSGPSGERGPPGPMGPPGLAGPPGEPGREGTPGNEGSAGRDGAAGPKGDRGETG	1024
O. niloticus	945	VGLPGQRGERGFPGLAGPVGEPGKQGPSGPSGERGPPGPMGPPGLAGAPGEPGREGTPGNEGAAGRDGAPGPKGDRGESG	1024
O. mykiss	946	VGLPGQRGERGFPGLAGQLGEPGKQGPGGPFGERGPPGPMGPPGLAGAPGEPGREGTPGNEGSSGRDGAAGPKGERGESG	1025
C. auratus	946	VGLPGQRGERGFPGLPGQSGEPGKQGPSGPSGERGPPGPMGPPGLAGPPGEPGREGTPGNEGSAGRDGAAGPKGDRGETG	1025

G. gallus	1030	PAGPPGAPGAPGAPGPVGPAGKNGDRGETGPAGPAGPPGPAGARGPAGPQGPRGDKGETGEQGDRGMKGHRGFSGLQGPP	1109
H. sapiens	1041	PAGPPGAPGAPGAPGPVGPAGKSGDRGETGPAGPAGPVGPVGARGPAGPQGPRGDKGETGEQGDRGIKGHRGFSGLQGPP	1120
P. troglodytes	1041	PAGPPGAPGAPGAPGPVGPAGKSGDRGETGPAGPAGPVGPVGARGPAGPQGPRGDKGETGEQGDRGIKGHRGFSGLQGPP	1120
M. mulatta	1041	PAGPPGAPGAPGAPGPVGPAGKSGDRGETGPAGPAGPVGPVGARGPAGPQGPRGDKGETGEQGDRGIKGHRGFSGLQGPP	1120
B. taurus	1040	PAGPPGAPGAPGAPGPVGPAGKSGDRGETGPAGPAGPIGPVGARGPAGPQGPRGDKGETGEQGDRGIKGHRGFSGLQGPP	1119
E. asinus	1040	PAGPPGAPGAPGAPGPVGPAGKSGDRGEAGPAGPAGPIGPVGARGPAGPQGPRGDKGETGEQGDRGIKGHRGFSGLQGPP	1119
C. lupus fam.	1037	PAGPPGAPGAPGAPGPVGPAGKNGDRGETGPAGPAGPIGPVGARGPAGPQGPRGDKGETGEQGDRGIKGHRGFSGLQGPP	1116
R. norvegicus	1030	PAGPPGAPGAPGAPGPVGPAGKNGDRGETGPAGPAGPIGPAGARGPAGPQGPRGDKGETGEQGDRGIKGHRGFSGLQGPP	1109
M. musculus	1030	PAGPPGAPGAPGAPGPVGPAGKNGDRGETGPAGPAGPIGPAGARGPAGPQGPRGDKGETGEQGDRGIKGHRGFSGLQGPP	1109
X. laevis	1027	PAGPPGAPGAPGAPGPVGPAGKSGDRGETGPSGPAGPAGTAGARGPAGPQGPRGDKGEAGEQGERGMKGHRGFNGPSGPP	1106
D. rerio	1025	PSGTPGAPGPPGAAGPIGPAGKTGDRGETGPAGVPGPAGPSGPRGPSGPAGARGDKGETGEAGERGMKGHRGFTGMPGPP	1104
O. niloticus	1025	PAGAPGAPGPPGAPGPVGPAGKTGDRGETGPAGPAGAAGPAGPRGPAGAPGLRGDKGETGEAGERGMKGHRGFTGMQGPP	1104
O. mykiss	1026	VAGASGAPGPPGAPGAVGPAGKSGDRGESGPAGPAGIAGPAGPRGPSGPAGARGDKGESGEAGERGMKGHRGFTGMQGPP	1105
C. auratus	1026	SAGTPGAPGPPGAPGPIGPAGKTGDRGESGPAGPAGAVGPAGPRGPAGPAGARGDRGETGEAGERGMKGHRGFTGMQGPP	1105

G. gallus	1110	GPPGAPGEQGPSGASGPAGPRGPPGSAGAAGKDGLNGLPGPIGPPGPRGRTGEVGPVGPPGPPGPPGPPGPPSGGFDLSF	1189
H. sapiens	1121	GPPGSPGEQGPSGASGPAGPRGPPGSAGAPGKDGLNGLPGPIGPPGPRGRTGDAGPVGPPGPPGPPGPPGPPSAGFDFSF	1200
P. troglodytes	1121	GPPGSPGEQGPSGASGPAGPRGPPGSAGTPGKDGLNGLPGPIGPPGPRGRTGDAGPVGPPGPPGPPGPPGPPSGGFDFSF	1200
M. mulatta	1121	GPPGSPGEQGPSGASGPAGPRGPPGSAGAPGKDGLNGLPGPIGPPGPRGRTGDAGPVGPPGPPGPPGPPGPPSAGFDFSF	1200
B. taurus	1120	GPPGSPGEQGPSGASGPAGPRGPPGSAGSPGKDGLNGLPGPIGPPGPRGRTGDAGPAGPPGPPGPPGPPGPPSGGYDLSF	1199
E. asinus	1120	GPPGSPGEQGPSGASGPAGPRGPPGSAGAPGKDGLNGLPGPIGPPGPRGRTGDAGPVGPPGPPGPPGPPGPPSAGFDFSF	1199
C. lupus fam.	1117	GPPGSPGEQGPSGASGPAGPRGPPGSAGSPGKDGLNGLPGPIGPPGPRGRTGDAGPVGPPGPPGPPGPPGPPSGGFDFSF	1196
R. norvegicus	1110	GSPGSPGEQGPSGASGPAGPRGPPGSAGSPGKDGLNGLPGPIGPPGPRGRTGDSGPAGPPGPPGPPGPPGPPSGGYDFSF	1189
M. musculus	1110	GSPGSPGEQGPSGASGPAGPRGPPGSAGSPGKDGLNGLPGPIGPPGPRGRTGDSGPAGPPGPPGPPGPPGPPSGGYDFSF	1189
X. laevis	1107	GPPGSSGEQGPSGASGPAGPRGPPGSSGNPGKDGSNGLPGPIGPPGPRGRTGDVGPAGPPGPPGPPGPPGQSGGGFDFSF	1186
D. rerio	1105	GPPGPSGESGPAGASGPAGPRGPAGSAGSAGKDGMSGLPGPIGPPGPRGRNGEIGPAGPPGPPGPPGAPGPSGGGFDIGF	1184
O. niloticus	1105	GPPGTSGESGPAGAAGPAGPRGPSGAAGAPGKDGVSGLPGPTGPPGPRGRSGEMGPAGPPGPPGPPGAPGAPGGGFDLGF	1184
O. mykiss	1106	GPSGQSGESGPAGASGPAGPRGPSGSAGAAGKDGMSGLPGPIGPPGPRGRSGEMGPSGTPGPPGPPGPPGPPGGGFDMGF	1185
C. auratus	1106	GPPGPSGEPGPAGASGPAGPRGPGGSAGAAGKDGMSGLPGPIGPPGPRGRNGEIGPAGPPGPPGLPGPPGPSGGGFDIGF	1185

G. gallus	1190	LPQPPQEKAHDGGRYYRADDANVMRDRDLEVDTTLKSLSQQIENIRSPEGTRKNPARTCRDLKMCHGDWKSGEYWIDPNQ	1269
H. sapiens	1201	LPQPPQEKAHDGGRYYRADDANVVRDRDLEVDTTLKSLSQQIENIRSPEGSRKNPARTCRDLKMCHSDWKSGEYWIDPNQ	1280
P. troglodytes	1201	LPQPPQEKAHDGGRYYRADDANVVRDRDLEVDTTLKSLSQQIENIRSPEGSRKNPARTCRDLKMCHSDWKSGEYWIDPNQ	1280
M. mulatta	1201	LPQPPQEKAHDGGRYYRADDANVVRDRDLEVDTTLKSLSQQIENIRSPEGSRKNPARTCRDLKMCHSDWKSGEYWIDPNQ	1280
B. taurus	1200	LPQPPQEKAHDGGRYYRADDANVVRDRDLEVDTTLKSLSQQIENIRSPEGSRKNPARTCRDLKMCHSDWKSGEYWIDPNQ	1279
E. asinus	1200	LPQPPQEKSHDGGRYYRADDANVVRDRDLEVDTTLKSLSQQIENIRSPEGSRKNPARTCRDLKMCHSDWKSGEYWIDPNQ	1279
C. lupus fam.	1197	LPQPPQEKAHDGGRYYRADDANVVRDRDLEVDTTLKSLSQQIENIRSPEGSRKNPARTCRDLKMCHSDWKSGEYWIDPNQ	1276
R. norvegicus	1190	LPQPPQEKSQDGGRYYRADDANVVRDRDLEVDTTLKSLSQQIENIRSPEGSRKNPARTCRDLKMCHSDWKSGEYWIDPNQ	1269
M. musculus	1190	LPQPPQEKSQDGGRYYRADDANVVRDRDLEVDTTLKSLSQQIENIRSPEGSRKNPARTCRDLKMCHSDWKSGEYWIDPNQ	1269
X. laevis	1187	MPQPPQEKSHDG-RFYRADDANVMRDRDLEVDSTLKSLSKQIENIRSPEGTRKNPARTCRDLKMCHSDWKSGEYWIDPNQ	1265
D. rerio	1185	IAQP-QEKAPDPFRHFRADDANVMRDRDLEVDTTLKSLSQQIESIISPDGTKKNPARTCRDLKMCHPDWKSGEYWIDPDQ	1263
O. niloticus	1185	MVQP-QEKAPDPFRMYRADDANVLRDRDLEVDSTLKSLSQQIEQIRSPDGTRKNPARTCRDLKMCHPDWKSGEYWIDPDQ	1263
O. mykiss	1186	IAQPAQEKAPDPFRHFRADDANVMRDRDLEVDTTLKSLSQQIENIRSPEGTKKNPARTCRDLKMCHPDWKSGEYWIDPDQ	1265
C. auratus	1186	IAQP-MEKAPDPFRSYRADDANVMRDRDLEVDTTLKSLSQQIESIMSPDGTKKNPARTCRDLKMCHPDWKSGEYWIDPDQ	1264

G. gallus	1270	GCNLDAIKVYCNMETGETCVYPTQATIAQKNWYLSKNPKEKKHVWFGETMSDGFQFEYGGEGSNPADVAIQLTFLRLMST	1349
H. sapiens	1281	GCNLDAIKVFCNMETGETCVYPTQPSVAQKNWYISKNPKDKRHVWFGESMTDGFQFEYGGQGSDPADVAIQLTFLRLMST	1360
P. troglodytes	1281	GCNLDAIKVFCNMETGETCVYPTQPSVAQKNWYISKNPKDKRHVWFGESMTDGFQFEYGGEGSDPADVAIQLTFLRLMST	1360
M. mulatta	1281	GCNLDAIKVFCNMETGETCVYPTQPSVAQKNWYISKNPKDKRHVWFGESMTDGFQFEYGGQGSDPADVAIQLTFLRLMST	1360
B. taurus	1280	GCNLDAIKVFCNMETGETCVYPTQPSVAQKNWYISKNPKEKRHVWYGESMTGGFQFEYGGQGSDPADVAIQLTFLRLMST	1359
E. asinus	1280	GCNLDAIKVFCNMETGETCVYPTQPQVAQKNWYISKNPKDKRHVWYGESMTDGFQFEYGGQGSDPADVAIQLTFLRLMST	1359
C. lupus fam.	1277	GCNLDAIKVFCNMETGETCVYPTQPQVAQKNWYISKNPKEKRHVWYGESMTDGFQFEYGGQGSDPADVAIQLTFLRLMST	1356
R. norvegicus	1270	GCNLDAIKVYCNMETGQTCVFPTQPSVPQKNWYISPNPKEKKHVWFGESMTDGFQFEYGSEGSDPADVAIQLTFLRLMST	1349
M. musculus	1270	GCNLDAIKVYCNMETGQTCVFPTQPSVPQKNWYISPNPKEKKHVWFGESMTDGFPFEYGSEGSDPADVAIQLTFLRLMST	1349
X. laevis	1266	GCILDAIKVYCNMETGETCIYPTQSSIPQKSWYTSKNLREKKHVWFGEAMSDGFQFEYGSEGSNSADVTIQLTFLRLMAT	1345
D. rerio	1264	GCNQDAIKVYCNMETGETCVNPTESAIPKKNWYTSKNIKEKKHVWFGEAMTDGFQFEYGSEGSKPEDVNIQLTFLRLMST	1343
O. niloticus	1264	GCTQDAIKVYCNMETGETCVSPTQREVAKKNWYISKNIKEKKHVWFGEAMNEGFQFEYGSEGSLPEDVNIQMTFLRLMST	1343
O. mykiss	1266	GCTQDAIKVYCNMETGETCVYPTEADIPKKSWYTSKNIKEKKHVWFGEAMTDGFQFEYGSEGSNAKDVNIQLTFLRLMAT	1345
C. auratus	1265	GCNQDAIKVYCNMETGETCVYPAESSIPKKNWYTSKNIKEKKHVWFGEAMTDGFQFEYGSEGSKPEDVNIQLTFLRLMST	1344

G. gallus	1350	EATQNVTYHCKNSVAYMDHDTGNLKKALLLQGANEIEIRAEGNSRFTYGVTEDGCTSHTGAWGKTVIEYKTTKTSRLPII	1429
H. sapiens	1361	EASQNITYHCKNSVAYMDQQTGNLKKALLLQGSNEIEIRAEGNSRFTYSVTVDGCTSHTGAWGKTVIEYKTTKTSRLPII	1440
P. troglodytes	1361	EASQNITYHCKNSVAYMDQQTGNLKKALLLQGSNEIEIRAEGNSRFTYSVTVDGCTSHTGAWGKTVIEYKTTKTSRLPII	1440
M. mulatta	1361	EASQNITYHCKNSVAYMDQQTGNLKKALLLQGSNEIEIRAEGNSRFTYSVTVDGCTSHTGAWGKTVIEYKTTKTSRLRII	1440
B. taurus	1360	EASQNITYHCKNSVAYMDQQTGNLKKALLLQGSNEIEIRAEGNSRFTYSVTYDGCTSHTGAWGKTVIEYKTTKTSRLPII	1439
E. asinus	1360	EASQNITYHCKNSVAYMDQQTGNLKKALLLQGSNEIEIRAEGNSRFTYSVTYDGCTSHTGAWGKTVIEYKTTKTSRLPII	1439
C. lupus fam.	1357	EASQNITYHCKNSVAYMDQQTGNLKKALLLQGSNEIEIRAEGNSRFTYSVTYDGCTSHTGAWGKTVIEYKTTKTSRLPII	1436
R. norvegicus	1350	EASQNITYHCKNSVAYMDQQTGNLKKSLLLQGSNEIELRGEGNSRFTYSTLVDGCTSHTGTWGKTVIEYKTTKTSRLPII	1429
M. musculus	1350	EASQNITYHCKNSVAYMDQQTGNLKKALLLQGSNEIELRGEGNSRFTYSTLVDGCTSHTGTWGKTVIEYKTTKTSRLPII	1429
X. laevis	1346	EASQNITYHCKNSVAYMDQATGNLKKALLLQGSNEIEIRAEGNSRFTYSVVEDGCTQHTGEWGKTVIDYKTTKTSRLPIT	1425
D. rerio	1344	EASQNITYHCKNSIAYMDQASGNLKKALLLQGSNEIEIRAEGNSRFTYSVTEDGCTSHTGAWGKTVIDYKTTKTSRLPII	1423
O. niloticus	1344	EASQNITYHCKNSVAYMDAAAGNLKKALLLQGSNEIEIRAEGNSRFTYSVLEDGCTSHTGTWGKTVIDYKTSKTSRLPII	1423
O. mykiss	1346	EASQNITYHCKNSIAYMDQQSGNLKKSLLLQGSNEIEIRAEGNSRFTYSVTEDGCTSHTGAWGKTVIDYKTTKTSRLPII	1425
C. auratus	1345	EASQNITYHCKNSIAYMDQASGNLKKALLLQGSNEIEIRAEGNSRFTYSVTEDGCTSHTGAWGKTVIDHKTTKTSRLPII	1424

G. gallus	1430	DLAPMDVGAPDQEFGIDIGPVCFL	1453
H. sapiens	1441	DVAPLDVGAPDQEFGFDVGPVCFL	1464
P. troglodytes	1441	DVAPLDVGAPDQEFGFDVGPVCFL	1464
M. mulatta	1441	DVAPLDVGAPDQEFGFDVGHVCFL	1464
B. taurus	1440	DVAPLDVGAPDQEFGFDVGPACFL	1463
E. asinus	1440	DVAPLDIGAPDQEFGIDIGPVCFL	1463
C. lupus fam.	1437	DVAPLDVGAPDQEFGMDIGPVCFL	1460
R. norvegicus	1430	DVAPLDIGAPDQEFGMDIGPACFV	1453
M. musculus	1430	DVAPLDIGAPDQEFGLDIGPACFV	1453
X. laevis	1426	DVAPMDIGAPDQEFGIDIGPVCFV	1449
D. rerio	1424	DIAPMDVGAPNQEFGIEVGPVCFL	1447
O. niloticus	1424	DIAPMDVGAPDQEFGFEVGPVCFL	1447
O. mykiss	1426	DIAPMDVGAPNQEFGIEVGPVCFL	1449
C. auratus	1425	DIAPMDVGAPNQEFGIEVGPVCFL	1448

Appendix B. Bone strength data published by J. D. Currey.

The data given in the table below were originally published in:

> Currey, JD. 1999. "The design of mineralised hard tissues for their mechanical functions." *The Journal of Experimental Biology* **202**:3285-3294.

They are included to illustrate the generalizations of bone mechanical properties given in the text in section 1.1.5. The generalizations are reiterated here for context.

1. The strength of compact femur bone is higher in compression than in tension.
2. The strength of compact femur bone is higher for larger mammals.
3. Primary lamellar bone has superior mechanical properties to secondary osteonal bone, and both are superior to woven bone.
4. Younger bone tissue is both stronger and tougher than older bone tissue, a fact that is dependent on remodeling, cross-linking, and resorption.

Table B.1 Bone strength data originally collected by J. D. Currey and published in *The Journal of Experimental Biology* (reference given above).

Specimen	Ultimate strength, σ_{ult}, tension (MPa)	Young's modulus, E (GPa)
Sarus crane (ossif. tendon)	271	17.7
Sarus crane (tibiotarsus)	254	23.5
Red deer (immature antler)	250	7.2
Axis deer (femur)	221	31.6
Fallow deer (radius)	213	25.5
Flamingo (tibiotarsus)	212	28.2
King penguin (ulna)	193	22.9
Wallaby (femur)	183	21.8
Human, adult (femur)	166	16.7
Polar bear (femur)	161	22.2
Horse (femur)	152	24.5
Roe deer (femur)	150	18.4
Cow (femur)	148	26.1

Appendix C. UCMP specimen catalogue information.

Table C.1 *Struthio* femur.

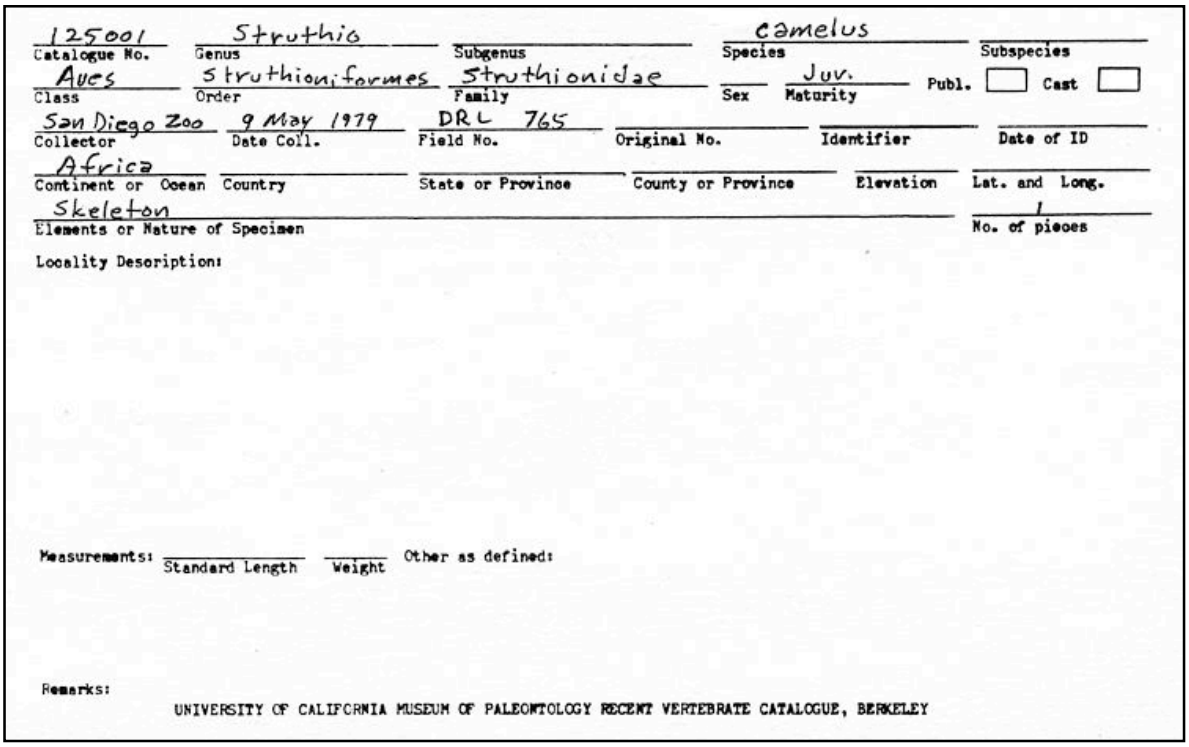

125001 | Struthio | | camelus | | |
Catalogue No. | Genus | Subgenus | Species | Subspecies |
Aves | Struthioniformes | Struthionidae | | Juv. | Publ. ☐ | Cast ☐ |
Class | Order | Family | Sex | Maturity |
San Diego Zoo | 9 May 1979 | DRL 765 | | | |
Collector | Date Coll. | Field No. | Original No. | Identifier | Date of ID |
Africa | | | | | |
Continent or Ocean | Country | State or Province | County or Province | Elevation | Lat. and Long. |
Skeleton | 1 |
Elements or Nature of Specimen | No. of pieces |
Locality Desoription:

Measurements: Standard Length | Weight | Other as defined:

Remarks:

UNIVERSITY OF CALIFORNIA MUSEUM OF PALEONTOLOGY RECENT VERTEBRATE CATALOGUE, BERKELEY

Table C.2 *Rhea* femur.

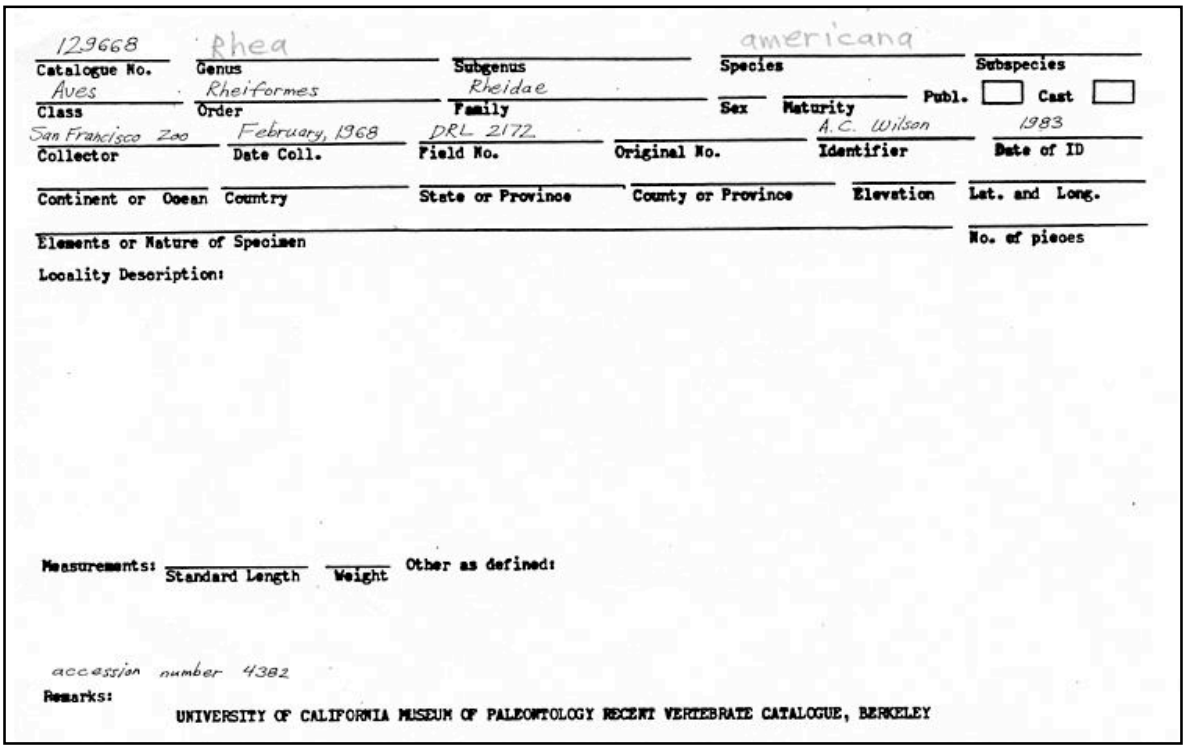

129668 | Rhea | | americana | | |
Catalogue No. | Genus | Subgenus | Species | Subspecies |
Aves | Rheiformes | Rheidae | | | Publ. ☐ | Cast ☐ |
Class | Order | Family | Sex | Maturity |
San Francisco Zoo | February, 1968 | DRL 2172. | | A.C. Wilson | 1983 |
Collector | Date Coll. | Field No. | Original No. | Identifier | Date of ID |
Continent or Ocean | Country | State or Province | County or Province | Elevation | Lat. and Long. |
Elements or Nature of Specimen | No. of pieces |
Locality Desoription:

Measurements: Standard Length | Weight | Other as defined:

accession number 4382

Remarks:

UNIVERSITY OF CALIFORNIA MUSEUM OF PALEONTOLOGY RECENT VERTEBRATE CATALOGUE, BERKELEY

Table C.3 *Caiman* femur.

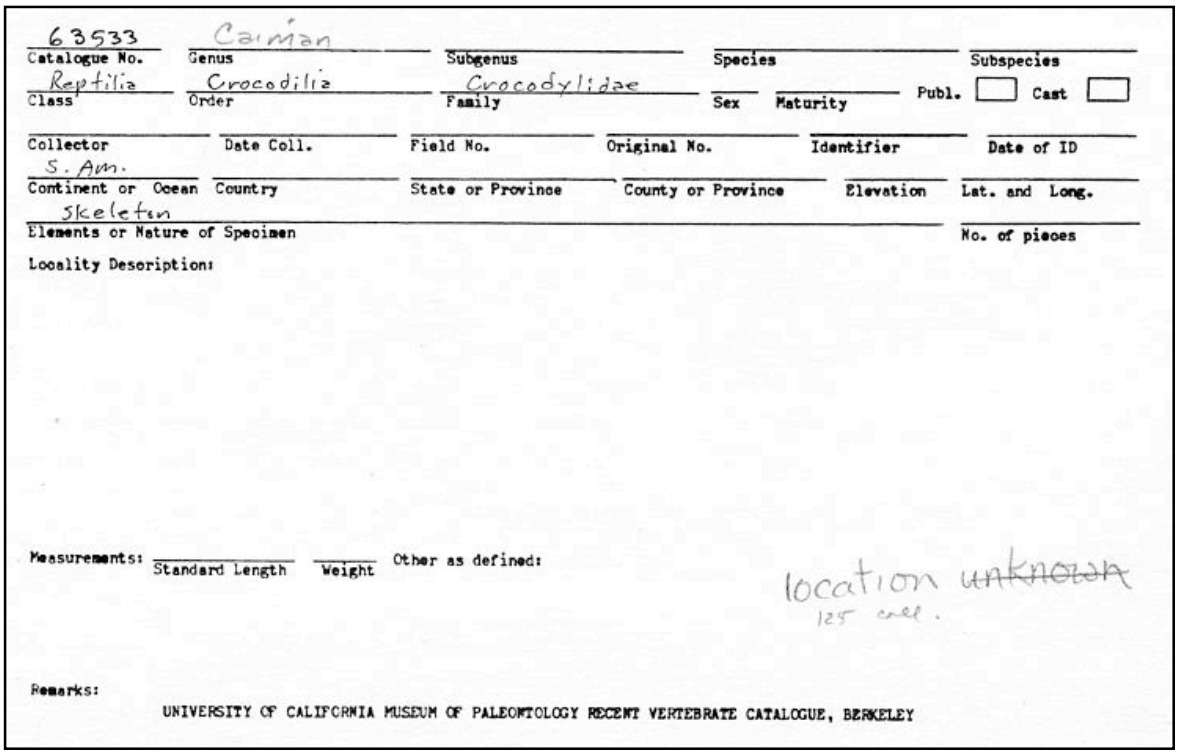
63533 Caiman
Catalogue No. Genus Subgenus Species Subspecies
Reptilia Crocodilia Crocodylidae
Class Order Family Sex Maturity Publ. ☐ Cast ☐
Collector Date Coll. Field No. Original No. Identifier Date of ID
S. Am.
Continent or Ocean Country State or Province County or Province Elevation Lat. and Long.
skeleton
Elements or Nature of Specimen No. of pieces
Locality Description:
Measurements: Standard Length Weight Other as defined:
location unknown
125 mile.
Remarks:
UNIVERSITY OF CALIFORNIA MUSEUM OF PALEONTOLOGY RECENT VERTEBRATE CATALOGUE, BERKELEY

Table C.4 *Pristichampsus* femur.

Catalogue no.	170767	**Class**	Reptilia
Location ID	V79006	**Order**	Crocodylia
Location name	Black Mountain SW 1	**Family**	Crocodylidae
Continent	North America	**Genus**	Pristichampsus
County	United States	**Species**	vorax
State	Wyoming	**Epoch**	Eocene
County	Sweetwater	**Storage age**	Bridgerian
Identified by	C. Brochu, 1998	**Formation**	Bridger
Collector	J. H. Hutchison	**Elements**	100+, skull, skeleton
Collection date	Aug. 1, 1971		

Table C.5 Hadrosaur radius.

Catalogue no.	175247	**Class**	Reptilia
Location ID	V85091	**Order**	Ornithischia
Location name	Poverty Bar - General	**Family**	Hadrosauridae
Continent	North America	**Era/eon**	Mesozoic
County	United States	**Period**	Cretaceous
State	Alaska	**Epoch**	Late cretaceous
County	North slope borough	**Storage age**	Maastrichtian
Identified by	G. Nelms, 1985	**Formation**	Prince Creek
Collector	UCMP field party	**Elements**	1, partial radius
Collection date	Aug., 1985		

Table C.6 Hadrosaur femur.

Hadrosaur femur			
Catalogue no.	169073	**Class**	Reptilia
Location ID	V85091	**Order**	Ornithischia
Location name	Poverty Bar - General	**Family**	Hadrosauridae
Continent	North America	**Era/Eon**	Mesozoic
County	United States	**Period**	Cretaceous
State	Alaska	**Epoch**	Late Cretaceous
County	North Slope Borough	**Storage age**	Maastrichtian
Identified by	M. B. Goodwin, 1999	**Formation**	Prince Creek
Collector	UC party	**Elements**	1, distal femur
Collection date	1985		

Table C.7 *Tyrannosaurus* femur.

***Tyrannosaurus rex* femur**			
Catalogue no.	136517	**Class**	Reptilia
Location ID	V83075	**Order**	Saurischia
Location name	Cake Walk	**Family**	Tyrannosauridae
Continent	North America	**Genus**	Tyrannosaurus
County	United States	**Species**	rex
State	Montana	**Period**	Cretaceous
County	Garfield	**Epoch**	Late Cretaceous
Identified by	M. T. Greenwald, 1982	**Storage age**	Maastrichtian
Collector	M. T. Greenwald	**Formation**	Hell Creek
Collection date	Aug., 1982	**Elements**	1, mid femur

Appendix D. Back-scattered electron surface maps of the specimen set.

Figure D.1 *Struthio* femur.

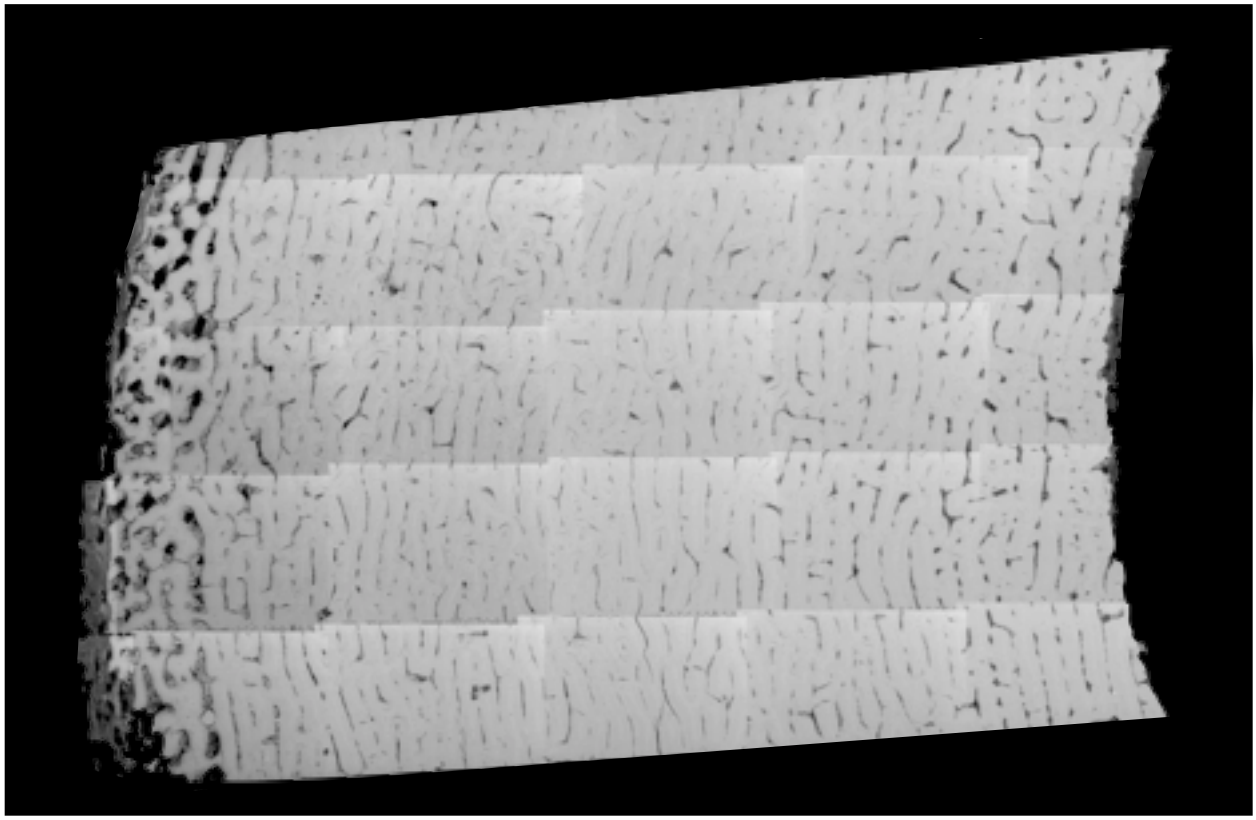

Figure D.2 *Rhea* femur.

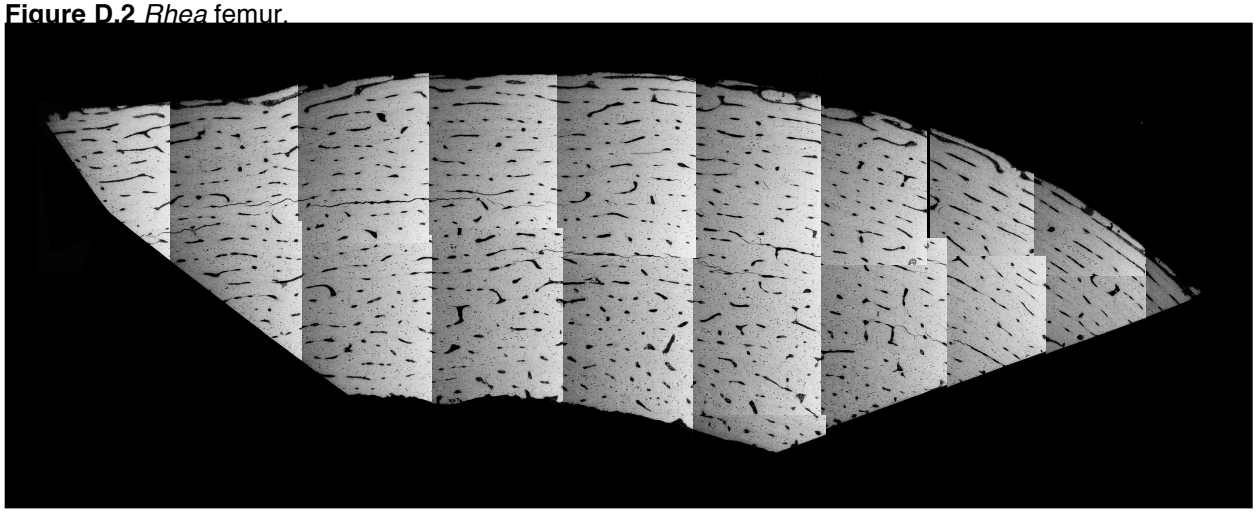

Figure D.3 *Caiman* femur.

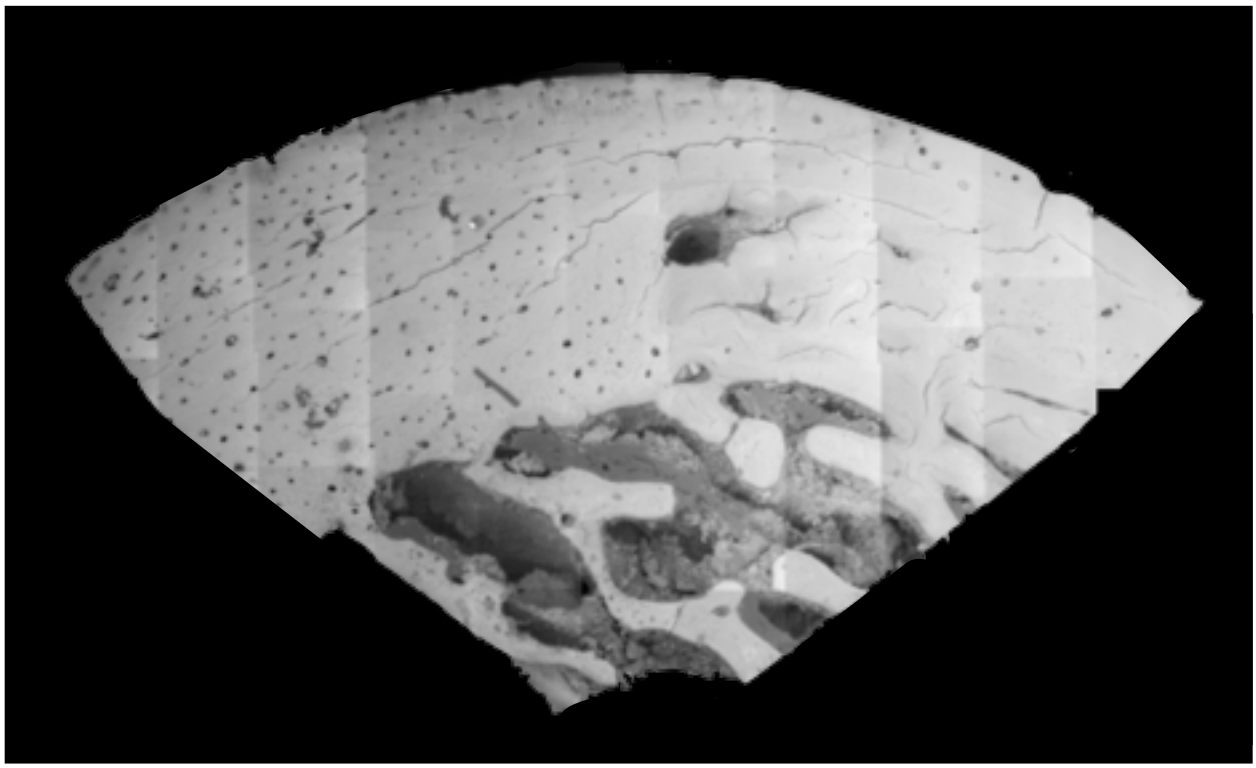

Figure D.4 *Pristichampsus* femur.

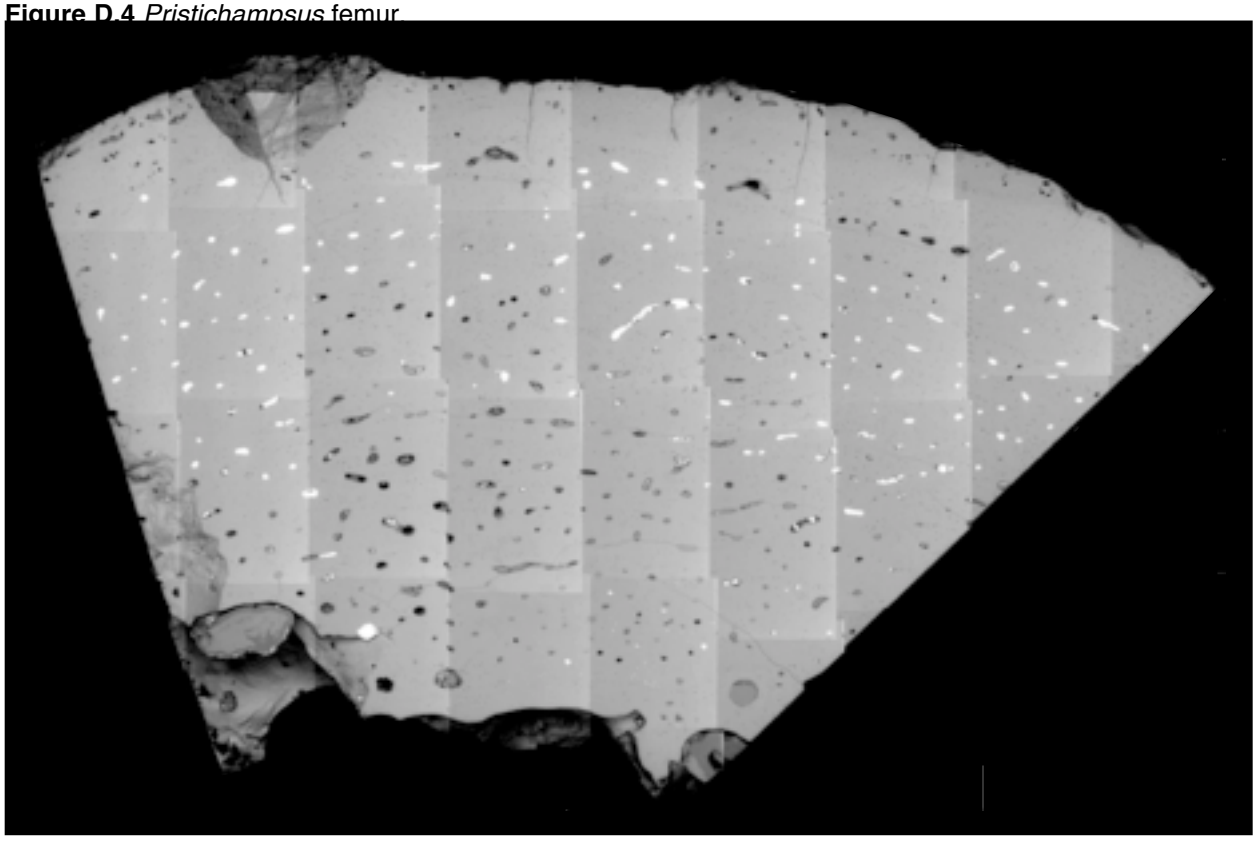

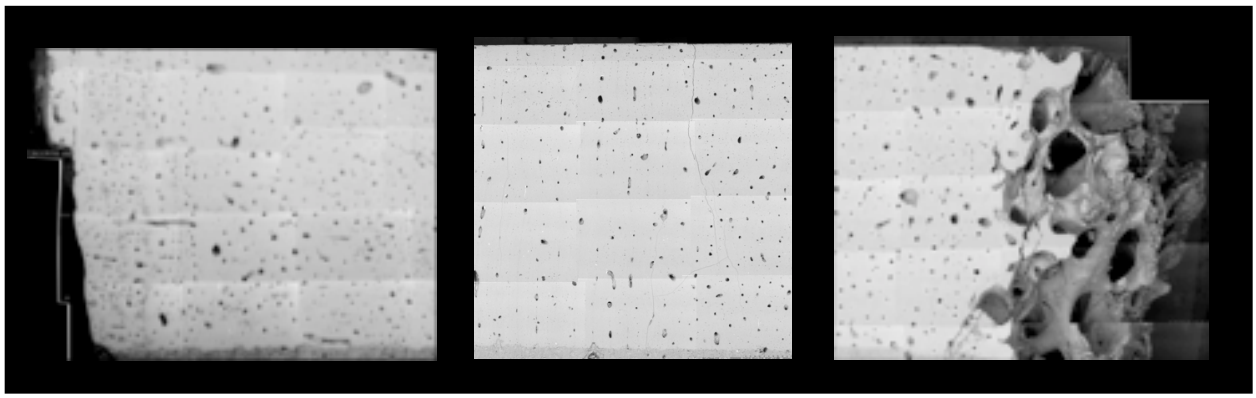

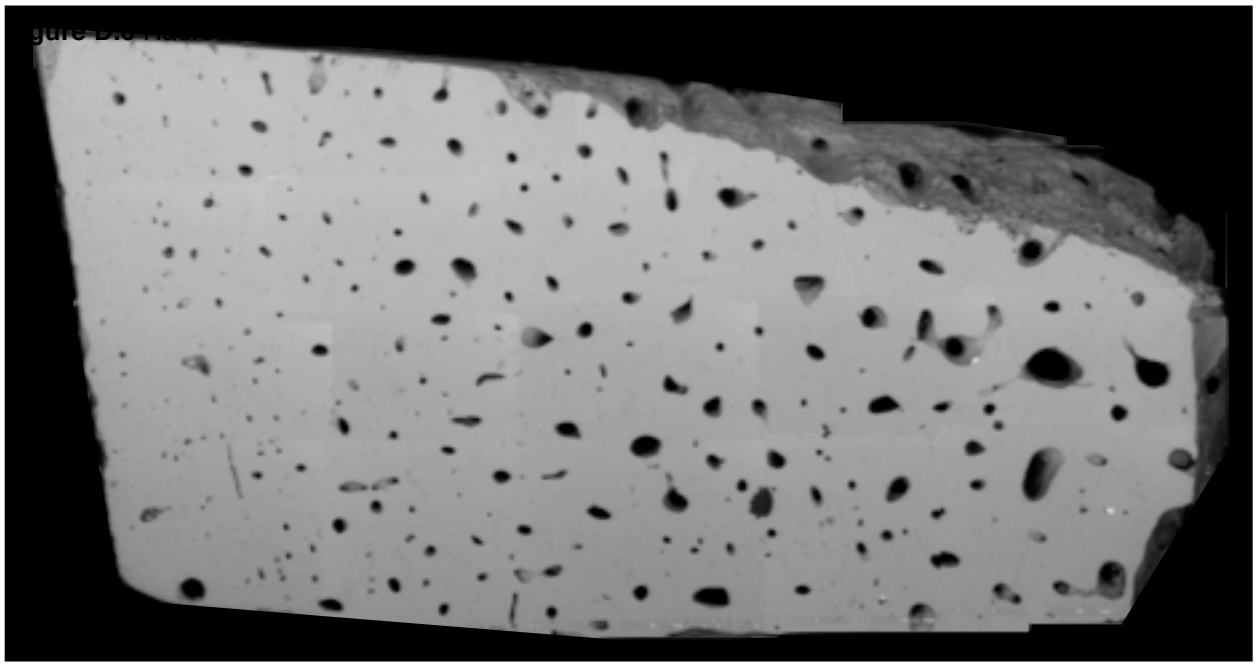

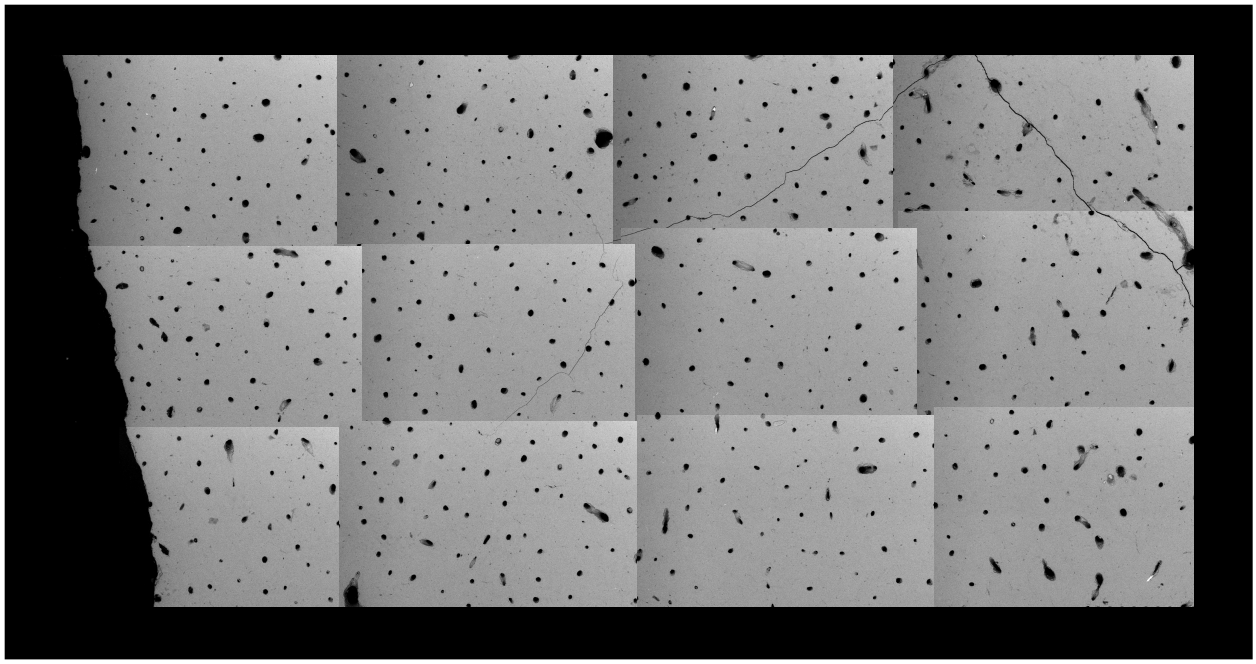

Appendix E. Supporting EDS data for *Tyrannosaurus* trabecular bone diagenetic alteration.

Figure E.1 Spot 1, in bulk bone.

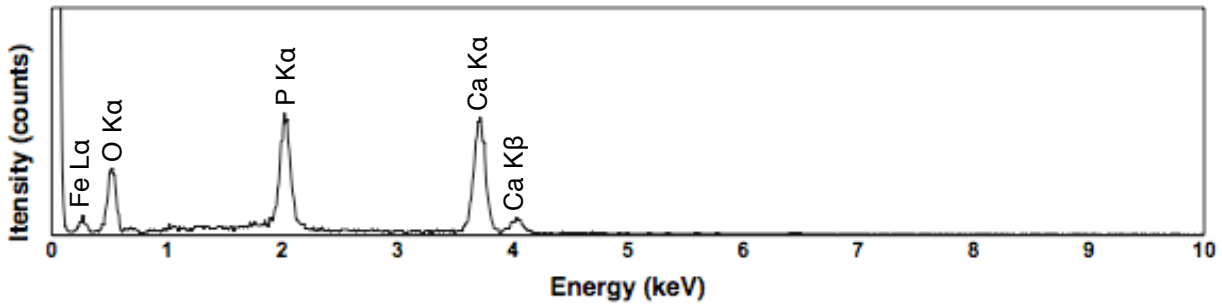

Figure E.2 Spot 2, in bulk bone.

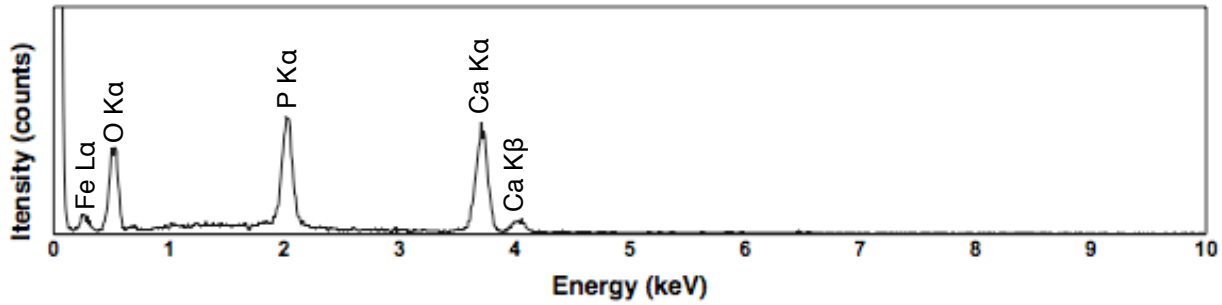

Figure E.3 Spot 3, in mineral crust.

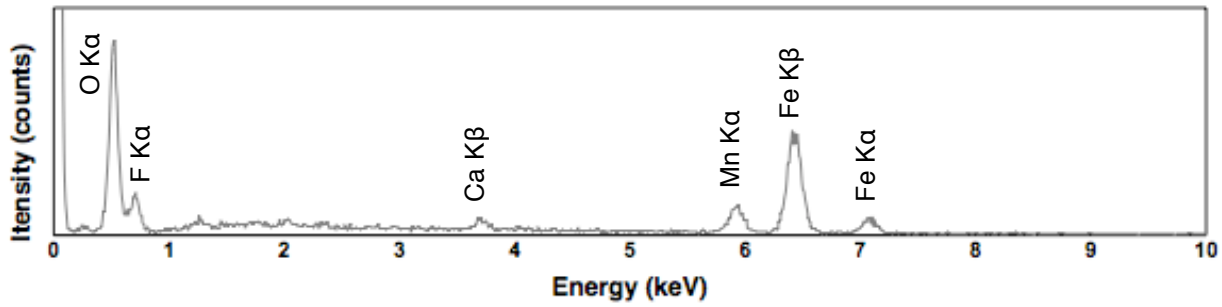

Figure E.4 Spot 4, in mineral crust.

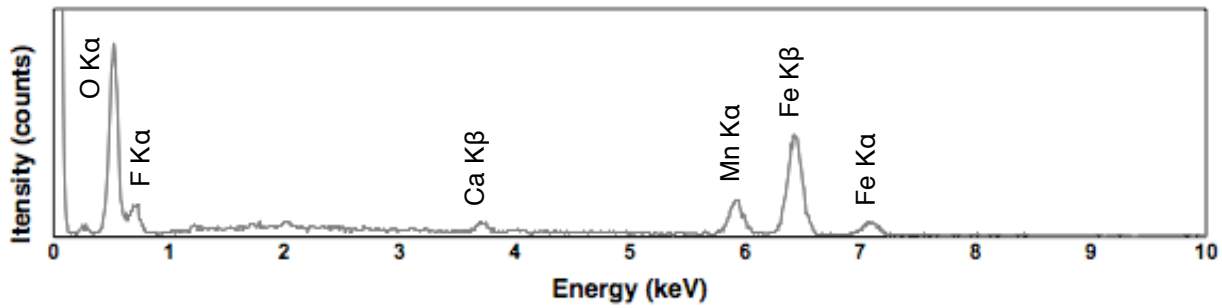

Appendix F. Physiological characters of significance

The following data set (Table F.1) was extracted from the *Pristichampsus*, hadrosaur radius, and *Tyrannosaurus* bones. The values reported here are averages obtained from multiple images. While this data is not the focus of my work, I did pursue the small side investigation to demonstrate that the extensive preservation of these features in fossil bone. This processing was carried out by an undergraduate student in the Department of Materials Science and Engineering as part of a research project. The processing protocol described in the text also was developed by this student, Riley Reese. The values (threshold, circularity) used for cut-off levels are given, as well. Examples of the specimen images following processing are shown in Figure F.1.

Table F.1 Example data gleaned from three fossil bone specimens following SEM image capture and image processing.

Pristichampsus			
Character	**Osteons**	**Osteocyte lacunae**	**Cut-off values**
Density (#/mm^2)	21.5	207.5	Threshold = 35
Area (μm^2)	1123.6	15.44	Circularity = 0.2 - 1
Diameter (μm)	37.8	4.4	**BV/TV**
Circularity	0.62	0.50	95.7%

Hadrosaur radius			
Character	**Osteons**	**Osteocyte lacunae**	**Cut-off values**
Density (#/mm^2)	19.2	94.6	Threshold = 160
Area (μm^2)	690.8	21.39	Circularity = 0.2 - 1
Diameter (μm)	29.7	5.2	**BV/TV**
Circularity	0.36	0.41	94.9%

Tyrannosaurus			
Character	**Osteons**	**Osteocyte lacunae**	**Cut-off values**
Density (#/mm^2)	46.7	56.48	Threshold = 113
Area (μm^2)	412.7	14.4	Circularity = 0.2 - 1
Diameter (μm)	22.8	4.3	**BV/TV**
Circularity	0.42	0.37	94.9%

Figure F.1 Example SEM images following image processing. In these images, the blue, highlighted regions indicate selections used to calculate the osteon mean values. Osteons remaining in black were either excluded due to violation of the circularity requirement or were not fully within the frame. (a) *Pristichampsus*, (b) hadrosaur radius, (c) *Tyrannosaurus.*

(a)

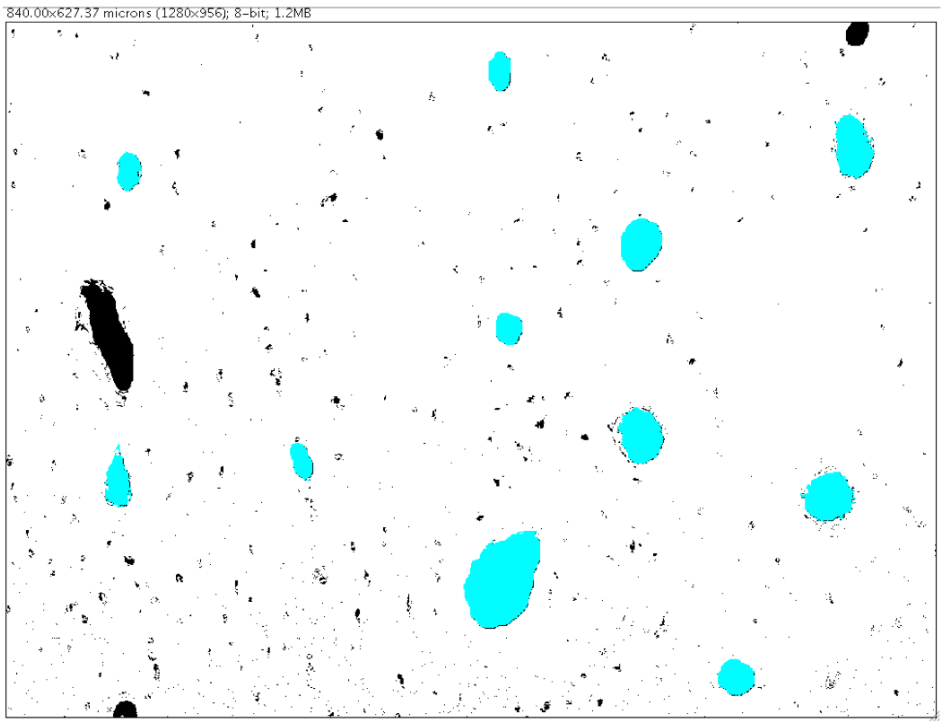

(b)

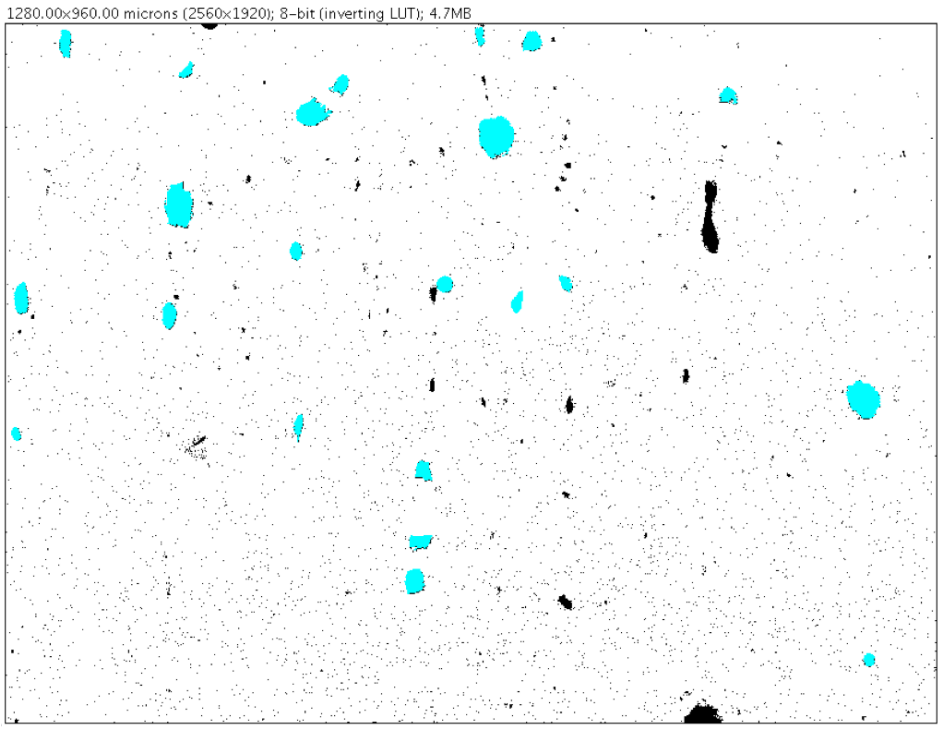

(c)

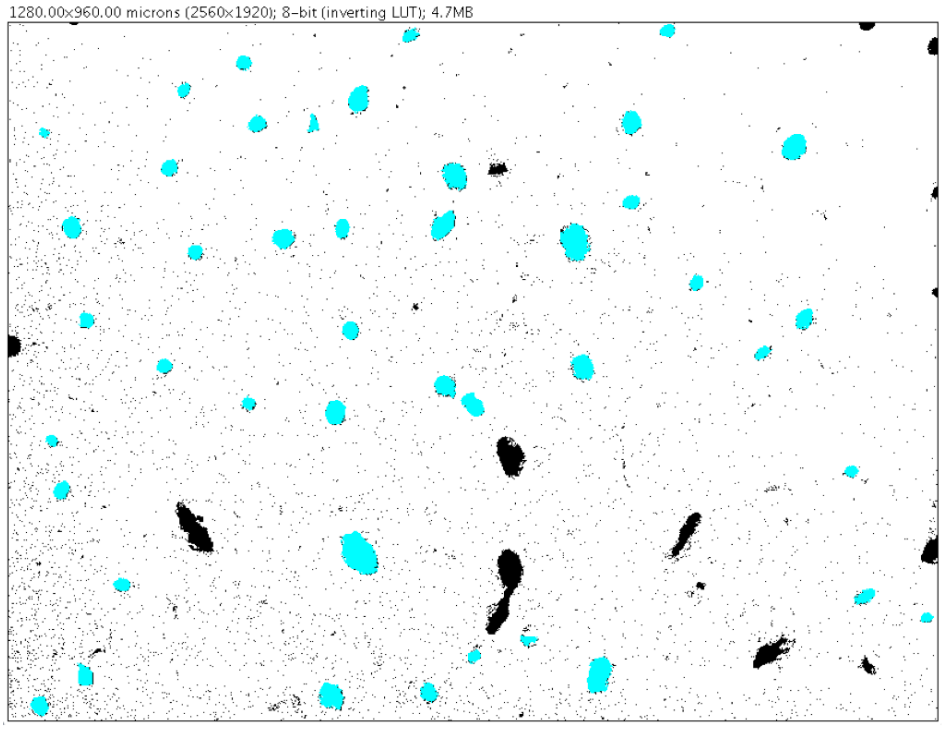

Appendix G. Electron microprobe WDS data.

The data set given below is the summary of all data collected from the electron microprobe WDS system. The values are reported for each element sampled, per specimen, as both the average (Avg) and standard deviations (St Dev) of 5-10 sampling points. The number of sampling points that could be selected depended on the specimen size and the degree of mineral in-filling, where distinctly in-filled regions were specifically avoided. It should be noted that the ostrich specimen was analyzed twice, for a total of 20 sample points. The total at.% values are given in the final row, summed from all of the average values.

Table G.1 Electron microprobe WDS data for the full specimen set. The bold-faced values are averages, and the lower values are standard deviations. All data was collected from between 5 - 10 sampling points, restricted between osteons and visible altered osteocyte lacunae. Specimen size restricted the number of samples that could be collected. Locations were chosen to span the specimen surfaces.

	Specimen						
	Struthio	***Rhea***	***Caiman***	***Pristich.***	**Hadro. radius**	**Hadro. femur**	***Tyrann.***
Element at.%	**Avg** +/- St Dev	**Avg** +/- St Dev	**Avg** +/- St Dev	**Avg** +/- St Dev	**Avg** +/- St Dev	**Avg** +/- St Dev	**Avg** +/- St Dev
O	**64.0624** +/- 0.6615	**65.4955** +/- 0.50604	**66.4129** +/- 0.40516	**63.0518** +/- 0.48094	**62.7792** +/- 0.20717	**60.6236** +/- 0.33507	**62.3534** +/- 0.15056
F	**0.0291** +/- 0.03923	**0.0045** +/- 0.01423	**0.241** +/- 0.25939	**3.7625** +/- 0.21273	**3.257** +/- 0.15131	**1.9188** +/- 0.02706	**3.1041** +/- 0.08814
Na	**0.5548** +/- 0.04949	**0.6693** +/- 0.04065	**1.1824** +/- 0.03553	**0.7985** +/- 0.02525	**0.4268** +/- 0.00683	**0.7284** +/- 0.01472	**0.45313** +/- 0.01394
Mg	**0.634** +/- 0.03288	**0.6045** +/- 0.03325	**0.4538** +/- 0.02168	**0.08775** +/- 0.00907	**0.0982** +/- 0.01254	**0.083** +/- 0.00616	**0.07263** +/- 0.00578
P	**12.8694** +/- 0.26945	**12.7674** +/- 0.22359	**11.2767** +/- 0.19764	**11.276** +/- 0.14359	**11.5778** +/- 0.07685	**12.682** +/- 0.11702	**11.9246** +/- 0.12764
Cl	**0.05445** +/- 0.0167	**0.0481** +/- 0.00789	**0.1078** +/- 0.01469	**0.01225** +/- 0.01008	**0.0396** +/- 0.01552	**0.0764** +/- 0.01019	**0.03813** +/- 0.01013
Ca	**21.8761** +/- 0.01687	**20.4804** +/- 0.37542	**20.3276** +/- 0.2053	**20.9148** +/- 0.17694	**21.4124** +/- 0.05104	**23.3446** +/- 0.23381	**21.8855** +/- 0.03788
Fe	**0.0042** +/- 0.00681	**0.0037** +/- 0.00558	**0.0048** +/- 0.00786	**0.097** +/- 0.01539	**0.4088** +/- 0.01033	**0.5432** +/- 0.01026	**0.16838** +/- 0.01950
TOTAL	100.0342	100.0734	100.0073	100.005	100	100	100

Appendix H. Summary of experimental XRD peak values for *Tyrannosaurus*.

The data table given below presents the tabulated experimental peak values for the powdered *Tyrannosaurus* specimen, compared against tabulated data from the NIST hydroxyapatite standard (SRM 2910). Of note are one unidentified peak, several absent peaks of low-intensity, and several peaks that could not be resolved due to close spacing. Based on this analysis, this spectrum clearly matches that of hydroxyapatite. In light of the WDS data, however, the data are interpreted to support the notion that this is bioapatite that has partially converted to fluorapatite. The low peak intensities are a consequence of nanocrystallinity and impurity, with emphasis placed on the former.

Table H.1 Peak values of interest for powdered *Tyrannosaurus*. The 2θ and relative intensity (I_{rel}) values also are reported for the NIST hydroxyapatite standard (SRM 2910). Only one unidentified peak was found. Several close peaks could not be resolved with this detector, and several low-intensity peaks could not be detected.

hkl	NIST 2θ (SRM 2910)	Experimental 2θ	I_{rel} (SRM 2910)
200	21.76	21.85	6
111	22.85	22.9	6
201	25.35	(absent)	2
002	25.86	25.85	35
(unidentified)		26.65	
102	28.11	28.1	9
210	28.93	29.1	16
211	31.77	32.0	100
112	32.18	(unresolved)	53
300	32.90	33.1	63
202	34.05	34.9	24
301	35.46	35.7	5
212	39.18	39.45	6
310	39.80	40.05	23
221	40.44	(absent)	2
311	41.99	42.35	6

hkl	NIST 2θ (SRM 2910)	Experimental 2θ	I_{rel} (SRM 2910)
302	42.31	(absent)	1
113	43.84	43.85	5
400	44.37	(absent)	1
203	45.30	45.4	5
222	46.69	46.9	28
312	48.07	48.3	13
320	48.59	(unresolved)	4
213	49.46	49.55	32
321	50.48	50.9	16
410	51.26	(absent)	11
402	52.07	52.3	12
004	53.17	53.15	14
104	54.43	(absent)	1
322	55.86	56.1	5
313	57.11	57.05	4
501	58.03	58.05	2
412	58.29	58.35	2
330	58.75	58.65	1
420	59.93	59.9	5

Appendix I. TEM electron diffraction pattern analysis.

The following is provided to demonstrate the process used to extract measurements from the TEM diffraction patterns collected from the fossil bone specimens. This approach is based on the standard calibration technique used for TEM diffraction pattern analysis. The standard used (Figure I.1) was polycrystalline aluminum, purchased from Ted Pella, Inc. All camera lengths on the JEOL JEM 2011 were 40 cm.

Step 1.
The polycrystalline aluminum diffraction pattern was recorded at a camera length (L) or 40 cm, at the same operating conditions used for all specimens. According to the calibration data (Table I.1) provided by Ted Pella, Inc., the rings in the aluminum diffraction pattern were indexed. Ring dimensions were collected based on width and height measurements (in pixels) of overlaid circles (Table I.2). These values were then averaged for each ring, yielding an average ring diameter. In Figure I.1, the rings are indexed, and an example circle is overlaid on the pattern.

Figure I.1 The polycrystalline aluminum diffraction pattern used to calibrate the fossil bone data, collected with a camera length of 40 cm under the same operating conditions as the fossil specimens.

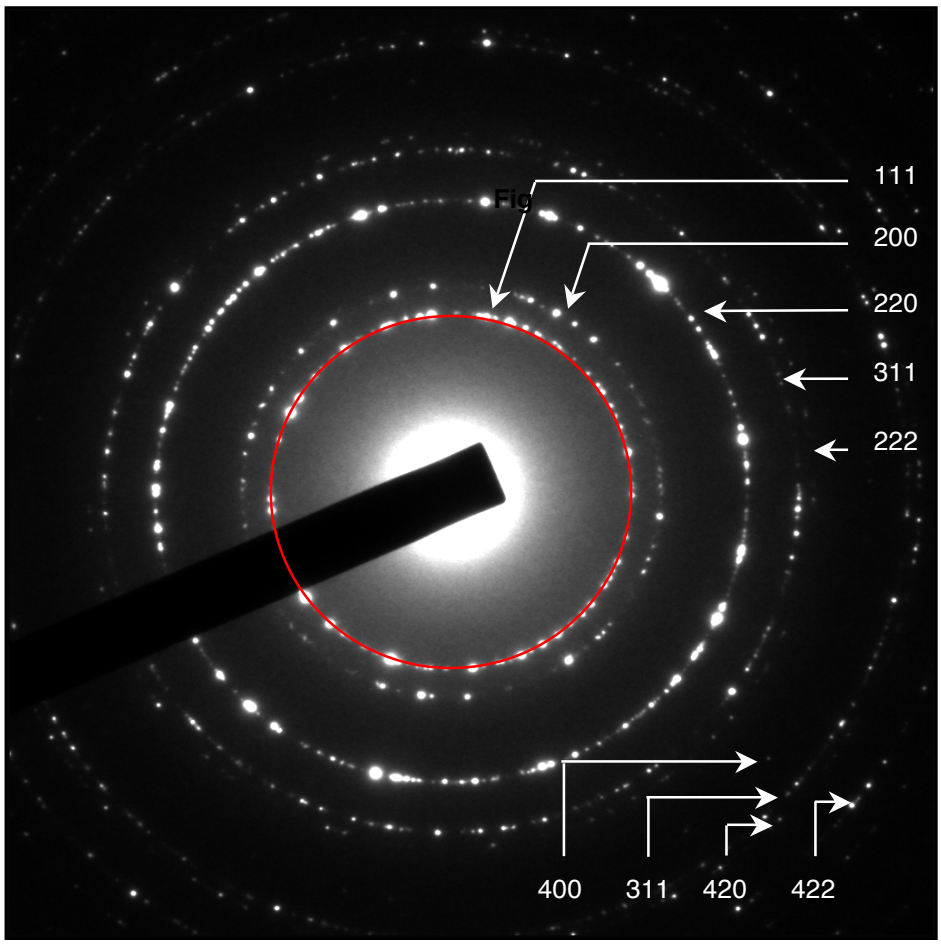

Table I.1 Tabulated data provided by Ted Pella, Inc., for the polycrystalline aluminum diffraction standard. These data were used to identify the rings in the diffraction pattern above.

hkl	d (Å)	I_{rel}
111	2.338	100
200	2.024	47
220	1.431	22
311	1.221	24
222	1.1690	7
400	1.0124	2
331	0.9289	8
420	0.9055	8
422	0.8266	8

Step 2.
After the measurements were extracted from the diffraction pattern, the d-spacing values were used to calculate the inverse d-spacing values (given in Table I.2). Then, according to the camera constant equation, which is given as

$$r \cdot d = \lambda L \qquad \text{(App. 1)}$$

the data can be plotted as r *vs.* 1/d, where the slope is given by the camera constant (λ L). Ideally, the slope should be linear. The plot is shown in Figure I.2 for 2r *vs.* 1/d.

Step 3.
The data points in the plot were fitted with a linear regression curve. The high correlation coefficient is indicates a good linear fit to these five data points. The slope in the line equation (632.74) is the camera constant (λ L) and can now be used to calculate the unknown d-spacings of the fossil samples from their respective diffraction patterns.

Step 4.
To calculate the d-spacings from the fossil samples, a similar approach was used. First, the rings were measured. This time, however, the average ring dimensions were the y-values, and using the equation in the linear regression fit from Figure I.2, the d-spacings were determined individually, for each ring of interest.

Table I.2 The width/height measurements extracted from the aluminum diffraction standard. The average pixel values (diameter = 2r) were calculated. This table also includes the calculated 1/d values used in the r *vs.* 1/d plot.

hkl	width	height	avg. (2r)	1/d ($Å^{-1}$)
111	272	268	270	0.4277
200	315	310	312.5	0.4941
220	446	438	442	0.6988
311	523	513	518	0.8190
222	546	538	542	0.8554
420	709	695	702	0.9878

Figure I.2 The plot of r *vs.* 1/d from the measurements given in Table I.2. The slope of the linear regression equation (632.74) was used to calculate the d-spacings of the unknown fossil samples given the ring measurements, collected under the same operating conditions and at a camera length (L) of 40 cm.